NASA CR-66718
LMSC-677802

A NEW CONCEPT FOR CONTROLLED LIFTING ENTRY FLIGHT EXPERIMENTS

13 April 1967 LMSC-677802

By R. L. Nelson, D. A. Price, and F. H. Delpino
Advanced Programs, Research and Development Division
Lockheed Missiles & Space Company

LOCKHEED MISSILES & SPACE COMPANY
Sunnyvale, California

Prepared under Contract No. NAS1-6740

NATIONAL AERONAUTICS AND SPACE ADMINISTRATION
Langley Research Center
Langley Station, Hampton, Va.

ABSTRACT

The report considers the feasibility of a guidance and control concept to provide trajectory control for a lifting configuration with roll modulation. Roll control is obtained without reaction controls or aerodynamic flaps by incorporating a motor driven moveable weight (control mass). Hardware components required include a longitudinal accelerometer, two visible light horizon sensors, a roll rate gyro, and guidance electronics. Entry is assumed to occur after separating from a spinning, inertially stable, burned out rocket motor at an altitude above the sensible atmosphere.

Results of the study indicate: (1) the guidance and control concept provides trajectory control that enables simulation of manned lifting entry corridor environments; (2) the systems can be packaged in small scale spacecraft; (3) the spacecraft can be boosted to a velocity in excess of circular orbit speed with a boost vehicle such as Scout; (4) the spacecraft can be despun from an entry spin rate of 3 cps utilizing the control mass as the despin mechanism.

CONTENTS

Contents (Concl.)

SYMBOLS

a_D	Drag deceleration - ft/sec^2
a_x	Axial acceleration - ft/sec^2
A	Reference area - ft^2
$A_{11,12...}$	Constant defined in text
$B_{11,12...}$	Constant defined in text
$C_{1,2}$	Constant defined in text
C_A	Axial force coefficient
C_D	Drag coefficient
C_f	Skin friction coefficient
C_l	Rolling moment coefficient
C_m	Pitching moment coefficient
C_n	Yawing moment coefficient
C_L	Lift coefficient component in the vertical (altitude) direction
C_N	Normal force coefficient
C_P	Pressure coefficient
C_Y	Side force coefficient
d	Reference length - ft
D	Drag - lbs
g	Acceleration of gravity - ft/sec^2
$G_{1,2...}$	Constant defined in text
h	Altitude - ft
$I_{x,y,z}$	Moment of inertia - slug ft^2

Symbols (Cont.)

$K_{1,2,3,..}$	Constant defined in text
k_x	Radius of gyration about the longitudinal axis - ft
k_z	Radius of gyration about the lateral axis - ft
L	Total lift - lbs
m	Mass - slugs
p	Roll rate - radians/sec
P	Pressure - lbs/ft^2
q	Pitch rate - radians/sec
$\dot{q}$	Heating rate - BTU/ft^2sec
$\bar{q}$	Dynamic pressure - lbs/ft^2
r	Radius of the earth- 20.9×10^6 ft
R_N	Nose tip radius - ft
R	Flight range - nautical miles
s	La Place transform
t	Time - sec
V	Velocity - ft/sec
V_{orb}	Orbital velocity in altitude range of test 25,600 ft/sec
W	Weight - lbs
XR	Crossrange - nautical miles
y_g	Center of gravity displacement from centerline - ft
y_m	Control mass center of gravity displacement - ft
α	Angle-of-attack - deg
β	Angle of sideslip - deg or inverse scale height 23,500 ft or time constant - sec

Symbols (Concl.)

γ	Flight path angle - deg
θ	Inertial attitude angle- deg
λ	Trim asymmetry orientation angle
ρ	Atmosphere density - slugs/ft^3
τ	Shear stress - lbs/ft^2
ψ	Azimuth angle - deg
ϕ	Roll angle - deg
ϕ_{xy}	Longitudinal principal axis inclination - deg
ω	Oscillation frequency radian/sec

A NEW CONCEPT FOR CONTROLLED LIFTING ENTRY FLIGHT

By R. L. Nelson, D.A. Price, and F. H. Delpino
Advanced Programs, Research and Development Division
Lockheed Missiles & Space Company

SUMMARY

For the future flight experiments applicable to advanced manned orbital and hyperbolic entry systems, a lifting trajectory capability will be required. A new technique has been developed which permits controlled lifting experiments with only a moderate increase in complexity over the ballistic spacecraft. Key to the system's simplicity is the employment of a moveable mass within the vehicle for roll (and trajectory) control. This study (NASA Contract NAS 1-6740) covers an investigation in depth to demonstrate applicability of the many concept elements to a reentry spacecraft sized to Scout constraints. Study elements include guidance and control system design and simulation, an entry dynamics and despin analysis, reentry shape development, a spacecraft conceptual design, and generation of optimized flight trajectories. The entry flight environment spectrum of the design is also compared to that for advanced manned entry systems.

The results show that precisely controlled Scout lifting reentry testing programs are practical through utilization of the suggested concept. Manned lifting reentry spacecraft heating can be duplicated by the test configuration both in level and in duration. For the flight profile selected optimum Scout performance is obtained with the maximum speed capability of 29,000 ft/sec indicated. The concept was not restricted by the Scout's volume and weight limitations. The concepted spacecraft had a weight of 190 lbs. and contained the guidance and control system, a complete data and ground command system, and a recovery system.

1. CONCEPT DESCRIPTION

1.1 Background Leading to the Study

With the crystalizing of requirements for the next generation of manned orbiting spacecrafts, especially those considerations relating to improved entry and space maneuverability and reuseability, it has become apparent that applicable lifting reentry model flight tests will be required. For these applications it is unlikely that ballistic flight tests will provide sufficient environment simulation to make such tests attractive. Of comparable importance, the attainment of controlled flight conditions through active guidance and the minimization of oscillatory motion can add considerably to the value of the tests.

In addition, the extension of these lifting entry flight test techniques to hyperbolic speeds required for planetary return mission research is also desirable. A controlled lifting entry can provide improved simulation and an added degree of simulation flexibility.

Because of the high cost of reentry flight testing, good simulation and minimization of the cost, complexity,and weight of the lifting reentry test model are almost mandatory. (Model development and testing costs which approach prototype costs are not saleable).

With these considerations in mind, a concept was formulated in the winter of 1964-1965 which appeared to be sufficiently attractive to suggest lifting entry tests from orbital velocity with the Scout as the injection vehicle. This study (NASA Contract NAS 1-6740) covers an integrated investigation in depth to demonstrate applicability of the many concept elements to future NASA lifting entry testing.

1.2 Description of the Concept

1.2.1 Trajectory Control

During reentry, the spacecraft is constrained to following preset deceleration history. A longitudinal accelerometer senses the acceleration error which provides the command to adjust the lift for climb or dive to the proper flight altitude. Thus, the atmosphere is used as an acceleration control device. A constant (1 g) deceleration program was chosen for study because of its simplicity. This level is also in the range of interest for manned lifting entry. Because of its good accuracy, as will be shown later, this approach has general application to manned and unmanned controlled entry. The configuration vertical lift is adjusted by rolling the spacecraft rather then by changing the angle-of-attack and thus follows the Gemini-Apollo control approach.

1.2.2 Hardware Components

The hardware philosophy was that minimum equipment additions would be permitted over those required for the ballistic entry spacecraft thus far flown on Scout. The evolved system concept ingredients for trajectory control are depicted in Fig. 1.1. The spacecraft configuration is modified sufficiently to provide the necessary aerodynamic lift while maintaining some of the desirable features of ballistic spacecraft such as flow symmetry and simplicity and the maintenance of good pitch stability. The major control element consists of a motor driven moveable weight (control mass) which together with the fixed body lift provides roll torques. To the longitudinal accelerometer normally required for reconstructing a ballistic spacecraft trajectory, a simple visible light horizon sensor, a roll rate gyro, and guidance and control electronics are added to provide trajectory control. This represents the total change from a ballistic spacecraft. Note that no external aerodynamic control surfaces are employed. Fig. 1.2 summarizes the application of these guidance and control system elements to the lifting reentry flight system.

1.2.3 Roll Control

As shown in the left hand plot of Fig. 1.2, the control mass is displaced laterally and held fixed during the initial portion of the reentry to provide

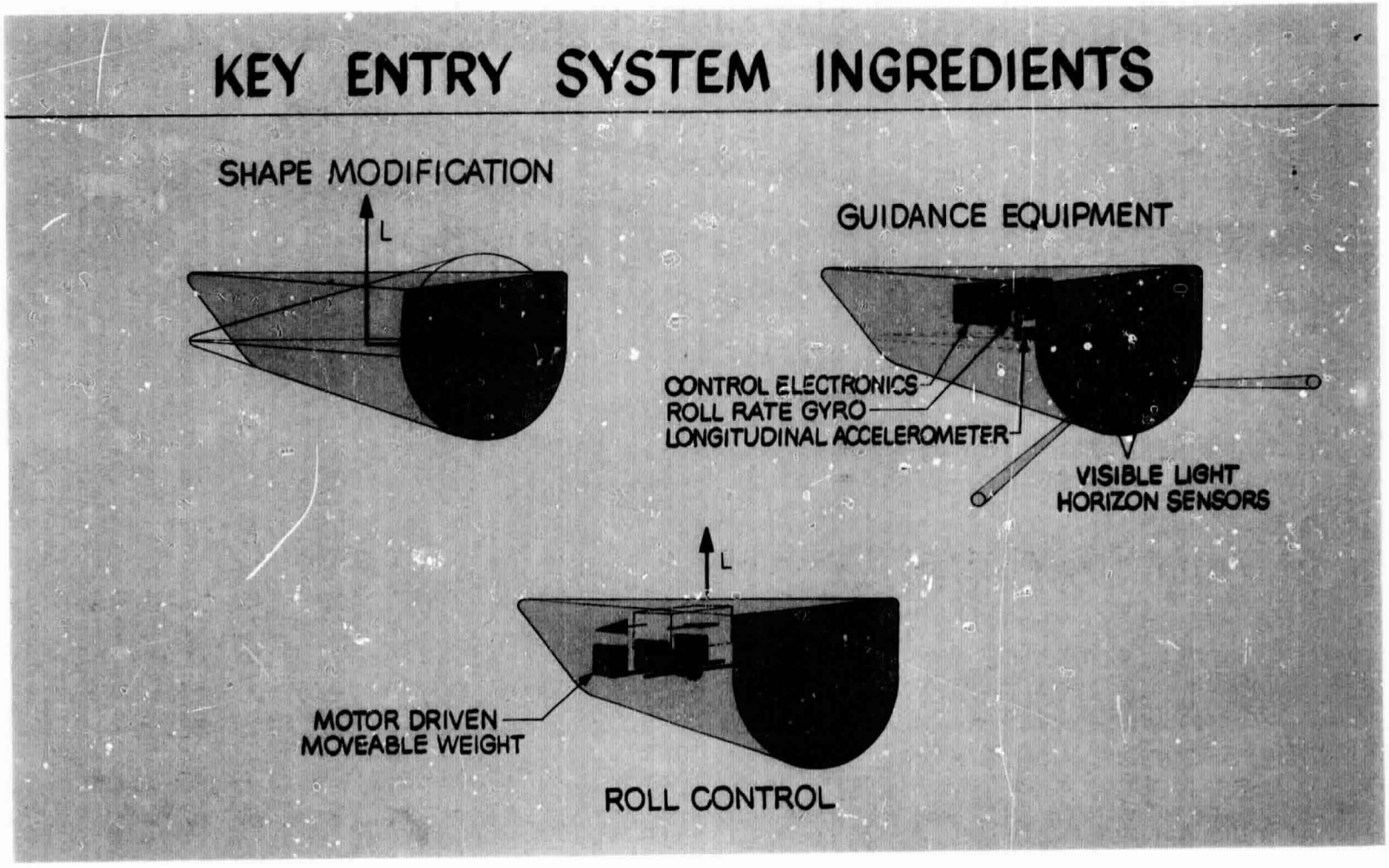
KEY ENTRY SYSTEM INGREDIENTS
SHAPE MODIFICATION
L
GUIDANCE EQUIPMENT
CONTROL ELECTRONICS
ROLL RATE GYRO
LONGITUDINAL ACCELEROMETER
VISIBLE LIGHT
HORIZON SENSORS
L
MOTOR DRIVEN
MOVEABLE WEIGHT
ROLL CONTROL

Fig. 1.1

APPLICATION OF GUIDANCE & CONTROL SYSTEM ELEMENTS

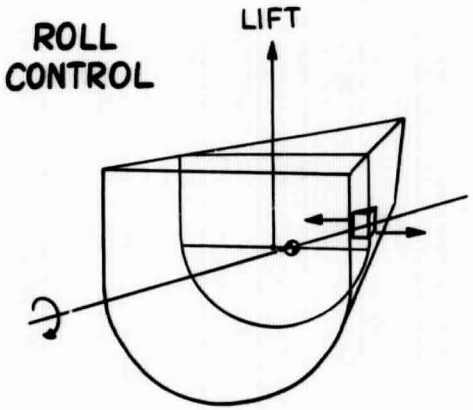

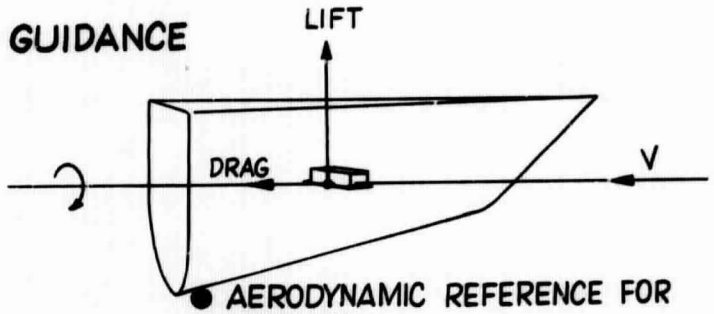

- AERODYNAMIC REFERENCE FOR GUIDANCE
- CONTROLLED DRAG DECELERATION HISTORY
- SINGLE AXIS ROLL ANGLE CONTROL

- FIXED CONTROL MASS DISPLACEMENT FOR DESPIN
- AUTOMATIC CONTROL MASS POSITIONING FOR ZEROING UNWANTED ROLL TORQUES
- CONTROL MASS DISPLACEMENT TO PROVIDE ROLL ANGLE COMMANDS

PREGUIDANCE ERROR DETECTION

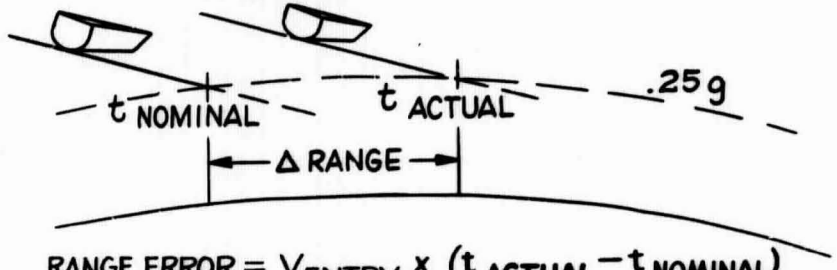

$$\text{RANGE ERROR} = V_{ENTRY} \times (t_{ACTUAL} - t_{NOMINAL})$$

Fig. 1.2

the braking moment for despin, since the lift can provide an opposing moment about the offset center of gravity. This application of the control mass eliminates the requirement for despin reaction controls on the spacecraft. Since spin is maintained down into the atmosphere whre despin is accomplished by aerodynamic action, the boost trajectory can be shaped to provide an angle-of-attack at burnout of the spinning last stage that results in a near zero angle-of-attack at atmospheric entry and is essentially unaffected by errors in time of entry.

After despin, the control mass zeros roll torques due to aerodynamic asymmetry and errors in lateral center of gravity position, thus eliminating controls or aerodynamic flaps for maintaining roll control. Finally, the control mass is displaced laterally from the zero position to provide the roll attitude positioning necessary for trajectory control.

The roll control concept was arrived at following studies of the roll-pitch coupling problems of reentering and ascent vehicles and the identification of mass and aerodynamic asymmetries as the source and mechanism for the loss of roll rate control and dynamic instability (Ref. 1 and 2).

1.2.4 Guidance

Inherent aerodynamic stability of the reentry configuration can provide the guidance reference system if the spacecraft is configured to have good pitch stability. This approach eliminates the need for an onboard inertial reference package or platform. A precise longitudinal accelerometer is aligned to the expected velocity vector direction. The concept infers that the trim angle-of-attack can be predicted to good accuracy on the basis of pre-flight estimates, wind tunnel testings, and flight calibration.

As described above, the reentry spacecraft is constrained to follow a controlled drag deceleration history. The benefits from following a preset drag deceleration history are not immediately obvious. Appendix A shows some key features for a number of physically desirable reentry descents based on the relationships derived in Ref. 3. As shown in Appendix A, a controlled drag deceleration profile provides the following benefits:

1) Flight path control is achieved
2) Range control is achieved
3) The trajectory adjusts for aerodynamic and air density uncertainties

The spacecraft is not disturbed in pitch for trajectory control since it relies on its aerodynamic stability to hold the guidance reference. (A change in angle-of-attack would produce a change in longitudinal acceleration which would call for change in altitude to hold the prescribed drag deceleration value). Single axis control of the trajectory is obtained by rolling the spacecraft about the velocity vector to provide the nominal lift required to follow the set drag deceleration history and to provide the incremental lift for deceleration corrections.

The combination of these guidance concept elements produces trajectory controllability that is relatively insensitive to the flight velocity and is proportional to the drag deceleration level so long as the equilibrium glide limit is not approached. Thus, the guidance concept can be extended to hyperbolic entry testing. Appendix B develops the relationships which form the basis for the extrapolation.

1.2.5 Pre-Guidance Error Detection

The Scout launch system will have injection errors at fourth stage burnout considerably greater than those systems which utilize inertial equipment for booster attitude control to injection. (The major Scout injection errors are attributed to tip off of the spun fourth stage). If the errors accrued to the impact point from the Scout were uncorrected, the dispersion would be unacceptable for the shallow reentries typical of lifting tests. Since the test spacecraft is guided to a given density altitude history, initial flight path angle errors will be corrected once capture to guided flight has taken place. However, the large error accrued up to the capture point remains. This pre-guidance dispersion due to injection altitude and flight path errors can be detected by measuring the time to a given deceleration level (Fig. 1.2). The accrued range error for shallow entry is simply the entry velocity multiplied by the error in time of arrival.

1.3 Study Scope

To demonstrate the applicability of the overall reentry test concept to Scout experiments, it was necessary to investigate in some detail the individual flight phases and systems elements to determine possible consequences of conflicting requirements. The chief study elements are illustrated in Fig. 1.3 and are described below.

1.3.1 Scout Performance

Of special concern were the boost trajectory shaping and performance for shallow low altitude reentries typical of lifting descents and the selection of the most satisfactory complete flight profile. It was also necessary to determine the effects of constraining the injection angle-of-attack so as to minimize oscillatory motion at the beginning of guidance. In determining Scout performance, the recently developed LMSC TOLIP program was employed. This made possible the generation of realistic Scout trajectories since the program is sufficiently comprehensive to be employed in pre-flight planning.

1.3.2 Entry Dynamics and Despin

To demonstrate satisfactory despin performance, it was necessary to consider in combination an initial angle-of-attack, the effects of vehicle pitch-yaw asymmetry and the time varying environment. Of special concern was the roll-resonance phenomena for a spacecraft purposely made geometrically asymmetric. A modification was made to the RPM computer program (Ref. 2) developed for NASA-Goddard to simulate these effects.

1.3.3 Guidance and Control

The guidance and control effort included evolving an overall guidance hardware concept, systems analysis, design and simulation. Of special concern was the demonstration of the satisfactory operation of the control system for all phases of flight from the initiation of despin to low speed. To accomplish this, a six degree-of-freedom simulation tailored to the guidance and control system was developed.

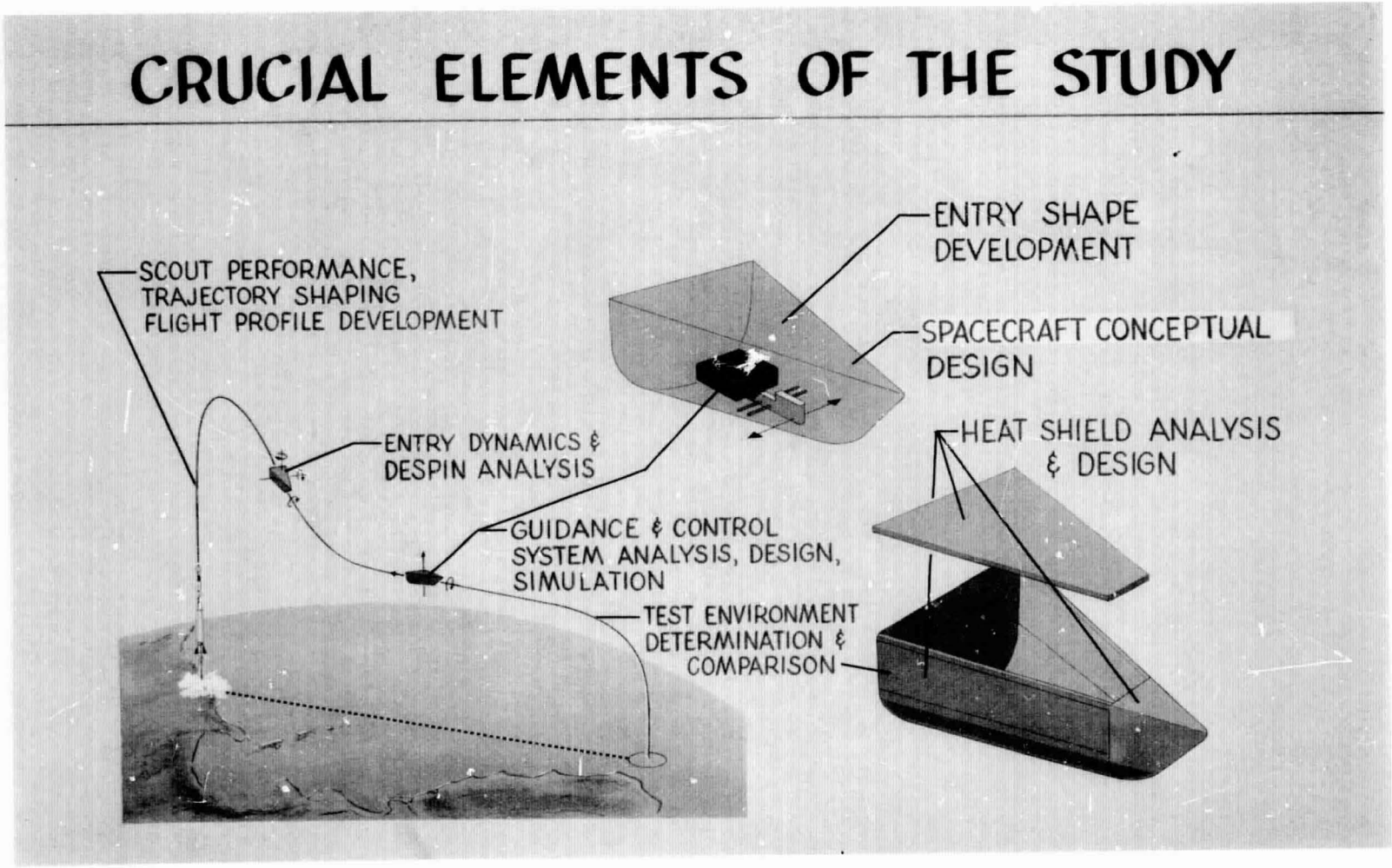
CRUCIAL ELEMENTS OF THE STUDY
SCOUT PERFORMANCE, TRAJECTORY SHAPING FLIGHT PROFILE DEVELOPMENT
ENTRY SHAPE DEVELOPMENT
SPACECRAFT CONCEPTUAL DESIGN
ENTRY DYNAMICS & DESPIN ANALYSIS
HEAT SHIELD ANALYSIS & DESIGN
GUIDANCE & CONTROL SYSTEM ANALYSIS, DESIGN, SIMULATION
TEST ENVIRONMENT DETERMINATION & COMPARISON

Fig. 1.3

1.3.4 Entry Shape Development

Since the guidance and control system concept required specified aerodynamic characteristics, it was necessary in the course of the study to investigate different configuration approaches in arriving at the selected reentry shape. A Newtonian aerodynamics computer program especially developed for configurations similar to those considered under the study was employed.

1.3.5 Heat Shield Analysis and Design

To demonstrate validity of the aerodynamic concept it was necessary to assess the consequences of ablation during guided flight. This required determination of the heating environment, the selection of heat shield materials, heat shield design and prediction of the response to the entry environment.

1.3.6 Spacecraft Conceptual Design

The spacecraft conceptual design was aimed at demonstrating that the test configuration sized to Scout dimensional constraints could house the required guidance and control equipment, a data system and a recovery system and that the resulting configuration would have satisfactory inertial properties.

1.3.7 Test Environment

To demonstrate the simulation capability of the final design, it was necessary to review the flight environment for advanced manned entry spacecraft and to compare that environment with the environment to be expected for the design. In demonstrating the environment simulation capability, a new approach to the environment comparison was developed so as to separate trajectory and configuration affects in a clear and meaningful way.

2. SPACECRAFT AERODYNAMICS

The proceding section has outlined the overall reentry system concept and has indicated some of the underlying technology responsible for selection of individual concept elements with good performance potential and growth. Evolution of the aerodynamic design is next treated since proof of the concept validity is well on the way if acceptable aerodynamics can be obtained.

2.1 Aerodynamic Requirements

2.1.1 Requirements for L/D

Figure 2.1 summarizes the requirements for lift-drag ratio which are set by the overall concept. For despin and capture to guided flight, a change in L/D will change the required control mass weight. The altitude (or g-level) for despin is dependent on the braking moment from the lift-force-offset center-of-gravity combination. For a given despin altitude or g-level the control mass weight must be increased to counter a reduced L/D. Also, for a set pullout g-level, the despin altitude must be increased for a reduced L/D. These combined relationships are illustrated in the left hand plot of Figure 2.1 for the specified entry conditions. Note that the curve becomes asymptotic for an L/D of .6, indication that the prescribed pullout conditions cannot be met for that value of L/D. Reduced control mass weight requirements for L/D's greater than 1 are readily evident. The required control mass weight will increase with a steepening entry angle and with a higher initial spin rate for a prescribed pullout g-level.

The limiting altitude (or g-level) for controlled reentry flight is the equilibrium glide trajectory. Thus, the ability to fly low g descents is limited by the spacecraft's L/D capability. For controlled model flight it is necessary to operate at altitudes lower than the equilibrium glide limit. In Appendix B, equations were developed relating flight drag deceleration and L/D for a fixed trajectory control capability. This

REQUIREMENTS FOR L/D

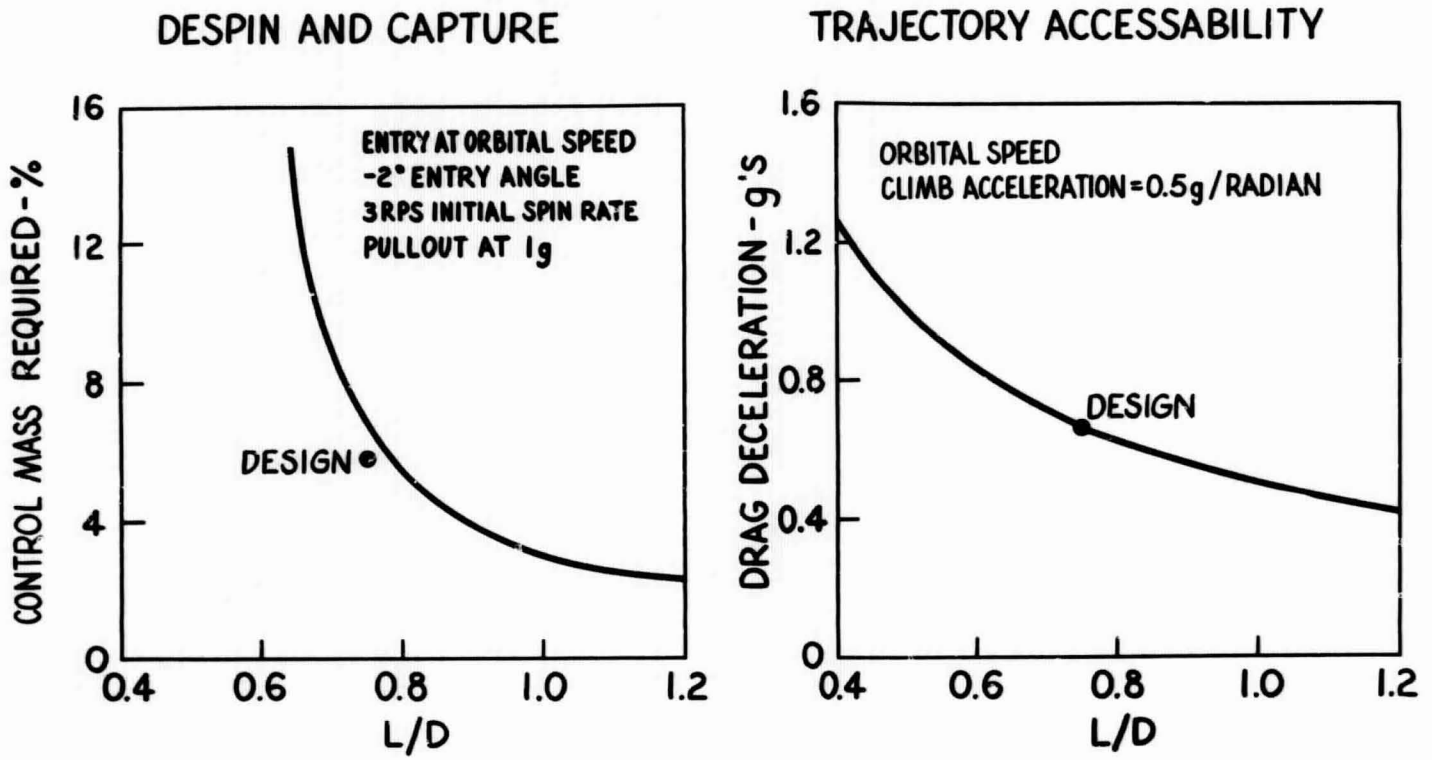

Fig. 2.1

relationship is shown in the right hand plot of Fig. 2.1. Flight at g-levels less than 1 is desirable since this is the expected range for manned orbital entry spacecrafts. Both plots demonstrate that an L/D on the order of 1 is desirable.

2.1.2 Trim Angle-of-Attack Requirements

One of the key points of the guidance concept is the employment of an aerodynamic reference system that makes possible the elimination of inertial reference equipment on the spacecraft. Errors in the aerodynamics references come about from misalignment of the velocity vector and the sensing longitudinal accelerometer. The primary error is introduced by a component of the lift being sensed by the longitudinal accelerometer. The impact range error resulting from such an effect is shown in the left hand plot of Figure 2.2 for a 1-g descent trajectory from orbital speeds. This error is directly proportional to the nominal guided flight range. In turn, the impact range error is inversely proportional to the g-level. Thus, a reduced g-level will produce increased error.

An error in the trim angle-of-attack will also contribute to the development of angle-of-attack oscillations, as a result of passage through roll resonance during despin. This effect is shown in the right hand plot of Fig. 2.2 for a 3 RPS initial spin rate and a 2° entry angle. This result was obtained from digital computer solutions which take into account aerodynamic asymmetry and the varying spin rate during entry. Note that large oscillations will develop if the trim angle-of-attack is not controlled closely. A 20° angle-of-attack oscillation is produced by a 2° angle-of-attack error. Reducing the initial spin rate will reduce the severity of the effect while steepening the entry angle will increase the magnitude of the oscillations.

Physically, the effect is produced by misalignment of the roll axis (the velocity vector) and the principal axis for spin. As a result, this figure may also be interpreted with the abscissa labelled as the

CONSEQUENCES OF A TRIM ANGLE OF ATTACK ERROR

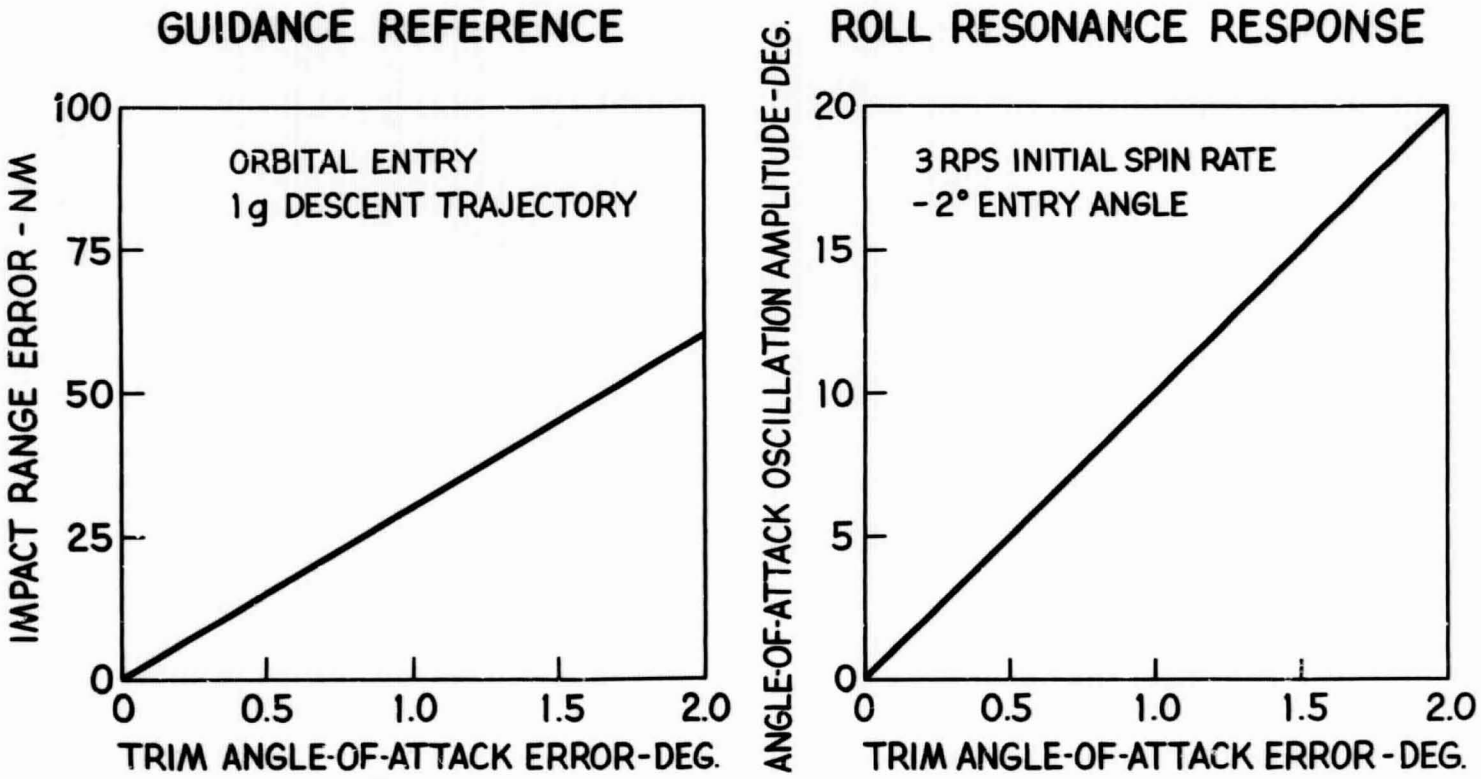

Fig. 2.2

angle between the velocity vector and the spin principal axis. Thus, alignment of the spin principal axis with the expected trim angle is also extremely important and implies that the trim angle-of-attack must be known to properly align the spin axis. From both the right and left hand plots, the trim angle-of-attack accuracy goal of about $.5^{\circ}$ appears appropriate for enhancement of the concept.

2.1.3 Roll Stability Requirements

Since the rolling moment for trajectory control is developed by disturbing the spacecraft symmetry, an angle of sideslip is developed from the drag moment acting about the center of gravity. The sideslip produces a side force which can produce a rolling moment which counteracts the rolling moment produced by the trim lift. This effect is illustrated in Fig. 2.3 where the rolling moment degradation is plotted against the governing parameter, the ratio $C_{\ell_\beta}/C_{n_\beta}$.

For a given rolling moment capability, the rolling moment degradation will require an increase in control mass weight. Note that for $C_{\ell_\beta}/C_{n_\beta}$ equal .7 the net rolling moment is zero. A design goal of C_{ℓ_β} equals zero has been selected.

The magnitude of C_{ℓ_β} is minimized by shaping the lateral planform so that its center of area lies near the flight center of gravity.

2.2 Prediction of Aerodynamic Properties

An aerodynamics shape meeting the requirements of Fig. 2.1 was evolved using Newtonian theory prior to the submission of the LMSC-proposed study proposal. The geometry of the configuration (referred to in this document as the basic configuration) is shown in Fig. 2.4. Governing condition in additional to the requirements of Section 2.1 was that the flow field be either axysymmetric or of two-dimensional character so that cross flow uncertainties would be minimized. In addition, it was felt advantageous to employ flat surfaces so that simple material test panels could be incorporated if desired.

CONSEQUENCE OF A NON-ZERO C_{ℓ_β}

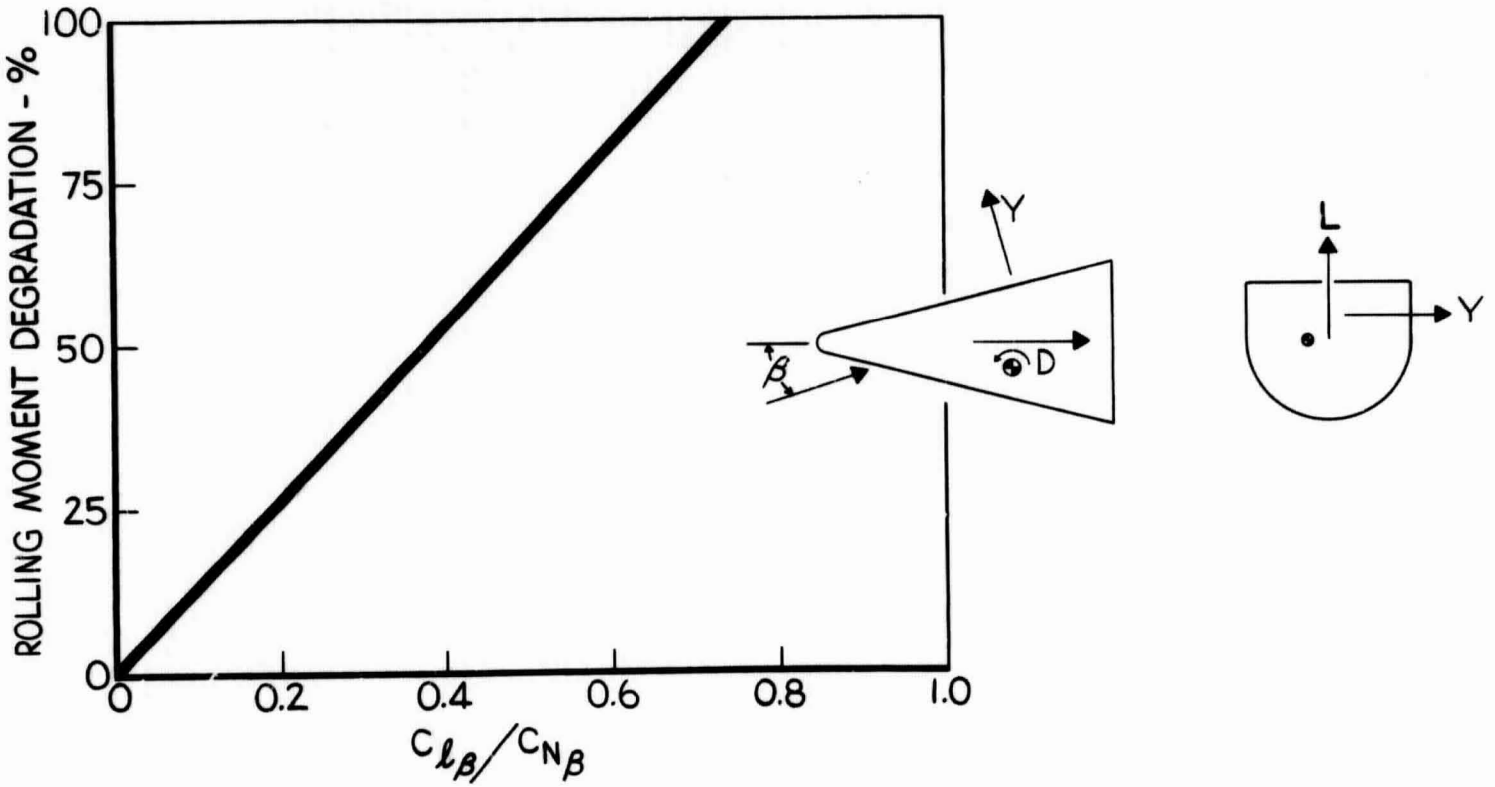

Fig. 2.3

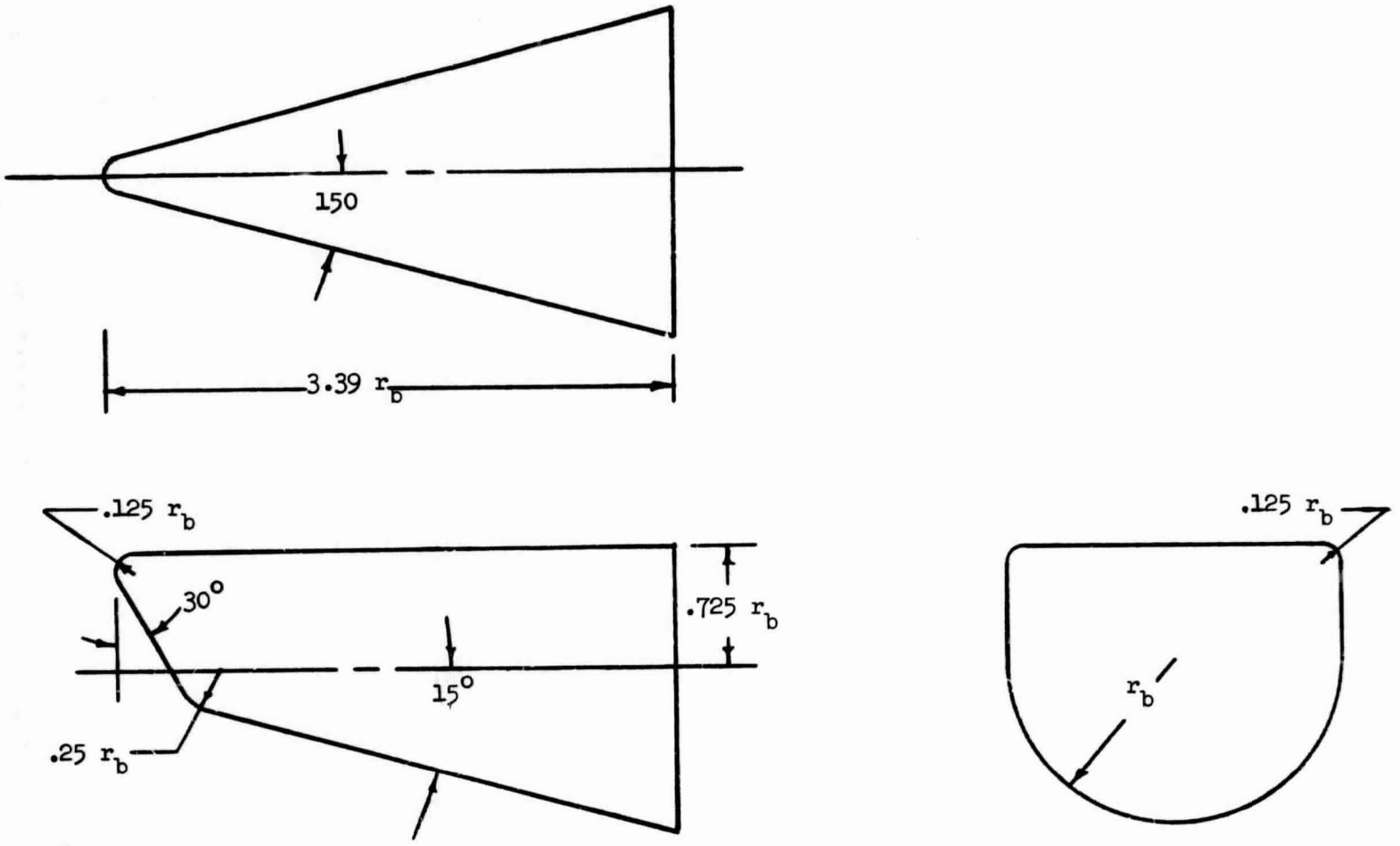

Fig. 2-4 BASIC CONFIGURATION DIMENSIONAL CHARACTERISTICS

The basic configuration was tested in the Langley Unitary Tunnel in 1964 and 1965. A comparison of the experimental results with design predictions generated prior to the tests is presented in Fig. 2.5. The agreement in the force characteristics is remarkable at the test Mach No. of 4.63. Also the agreement between measured and theoretical centers of gravity for trim give confidence in the predictability of the trim angle-of-attack.

Early in the study it became apparent that the agreement shown in Fig. 2.5 would not necessarily hold at orbital entry speeds. Examination of the predictions and measurements of the effects of nose bluntness induced pressures on cones indicated that the severity of these effects would be suppressed at the tunnel test Mach number (4.63) but could be considerable at higher speeds. As a result, it was felt necessary to make allowances for bluntness induced pressures on configurations having the general geometry of the basic configuration of Fig. 2.4.

For the more detailed examination of aerothermodynamics phenomena, the flow field models of Fig. 2.6 have been assumed. Since the extent and magnitude of bluntness induced pressures has been correlated with nose drag (Ref. 4 and 5) equivalent drag hemispherically tipped conical surfaces have been utilized in the determination of local flow properties. For the conical nose tip and the top of the body, the exact geometry was used in the calculations. The employment of the equivalent body approach allows inclusion of effects of vorticity (shock wave curvature) on both the inviscid and boundary layer flows using digital computer methods of Ref. 6. Within the scope of this study, more exact treatment of the flow field was not possible.

The effects of nose bluntness induced pressures will effect mainly the aerodynamic properties of the conical lower body which generates the major portion of the configuration lift. Reference 7 develops an approximate method for correcting the cone aerodynamic characteristics for these effects. The primary assumption in the development is that the

AERODYNAMIC CONFIGURATION CHARACTERISTICS

(ZERO ANGLE-OF ATTACK)

QUANTITY	DESIGN PREDICTION	LANGLEY UNITARY TUNNEL M=4.63
C_D	0.21	0.20
C_L	0.18	0.19
L/D	0.87	0.92
C_{m_α}	-0.34	-0.42
C_{n_β}	+0.18	+0.10

CENTER OF GRAVITY FOR TRIM

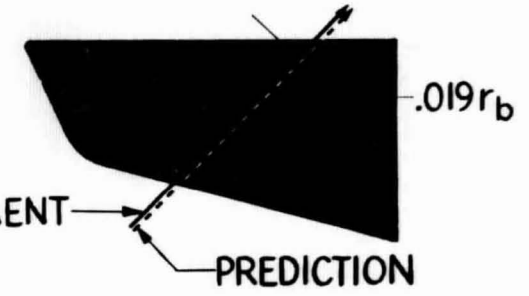

Fig. 2.5

FLOW FIELD MODELS

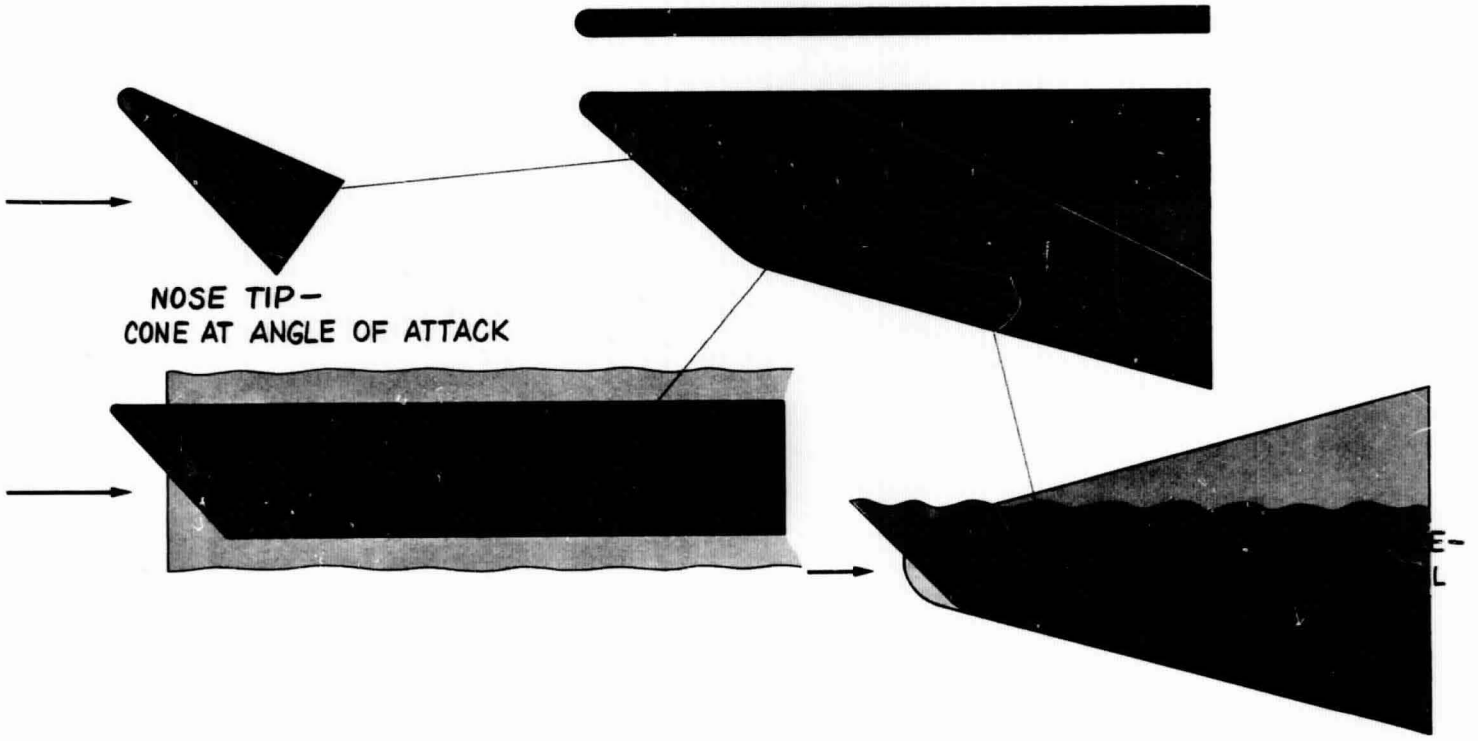

Fig. 2.6

usual overexpansion correlation relationship holds at both zero and small angles-of-attack for the half cone configuration. Application of the method to the basic configuration shows that a reduction of the inviscid L/D from .88 to .69 could result. While not catastrophic, this reduction would have a significant effect on the spacecraft performance.

The general dimensions of the test model are set by the available space within the Scout shroud. For the nominal 1-g descent trajectory and for values of W/C_DA between 200 and 250, the descent Reynolds number is quite low at orbital speed. (The free stream Reynolds number based on body length is about 150,000). Using the method developed by Maslen in Ref. 8, the corresponding skin friction drag is .05 at the pullout condition. With both bluntness induced pressures and skin friction drag included in the correction to the Newtonian L/D, a value of L/D of .55 results. This was felt so low as to require a change from the basic study configuration to regain some of the lost L/D.

2.3 Selected Configuration Characteristics

A number of separate directions were taken to improve the lift-drag ratio characteristics of the design. These include operating the cone at angle-of-attack, extending the vehicle length without disturbing the forebody geometry, toeing in the body sides, and changing the nose tip geometry. The results of these investigations are presented in Appendix C. It was found that the only satisfactory solution meeting the requirements of Section 2.1 was a change in nose tip geometry. In fact, Appendix C shows that changing nose tip geometry was the only way to improve L/D without degrading either the lateral or roll stability. Appendix C also shows that for the bluntness ratios under consideration, the over expansion and friction drag will have little effect on the trim characteristics.

The selected spacecraft configuration is presented in Fig. 2.7. It differs from the basic configuration only in nose geometry. The upper body radius has been reduced from 1.25 inches to 3/4 inch while the lower body radius has been increased from a 3-inch to a 4-inch radius. The resulting sweepback of the nose has been increased from 30 to 45 degrees. The cone angle and wedge height are the same as those for the basic configuration.

Fig. 2.8 shows the division of aerodynamic forces between the nose, the conical lower body, and the sides. Note that the nose force is greater than that for the cone when bluntness induced pressures are taken into account as indicated by the change from the dashed to the solid vectors. Also the nose tip produces over $\frac{1}{2}$ the total Newtonian drag while providing the trimming moment. This reduces the value of W/C_DA to $\frac{1}{2}$ the value of the wedge and cone surfaces and $\frac{1}{4}$ that of the half cone at zero angle-of-attack. This reduction in W/C_DA is in good measure responsible for the low cone and side heating levels to be shown in later sections. The inset figure shows the change in L/D with changing speed. This varying L/D comes about primarily from the changing friction drag with increasing Reynolds numbers during the 1-g descent trajectory. The L/D varys from .74 at orbital speed to a .9 at $\frac{1}{4}$ orbital speed.

Figure 2.9 summarizes the stability characteristics for the selected design.. Both pitch and yaw stability margins have been improved through the modification for design CG placed very close to the roll stability limit. Values of pitch and yaw oscillation periods are less than 1 second and remain nearly constant since the dynamic pressure is approximately constant for the descent trajectory. As will be shown later in the roll control discussion, the pitch and yaw periods differ from the roll period by an order of magnitude. This separation will minimize any coupling between pitch, yaw and roll by suppressing the development of oscillations due to control mass displacement during trajectory control.

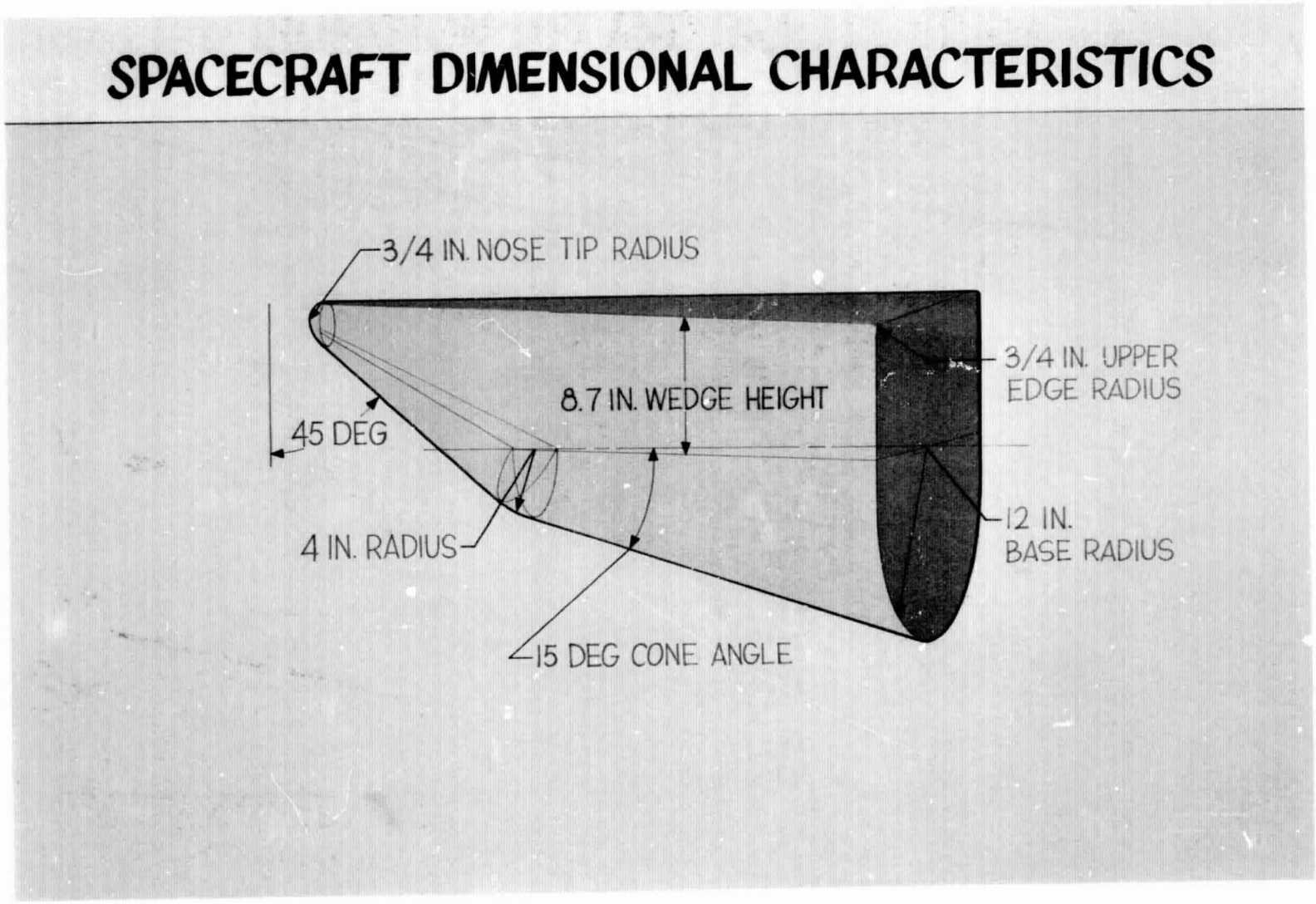
SPACECRAFT DIMENSIONAL CHARACTERISTICS
3/4 IN. NOSE TIP RADIUS
8.7 IN. WEDGE HEIGHT
45 DEG
3/4 IN. UPPER EDGE RADIUS
4 IN. RADIUS
12 IN. BASE RADIUS
15 DEG CONE ANGLE

Fig. 2.7

CONFIGURATION LIFT AND DRAG CONTRIBUTORS

INVISCID FLOW

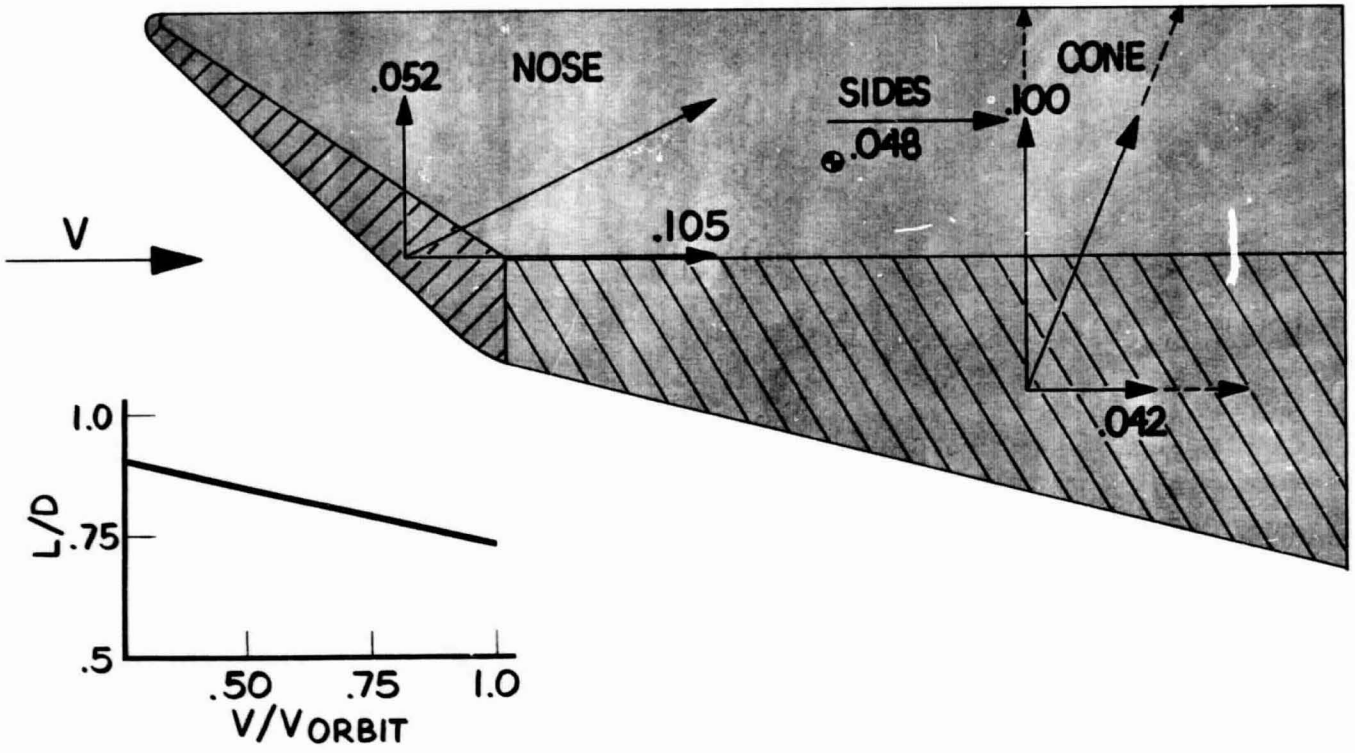

Fig. 2.8

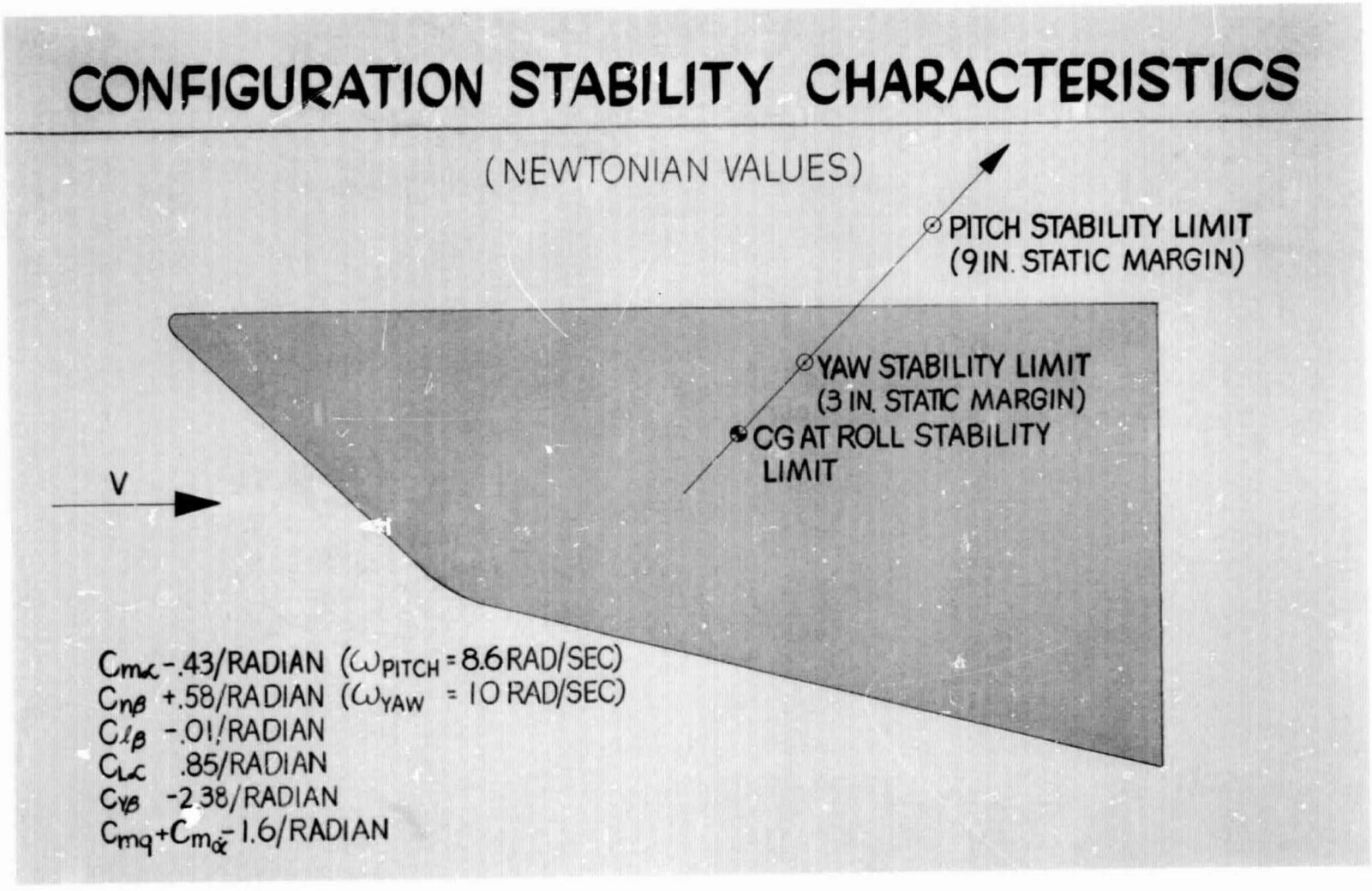
CONFIGURATION STABILITY CHARACTERISTICS
(NEWTONIAN VALUES)
PITCH STABILITY LIMIT
(9 IN. STATIC MARGIN)
YAW STABILITY LIMIT
(3 IN. STATIC MARGIN)
CG AT ROLL STABILITY
LIMIT
V
C_{m_α} -.43/RADIAN (ω_{PITCH} = 8.6 RAD/SEC)
C_{n_β} +.58/RADIAN (ω_{YAW} = 10 RAD/SEC)
C_{l_β} -.01/RADIAN
C_{L_α} .85/RADIAN
C_{Y_β} -2.38/RADIAN
$C_{m_q}+C_{m_{\dot\alpha}}$ -1.6/RADIAN

Fig. 2.9

2.4 Effects of Ablations on Trim

Section 3 covers the prediction of the heating environment over the test configuration and the heat shield design and its responses to the environment. The primary effects shown are the mass loss histories, the char layer build-up, and the surface recession of the nose tip. The validity of the overall reentry system concept is sensitive to trim angle-of-attack changes resulting from the effects of ablation. These effects can be surpressed if sufficient static stability is built into the vehicle and if effective changes are in themselves small. Figure 2.10 summarizes the effects of the calculated ablation on the trim characteristics. The weight loss computed at 5.7 lbs. produces a net effective pitching moment arm of .054 inches. The change is so small because the nose tip weight increment and the afterbody weight increments balance about the flight center of gravity. As a result, the trim change due to the center of gravity movement is only $.15^{o}$. The expected nose tip recession produces a somewhat larger effect, however, this effect is still of the order of accuracy of the trim angle-of-attack prediction. Other effects such as unexpected removal of char from a portion of the afterbody were examined. These effects on the trim were undetectable. As a result of this assessment, it appears that for entry from orbit along low g descents of primary interest, the effects of ablation do not appear to effect the validity of the test concept.

EFFECTS OF ABLATION ON TRIM

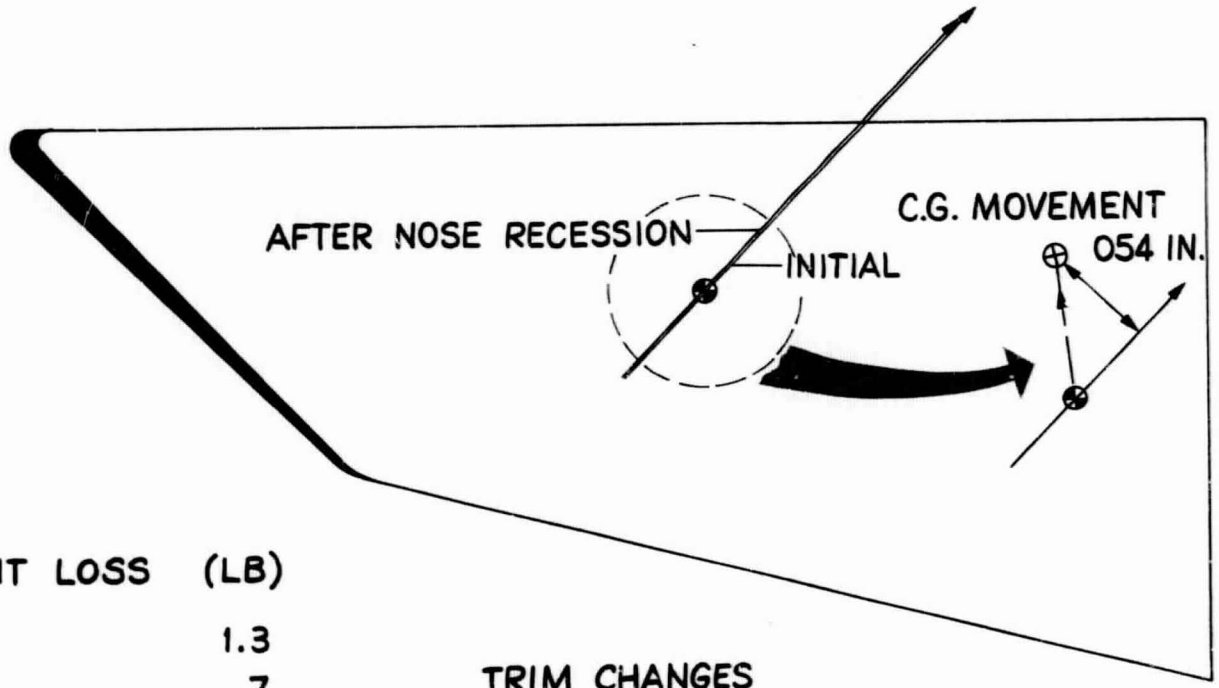

WEIGHT LOSS	(LB)
NOSE	1.3
TOP	.7
SIDES	1.4
CONE	2.3
TOTAL	5.7

TRIM CHANGES

- WEIGHT LOSS −.15°
- NOSE TIP RECESSION +.4°

Fig. 2.10

3. SPACECRAFT THERMODYNAMICS

3.1 Flow Field Criteria

In order to determine the effects of the aerothermodynamic environment upon the overall reentry concept, it was necessary to provide an evaluation of the reentry heating environment, the heat shielding requirements and the heat shield mass loss characteristics for the reference reentry trajectory. It was, therefore, necessary to provide a flow field model that would adequately represent the various surfaces of the test spacecraft while attempting to account for such phenomena as the bluntness induced static pressures on the sides, and the lower conical surface of the spacecraft and the effect of the shock induced vorticity (the enthalpy layer associated with blunt leading edge configurations) upon the magnitude of the heating rate.

Due to the complex three-dimensional shape of the spacecraft, which makes it incompatible with existing analytical flow field solutions, the final test of the adequacy of the assumed flow field criteria should be its ability to correlate the static pressures and heat transfer data from ground facility tests.

The selected flow field model was the same as that used for the spacecraft aerodynamics (Figure 2.6). The spacecraft was analyzed as isolated geometric components and the effects of the combined flow fields were neglected.

The various isolated components were:

1) A blunt triangular flat plate at zero angle-of-attack for the top centerline of the spacecraft,
2) A blunt 15° half angle wedge at zero angle-of-attack (corresponding to zero sideslip angle) for the sides,
3) A hemisphere (3/4 in. radius) - 12.6° half angle cone at 32.4° angle-of-attack for the swept nose section,

4) An "effective" hemisphere (3 in. radius) - 15° half angle cone at zero angle-of-attack for the lower conical surface.

The 3-in. hemisphere radius was an effective value based upon the drag coefficient of the lower nose section, and was used to approximate the effect of both the static pressure over-expansion and the entropy layer upon the heating to the lower conical surface.

3.2 Heating Distribution

The maximum cold wall heat rate distribution, which occurs at the pullout condition, is shown in Fig. 3-1. The results for the nose tip were obtained from the ENVY digital computer program (Ref. 6) which accounts for the combined effects of the entropy layer and crossflow upon the heating level of the windward element of sphere-cones. It utilizes curve fits of both a shock shape correlation and a static pressure correlation based upon nose drag (similar to that of Ref. 5). The effect of the entropy layer upon the heating is obtained by assuming "similar" velocity profiles in the boundary layer and utilizing a mass balance between the shock and the boundary layer edge to obtain the position on the shock from which the edge streamline emanated. This procedure was introduced by Hearne, et al in Ref. 9. The crossflow procedure of Vaglio-Laurin (Ref. 10) has been employed for the windward element only.

The method of Fay and Riddell (Ref. 11) was used for stagnation heating while the Lee's distribution function (Ref. 12) was used for heating from a laminar boundary layer.

The increase in the heat rate shown in Fig. 3-1 at $x/R_N = 6$ indicates that the full entrainment distance for the entropy layer has been achieved and the remainder of the nose tip heating is in effect the sharp cone value. Also shown at $x/R_N = 17$ is a value for a swept cylinder based upon the local radius of 4-in., which indicates that the cone at angle-of-attack value may be somewhat conservative.

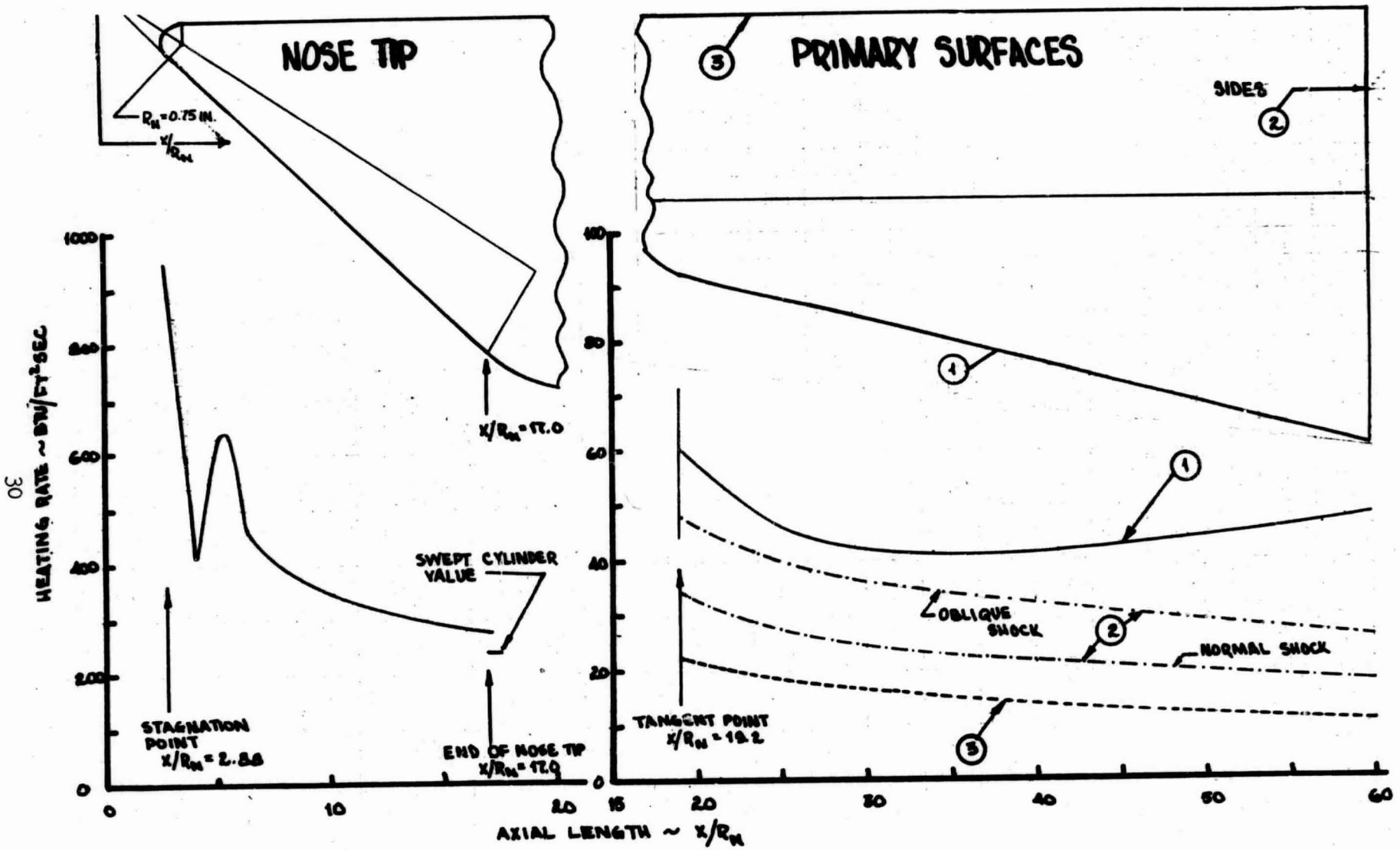

Fig. 3-1 TEST VEHICLE HEAT RATE DISTRIBUTION
(At Pullout Condition)

The right side of Fig. 3-1 shows the maximum heat rate distributions for the primary surfaces of the spacecraft. The values for the top centerline were obtained by utilizing Lee's laminar distribution for a hemisphere to a position 90° from the stagnation point and there utilizing Eckerts laminar strip theory (Ref. 13) to distribute the heating along the remainder of the upper surface centerline.

The sides of the spacecraft were evaluated by using the static pressure distribution recommended by Cleary and Axelson (Ref. 16) along with the normal shock total pressure and the oblique shock total pressure to obtain the local Mach number and the reference enthalpy method of Eckert for laminar flow (Ref. 13) was then used to provide the heat rate limits shown. For a 2-dimensional flow field, it would be expected that the entropy layer would not be entrained as close to the nose section as in the axi-symmetric situation and hence, the normal shock value of heating is used in subsequent calculations.

In accounting for the effect of the nose bluntness upon the heating to the lower conical surface of the spacecraft, the ENVY program utilized an "effective" hemisphere-cone (R_N = 3-in.). Subsequent calculations for the lower surface using sharp cone heating (based upon the wetted distance from the stagnation point, x/R_N = 2.88) indicated that the heat rate was approximately 25%, 45% and 5% greater ENVY results at the lower tangent point (x/R_N = 19.2), the approximate midpoint (x/R_N = 33) and the end of the spacecraft (x/R_N = 60) respectively. The sharp cone heating level produced only minor differences in the subsequent char layer build-up and substrate temperature rise, therefore, even if these heating levels existed, the structural integrity of the test spacecraft would not be affected as will be evident from Section 3.4.

Cold wall heat rates for the stagnation point and the lower surface at x/R_N = 19.2 are shown in Fig. 3-2. The shear stress distribution along the nose tip and lower conical surface is shown for the pullout condition in Fig. 3-3.

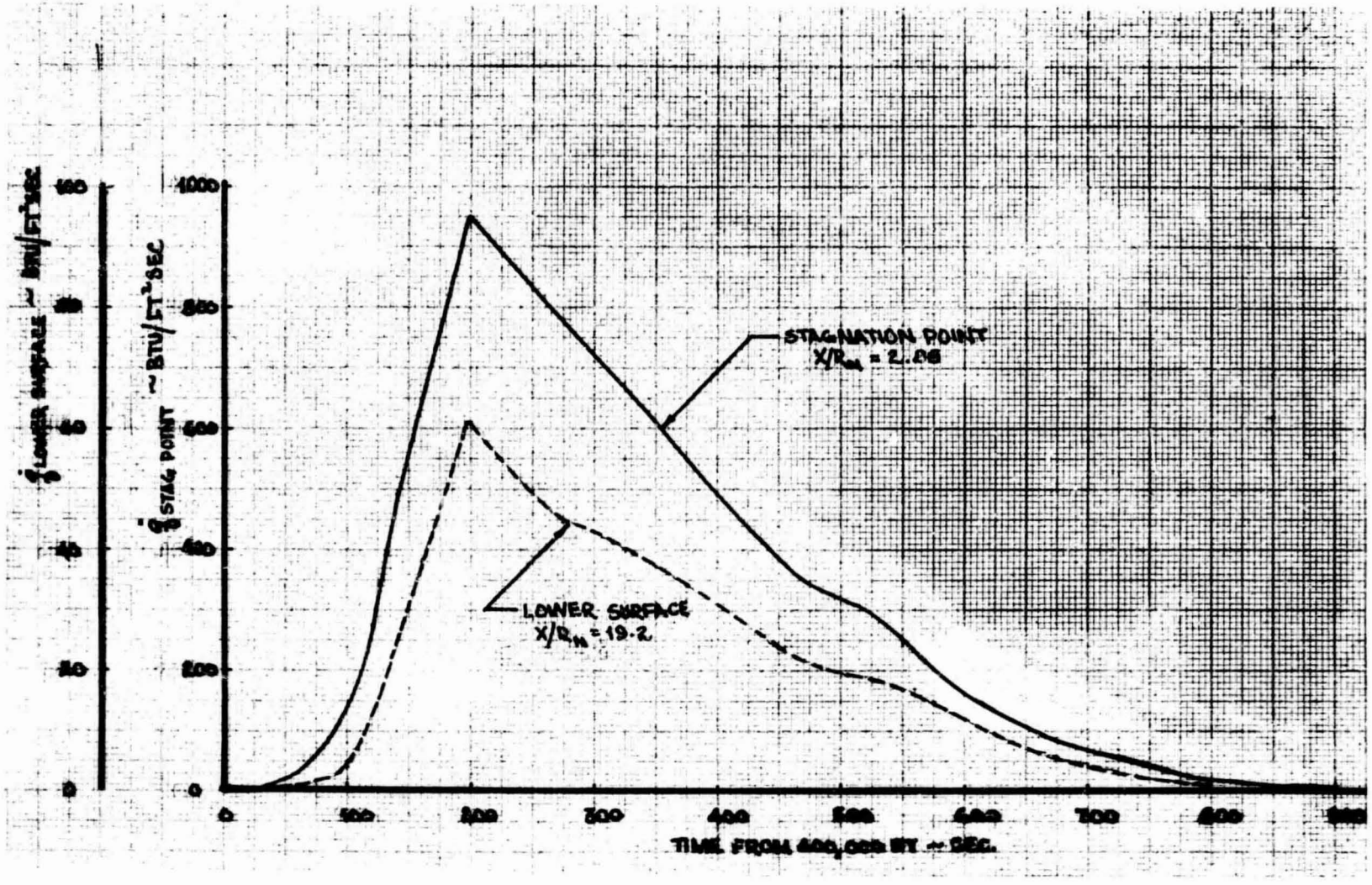

Fig. 3-2 COLD WALL HEAT RATE HISTORIES FOR STAGNATION POINT AND LOWER SURFACE OF TEST VEHICLE

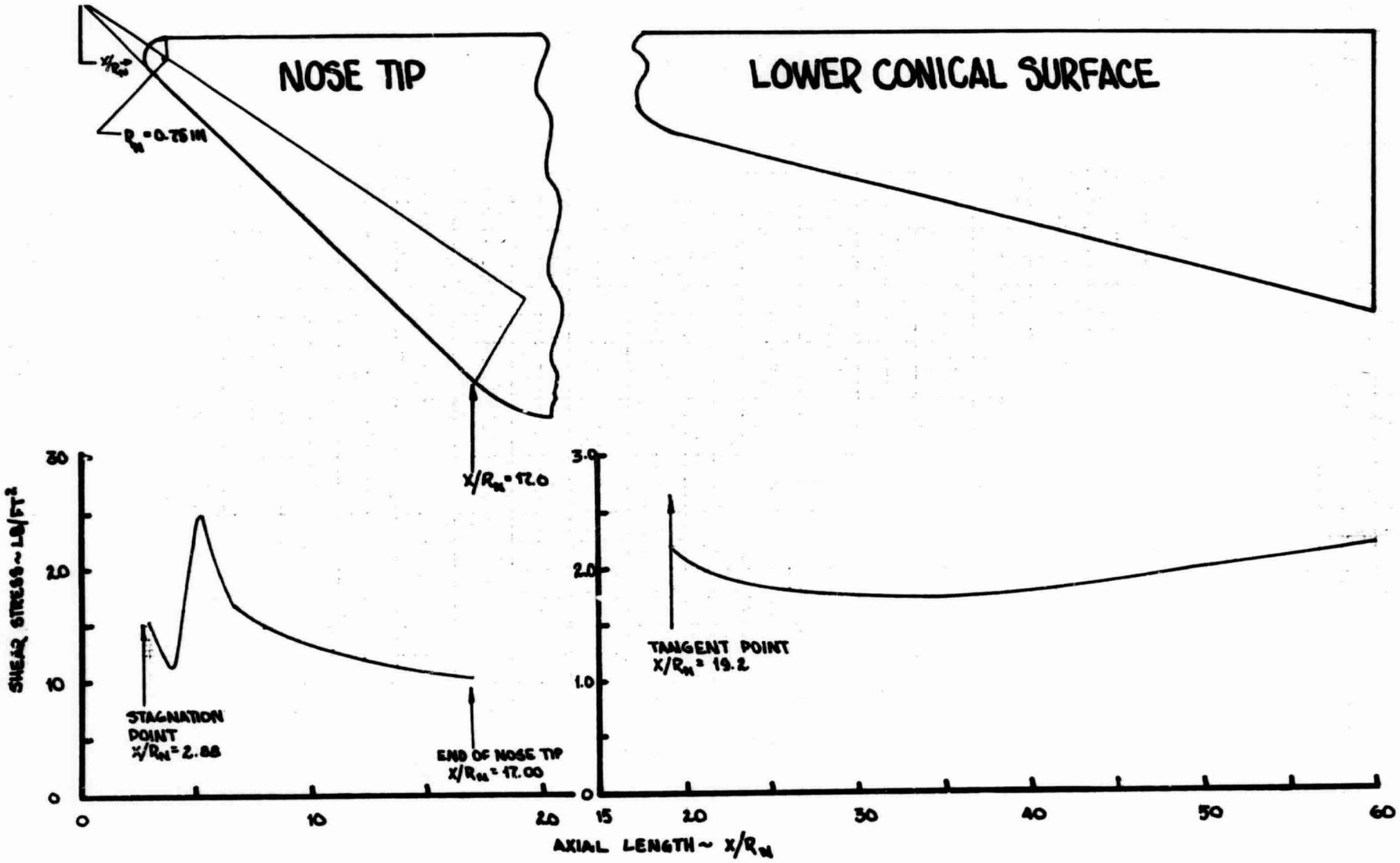

Fig. 3-3 TEST VEHICLE SHEAR STRESS DISTRIBUTION
(At Pullout Condition)

3.3 Angle-of-Attack Effects

The effect of various angles-of-attack on the heating rate at the pullout condition is indicated in Fig. 3-4. This effect was approximately by using the "equivalent" hemisphere-cone model and the ENVY computer program. Notice that at the pullout condition the heating at the aft portions of the test vehicle could be doubled when the spacecraft is at 5 degrees angle-of-attack. As the spacecraft penetrates deeper into the atmosphere, which implies a lower velocity, this increase in heating at the aft end is minimized due an overriding effect of the bluntness. Hence, at lower altitudesand velocities the full entrainment distance for the entropy layer increases and the sharp cone heating occurs at a location further downstream from the nose section.

3.4 Materials Selections and Heat Shield Design

On the bases of the heating rates and shear stresses shown previously the selected materials were carbon-phenolic for the nose section and purple blend-a silicon elastomer for the primary surfaces.

The basic heat shield consisted of the 0.8 in of purple blend bonded to a 0.05 in aluminum substrate and separated from the primary structure by a $\frac{1}{2}$ in. gap. Attachment of the heat shield to the primary structure was accomplished through several aluminum rings. The heat shield calculations neglected the effect of internal conduction and radiation to the primary structure. Radiation from the substrate to the primary structure was considered negligible. The gap could be filled with a low density microquartz to deter both radiation and convection if required.

The heat shield thickness for the primary surfaces was based upon the total heat load at the lower tangent point $x/R_N = 19.2$. The hot wall value was approximately 14,000 BTU/ft^2. A thickness of 0.8 in. of

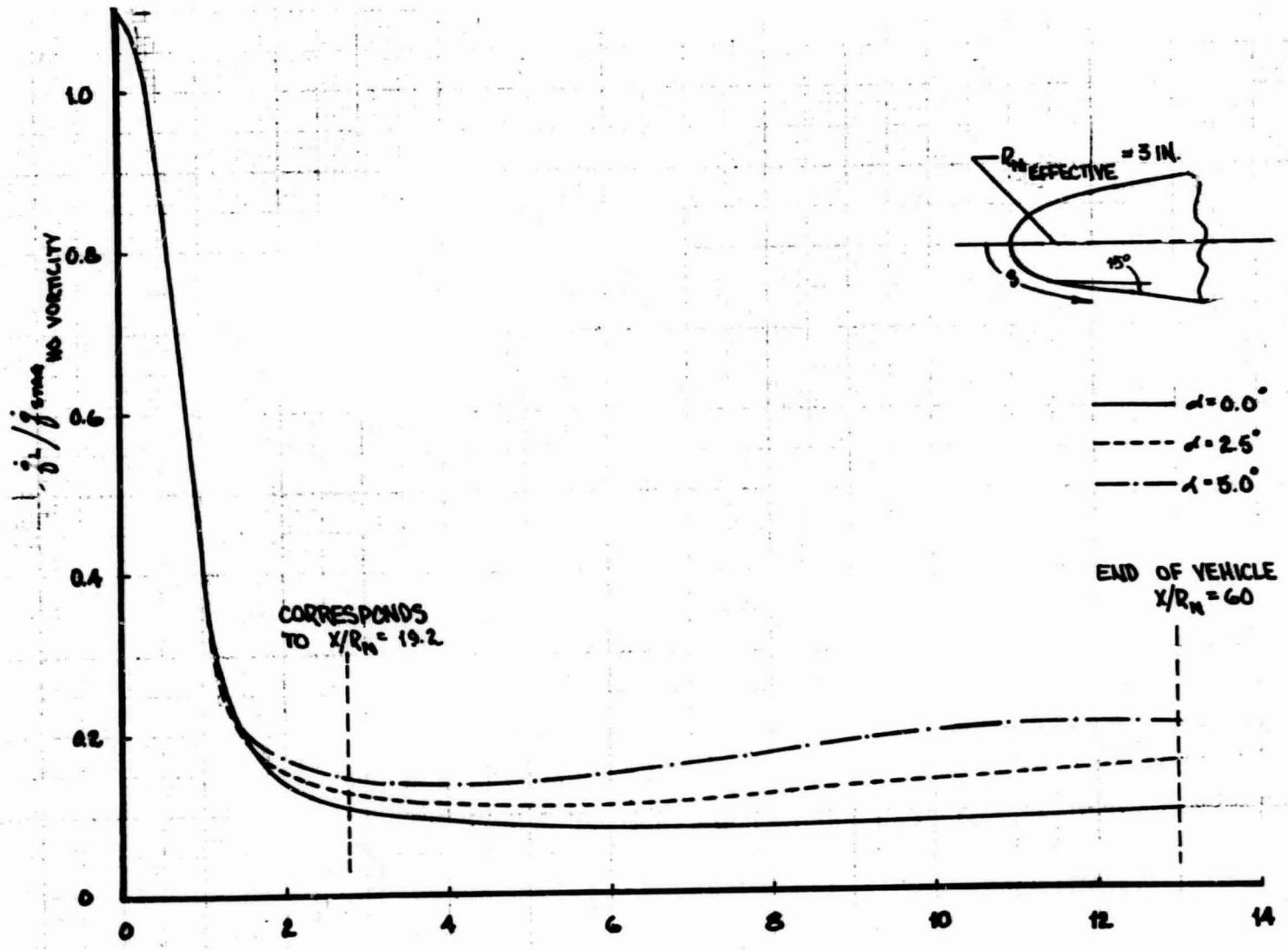

Fig. 3-4 EFFECT OF ANGLE-OF-ATTACK ON HEATING DISTRIBUTION OF THE LOWER CONICAL SURFACE (At the Pullout Condition)

purple blend was required to restrict the substrate temperature to 350° F at the parachute deployment condition.

The response of the purple blend and aluminum substrate was determined with the aid of the CHIRP digital computer program (Ref. 14) that employs a numerical method for solution of a one-dimensional heat conduction equation with depolymerizing plastics as the conduction medium. The program uses an Arrhenius type rate equation for the depolymerizing process (Ref. 15).

The surface erosion for the carbon-phenolic nose tip was based upon oxidation only and is shown in Fig. 3-5. The char layer build-up assuming no mass loss due to shear forces is shown in Fig. 3-6. The char thickness at the parachute deployment condition were 0.28 in. for the bottom, 0.21 in. for the side and 0.15 in. for the top of the test spacecraft.

When the sharp cone heat rate (based upon the wetted length from the stagnation point, $-x/R_N = 2.88$) was used at the lower tangent point, $-x/R_N = 19.2$, the estimated increase in total heating was approximately 25% and the resulting increase in char build-up was approximately 12% or 0.03 in. with an increase of 20° F in the substrate temperature to 375°F. Hence, even with the most conservative heat rate prediction for the lower surface, the substrate temperature at the parachute deployment condition would be less than 400°F at the lower tangent point. The substrate temperature rise would be less for all locations aft of the lower tangent point since a constant shield thickness of 0.81 in. was used on all the primary surfaces.

Typical temperature distributions through the purple blend are depicted in Figures 3-7, 3-8 and 3-9 at location $x/R_N = 19.2$ for the top, side and lower surface respectively.

Typical temperature distributions normal to the airstream are shown in Fig. 3-10.

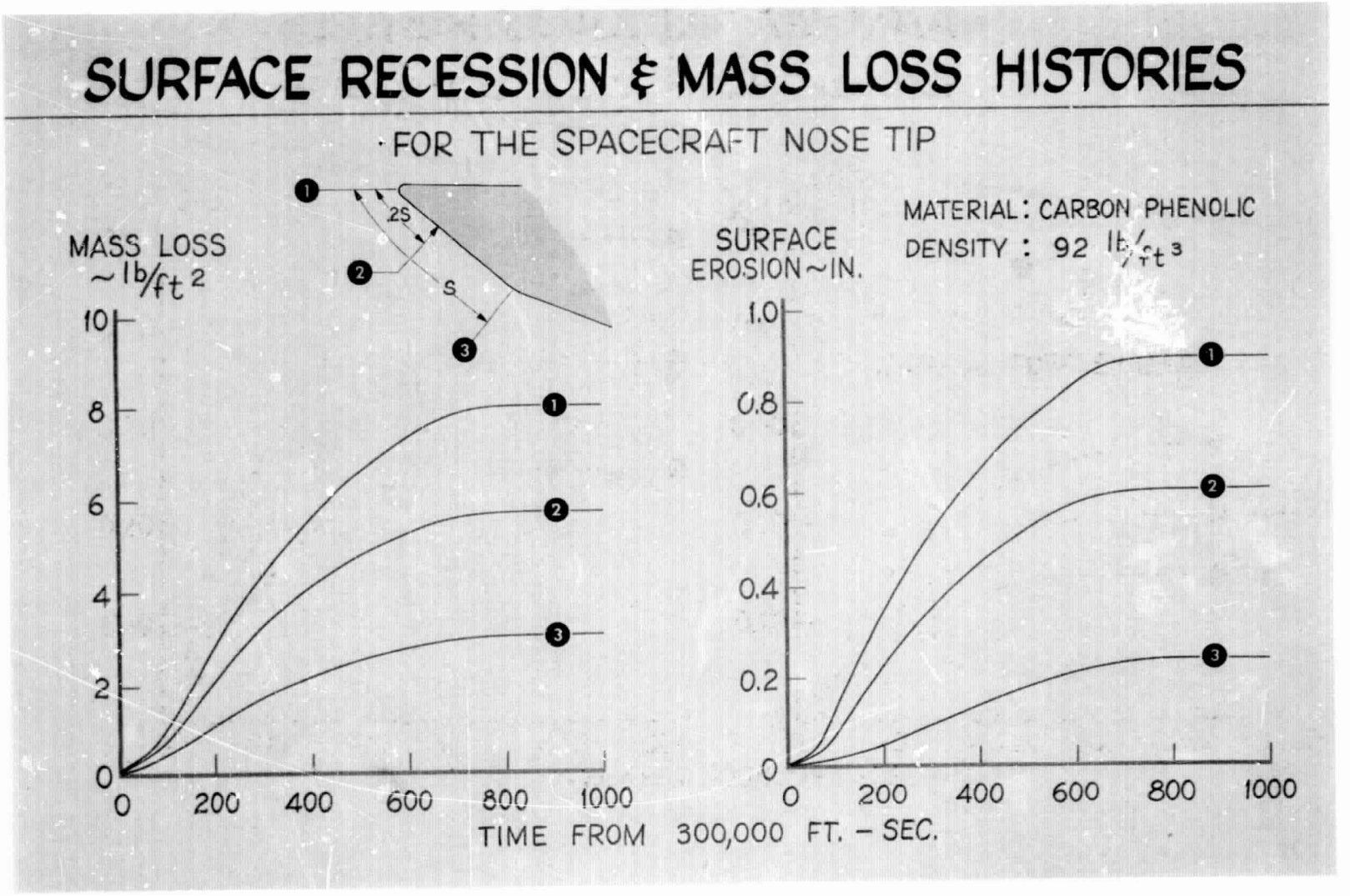
SURFACE RECESSION & MASS LOSS HISTORIES
FOR THE SPACECRAFT NOSE TIP
MATERIAL: CARBON PHENOLIC
DENSITY : 92 lb/ft³
MASS LOSS ~lb/ft²
SURFACE EROSION ~IN.
2S
S
1
2
3
0
2
4
6
8
10
0.2
0.4
0.6
0.8
1.0
0
200
400
600
800
1000
TIME FROM 300,000 FT. – SEC.

Fig. 3.5

CHARLAYER BUILDUP AND MASS LOSS

FOR TYPICAL LOCATIONS ON THE SPACECRAFT

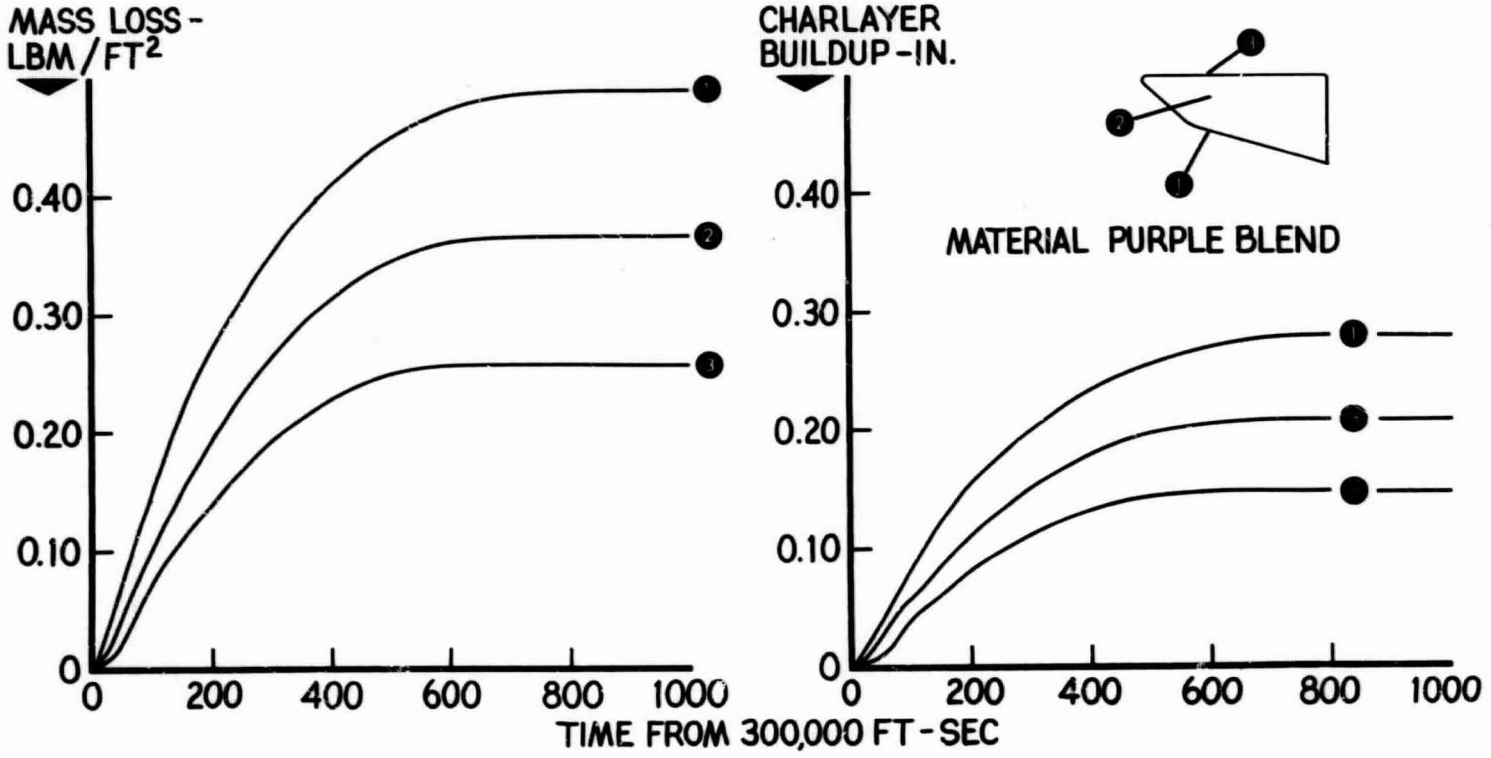

Fig. 3.6

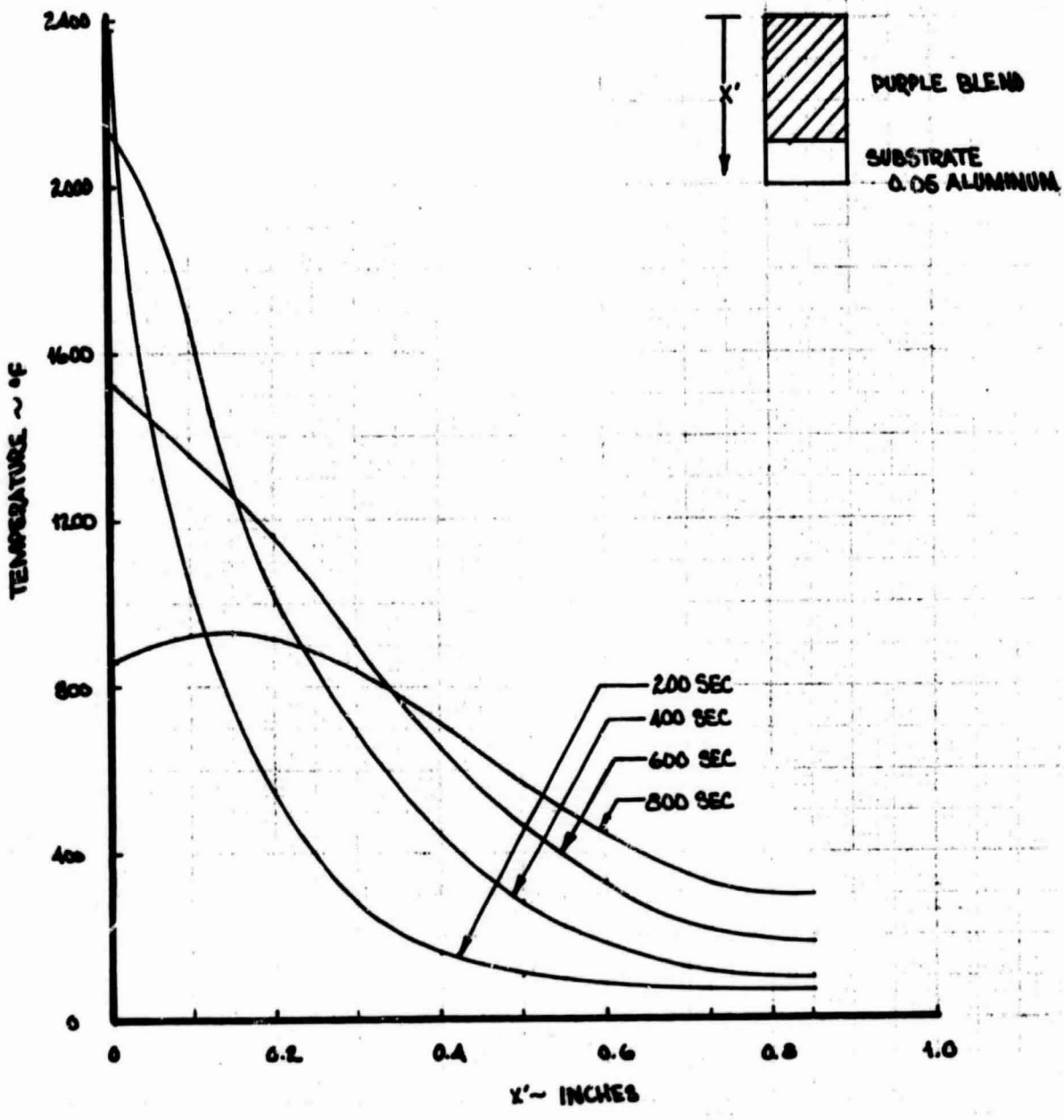

Fig. 3-7 TEMPERATURE DISTRIBUTION FOR PURPLE BLEND AT VARIOUS TIMES DURING RE-ENTRY
(Lower Surface of Test Vehicle) $x/R_N = 19.2$

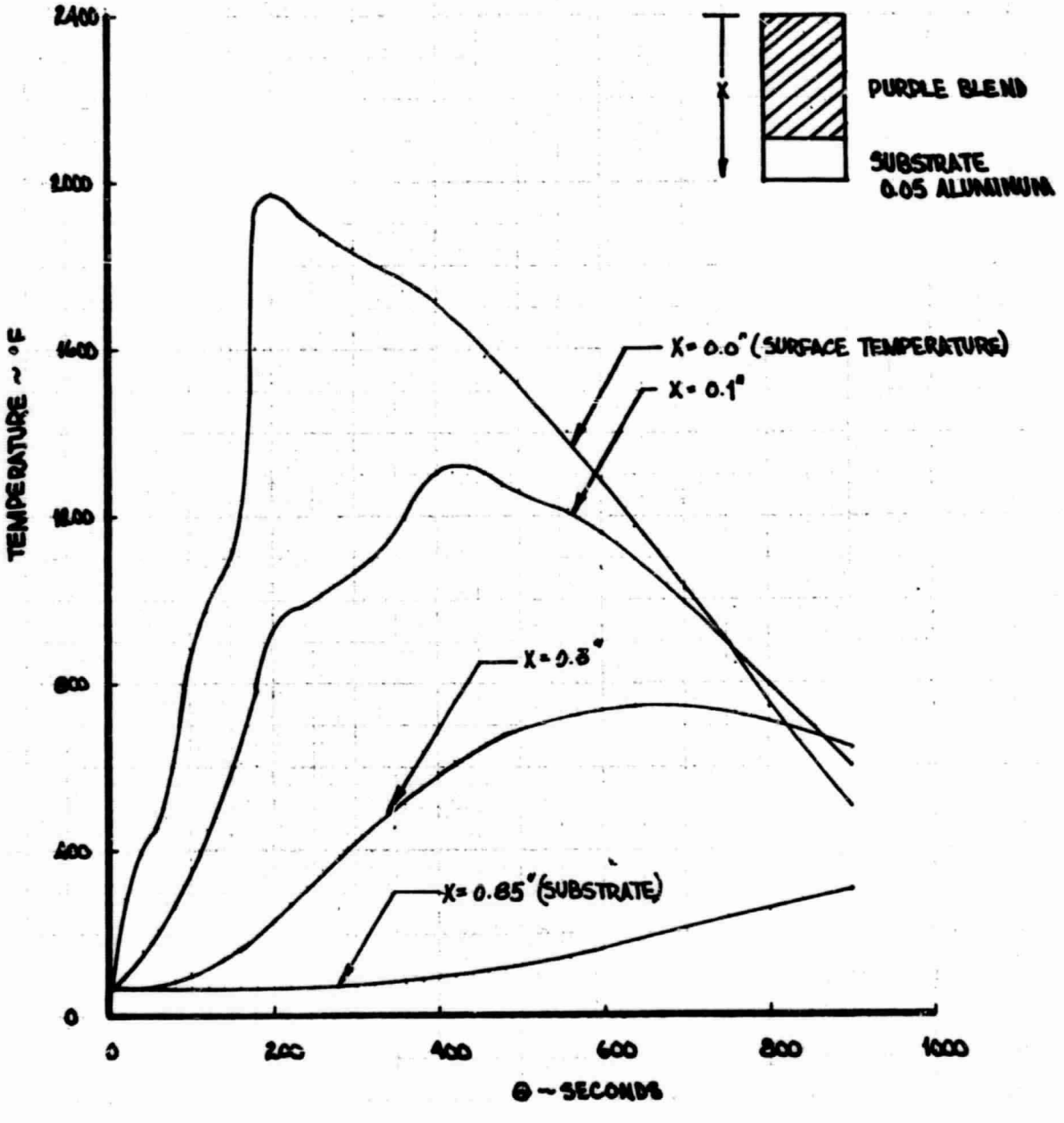

Fig. 3-8 TEMPERATURE HISTORIES OF SELECTED POINTS IN THE HEAT SHIELD (Side of Test Vehicle) $x/R_N = 19.2$

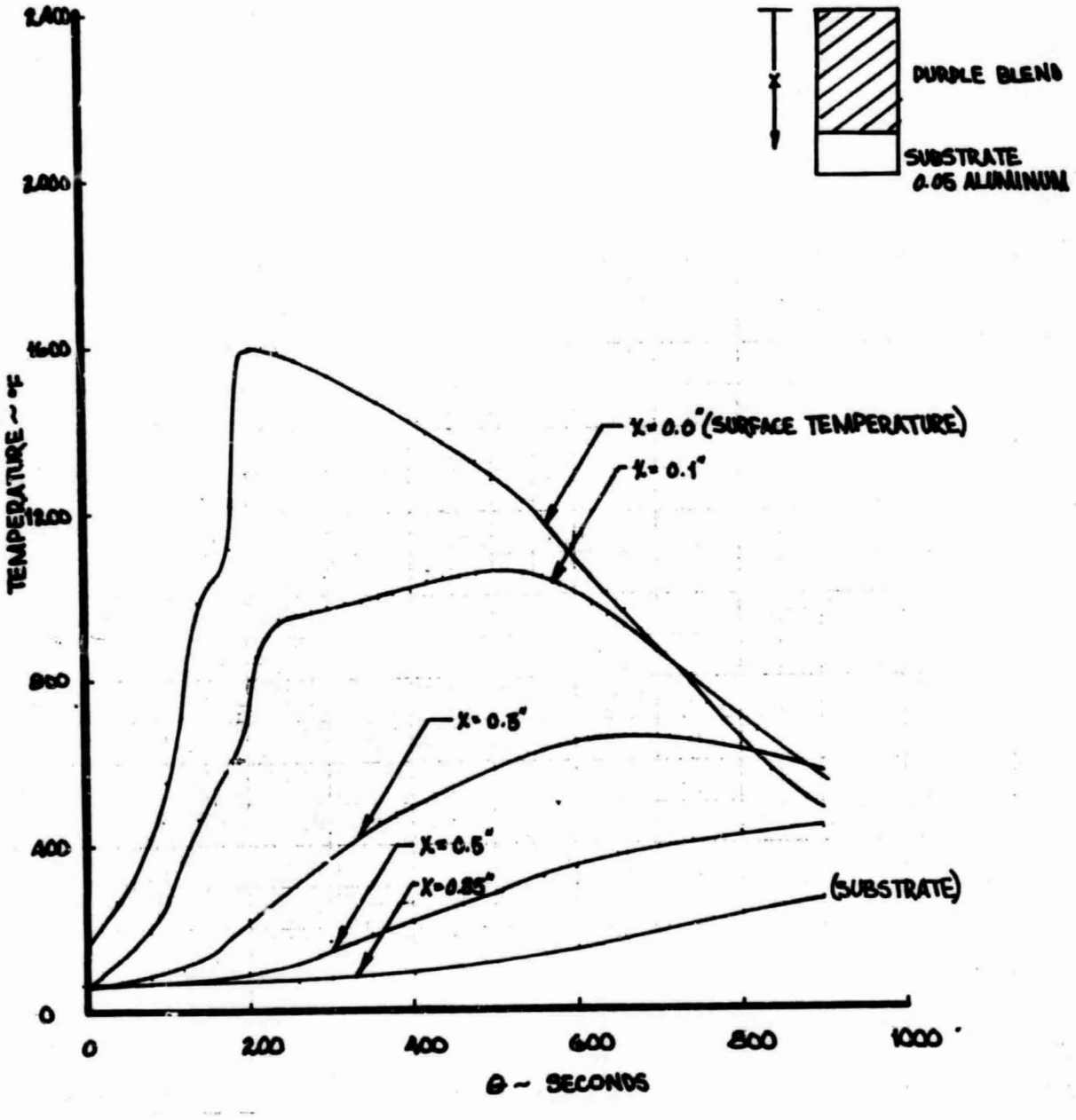

Fig. 3-9 TEMPERATURE HISTORIES OF SELECTED POINTS IN THE SHIELD (Upper Surface of Test Vehicle) x/R_N = 19.2

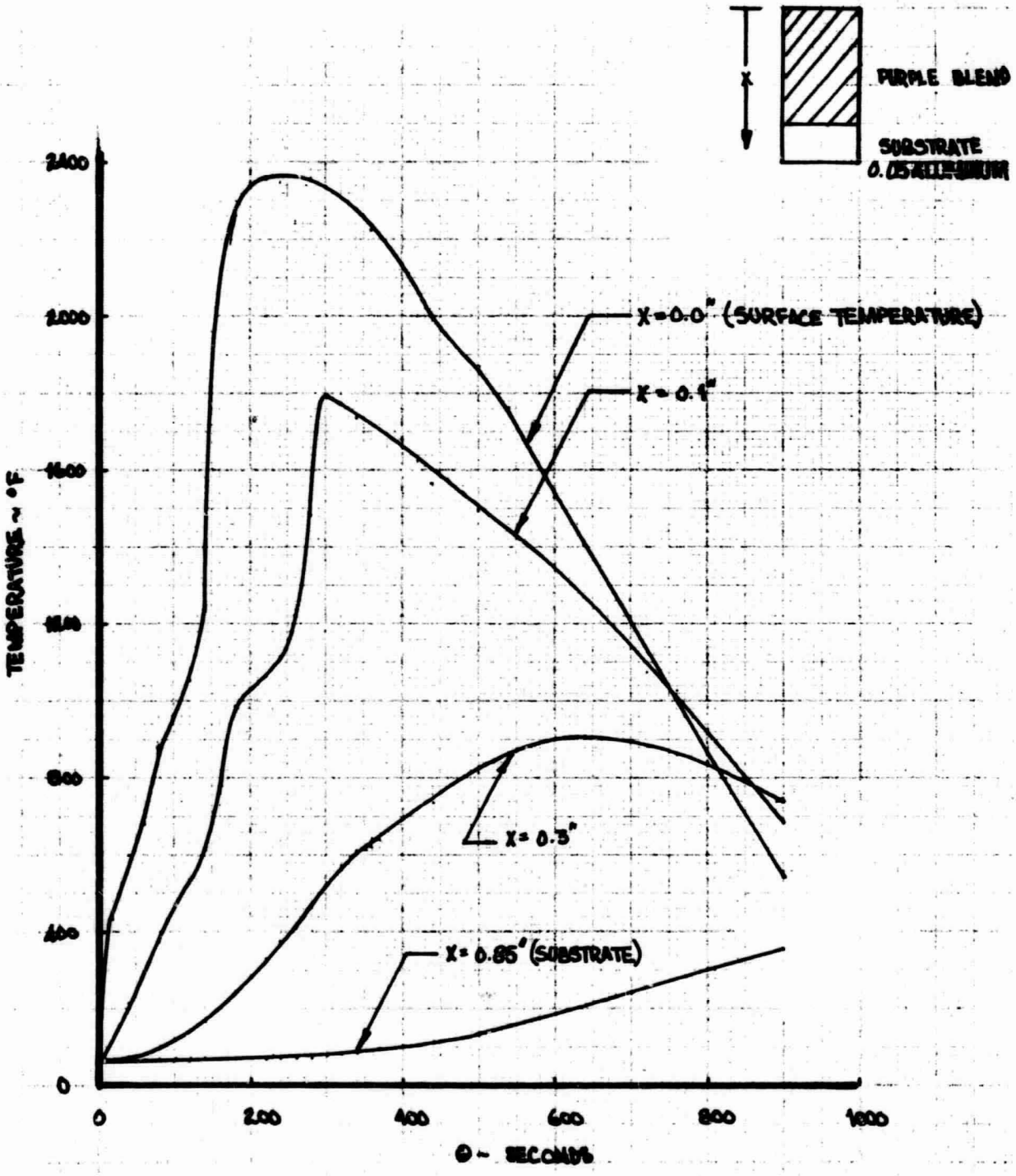

Fig. 3-10 TEMPERATURE HISTORIES OF SELECTED POINTS IN SHIELD
(Lower Surface of Test Vehicle)
$x/R_N = 19.2$

4. REENTRY GUIDANCE AND CONTROL

The guidance and control concept described in Section 1.2 derives it's basic simplicity and unique capability from several fundamental characteristics of lifting reentry trajectories. These features of programmed deceleration descents are illustrated in Fig. 4.1 in terms of the altitude range profile and the vertical lift to drag requirements.

Most notable is that for a given deceleration program, a constant range accrues during guided flight within the atmosphere regardless of the spacecraft aerodynamic characteristics or atmospheric density profile. For the case of a constant deceleration of $a_D/g = 1.0$ illustrated here, a range of about 1800 n.m. is attained from the 0.25 g point to impact. The variation in the aerodynamic characteristics W/C_DA by a factor of 10 merely changes the operating altitude by about 60,000 ft. In essence, a density altitude profile is followed in order to maintain the prescribed deceleration program. Even with a highly variable drag such as obtained with angle-of-attack modulation, the descent profile varies only slightly during the major portion of the flight and again yields constant guided range. The degree of impact range control is then directly proportional to the accuracy with which the deceleration profile can be maintained. Furthermore, an initial injection point dispersion in range shifts the complete descent profile correspondingly. Since the atmospheric flight range is fixed by the deceleration profile, the injection dispersion can be corrected by selecting the appropriate deceleration profile.

The second important feature of low deceleration descent is the shallow flight path clearly evident in Fig. 4.1. During constant deceleration, the flight path angle is less than 2 degrees over 95% of the guided flight range. The nearly horizontal trajectory indicates that only small path angle and subsequent altitude changes need be made to correct deviations in the desired deceleration level due to atmospheric density variations, aerodynamic drag uncertainties, and vehicle weight or shape changes.

TRAJECTORY CHARACTERISTICS

FOR CONSTANT DECELERATION DESCENTS

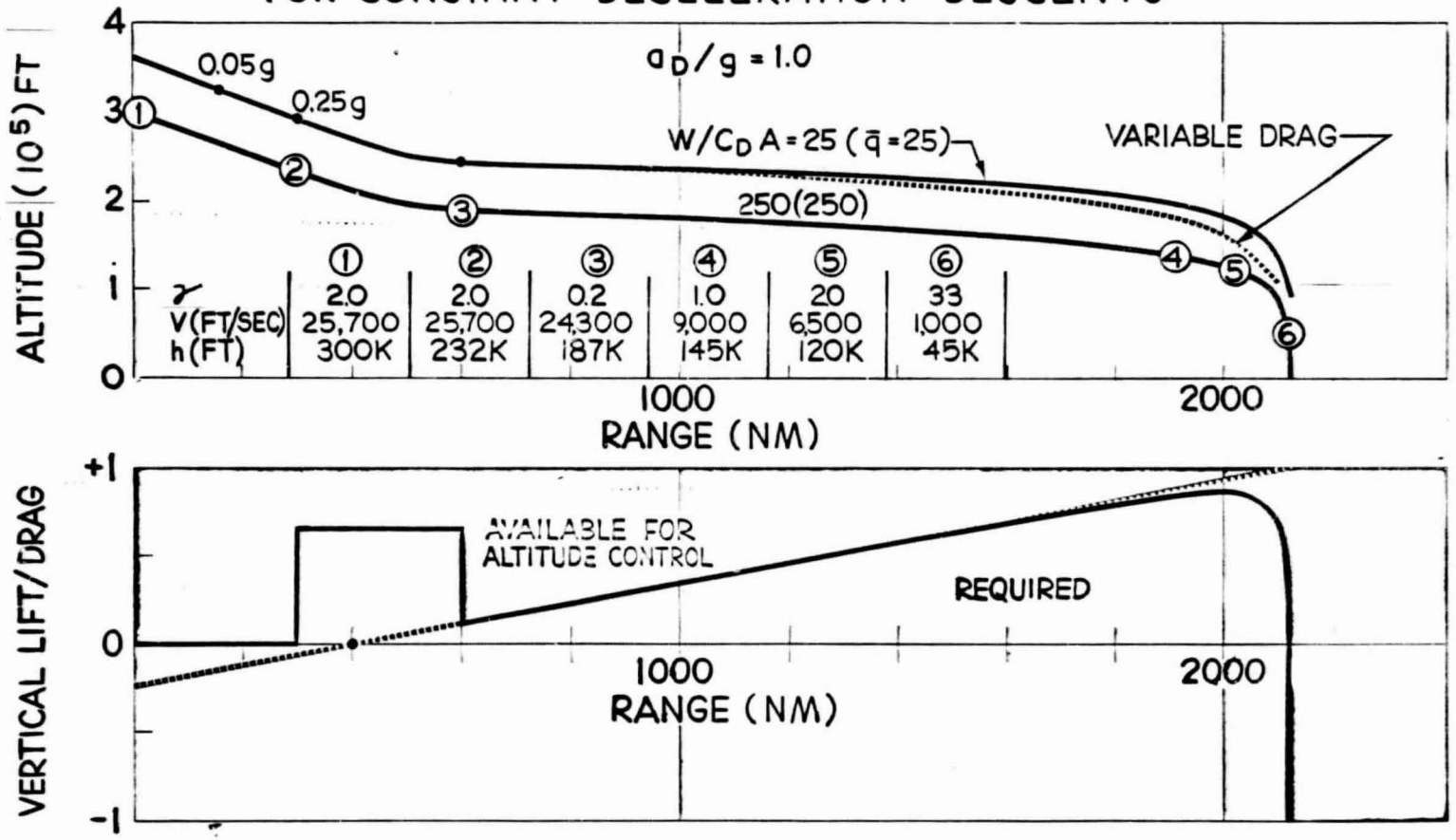

Fig. 4.1

The crucial aerodynamic characteristic for flying the example constant deceleration profile is depicted in the lower diagram of Fig. 4.1. The vertical component of the Lift-Drag ratio required to maintain 1 g is seen to vary essentially linearly with range from zero at orbital speed to nearly + 1.0 at the end of the trajectory. Above orbital speed negative values are required to overcome the centrifugal acceleration. During reentry, an L/D of 0.7 is required to pullout smoothly from the 2 degree dive while toward the end of flight, the required L/D drops off rapidly due to the steepening path angle. The spacecraft L/D requirement is then set by the maximum magnitude of about 0.87 at the 2000 n.m. point. For a convenient rule of thumb, the product $(L/D)(a_{D/g}) = 1.0$ provides the nominal L/D requirement. The difference between the spacecraft capability and the required L/D yields a measure of the altitude control available. At the pullout point nearly the full capability of the spacecraft is available for this function. For the spacecraft characteristics of Section 2, good altitude control is assured for the descent down to quarter orbital speed or for 95% of the range.

For the trimmed lift roll control mode of operation utilized herein, the vertical L/D requirement can be interpreted as the cosine of the roll angle. Hence, at orbital speed, the spacecraft is flown at 90 degrees and gradually rolled toward zero or "wing's level." The guidance scheme then commands a pullup maneuver (90 to zero degree roll angles) to decrease deceleration or a pulldown maneuver (90 to 180 degree roll angles) to increase deceleration toward the programmed value.

The operation of the guidance system is illustrated in Fig. 4-2 for the nominal 1 g descent profile with a 2 degree reentry path angle. A "command reference" acceleration computed onboard the reentry spacecraft is compared with the measured axial acceleration. When this reference is less than the axial acceleration, a wings level pullup is commanded. When it is greater than the axial acceleration by a preset bias (0.05 g's in this illustration), a hard pulldown is commanded. When the command

GUIDANCE SYSTEM OPERATION

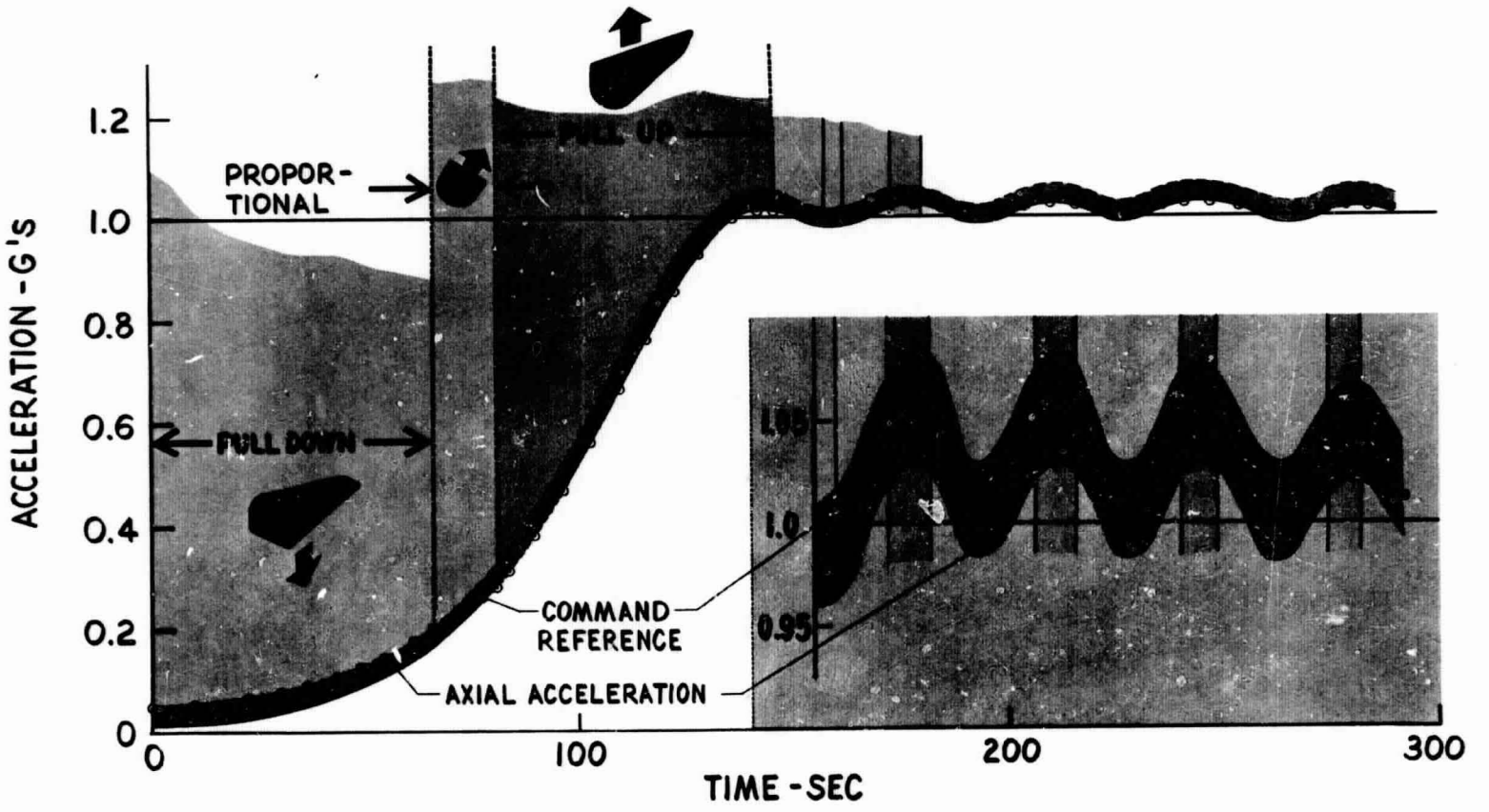

Fig. 4.2

reference is between these limits, proportional roll control is requested. The rate of change of the command reference is proportional to the acceleration error from the programmed value. Note also that the magnitude of the command reference is reset equal to either the axial acceleration or the axial acceleration plus the bias whenever it is outside the proportional control zone. The effect is to introduce an artificial damping of the acceleration error oscillation as illustrated in the enlarged portion of Fig. 4-2. The rate of change of the command reference is limited to provide a smooth pullout during the reentry phase and to accommodate injection path dispersions. The magnitude of the command reference is set to zero initially which causes a pulldown maneuver during the early portion of reentry. The maximum rate limit causes proportional control until about 0.25 g is encountered after which a wings level pullup is commanded until pullout at 1 g. Steeper or shallower reentry paths will then result in a full pullup earlier or later, respectively.

4.1 Guidance Requirements

Two objectives of the guidance system are to be considered in selecting the basic conept. The first objective is to provide the desired deceleration so that a predictable heating environment may be generated. Emphasis is placed on the initial 250 to 300 seconds of flight time when the peak heat rate is in effect. Secondary emphasis is on time of flight which determines the "soak" capability of the flight. The second objective of the basic concept is to provide a predictable point of impact so that the test vehicle may be recovered.

The requirement for a prescribed heating environment (i.e. a commanded deceleration level) precludes the possibility of an independently commanded impact point since the two are physically related through the horizontal velocity history. The only leeway allowed is through the interpretation of the relative importance of the first few hundred seconds of flight time versus the balance of the flight. If the beginning of the flight

is aimed at getting the required flight data at a certain deceleration level, then the remainder might be used to fix the total range and thereby set the impact area. With the above in mind, the downrange correction concept selected involves the simplest approach - a deceleration-level controlled system which maintains the measured longitudinal deceleration at a commanded value. If the control system is capable of delivering the commanded value with sufficient accuracy and with sufficiently rapid response, then a pre-programmed deceleration time history will determine the impact area with a predictable accuracy.

As described in Section 1.2, the method of vertical lift modulation chosen is by control of the vehicle roll angle, from "wing level" for maximum climb to "inverted flight" for maximum dive. The roll moments required to control the roll position are derived from the lateral displacement of an internal mass. The resulting shift of the spacecraft center of gravity with respect to the line of action of the aerodynamic normal force vector generates the roll moment needed to control the vehicle about the roll axis. The factors involved in the method selected are not entirely guidance and control considerations, but partly aerodynamic considerations. By flying the entire flight at a fixed angle of attack and without external aerodynamic control surfaces, the air flow is undisturbed and modified only by the normal changes which take place as a function of velocity. The spacecraft itself initiates no disturbances as a result of guidance and/or control activity. The only guidance consideration is the use of a body-mounted accelerometer as a consequence of the zero aerodynamic pitch trim angle of attack. The required input elements are illustrated in Fig. 4-3.

The information inputs needed are:

1) The longitudinal deceleration of the spacecraft
2) The spacecraft roll angle
3) The spacecraft initial geographical position
4) The spacecraft initial velocity

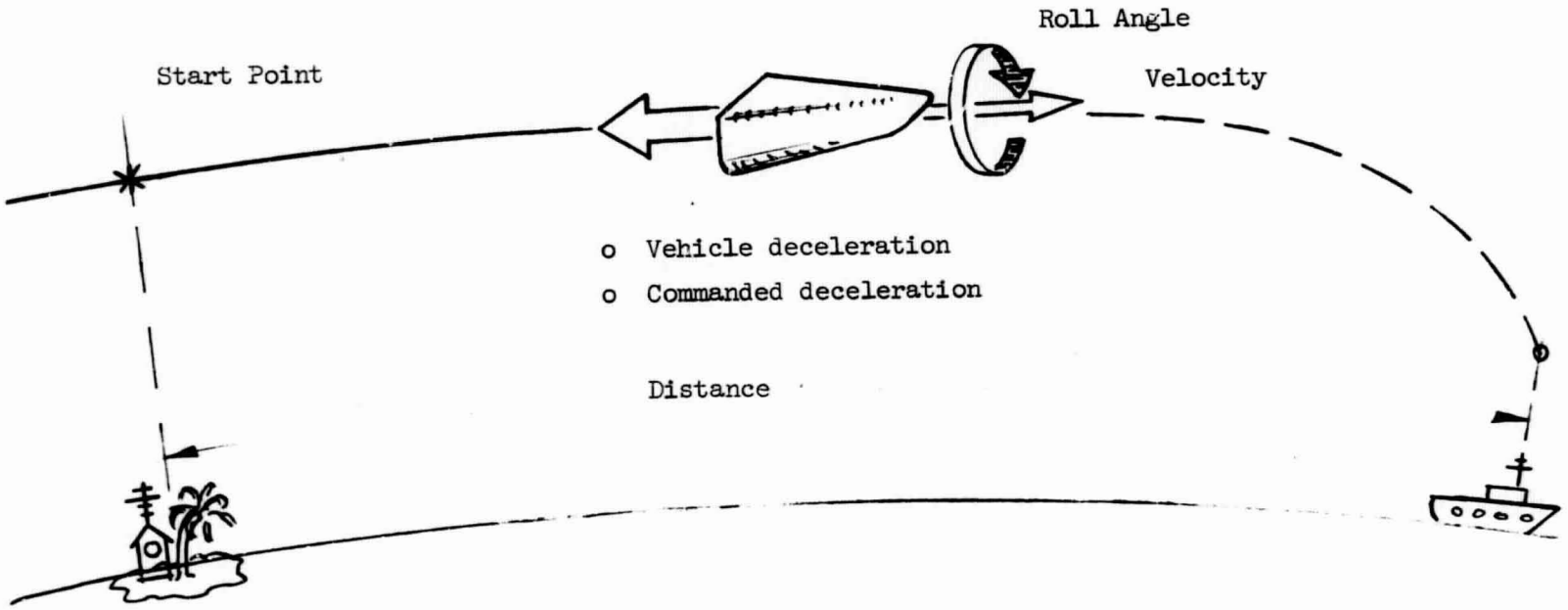

Fig. 4-3 REQUIRED INPUT ELEMENTS

5) The desired deceleration level
6) The desired flight distance
7) The logic defining the preference for deceleration level versus time in the event of an incompatibility between 5) and 6)

It will be noted that all except the first two are preset inputs unless some form of real-time ratio information is provided.

The controlled variables in the system are:

1) Longitudinal acceleration level
2) Roll angle direction and magnitude

In its initial concept, the spacecraft had no information as to its geographical position other than what could be inferred from a programmed "start" time. It now appears that the optimum solution to tolerances in the initial conditions will be different depending upon the magnitude of those tolerances.

In order that the final system has the maximum flexibility, a sharp division is made between the guidance and the deceleraion control functions. The deceleration control system has only the task of delivering the commanded deceleration level and crossrange angle. The guidance system contains whatever logic is required to determine what deceleration level should be commanded to perform the desired mission with particular attention to the effects of initial condition tolerances.

Figure 4-4 shows the chain of command. Guidance uses the time of separation and the acceleration measurement to determine what the reentry initial condition error is and make command decisions. The details of the development of the basic guidance scheme and its performance evaluation are presented in Appendix D and E.

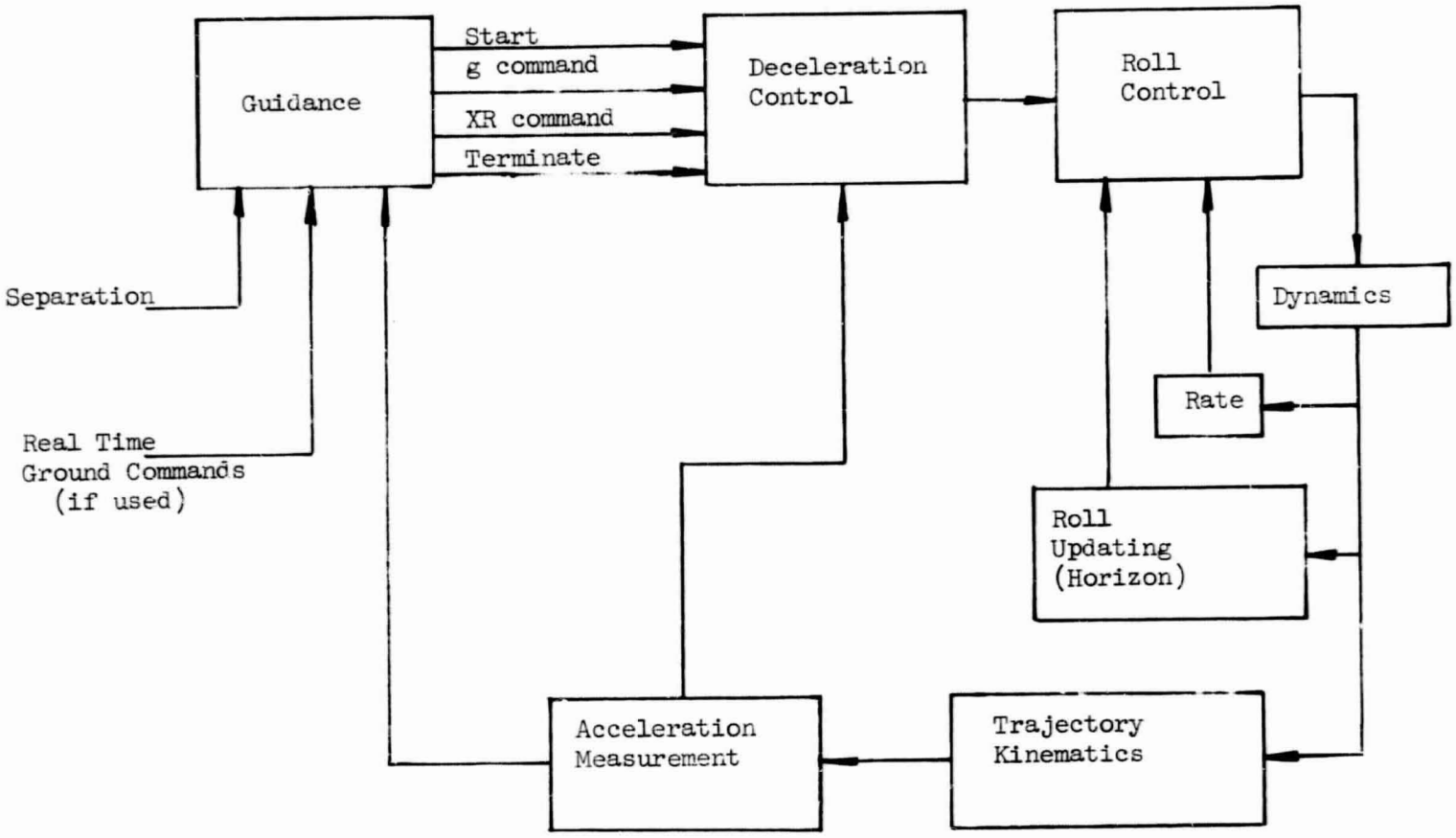

Fig. 4-4 GUIDANCE SYSTEM CONCEPT

4.1.1 Guidance System Mechanization

The selected mechanization of the guidance scheme is shown in Fig. 4-5 for the deceleration level control mode. The main chain of command is shown at the top of the block diagram where the measured deceleration is compared to the desired deceleration to produce the acceleration error signal and the computed roll angle. The commanded roll angle output is limited to zero (wings level) and $\pm$ 180 degrees (inverted flight) depending upon the direction of roll required for cross range maneuvering.. The two lower blocks generate the command reference signal which modifies the acceleration error in order to damp out the high amplitude oscillations and to absorb the reentry range and path angle dispersions.

The velocity error circuit accumulates the measured acceleration until the 0.25 g level is attained after which the acceleration error is integrated. This integrated velocity error provides the assessment of and the correction bias for the range errors accrued during the initial portion of guided flight due to injection dispersions. The comparison of the time at which 0.25 g was achieved compared to the nominal time for this event yields an assessment of the geographical range error at the start of guidance. This time difference is used to suitably adjust the desired acceleration level or to terminate the flight for recovery within the predetermined impact area.

The command reference level is maintained within the acceleration error band of Fig. 4-2 by the high gain feedback from the roll angle limits. The command reference feedback then provides a rate of change essentially proportional to the acceleration error. This rate of change of the command reference is limited ($\pm$ .01 g/sec for this illustration) to provide the initial pullup maneuver and to damp the acceleration oscillations as noted in Fig. 4-2. The velocity error circuit effectively modifies the command reference such that the deceleration level is biased for correction of the guided flight range errors.

GUIDANCE MECHANIZATION

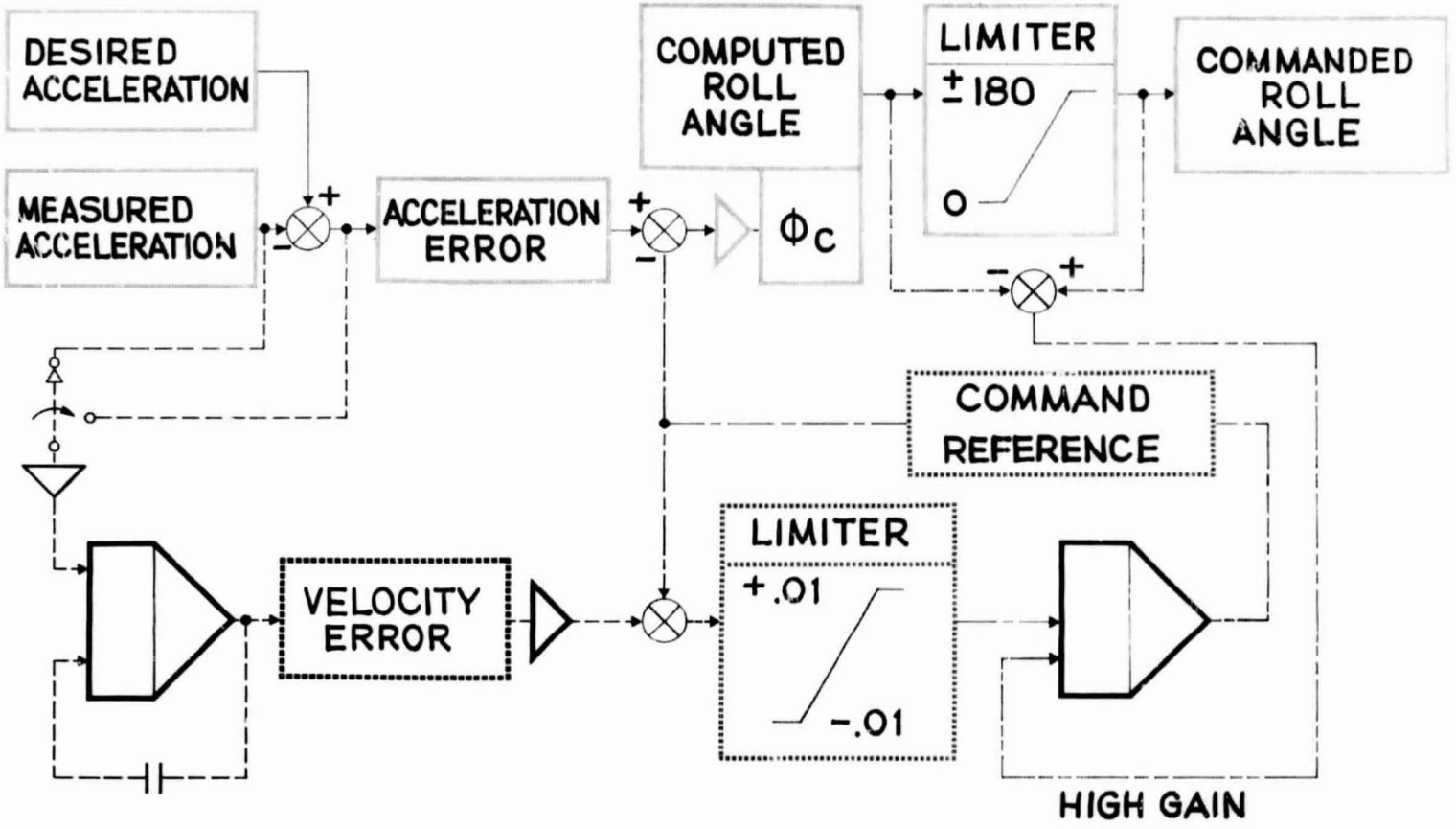

Fig. 4.5

4.1.2 Guidance System Performance

The excellent performance of the guidance mechanization of Fig. 4-5 is demonstrated in Fig. 4-6 for deceleration level guidance only by means of the Entry Guidance and Dynamics Simulation (EGADS). The velocity error gain has been set to zero; i.e., no correction for guided range errors was made. From reentry at 300,000 feet, the nominal case for $\gamma = 2$ degree pulls out smoothly to the 1 g deceleration level with oscillations of $\pm$ 0.025 g with a period of about 50 seconds which are subsequently damped out. Good performance is also achieved over the range of path deviations resulting from Scout injection dispersions ($\pm$ 3 sigma). The principal effect is to delay the attainment of the 1 g deceleration level by about 100 seconds. The over-shoot to about 1.6 g is due to the inadequate L/D for steeper reentry trajectory. The decay to 1 g is controlled by the limit on the rate of change of the command reference (0.005 g/sec for this example). The deviations from the desired g-level later in the flight are due to reduction in altitude control when the required L/D approaches the spacecraft capability.

An indication of the degree of trajectory control resulting from the deceleration guidance is depicted in the right hand side of Fig. 4-6. Altitude deviations are maintained within $\pm$ 750 feet once the desired g-level is attained. The corresponding flight path angle deviations are within $\pm$ 0.3 degrees. Similar behavior is achieved for the -3 degree case at a lower altitude.

The guidance performance with the velocity error loop included is illustrated in Fig. 4-7. The nominal reentry g-level control is altered only slightly. However, significant overshoots occur for both shallow and steep trajectory extremes. The shallow reentry overshoot is moderate and decays smoothly. The initial overshoot for the steeper reentry path causes subsequent oscillations which persist for about 500 seconds. Adjustment of the command reference rate limit yields only minor differences.

GUIDANCE SYSTEM PERFORMANCE

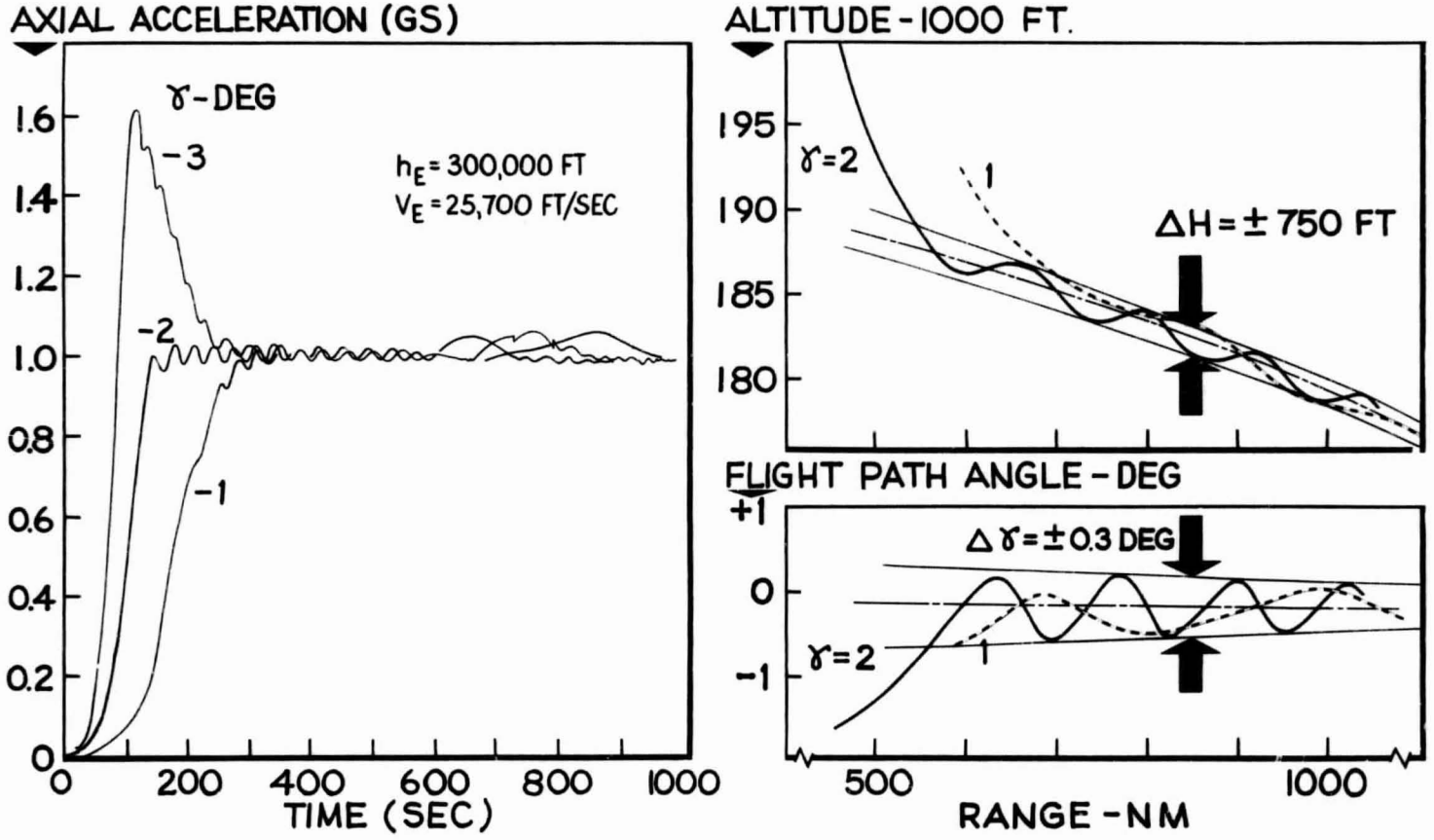

Fig. 4.6

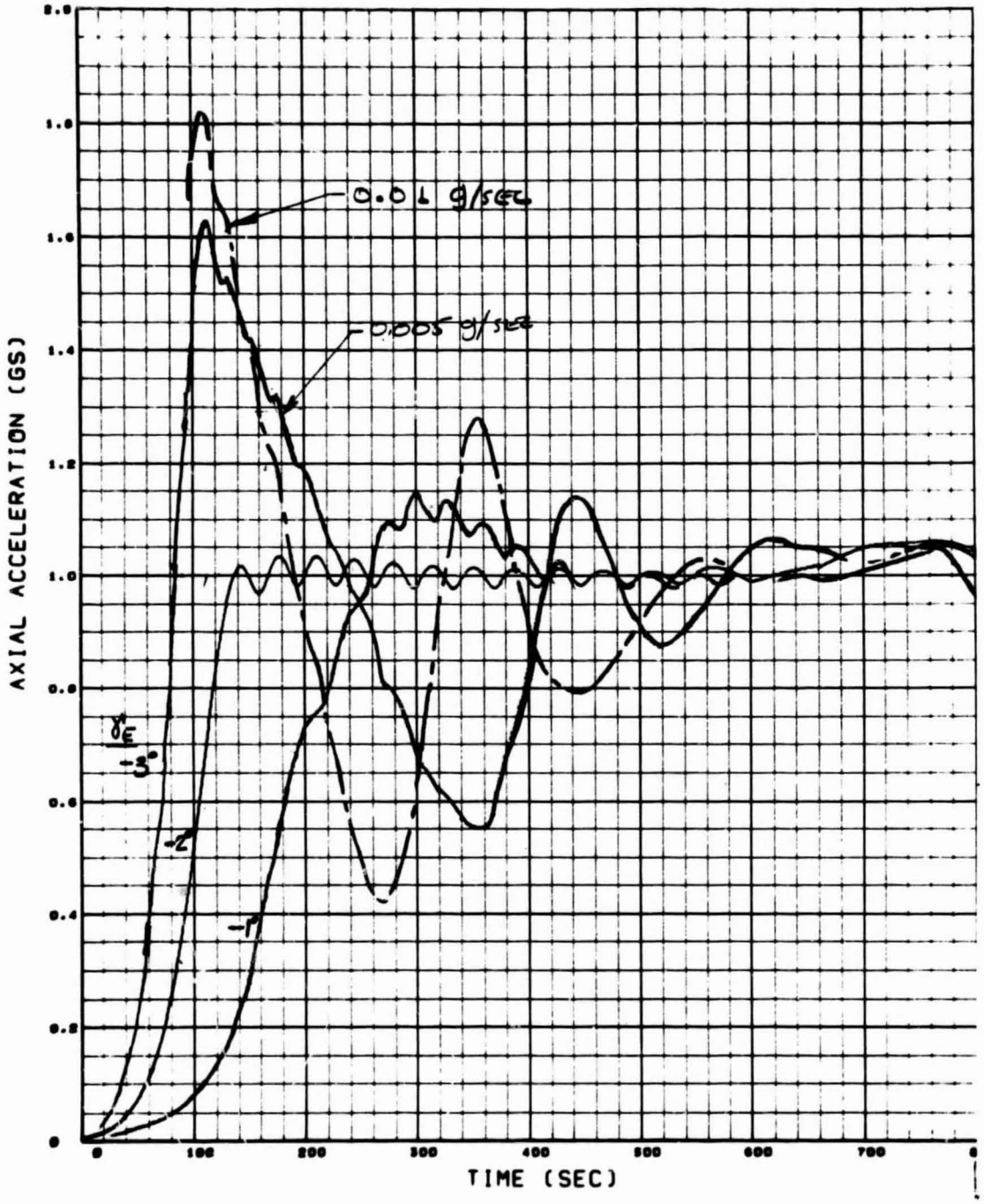

Fig. 4-7 GUIDANCE PERFORMANCE WITH VELOCITY ERROR INCLUDED

These comparisons represent extreme cases due to the 3 sigma Scout injection dispersions. The control of the g-level and hence the environment is obviously degraded in order to maintain good impact range control during the guided flight. However, the range dispersions accumulated prior to reentry (See Section 6) are a factor of 2 larger than those accrued during g-level guided flight (250 n.m.).

Range control afforded with the velocity error loop included has been evaluated in Appendix D. The results are summarized in Table 4-I in terms of the deviation in g-level and the corresponding range dispersion. For the sources and conservative magnitudes shown, an RSS range deviation of 14.5n.m. accrues for a 0.8% error in g-level. The contributions of guidance electronics is not included (See Section 4.3). A statistical analysis of the error sources of Table 4-I will yield smaller RSS value than shown because many of the errors are unidirectional and may be partially biased out.

4.2 Control Concept Development

4.2.1 Control System Mechanization and Performance

The single axis roll control system concept employed for modulation of the vertical lift to drag ratio is illustrated in Fig. 4-8. The roll angle commanded by the guidance system is compared with the spacecraft roll angle. The resulting roll angle error signal together with feedback from the control mass position and rate and the spacecraft roll rate are fed to the control mass motor to position the c.g. appropriately. The roll moment generated by the trim normal force about the displaced c.g. then generates the roll aceleration $\ddot{\phi}$. Integration of the measured roll rate yields the roll angle position for comparison with that commanded by the guidance system. The integrated roll position is updated from the horizon sensors with each traverse of the horizon.

Table 4-I

GUIDANCE SYSTEM DOWNRANGE ERRORS

Source	Error	Performance Penalty g-level	Range
Pitch Trim & Accelerometer Alignment	$\pm$ .4°	$\pm$ .64%	$\pm$ 11.4 n.m.
Yaw Trim & Accelerometer Alignment	$\pm$ .2°	- .06%	- 0.8 n.m.
Wind			
Downrange	Any	Negligible	Neg.
Pitch Oscillation	$\pm$ 2.5° ($\bar{}$Peak)	- .1%	- 1.5 n.m.
Yaw Oscillation	$\pm$ 2.5° ($\bar{}$Peak)	- .5 %	- 8 n.m.
Roll Angle Error	$\pm$ 1.5°	-	$\pm$ .1 n.m.
	RSS <	.8%	14.5 n.m.

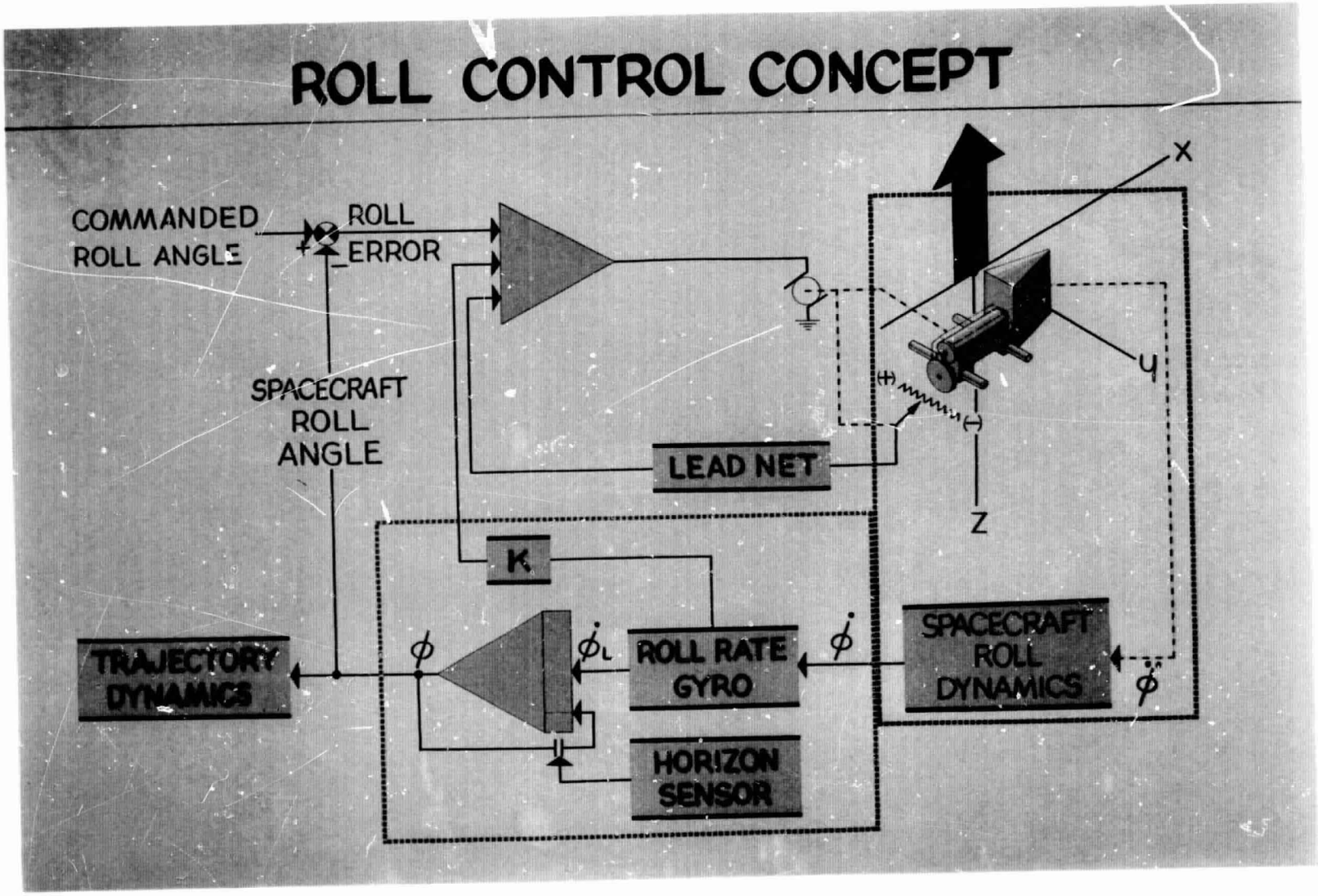
ROLL CONTROL CONCEPT
COMMANDED ROLL ANGLE
ROLL ERROR
SPACECRAFT ROLL ANGLE
LEAD NET
K
TRAJECTORY DYNAMICS
ROLL RATE GYRO
HORIZON SENSOR
SPACECRAFT ROLL DYNAMICS
X
Y
Z

Fig. 4.8

The roll control performance for this system is summarized in Figure 4-9. The determination of the system gains, stability characteristics and transient response used for this evaluation are described in Appendix G. The spacecraft roll response to step input commands of 10, 30 and 60 degrees is illustrated on the left. The commanded value is first attained in about 2.5 seconds for the control mass alone, with about 25% over-shoot. Early in the study it was thought that faster response could be gained by rotating as well as translating the control mass. The increased complexity is clearly unwarranted by the small improvement demonstrated by the curves labelled "wheel." Hence, the wheel concept was eliminated from further consideration.

The response to guidance commands with the translating control mass only exhibits the same behavior during 1-g guided flight. The spacecraft roll angle shows about 2.5 seconds delay from the commanded value while the over-shoot is limited to about 15 degrees.

The roll control system also provides for the aerodynamic despin after separation from Scout forth stage as a normal consequence of its operation. The high spin rate causes the control mass to translate to its maximum deflection. The control mass is determined by requirement to despin at a sufficiently small deceleration level so that a smooth pull up to the 1-g environment can be achieved as described in Section 2 and in Appendix H. For the selected vehicle characteristics, a weight of 10 lbs. is adequate to provide despin at $a_x/g = 0.3$ along the nominal trajectory.

4.2.2 Despin Behavior

The despin maneuver from 300,000 feet altitude takes 89 seconds for the nominal reentry path as shown in Figure 4-10, and is controlled down to the commanded wings level within 100 seconds. Satisfactory despin is achieved also for the 3 sigma low and high dispersion cases including initial altitude and velocity deviations. The 3 sigma high case

CONTROL SYSTEM PERFORMANCE

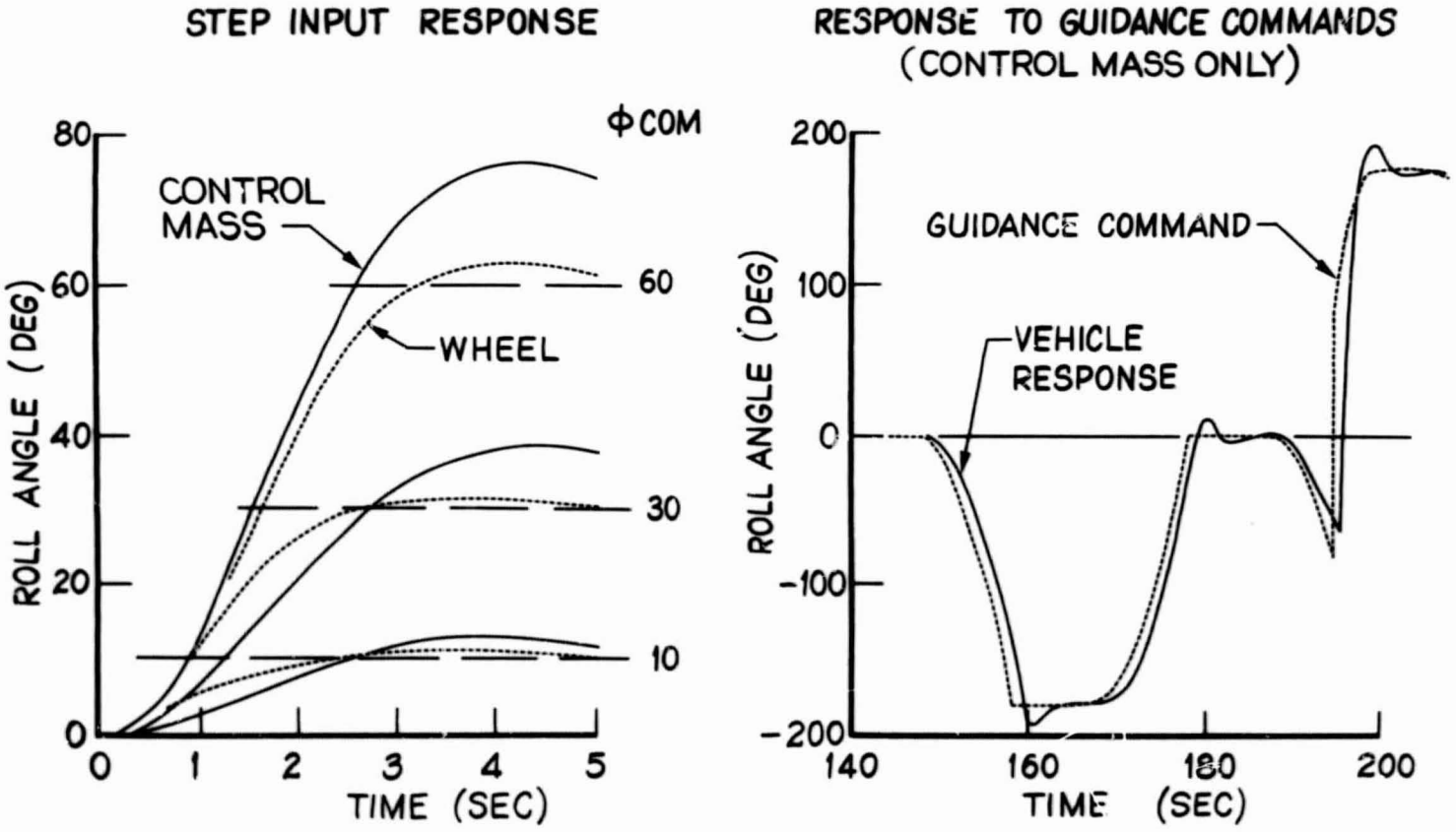

Fig. 4.9

DESPIN & ANGLE-OF-ATTACK CONVERGENCE

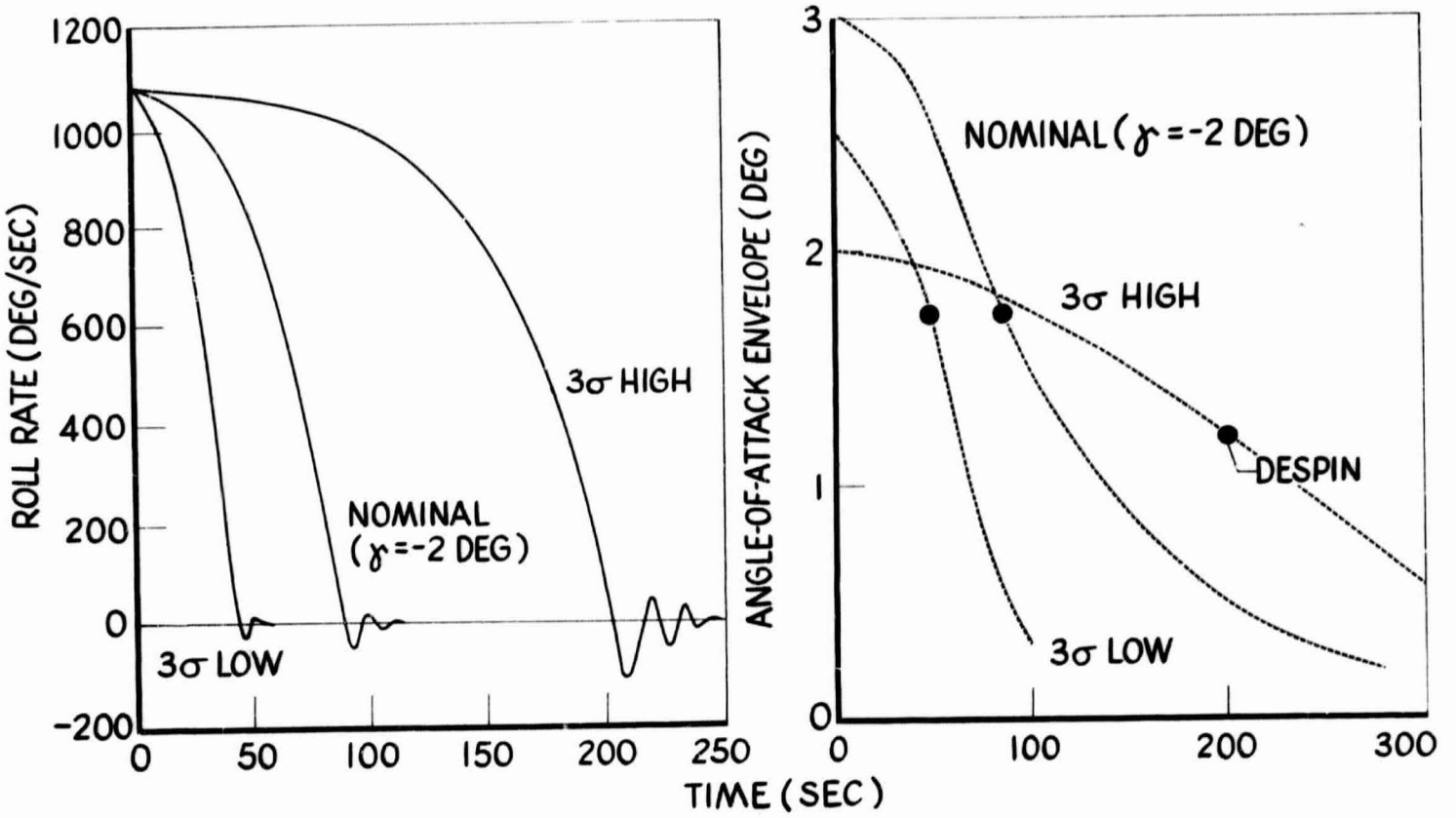

Fig. 4.10

(γ = -1 deg) takes slightly longer to settle down to the commanded roll angle due to the lower dynamic pressure environment ($a_x/g = 0.16$).

Good angle-of-attack convergence during and after despin is obtained as illustrated in the right hand side of Figure 4-10. The initial angle-of-attack varies within only 1 degree despite the large range and flight path deviations of the Scout. The angle-of-attack envelopes are reduced by a factor of two during despin. The subsequent pitch angle-of-attack converges to less than 0.5 degree during the initial guidance to the 1-g environment. The sideslip oscillations (omitted for clarity) are about one-half the pitch oscillations.

Build-up of yaw trim due to lateral c.g. displacement has been controlled by appropriate placement of the control mass forward of the spacecraft longitudinal center of gravity. As developed in Appendix H, the rotation of the principal axis with mass displacement is just equal to the yaw trim angle, which is also proportional to mass displacement. During despin the maximum control mass displacement of 4.5 inches causes a principal axis rotation and trim angle of yaw of about 0.5 degrees. For a 0.5 degree difference between the principal axis and yaw trim, during passage through roll resonance, the trim amplification would result in subsequent yaw oscillations of about 5 degrees. With the control mass located about 2.8 inches forward of the spacecraft c.g., the trim amplification is reduced to negligible proportions as demonstrated in Fig. 4-10. In addition, sufficient aerodynamic damping exists for the 1-g descent profile to reduce the spacecraft oscillations by a factor of ten after 400 seconds of flight.

4.2.3 Guidance - Control - Dynamic Interactions

Feedback of the pitch-yaw dynamics into the guidance system is virtually eliminated by the wide separation of the corresponding natural frequencies. The long period of the deceleration oscillations noted in Figure 4-2 and 4-6 due to the guidance system is a factor of 50 greater than the pitch and yaw periods shown in Section 2.

The roll control response has a significant effect upon the deceleration control as illustrated in Fig. 4-11. The amplitude of the acceleration oscillation are increased to about ± 0.05 g with roll control over the ± 0.025 g amplitude obtained with instantaneous roll response (guidance only). In addition, the period is increased somewhat to 40 seconds. Spacecraft dynamics (pitch-yaw oscillations) resulting from the despin performance of Fig. 4-10 seem to have a minor effect during the first overshoot but exhibit neglible difference thereafter. These observations are reinforced by examination of the roll response. Appreciable roll angle oscillation about the commanded 180 degrees occurs early in the reentry because of the low dynamic pressure. Thereafter, the principal difference is due to the larger deceleration oscillation and period. Again spacecraft pitch-yaw oscillation has negligible effect.

The control mass position history yielding the roll angle and deceleration response described above is shown in the lower right hand plot. During initial despin, the control mass is translated to its maximum displacement of 4.5 inches. Thereafter, the control excursions are limited to about ± 0.5 inches except when the direction of roll is changed to correct crossrange build-up. The remaining 4.0 inches of travel are then available for roll trim control. Similar behavior was obtained with a lateral c.g. uncertainty of 0.052 inches except that control mass motions then centered about a one inch displacement.

The despin maneuver has negligible influence on the g-level control capability for the nominal case and shallow dispersion as shown in Fig. 4-12. Since despin occurs at low g-level, sufficient L/D is available to pullout smoothly. However, the despin for the steep dispersion occurs at considerably higher acceleration (0.5 g's) due to the lower initial altitude and steeper flight path angle. The peak acceleration overshoot is increased, however, only moderately to 1.8 g's from 1.6. Hence, even for the maximum 3 sigma dispersion from Scout despin , g-level guidance capture is achieved.

GUIDANCE-CONTROL SPACECRAFT INTERACTION

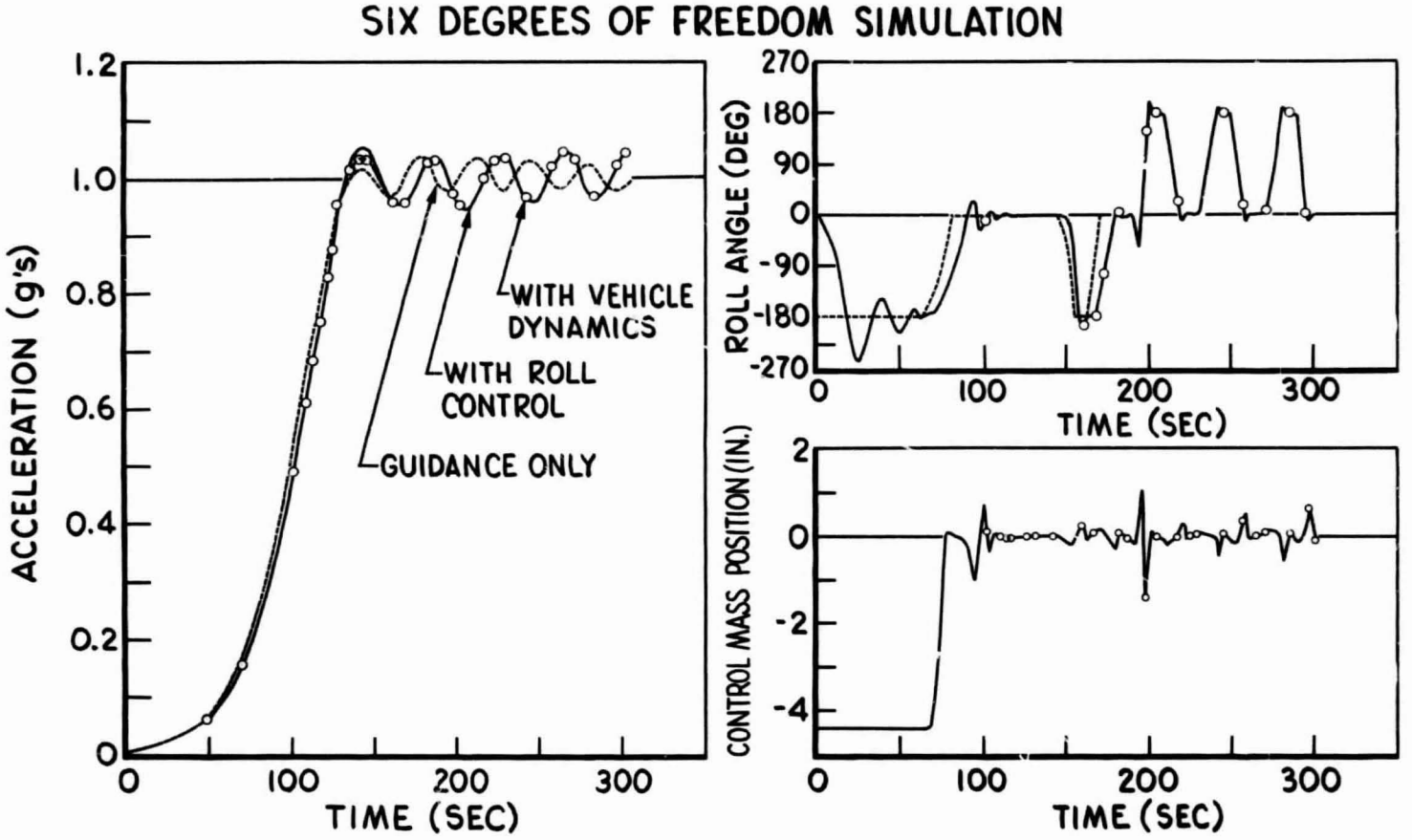

Fig. 4.11

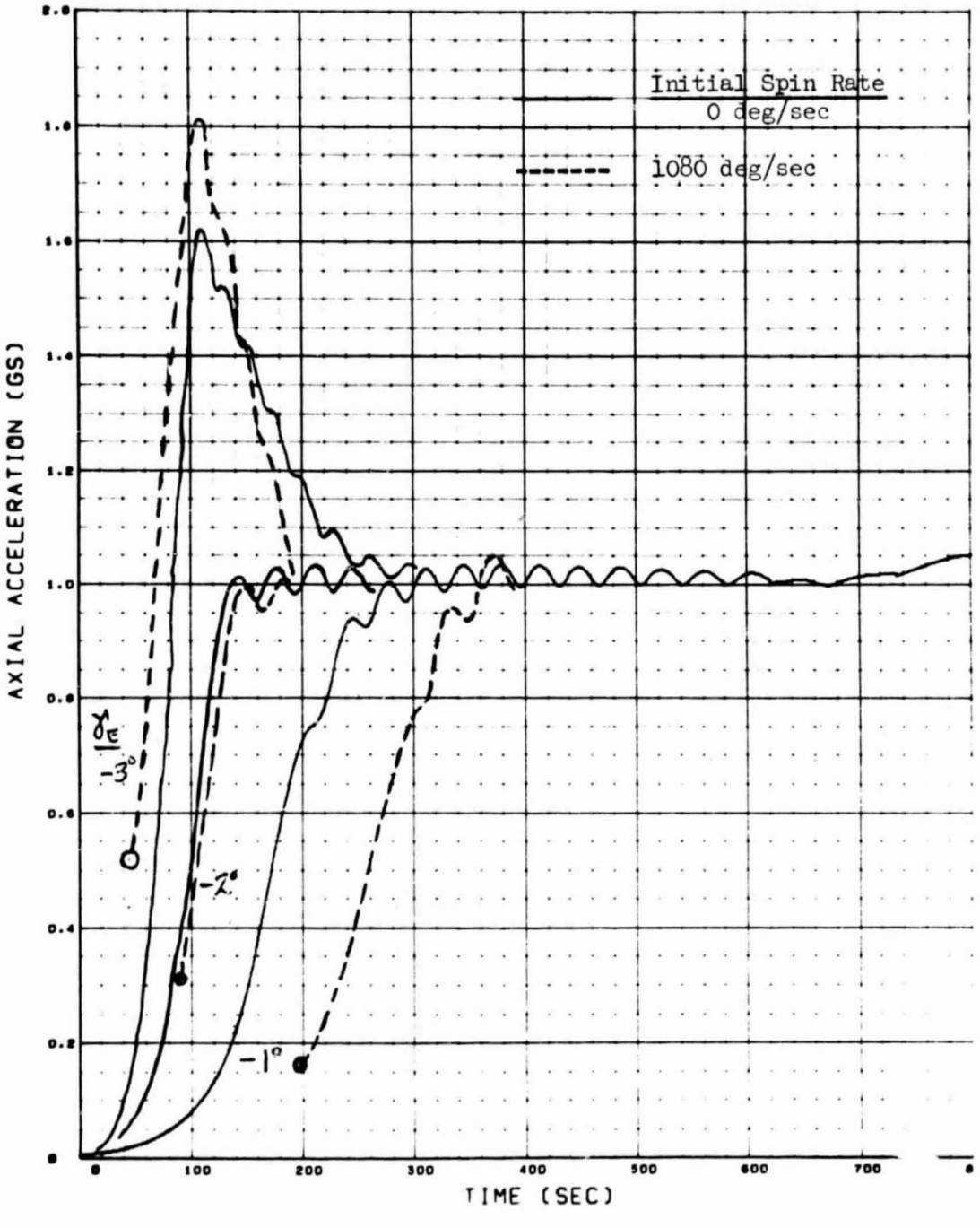

Fig. 4-12 GUIDANCE PERFORMANCE WITH SCOUT INJECTION DISPERSION AND DESPIN

4.3 Control System Design

4.3.1 Component Selection

Design of the guidance and control system has been pursued to the extent of selecting hardware and electronics suitable for flight application. A breadboard simulation, constructed under the LMSC Independent Development Program, provided an excellent base point for this study. Figure 4-13 illustrates the arrangement of operational amplifiers used in the guidance and control circuits and the roll axis simulation of the spacecraft. The roll rate gyro and horizon disc are mounted on the motor shaft and the weights simulate the spacecraft roll inertia. Numerous reentry guidance and control runs made with the Donner analog incorporated in the simulation demonstrated the basic efficacy of the concept. This background work has contributed significantly to the conduct of this study and provided a solid base for assessment of guidance and control system operational characteristics and hardware errors.

The circuitry and components used for this guidance and control system simulation are directly applicable to the flight system. The major components selected for the guidance and control systems are summarized in Table 4-II corresponding to the functions associated with the various blocks of Figure 4.5. These major components account for only about 40% of the total guidance and control system electronics weight. The remainder of the weight is alloted to minor circuit elements, wiring, packaging and connections.

4.3.2 Horizon Sensor Description

The horizon sensors perform two important functions: 1) provide the initial vertical reference and, 2) update the roll angle computation. Application of these devices allows the use of a low range roll rate gyro sized primarily for guided flight and removes the need for a high accuracy roll circuit. The horizon sensor shown in Fig. 4-14 operates in the blue light range (3000-5000 Å). This constrains the spacecraft flight to launch after dawn and impact before sunset in the recovery area.

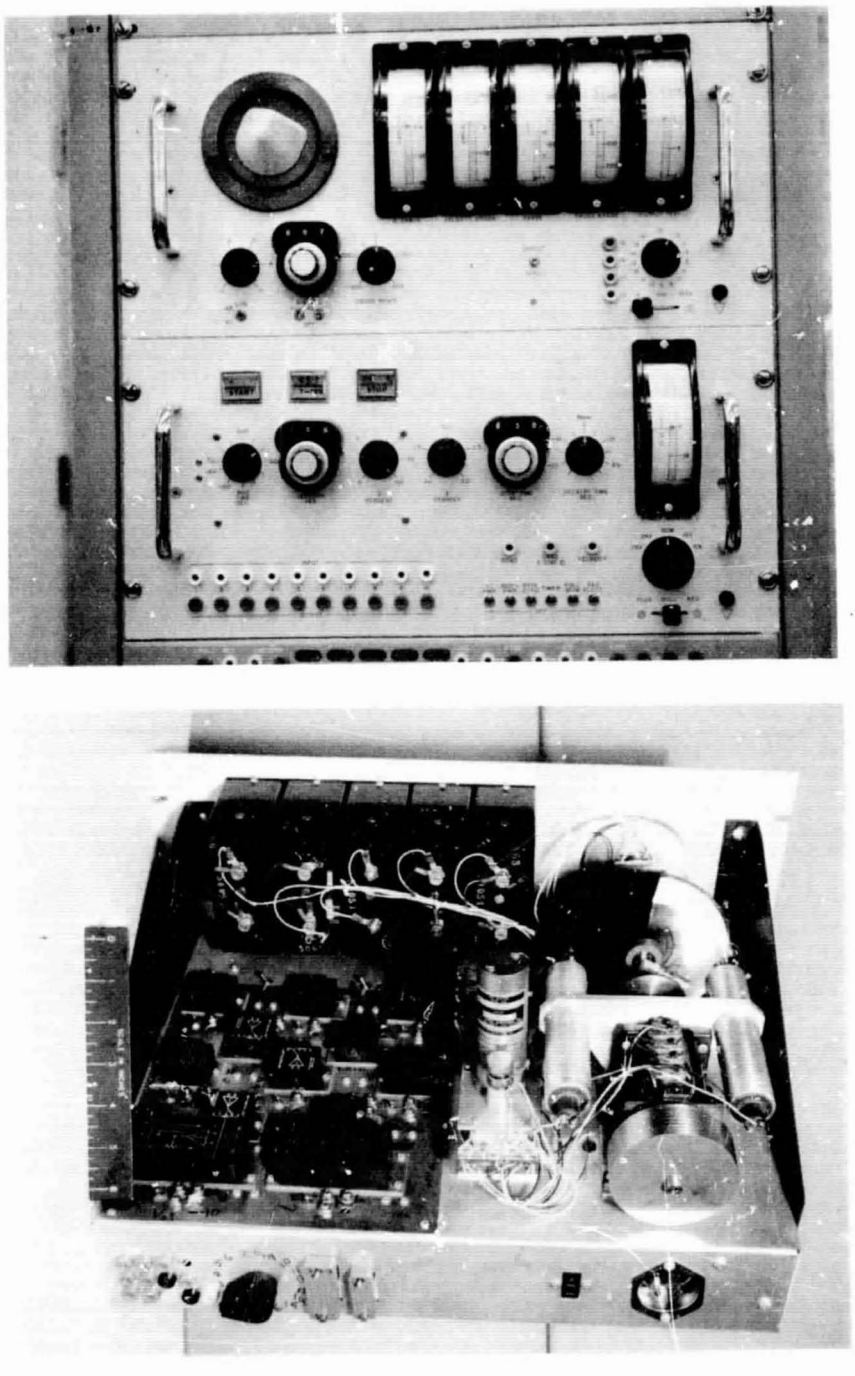

Fig. 4-13 LMSC ENTRY GUIDANCE AND CONTROL SIMULATION

Table 4-II

MAJOR GUIDANCE AND CONTROL COMPONENTS

Circuit Function	Reference Figure	Component	Make & Model	Weight oz.
Guidance	4.5			
Vehicle deceleration		Accelerometer	Donner Model 4310	4.0
Acceleration Error		Operational Amplifier	Nexus CQA-22	1.5
Velocity error integration		"	Nexus SA-60	4.0
Command Reference		"	Nexus CQA-22	1.5
Crossrange computation		"	Nexus CQA-3	1.5
Roll Control	4.8			
Roll rate		Rate gyro	U.S. Time 98-60,000	3.8
Roll angle error		Operational Amplifier	Nexus CQA-3	1.5
Roll trim		"	Nexus CQA-22	1.5
Slug position command		"	Nexus CQA-22	1.5
Slug position limit		Relay	Sigma 22RJC	1.0
Slug drive		Motor	Globe LL-2-45	7.3

Table 4-II(Concl.)

Circuit Function	Reference Figure	Component	Make & Model	Weight Oz.
Roll Angle Computation	4.8			
Horizon Sensor		Photo Transition & Optics	Texas Instr. LS-400	1.0
		Relay	Sigma 22RJC	1.0
Roll angle detection		Operational Amplifier	Nexus CQA-3	1.5
Roll angle reset		"	Nexus CQA-22	1.5
Roll angle integrator		"	Nexus SA-60	4.0
Roll Direction		"	2 Nexus CQA-22	3.0
		Relay	Sigma 22RJC	1.0
Programmer		Timer	Gayloard Reeves B322	8.0
				50.1

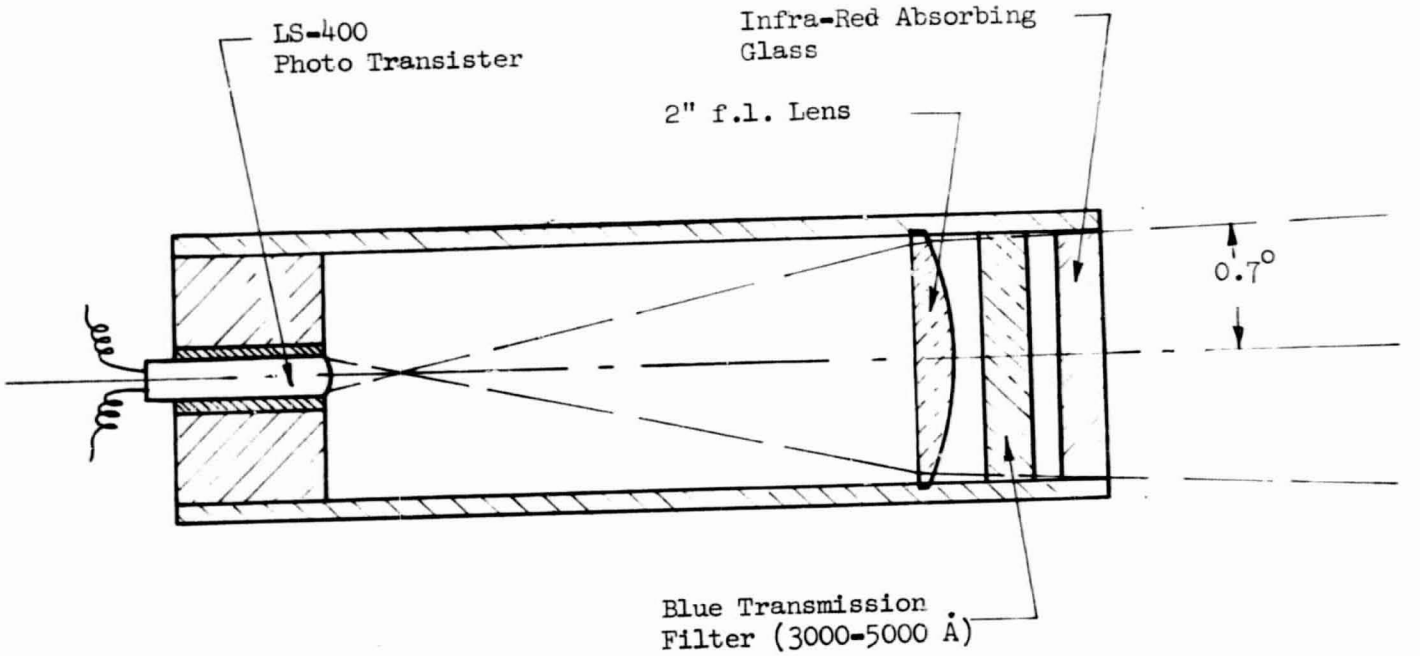

Fig. 4-14 BLUE LIGHT HORIZON TRANSIT SENSOR

No significant contribution to the background radiation is expected in the "blue" region due to ionized plazma sheath for the heating rates encountered. Ablating material primarily from the nose tip will be incandescent and emitting as black body radiators. The density of material is low and therefore will not significantly affect the transmission of radiation from the horizon. The effect is to reduce the contrast between space-earth by increasing the apparent brightness of the background although the absolute magnitude of the difference between space-earth remains unchanged.

The radiation from the plazma is somewhat noisy due to differences in the amount of ablating material passing through the field-of-view of each instrument.

The noise spectra is in two frequency domains: high frequencies associated with the transmit time of a particle through the field-of-view, and lower frequencies associated with the aerodynamic oscillations of the vehicle. The high frequencies can be filtered out in the electronics but the low frequencies are within the frequency range for indicating vehicle roll.

The earth's limb radiance profile has been calculated for 4200 Å and is found to peak in the vicinity of 50,000 feet above the earth surface. Good agreement with limb radiance profiles measured with different filters during the Gemini series of flights was found (Ref. 19). The limb decays from 90% to 10% in 50,000 feet which represents approximately 1.1 degrees roll angle difference to the horizon at the flight altitude of 150-200 thousand feet. The intensity is expected to vary along the horizon line. However, the normalized profiles should be similar. Thus, the roll angle measurement difference between right and left horizons will be significantly less than 1 degree. The one-half radiance point is about 7 degrees below the yaw plane. The peak radiance value will be approximately $1\text{-}5 \times 10^{-3}$ watts/ cm^2 -sterad in a 2000 Å band about 4000 Å.

The optical part of the horizon sensor, Fig. 4-14, comprises two small tubes each containing a simple lens, filters, and a solid state photo device. An ambiguity resolver utilizes one photo diode to differentiate between roll angles less than 90 degrees and more than 90 degrees.

The two tubes are pointed left and right out of the spacecraft at angles of 5 degrees below the horizontal. At altitudes of about 200,000 feet, the horizon is down 8 degrees from the horizontal, so the net sensor angle, with the horizontal plane, is -3 degrees.

The operation of the horizon sensor circuit is illustrated in Fig. 4-15. With wings level both the sensors see the dark sky and their outputs to the differential amplifier are balanced to about zero net output. More than five degrees roll will light one sensor and cause a saturated output from the differential amplifier, either plus 10 volts or minus 10 volts, for right or left roll, respectively. Since a roll of more than 169 degrees also causes both sensors to see the dark sky, an ambiguity resolver is included in the system, which simply detects the difference between sky and earth to tell whether the vehicle is right side up or upside down.

The only information delivered to the roll control system is the output of the roll angle computer, which takes the roll rate as an input and integrates it to generate the roll angle. The voltage "E" represents roll angle, and is limited to 60 volts or 270 degrees. "E" is operated on by the horizon sensor to make the computed angle agree with the true roll angle at certain discrete points. Between these correction points it is assumed that the computed angle will follow closely enough to do the required job.

Note that it doesn't really matter whether or not the commanded roll angle is actually attained - at least for reasonably short periods of time. If the roll angle arrived at is insufficient to effect the desired correction in g-level, then a bigger roll angle correction is commanded until the desired g-level is obtained. In the same sense, errors in roll angle from the horizon sensor are accommodated.

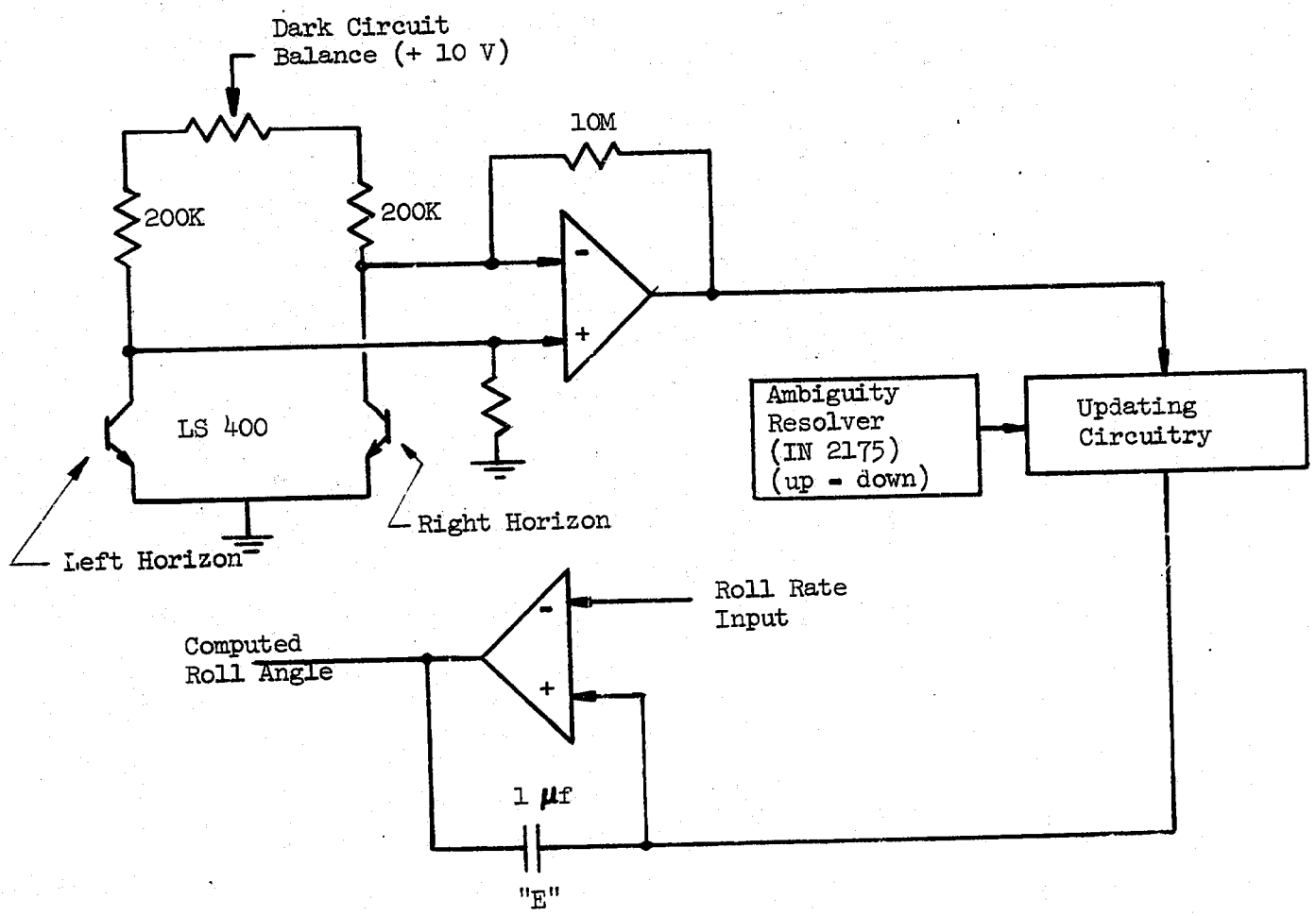

Fig. 4-15 HORIZON SENSOR CIRCUIT DIAGRAM

Normally the computed and actual roll angles are synchronized during pullout when wings level is asked for and barring unforeseen perturbations the two will remain fairly close from then on. If they drift apart from any cause, re-synch occurs every time the computed angle is 5 degrees, the actual angle is 5 degrees or less, the actual angle is 169 degrees or more, or whenever the computed angle is opposite in polarity from the actual angle.

Generally, the small amplitude oscillations in g-level will cause the roll angle to be commanded through zero about every 10 to 15 seconds early in the flight, and more often later on. The re-synch frequency then is fairly high. The alternate passage of each sensor past the limb radiance peak yields a signal which effectively bisects the sensor viewing angle to provide the vertical reference. Therefore, variations in altitude of peak radiance with sensor wave length or atmospheric conditions is automatically compensated.

4.3.3 Component Error Analysis

Recent advances in the transistor sciences, particularly in the area of the field effect transistor, (FET), have made off-the-shelf operational amplifiers available with remarkable drift stability. The units tested for this application are the product of the NEXUS LABORATORIES, and three different sizes were checked. The highest quality unit, suitable for use as an integrator and capable of $\pm$ 60 volt output, has a volume of 3 cu. inches. Lower performance units good for $\pm$ 20 volts and $\pm$ 10 volts output are only .7 cu. inches in volume. This error analysis is based on the Nexus amplifiers produced in 1965 but since that time many improved models have been marketed. The analysis presented, then, may be considered very conservative.

The g-error integrator computes a velocity error which in turn controls the g-level. If this integrator has an erroneous RC (Resistance - Capacitance) time constant, the effect is identical to an equivalent error in time rate. Time rate error effects are minimized by working around a null, where the integral of zero is still zero regardless of the error. During pullup, the g-errors are not zero and therefore an integrator error during the initial period of reentry will accummulate an error in integrator output. The

conservative figure is 1.8 miles per percent since a good integrator should do better than 1 percent.

For solid state devices the integrator drift is a function of temperature. The figure given is computed for a constant drift rate starting at time zero and ending at 800 seconds. This figure is directly effected by the scaling used and the maximum available voltage level of the integrator. 10 micro g's per second is a representative value considering the application, and this source is the largest single contributor to the range error.

Integrator initial condition is the manually input "velocity offset." Nominally, this input is between 300 and 800 ft/sec. Allowing 1000 ft/sec as the maximum, the range error is 1.5 miles per percent of full scale. Any error in setting the velocity offset is effectively an error in velocity during the whole 800 seconds of flight time.

Amplifier gain which determines the commanded roll angle per error in g-level contributes no measurable range error. Offset in this amplifier must be considered because it causes the vehicle to be steered to a slightly different g-level than commanded. The effect is almost completely wiped out by the velocity integrator, leaving only a small probable range error.

The timer is important only in its determination of the start of controlled flight. Since the spacecraft is traveling about 5 miles/second, the range error will be 5 miles for every second of error in the timer.

The accelerometer selected is the nulling type which is set to read zero at the desired g-level. The advantage of such a system is that the desired g-level is set in mechanically and can be calibrated in the laboratory rather than determined electronically with the attendant errors of on-board temperature coefficients. An error of 0.1% represents a very conservative

estimate for this type of application and includes temperature drift as well as repeatability.

The accelerometer gain, or volts output per g, is of importance only during pullup. A nominal reentry will start with the accelerometer reading a 1-g error and decreasing to zero error at t-75 seconds along a fairly straight line. After once reading the 1-g level (or zero g error) the accelerometer characteristics are relatively unimportant because the output will vary plus and minus about the zero point and one will cancel the other. However, during pullup, accelerometer errors will not cancel out and the velocity loop will compute an inaccurate velocity error. A figure of 1.5 miles per percent is conservative since most pullups will occur in less than 75 seconds.

Standard linearity is in the 1 percent region and is predictable in its effect on range. Linearity error, the departure from standard, is estimated to be 1 percent and its effect computed as listed.

Hysteresis is another characteristic whose effects cancel during the oscillation about the nominal but accumulate during pullup. Based on a 75 second pullup, the effect is negligible.

The effect of these errors on impact range dispersion for a 1-g flight of 800 seconds is summarized in Table 4-III. The errors listed include every source of error in the electronics of the guidance and control system. The root sum square of these will result in a probable range error of 7.5 miles attributable to the hardware. Combined with errors from other sources (Table 4-I) the net is 16.3 miles. The important conclusion to be drawn from the analysis is that errors arising from physical construction of the spacecraft (i.e., pitch and yaw trim) are much greater than those arising from run-of-the-mill hardware.

Table 4-III

RANGE ERRORS FROM GUIDANCE SYSTEM COMPONENTS

Error Source	Error Rate	Off-The-Shelf Equip Error	Range Error(n.m.)
Accelerometer			
Null Accuracy	2000 miles/g	.1%	2
Gain Error	1.5 miles/%	1%	1.5
Linearity Error	1.3 miles/%	.1%	.13
Hysteresis	150 miles/g	.01%	.015
Velocity Loop			
Integrator Error	1.8 miles/%	1%	1.8
Integrator Drift	640,000 miles/g	.00001 g/sec	6.4
Integrator Initial Condition	1.5 miles/%	1%	1.5
Amplifier Gain	0	1%	1.5
Amplifier Offset	300 miles/g	.001 g	.3
(Timer)			
Error prior to reentry	5 miles/sec	.1 sec	.5
			7.5 RSS

4.4 System Synthesis and Simulation

The operation of the guidance and control system, g-level control, impact dispersion and spacecraft despin dynamics have been analyzed and demonstrated with several simulations of varying complexity and sophistication.

The guidance concept was first demonstrated by incorporating the guidance equations into the PRESTO trajectory simulation (Ref.17). The vehicle roll response was approximated by an exponential transfer function $(1/(s+\alpha))$ of Appendix E. From this simulation with constant aerodynamic and spacecraft characteristics, the fundamental behavior of the guidance concept and its capability to control to a constant deceleration level and precise impact range were established. The majority of the results shown in Appendices D and E were verified with this simulation.

The spacecraft despin and dynamic motion behavior were demonstrated with a modification (RPM Version III) to the Roll-Pitch Motion program originally developed for roll resonance analyses of sounding rockets (Ref. 1 & 2). The basic program calculated angular motions (pitch-yaw-roll) about a prescribed trajectory of a symmetrical vehicle with lateral c.g. offset and longitudinal lift trim. The modification for these analyses incorporated asymmetric aerodynamic characteristics and inertial properties and a roll control system for the translating control mass.

The final system synthesis and demonstration were accomplished with a second modification (RPM Version IV) of the Roll-Pitch Motion program to incorporate the translational degrees of freedom and the guidance equations for the mechanization described in Section 4.2. The results described in the main body of the report were generated with this 6-D Entry Guidance and Dynamics Simulation (EGADS). The program is described briefly in Appendix I. The most notable features of the program are its operating economy (4 seconds of flight per sec of UNIVAC 1180 computer time) for complete guidance, control and dynamics simulation, simple

input procedures and plotted output. Furthermore, within the small angular motion constraints excellent agreement with more complete and complex 6-D simulation is expected.

5. SPACECRAFT DESIGN

The objective of the conceptual design effort was to demonstrate the feasibility of packaging the required guidance and control hardware, instrumentation, and recovery gear within the size, volume, and weight constraints of the four-stage Scout launch vehicle. Existing hardware items were selected in so far as possible in order to provide representative component weights and dimensions and to yield a realistic equipment arrangement to meet the weight and balance requirements of Section 2. A construction concept was devised to provide a basic spacecraft system which could accommodate various heat shield materials and fabrication techniques as well as individual test panels. In addition a "clean" interface between the heat shield experiment and the spacecraft systems was considered highly desirable, so that experimental instrumentation control could be retained by the experimenter.

5.1 Spacecraft Description

The essential features of the concepted spacecraft are summarized in Fig. 5.1. The spacecraft has a span of 2 feet and a length of 3.5 feet. The aerodynamic reference axis is 2.6 inches above the cone centerline. The primary structure consists of an aluminum monocoque sealable shell with external ribs to which the main heat shield is attached. The molded carbon phenolic nose tip is attached to the forward bulkhead followed by a fixed forward panel and leading edges of purple blend ablator. The heat shield test sections are attached to the external ribs with a 1/2-inch gap between the primary structure, thus allowing test of double wall shields.

All flight equipment components are mounted on a sliding tray attached to the base plate. By unbolting the base plate from the primary shell, the flight systems and test instrumentation are completely accessible for inspection, adjustment, and checkout. The spacecraft is attached to Scout with the standard Scout E section and the standard payload support ring. Spacecraft service for ground checkout and inflight start up from Scout is through the two

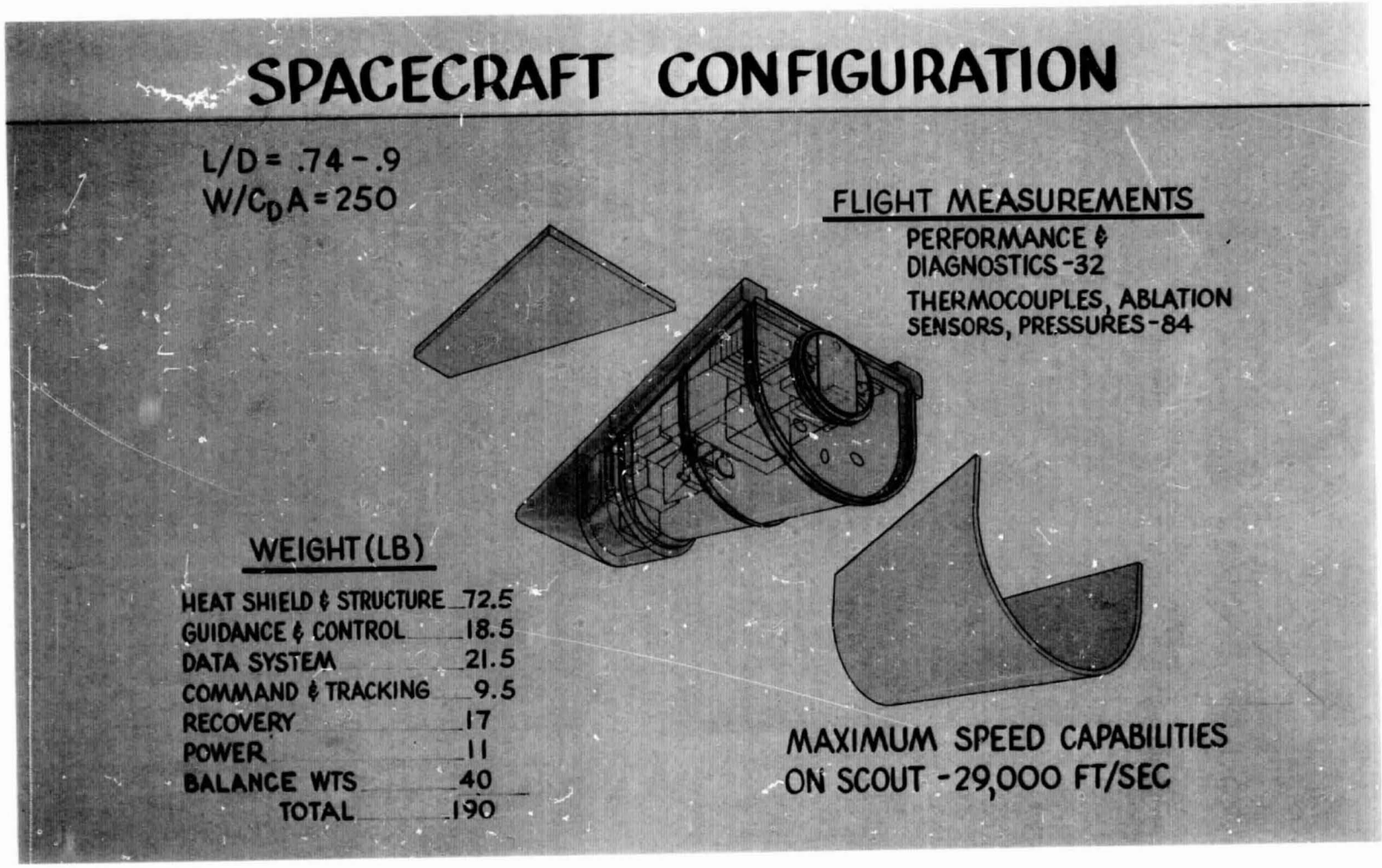
SPACECRAFT CONFIGURATION
L/D = .74 - .9
W/C_D A = 250
FLIGHT MEASUREMENTS
PERFORMANCE & DIAGNOSTICS - 32
THERMOCOUPLES, ABLATION SENSORS, PRESSURES - 84
WEIGHT (LB)
HEAT SHIELD & STRUCTURE 72.5
GUIDANCE & CONTROL 18.5
DATA SYSTEM 21.5
COMMAND & TRACKING 9.5
RECOVERY 17
POWER 11
BALANCE WTS 40
TOTAL 190
MAXIMUM SPEED CAPABILITIES
ON SCOUT - 29,000 FT/SEC

Fig. 5.1

standard fly-away umbilicals on the payload support ring. The recovery parachute container is mounted within the payload support ring. The recovery parachute container is mounted within the payload support ring for easy normal flight deployment. Just below the payload support ring, the horizon sensors are evident.

The translating control mass mounted below the equipment is triangular shaped for a snug fit against the side wall at maximum displacement.

The total spacecraft weight is 190 pounds which yields a ballistic factor of $W/C_DA = 250$ lb/ft^2. For this weight the maximum speed capability with Scout is 29,000 fps. The lift-to-drag ratio varies from 0.74 at orbital speed to 0.9 near the end of the trajectory primarily due to the variation of the friction drag.

The instruments and data system have been sized to provide six continuous channels and two commutated channels of 60 points each with a sample rate of 1 point per second. The measurements to be made along with the sample frequency and channel assignment are given in Table 5-I.

5.2 Design Constraints and Requirements

The only dimensional constraints for the spacecraft were that the standard Scout shroud and "E" section adaptor be used if possible. Figure 5-2 demonstrates that the vehicle fits into the standard Scout shroud with adequate clearance for the 24-inch span with the principal axis aligned with the Scout fourth stage spin axis. The clean aerodynamic shape is maintained by the indented base mounting arrangement on the "E" section. The separation clamp has been rotated in order to satisfy the clearance zone limits noted. The top near edge intercepts this zone slightly. If this proves unacceptable, a shallow indentation along the top trailing edge can yield sufficient relief. No additional ground service connections through the shroud appear necessary by virtue of the pair of twelve-point umbilicals on the standard

Table 5-I

LIST OF FLIGHT MEASUREMENTS

Measurement	Data Rate	Channel	Range	Measurement Objective
Pitch rate	Cont.	6		Entry attitude & despin characteristics
Yaw rate	Cont.	7		Entry attitude & despin characteristics
Roll rate	Cont.	8	High	Entry attitude & despin characteristics
Normal acceleration	Cont.	9		Angle-of-attack during test period
Lateral acceleration	Cont.	10		Angle-of-attack during test period
Longitudinal acceleration	Cont.	11		Trajectory status & guidance system performance
"g" Reference	1 pt/sec	15		Trajectory status & guidance system performance
"g" Error	"	15		" " "
Velocity error	"	15		" " "
Roll rate	"	15	Low	" " "
Differential horiz. output	"	15		" " "
Crossrange computation	"	15		" " "
400 cycle frequency	"	15		" " "
Roll command	"	15		Guidance & control diagnostic
Left-right roll direction	"	15		" " "

Table 5-I Cont.

Measurement	Data Rate	Channel	Range	Measurement Objective
Slug position	1 pt/sec	15		Guidance & control diagnostic
Roll position	"	15		" " "
Battery voltage	"	15		Spacecraft status
Plus supply current	"	15		" "
Minus supply current	"	15		" "
Plus 75v supply	"	15		" "
Differential 75v supply	"	15		" "
Plus 15v supply	"	15		" "
Differential 15v supply	"	15		" "
400 cycle phase A	"	15		" "
400 cycle phase B	"	15		" "
Calibrate 1				Calibrate
Calibrate 2				"
Calibrate 3				"
Sync. 1				"
Sync. 2				"
VSWR(1) Transmit	1 pt/sec.	15		Blackout severity
VSWR(1) Reflect	"	15		" "
VSWR(2) Transmit	"	15		" "
VSWR(2) Reflect	"	15		" "
VSWR(1) Temp	"	15		" "
VSWR(2) Temp	"	15		" "
29 Pressure/ Ablations Sensors	"	15		Mtls Expt. objective

Table 5-I Concl.

Measurement	Data Rate	Channel	Range	Measurement Objective
55 Thermocouples	1 pt/sec	18		Mtls Expt. Objective
Calibrate 1	"	18		Calibrate
Calibrate 2	"	18		"
Calibrate 3	"	18		"
Sync. 1	"	18		"
Sync. 2	"	18		"

SCOUT INSTALLATION

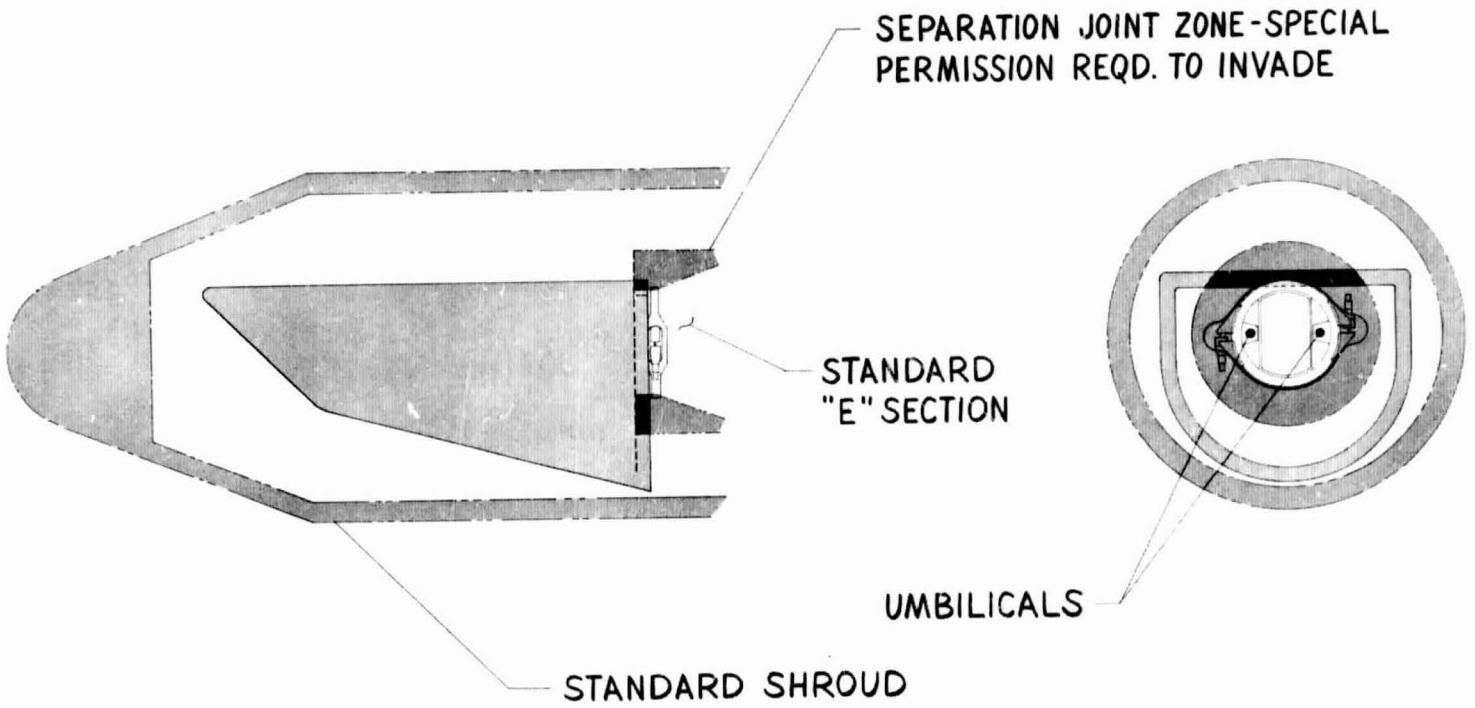

Fig. 5.2

"E" section. The spacecraft longitudinal c.g. position is well with the Scout payload envelope.

The relatively mild reentry test environment placed no stringent requirements on the spacecraft design. The most significant loading requirement arose from the Scout thrust acceleration during fourth stage firing.

The important requirements imposed on the conceptual design are summarized below:

- Environment
  + 20 g maximum longitudinal acceleration at fourth stage B.O.
  - 20 g maximum longitudinal shock at parachute shock
  300°F maximum temperature at heat shield substrate
  180 rpm maximum spin rate
  30 deg. maximum coning angle at parachute deployment
  500 psf maximum dynamic pressure
- Recovery
  Subsonic parachute deployment
  30 fps maximum descent speed
  Floatation with 2-inch minimum free board
  Tracking beacon
- Communications and Data
  S-band tracking and T/M
  Command link for destruct, or ground control
  6 continuous channels
  2 commutated channels (60 measurements each)
  Tape recorder with multiple playback
- Instrumentation
  Heat shield thermocouples, ablation sensors and pressure taps
  Longitudinal, normal, and lateral accelerometers
  Roll, pitch, and yaw rate gyros

Blackout sensors (2 VSWR)
Monitor G&C system operation

- Mass Properties
  350-pound maximum weight
  Minimum roll moment of inertia
  Roll principal axis parallel to cone centerline

5.3 Internal Arrangement

The arrangement of the selected equipment to satisfy the design requirements is illustrated in Fig. 5-3. The major subsystems are coded according to the table on the right. The guidance instruments and electronics are grouped about the vehicle center of gravity with the control mass motor mounted directly below. The control mass is position ahead of the c.g. and translates laterally below the data system commutator and signal conditioner/oscillator. The tape recorder is located directly forward and flanked by the transmitter units. The command encoder and recovery sequencer are placed immediately behind the c.g. The batteries are located at the top rear corners surrounding the parachute drogue gun. Diametrically opposite, the dynamic balance weights are disposed about the front of the tape recorder and transponder. The horizon sensors are mounted on the base below the mounting ring and parachute cannister with the antenna flanking above.

A relatively spacious arrangement results with the representative equipment items employed with easy access for checkout, repair or replacement of components and for recharging or replacing batteries.

The design of the translating control mass is shown in greater detail in the upper right of Fig. 5-3. The unit is mounted on two transverse support tubes attached to the primary structure. The motor and integral speed reducer translate the overhanging control mass, motor, and housing through the spur gear train and rack on the aft support tube. The slug is configured

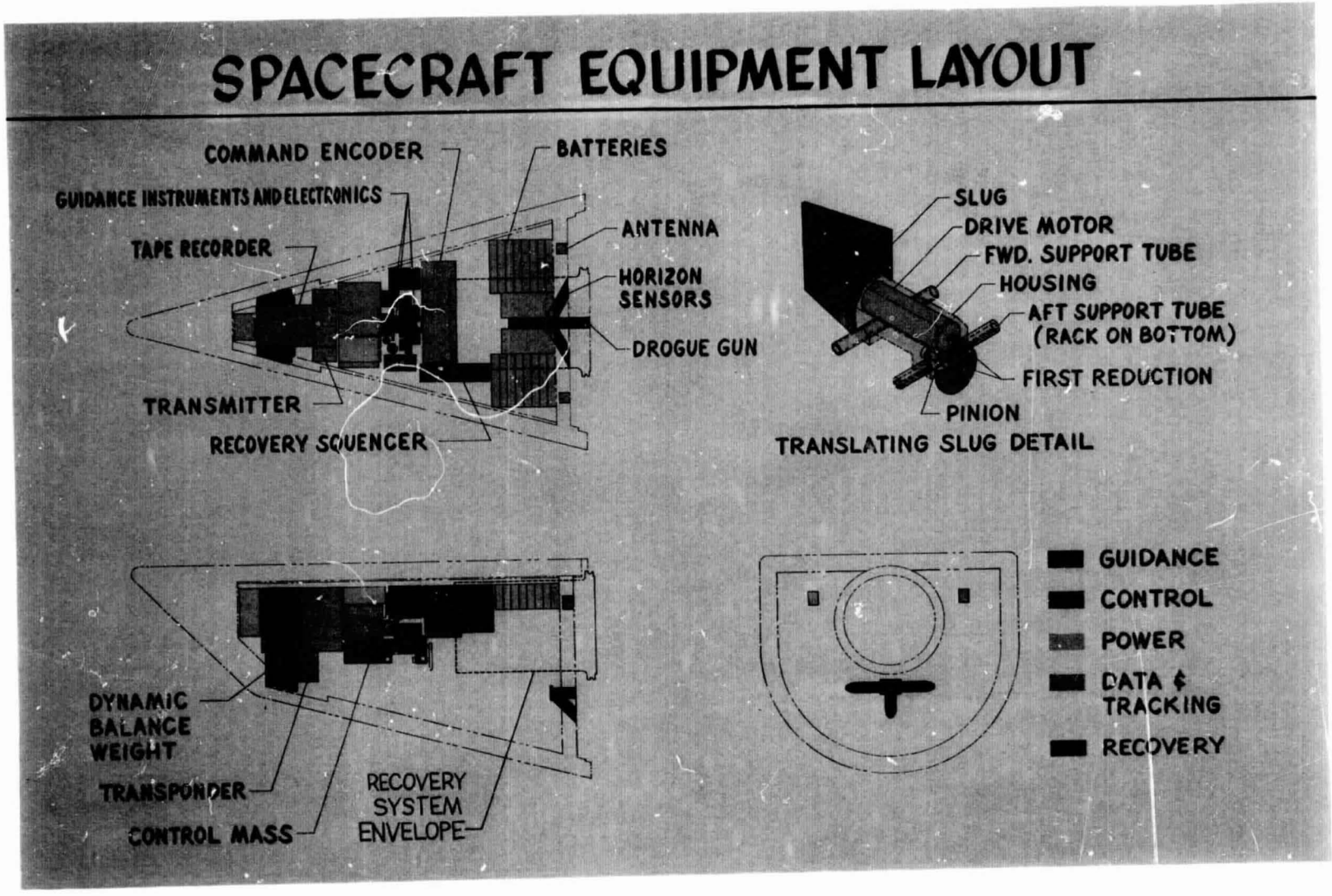
SPACECRAFT EQUIPMENT LAYOUT
COMMAND ENCODER
BATTERIES
GUIDANCE INSTRUMENTS AND ELECTRONICS
ANTENNA
TAPE RECORDER
HORIZON SENSORS
DROGUE GUN
TRANSMITTER
RECOVERY SQUENCER
SLUG
DRIVE MOTOR
FWD. SUPPORT TUBE
HOUSING
AFT SUPPORT TUBE (RACK ON BOTTOM)
FIRST REDUCTION
PINION
TRANSLATING SLUG DETAIL
DYNAMIC BALANCE WEIGHT
TRANSPONDER
CONTROL MASS
RECOVERY SYSTEM ENVELOPE
GUIDANCE
CONTROL
POWER
DATA & TRACKING
RECOVERY

Fig.5.3

to a symmetrical 30-degree wedge for a snug fit to the spacecraft side to obtain maximum displacement. The drive motor maximum speed of 24,000 rpm provides a peak translation rate of 12 inch/sec.

5.4 Equipment List and Weight Breakdown

The major spacecraft components and internal equipment items are summarized in Fig. 5-4. The structure and heat shield including the experimental panels account for about one-third of the spacecraft weight. Since the primary heat shield constitutes only 50 percent of this weight, selection of heat shield materials other than Purple Blend specified for the study would not appreciable alter the total weight or balance. The low backface temperature limit ($300^{o}F$) allows use of aluminum for structural members throughout. The guidance and control system including the 10-pound control mass require only a small portion (10%) of the total weight due to its basic simplicity and elimination of external control surfaces and actuators and/or reaction control systems.

The data and tracking systems account for about 17 percent of the total spacecraft weight. The individual equipment items were selected from flight proven hardware and the circuitry based on experience with the Polaris reentry test data systems.

The recovery system represents a straight forward design application of current state-of-the-art technology and available hardware. For the maximum impact velocity with subsonic parachute deployment, the weight allowance for recovery is only 9 percent. A reflector incorporated into the canopy may be desirable to improve data transmission. For air retrieval, an additional allowance of 7 pounds for larger parachute (21.5 ft/sec. maximum descent speed) and increased structure would be required. The floatation requirement is exceeded for the conceptual design. With the parachute container and heat shield air space filled, a freeboard of 3 inches is achieved in the

SPACECRAFT EQUIPMENT AND WT BREAKDOWN

	MATERIAL / SUPPLIER	WEIGHT (LB)	
STRUCTURE			72.5
HEAT SHIELD (INCL. EXPT)	PURPLE BLEND/AL SUBSTRATE	46	
NOSE TIP	CARBON PHENOLIC	11	
PRIMARY STRUCTURES	AL	15.5	
GUIDANCE AND CONTROL			18.5
ELECTRONICS	CUSTOM (LMSC)	8.5	
CONTROL MASS		10.0	
DATA SYSTEM			21.5
TAPE RECORDER	BORG-WARNER	8.0	
TRANSMITTER (S-BAND)	CONIC CTM-UHF-1A	0.7	
COMMUTATORS (60×10) (2)	LIND	1.3	
ANTENNA		1.2	
MISC. ELECTRONICS	LEDER/LMSC/ELECTRO DEV	6.3	
INSTRUMENTATION & WIRING		4.0	
TRACKING AND COMMAND			9.5
TRANSPONDER (C-BAND)	MOTOROLA	3.3	
ENCODER / DECODER	KELTECH	5.0	
ANTENNA	LMSC	1.2	

Fig. 5.4

SPACECRAFT EQUIPMENT AND WT BREAKDOWN

	MATERIAL/SUPPLIER	WEIGHT (LB)	
RECOVERY			17.0
PARACHUTE	IRVING	6.2	
DROGUE GUN	McCORMICK-SELPH	1.5	
RECOVERY SYS SEQUENCER	NORTHROP, VENTURA	1.3	
BEACONS	LMSC	2.0	
CONTAINER	FIBERGLAS	4.8	
MISC. EQUIPMENT		1.2	
POWER			11.0
BATTERIES	YARDNEY HR-10	11.0	
DYNAMIC BALANCE WEIGHTS			40.0
	TUNGSTEN		
	TOTAL		190

Fig.5.4(concl)

nose down attitude. Adequate metacentric stability is assured for the longitudinal c.g. location of this configuration.

The Yardney silver cell batteries represent 6 per cent of the spacecraft weight.

The dynamic balance weight allotment of 40 pounds arises primarily from the asymmetric configuration in the pitch plane. The principal axis of the spacecraft structure and heat shield is tilted up from the desired spin axis by 4 degrees and would result in unacceptable pitch oscillations following passage through resonance during despin. The weight and balance and inertia summary analysis for the design is presented in Table 5-II.

For the design described above, the principal spacecraft characteristics are summarized below:

Base radius	= 12 in.
Cone angle	= 15 deg.
Length	= 3.38 ft.
A_{ref}	= 3.14 ft.^{2}
A_{base}	= 3.01 ft.^{2}
A_{surf}	= 14.3 ft.^{2}
Vol	= 4.24 ft.^{3}
Bouyancy	= 248 lbs. (minimum)
Weight	= 190 lbs.
W/C_DA	= 250 lb/ft.^{2}
W/C_LA	= 290 lb/ft.^{2}

5.5 Design Implications

The conceptual design investigations conducted during this study and summarized in this section have demonstrated the feasibility of packaging the spacecraft and equipment within the standard Scout shroud as well as

Table 5-II

SPACECRAFT INERTIA CONTRIBUTORS

Item	Weight -lbs	[1] X_{cg} in	[2] Z_{cg} in	[3] I_{xx} lb-in^2	[3] I_{yy} lb-in^2	[3] I_{zz} lb-in^2	[3] I_{xz} lb-in^2
Cone[4]	22.8	32.5	5.5	2580	4380	3640	-1490
Top[4]	11.6	32.9	-5.4	995	1595	2020	433
Sides[4]	18.8	29.6	-4.4	569	880	1940	131
Base	5.1	43.0	2.4	389	1653	1625	- 204
Nose	11.5	11.0	2.6	200	2600	2600	-
Misc. Struct.	2.7	26.2	2.6	-	-	-	-
Equip.	74.5	29.79	3.5	714	6498	5872	734
Misc. Equip.	3.0	26.2	2.6	-	-	-	-
Sub Total	150.0	-	-	5474	17475	17697	- 496
Ballast	40.0	16.0	1.4	200	4200	4100	500
Total	190.0	26.2	2.6	5674	21675	21797	4
Moment of Inertia - slug - ft^2				1.22	4.68	4.70	0
Radius of gyration-ft.				0.45	0.88	0.89	

1. Measured from cone vertex
2. Measured from cone centerline
3. Transferred to design center of gravity
4. Includes heat shield, substructure, rings, etc.

utilizing the standard "E" section payload adaptor. Furthermore, preflight checkout can be accomplished through the existing service umbilicals. An attractive construction concept has been devised for flight testing heat shield panels and independent preparation and checkout of spacecraft and experiments. Furthermore, the design concept indicates excellent potential for reuse of the primary structure and equipment.

6. FLIGHT TEST PROFILE

The proposed flight test profile evolved from consideration of the spacecraft descent profile, the Scout performance capability and dispersion characteristics, range safety, tracking and data acquisition, and finally, spacecraft recovery.

6.1 Scout Performance and Dispersion

The Scout trajectory shaping was achieved within current operational constraints yet obtained optimum performance to specified injection conditions. The Scout profile was generated with the TOLIP program (Ref. 20) developed by LMSC expressly for Scout preflight planning including performance optimization, linear pitch programming, injection dispersions, range safety and stage impact, and ground tracking programming. This tool allowed realistic and comprehensive performance and dispersion evaluation to be accomplished early in the study to provide a solid basis for selection of the nominal flight test profile.

The four-stage Scout vehicle consisted of the Algol IIB, Castor XM33E5, Antares X259-A3, and FW4S motors. The nominal propulsion, mass, and aerodynamic characteristics were supplied by the Scout Project Office at NASA-LRC and Reference 21. The performance was evaluated for a reentry flight path angle of -2 degrees at 300,000 and 400,000 ft. altitude. The principal operational constraints imposed on the trajectory shaping were a maximum dynamic pressure of 1.0 lb/ft^2 at third stage ignition and shroud separation, and max $\bar{q}$ = 2000 lb/ft^2.

The performance capability and trajectory shaping are summarized in Fig. 6.1. "Optimized powered trajectories with final stage burnout at 300,000 ft and a -2 degree relative path angle yield reentry payload capability of 350 lb at orbital speeds (25,700 fps) to 100 lb at 32,000 fps. If burnout altitude is constrained to 400,000 ft., a 15 lb payload penalty is incurred for a given velocity. The burnout range for the optimum trajectories varies from 380 N.M. at orbital velocity to 410 N.M. at the higher velocity. The angle of attack varies from 2^o to 3^o over this range.

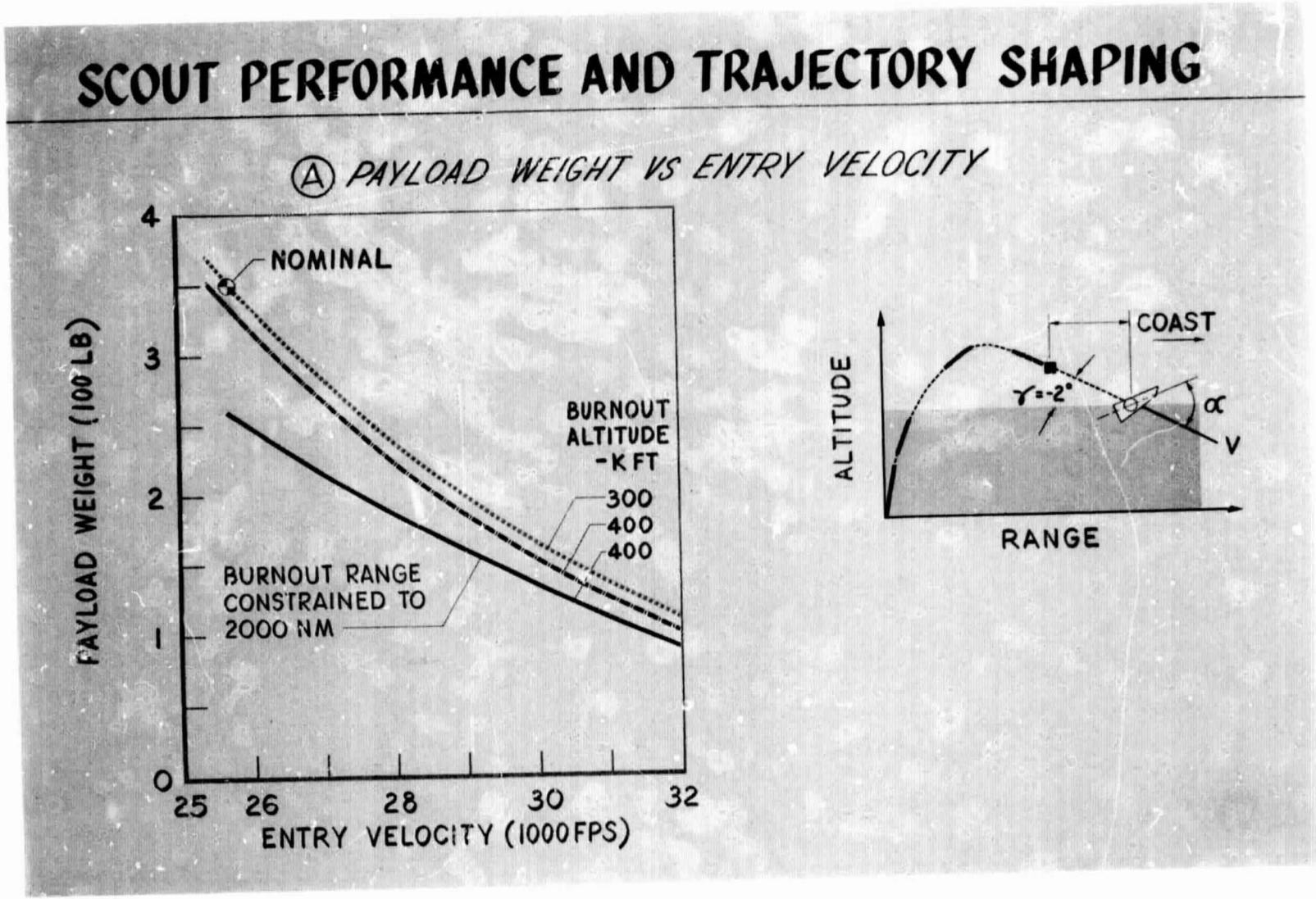
SCOUT PERFORMANCE AND TRAJECTORY SHAPING
Ⓐ PAYLOAD WEIGHT VS ENTRY VELOCITY
PAYLOAD WEIGHT (100 LB)
ENTRY VELOCITY (1000 FPS)
NOMINAL
BURNOUT ALTITUDE -K FT
300
400
400
BURNOUT RANGE CONSTRAINED TO 2000 NM
ALTITUDE
RANGE
COAST
γ=-2°
α
V

Fig.6.1

SCOUT PERFORMANCE AND TRAJECTORY SHAPING

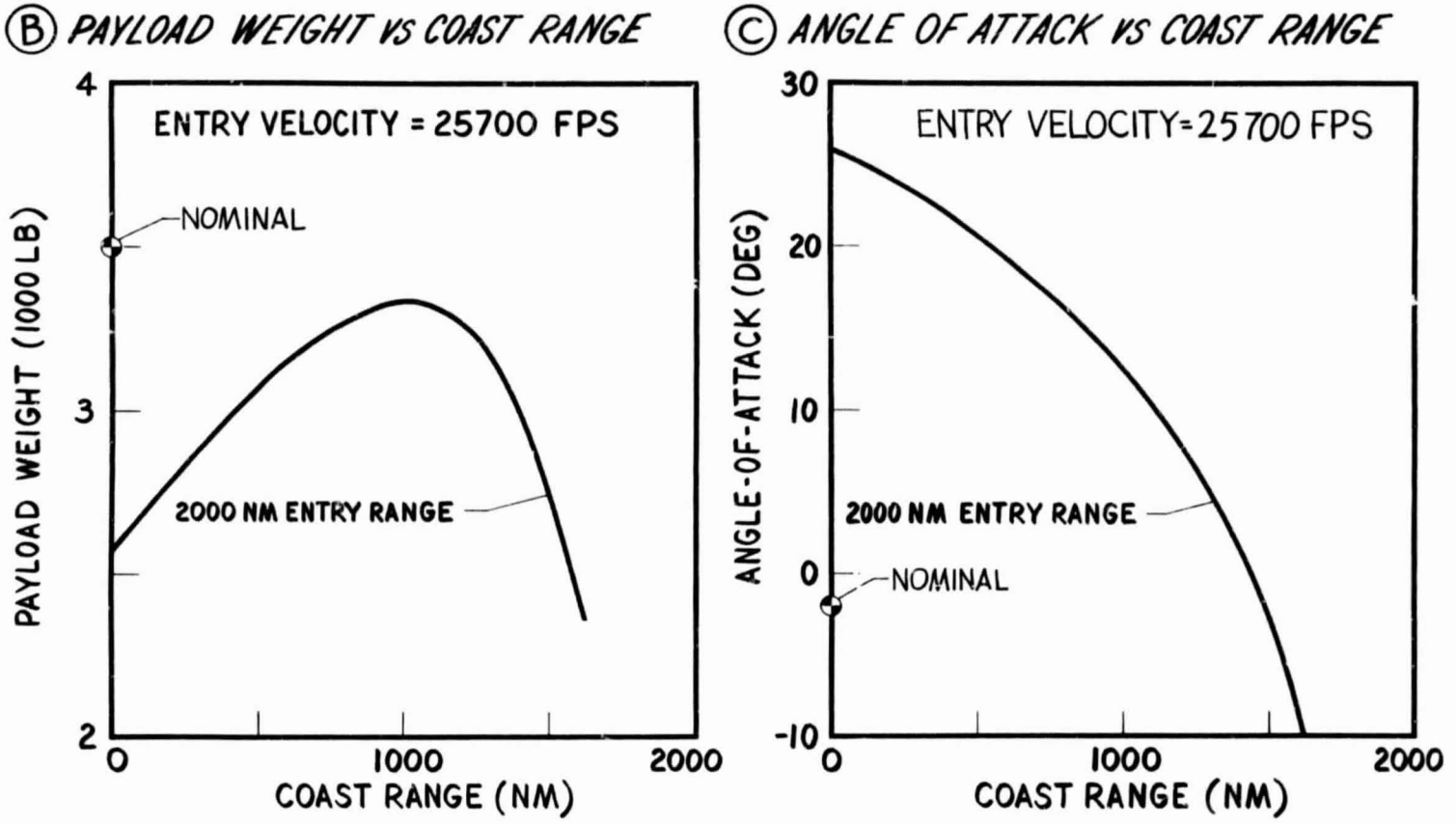

Fig.6.1(concl)

Constraining the burnout range to 2,000 N.M. to achieve flight test termination and recovery at Ascension Island (assuming launch from Wallops Island) causes a significant reduction in payload at orbital speeds as indicated by 6.1 (a). In addition, an angle-of-attack of 25° results which is undesirable during despin and guidance capture. The Ascension Island entry can be achieved by burnout uprange at a higher altitude followed by a coast to the desired reentry path angle and altitude as shown in the sketch of Fig. 6.1. Payload degradation and angle-of-attack at reentry are both reduced as shown in Fig. 6.1(b) and (c). Optimum reentry in the Ascension recovery area can be achieved with a coast range of 1000 N.M. and an entry angle-of-attack of 12°.

Scout dispersions were evaluated for a 400 N.M. downrange entry and a 2000 N.M. downrange entry (1000 N.M. coast range) with the sources and performance, spacecraft, and wind deviations summarized in Table 6-I. The three sigma RSS dispersions accrued through fourth stage burnout are also summarized in the table as dispersion elements. The principle contributor to the flight path dispersion is the fourth stage tip-off angle (2.72 degrees) which alone causes a .85 degree deviation in flight path. The primary sources of the altitude error are the first stage thrust deviations resulting in final altitude dispersions of +16,000 ft and -24,700 ft. These burnout dispersions propogate to the start of guidance (0.25g) as shown in Table 6-II for the two cases considered. With no range control or correction, these deviations propogate directly to impact. Downrange and crossrange control techniques are described in Appendix F.

The initial position and velocity dispersions propagate directly unless corrections are commanded based on tracking data. However, these effects are negligible (about 1.5 n.m. for the velocity error) in comparison to the flight path induced dispersions.

6.2 Spacecraft Performance

The reentry trajectory profile for the nominal 1-g descent of the spacecraft is shown in Table 6-III. The guided range is 1570 n.m. from capture at 1-g deceleration. Despin from the maximum 3 RPS occurs at 0.32 g for the selected control mass of 10 pounds at about 220,000 feet altitude. Pull-up to the 1-g point is accomplished at 188,000 feet altitude and 24,850 fps velocity.

Table 6-I

SCOUT DISPERSION SOURCES AND INJECTION DISPERSIONS

Source	Magnitude (3σ)
Thrust & Weight	
Stage 1	± 5.0%
2	± 4.4%
3	± 5.9%
4	± 3.6%
Drag	± 10%
Stability Margin	± 20 inches
Thrust Misalignment	0.25 deg
Control System Deadband	0.8 deg
Fourth Stage Tipoff	2.72deg
Launch Azimuth	0.2 deg
Launch Attitude	0.1 deg
Winds	per NASA TN D-1249

Dispersion Element	High	Low	Yaw
Altitude- ft.	27905	-40849	-15743
Velocity - ft/sec	110	- 179	- 39
Flight path - deg	0.95	- 1.03	- 0.20
Down Range - n.m.	3.4	- 7.1	- 1.4
Cross Range - n.m.	-	± 2.1	± 8.3

Table 6-II

ACCRUED DISPERSION AT START OF REENTRY GUIDANCE

Impact Range - n.m.	2430		4370	
	High	Low	High	Low
Time - sec.	+ 131	- 52	+ 283	- 94
Range - n.m.	+ 555	- 221	+ 1200	- 400
Crossrange - n.m.	± 3.8	± 3.8	± 7.0	± 7.0

Table 6-III

REENTRY TRAJECTORY

$t^{(1)}$ Sec.	h 1000 ft.	V 1000 FPS	Deg.	Ax/g g's	R N.M.
0	300.0	25.71	-2.00	0	380
78	226.3	25.80	2.00	0.25	814
143	188.5	24.85	0.16	1.00	892
169	187.1	24	.17		997
231	182.4	22	.21		1232
293	177.3	20	.25		1446
355	174.5	18	.31		1640
417	171.3	16	.39		1813
479	167.6	14	.51		1966
541	163.4	12	.70		2099
603	158.5	10	1.02		2211
665	152.7	8	1.63		2303
727	145.2	6	2.85		2374
758	135.7	5	3.85		2402
789	124.3	4	6.13		2425
820	110.5	3	11.6		2943
851	91.8	2	26.9	1.00	2455
882	61.4	1	90.0	-	2462

(1) Time measured from 300,000 ft.

Sufficient time for spacecraft separation prior to 0.05 g is provided. No difficulty with adequate separation distance between the spent Scout fourth stage is anticipated because of its very low ballistic factor ($W/C_DA \approx 10$ lb/ft^2). If an added margin of safety is desired, retro rockets to slow and tumble the fourth stage can be utilized with minor performance penalty.

6.3 Flight Test Profile Description

The selected flight profile is summarized in Fig. 6.2. Launch is from Wallops Island along an azimuth of 130 degrees with fourth stage burnout at 300,000 feet about 400 n.m. downrange. Spacecraft separation, despin and guidance capture to 1-g deceleration are monitored from Bermuda, as well as Scout injection performance. The principal test period occurs between 200,000 and 150,000 feet altitude with recovery off the coast of South America. Continuous tracking coverage and data acquisition are maintained after Bermuda from Antigua and two ships. A recovery ship is stationed in the impact zone. The total range from Wallops Island is 2430 n.m.

With the 1-g descent profile adopted as a baseline for the study, the atmospheric portion of the flight range is fixed as described in Section 4. While the long-range trajectory (4370 n.m. from Wallops Island) could be obtained from the four-stage Scout with near maximum performance, unacceptable range dispersion were encountered as illustrated in Fig. 6.3. The large range dispersions are due to the combination of long coast range from Scout burnout to the 0.25 g altitude and the $\pm$ 1 degree path deviations. Since guidance capture would occur just short of Ascension Island for the shallow (+ 1 degree) dispersion case, recovery near Ascension is precluded. Reshaping the Scout trajectory to yield burnout at 300,000 feet reduces the range deviations from Scout to within manageable magnitude. Furthermore, injection angles-of-attack are maintained small (2-3 degrees).

A preliminary sequence of events from launch to impact is presented in Table 6-IV. This sequence demonstrates compatibility with the Scout programmer for the proposed launch trajectory and establishes spacecraft programmer requirements. Events and timer functions were taken from Ref. 18. A delay of 8.8 seconds between fourth stage spin-up and ignition allows sufficient time for

FLIGHT TEST PROFILE

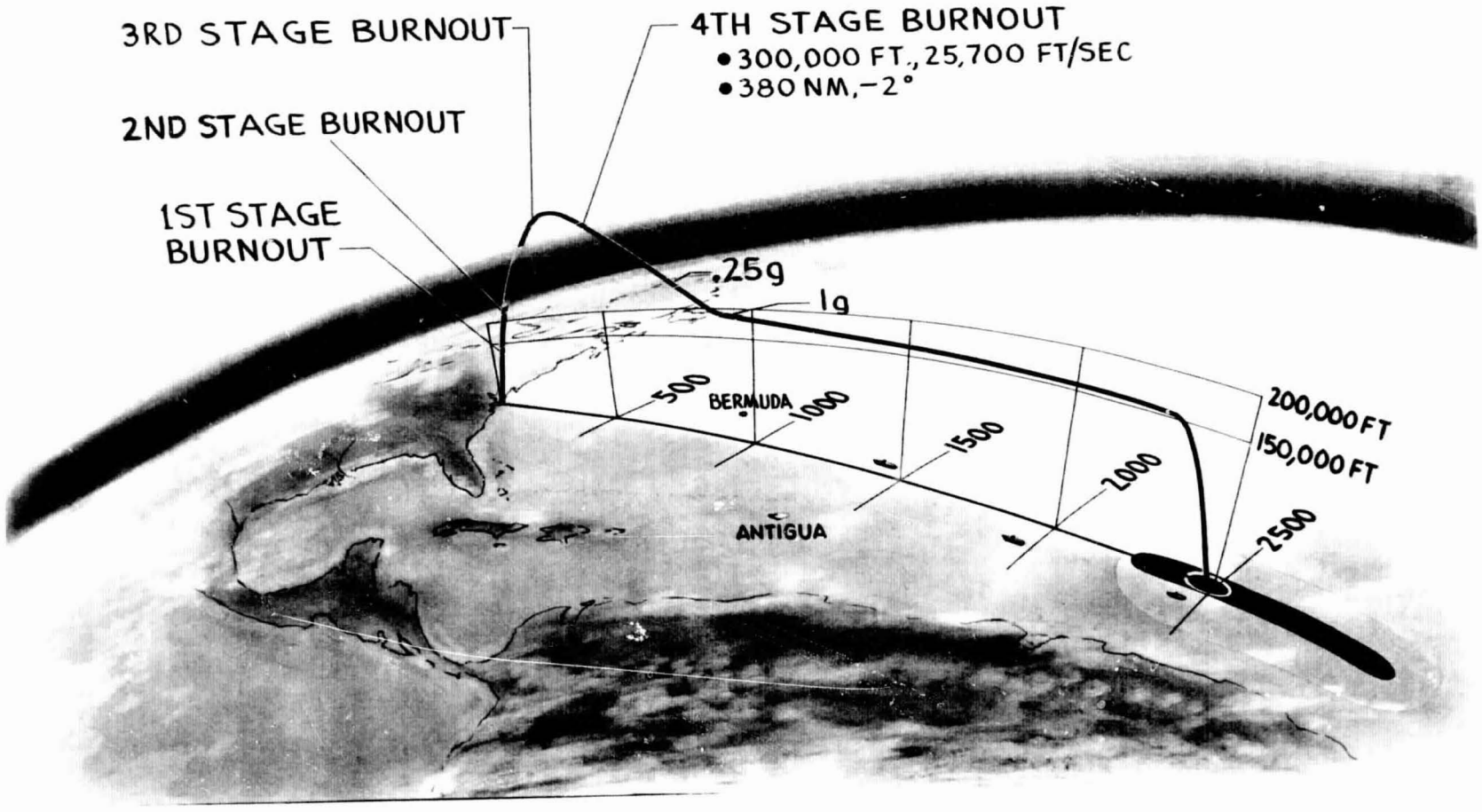

Fig. 6.2

TEST FLIGHT PROFILE SELECTION

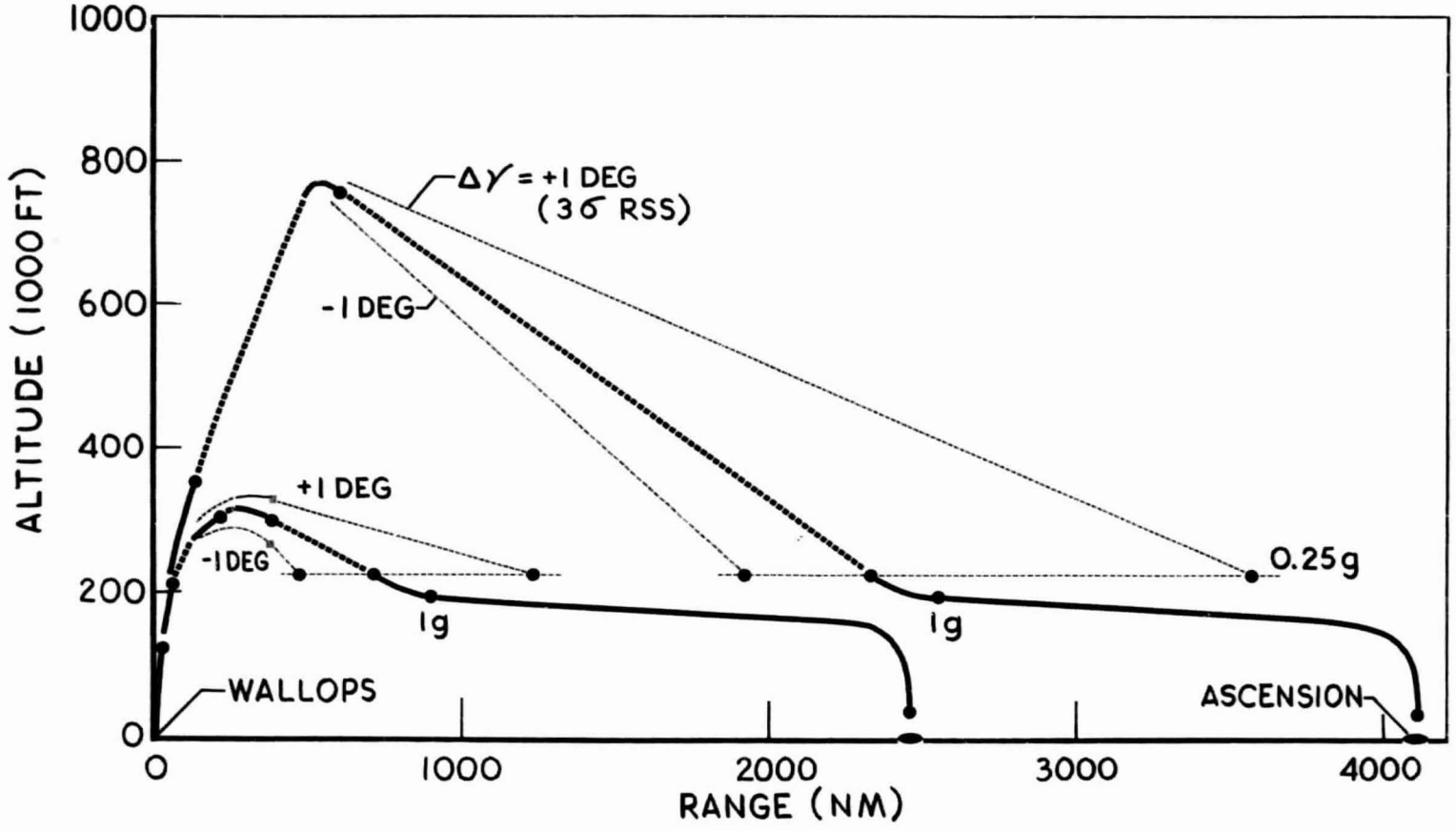

Fig. 6.3

Table 6-IV

SEQUENCE OF EVENTS

Time(Sec.)	Event	How Accomplished	Trajectory Parameters h Ft.	V FPS	Deg	R N.M.
- 1.00	Start payload programmer. Place guidance on stand-by.	Blockhouse				
0.00	1. Stage I ignition 2. $\theta_C = 0.0$	Blockhouse	0	0	90.0	0
0.20	Start timer. Start payload clock	Flyaway Flyaway				
3.00	$\theta_{C1} = 2.82530'$	Timer Function 1	141	96	90.0	0.8
8.50	$\theta_{C2} = 1.19724$	Timer Function 2	1,205	298	81.8	0.8
18.12	$\theta_{C3} = 0.79303$	Timer Function 3	5,948	771	66.3	0.8
34.62	$\theta_{C4} = 0.391774$	Timer Function 4	23,810	1,877	51.6	2.3
41.49	Maximum Dynamic Pressure		35,186	2,525	47.6	3.8
78.60	1. Stage 1 burnout 2. $\theta_{C5} = 0.50537$	Timer Function 5	116,928	3,350	33.1	19.6
87.59	1. Stage 2 ignition 2. Activate B controls 3. Separate first stage 4. Remove first stage control 5. Switch in body bending filter 6. $\theta_{C6} = 2.86779$	Timer Function 6 Timer Function 6 Stage 2 ignition Stage 1 separation Timer Function 7 Timer Function 8	132,026	3,198	28.9	23.7

Table 6-IV (Cont.)

Time(Sec.)	Event	How Accomplished	Trajectory Parameters h Ft.	V FPS	R Deg	R N.M.
89.62	θ_{C7} = 0.41318	Timer Function 9	135,163	3,341	27.8	24.7
128.19	1. Stage 2 burnout 2. θ_{C8} = -0.12016	Timer Function 10	207,281	9,998	12.8	62.4
165.0	1. Shroud separation squib ignition	Timer Function 11	272,785	9,775	7.0	123.7
	2. Activate "C" burn controls	Timer Function 11				
	3. Separate second stage	Timer Function 11				
	4. Remove second stage controls	Stage 2 separation				
	5. Third stage squib ignition	Timer Function 11				
167.6	1. Stage 3 ignition 2. θ_{C9} = 0.17594	Squib delay	273,552	9,773	6.9	124.7
203.1	1. Stage 3 burnout	Timer Function 12	304,453	17,660	2.0	201.6
	2. Activate "C" coast controls	Timer Function 12				
	3. Switch out body bending filter	Timer Function 12				
	4. θ_{C10} = 1.00000	Timer Function 12				
211.1	θ_{C11} = 0.0000	Timer Function 13				
218.6	1. Spin motor ignition	Timer Function 14	310,668	17,650	1.35	239.3
	2. Fourth stage squib ignition	Timer Function 14				
	3. Start E Section Timer	Timer Function 14				
220.1	1. Explosive bolt ignition	Timer Function 15				
	2. Separate Third stage	Explosive bolt ignition				
221.1	Retro force command	Timer Function 16				
225.1	Stage 4 ignition	Squib delay	313,369	17,645	.91	264.5
228.8	Retro end	H_2O_2 depletion				

Table 6-IV (Cont.)

Time(Sec.)	Event	How Accomplished	Trajectory Parameters h Ft.	V FPS	Deg	R N.M.
258.2	Stage 4 burnout		300,000	25,713	-2.00	379.5
278.2	1. Explosive bolt ignition 2. Separate 4th stage	"E" Section timer Explosive bolt ignition	282,000	25,713	-2.00	463.9
283.2	1. Activate payload control system 2. Move control mass to maximum offset 3. Start data recorder	Payload programmer function 1 Control system Programmer Function 1	277,500	25,713	-2.00	485.0
284.3	Ax/g = 0.05		267,500	25,713	-2.00	
298.2	Despin to p=0.0 Start Guidance	Aerodynamic despin	264,000	25,750	-2.00	
336.0	$a_x/g = 0.25$ Index clock Function 2	Signal from guidance accelerometer	226,300	25,750	-2.00	714
401	$a_x/g = 1.0$	G&C system	194,500	24,850	-0.16	892
691.0	Start data readout real time & recorded	Clock function	169,000	15,000	-0.45	1879
726	1. Command range correction	Programmer Function 2	168,000	14,400	-1.0	1935
1106	1. Command, pulldown	Programmer Function 3	91,900	2,000	-26.9	2455
1300	1. Parachute squib ignition	Baro switch	6,000	220	-90.0	2459
1305	1. Deploy parachute	Delay squib	5,000	220	-90.0	2459

Table 6-IV(Concl.)

Time(Sec.)	Event	How Accomplished	Trajectory Parameters h Ft.	V FPS	Deg	R N.M.
			0	30.0	-90.0	2459
1555	1. Impact 2. Release parachute 3. Start recovery aids	"G" switch "G" switch				

separation and third stage retro. A 20-second delay between fourth stage burnout and payload separation was chosen to account for thrust tail-off. The spacecraft control mass which is centered during launch is moved to the maximum offset for despin by the normal operation of the control system about 5 seconds later. Despin and capture to the roll orientation commanded by the guidance computer occurs at 298 sec. The range correction reference time is noted when $a_x/g = 0.25$ at 336 sec. The nominal test condition of $a_x/g = 1.0$ is attained at 401 sec. and maintained until t = 726 sec. when the range correction is switched in. End of guided flight is assumed at 1106 sec. when a hard pulldown is commanded by the programmer. Data readout from the recorder is begun 400 sec after entry and continued during parachute descent until impact. About 200 seconds are available in the event the parachute fails to function. After the parachute is deployed at 5000 ft. altitude, approximately 4 minutes are available for data readout. The parachute is released and recovery aids started with impact at 1555 seconds.

6.4 Tracking Coverage and Range Safety

The plan view of the test trajectory is illustrated in Fig. 6-4 corresponding to a launch azimuth of 130 degrees from Wallops. The Scout third and fourth stage burns, separation, despin, and guidance capture are easily monitored from Bermuda. Complete trackage coverage for the remainder of the flight is maintained from Antigua and three ships. (A minimum radar elevation angle of 3 degrees was assumed). The maximum maneuver capability foot-print of $\pm$ 450 n.m. has been used to determine the closest approach to the Windward Islands and defines the selected launch azimuth. This represents a worst-on-worst condition since it assumes that a malfunction leading to the maximum lateral range takes place at entry, that a command spin-up or destruct capability after blackout does not exist, and that deployment of the recovery system parachute does not influence the range safety ground rules. More detailed analysis may improve the Antigua tracking coverage sufficiently to eliminate the third tracking ship. The estimated dispersion foot-print for test spacecraft nominal guidance operation represents about 0.1 of the maximum maneuver capability.

For the combined dispersions due to Scout and spacecraft with no range control or correction, the total RSS impact dispersions are:

FLIGHT TEST TRACKING COVERAGE & RANGE SAFETY

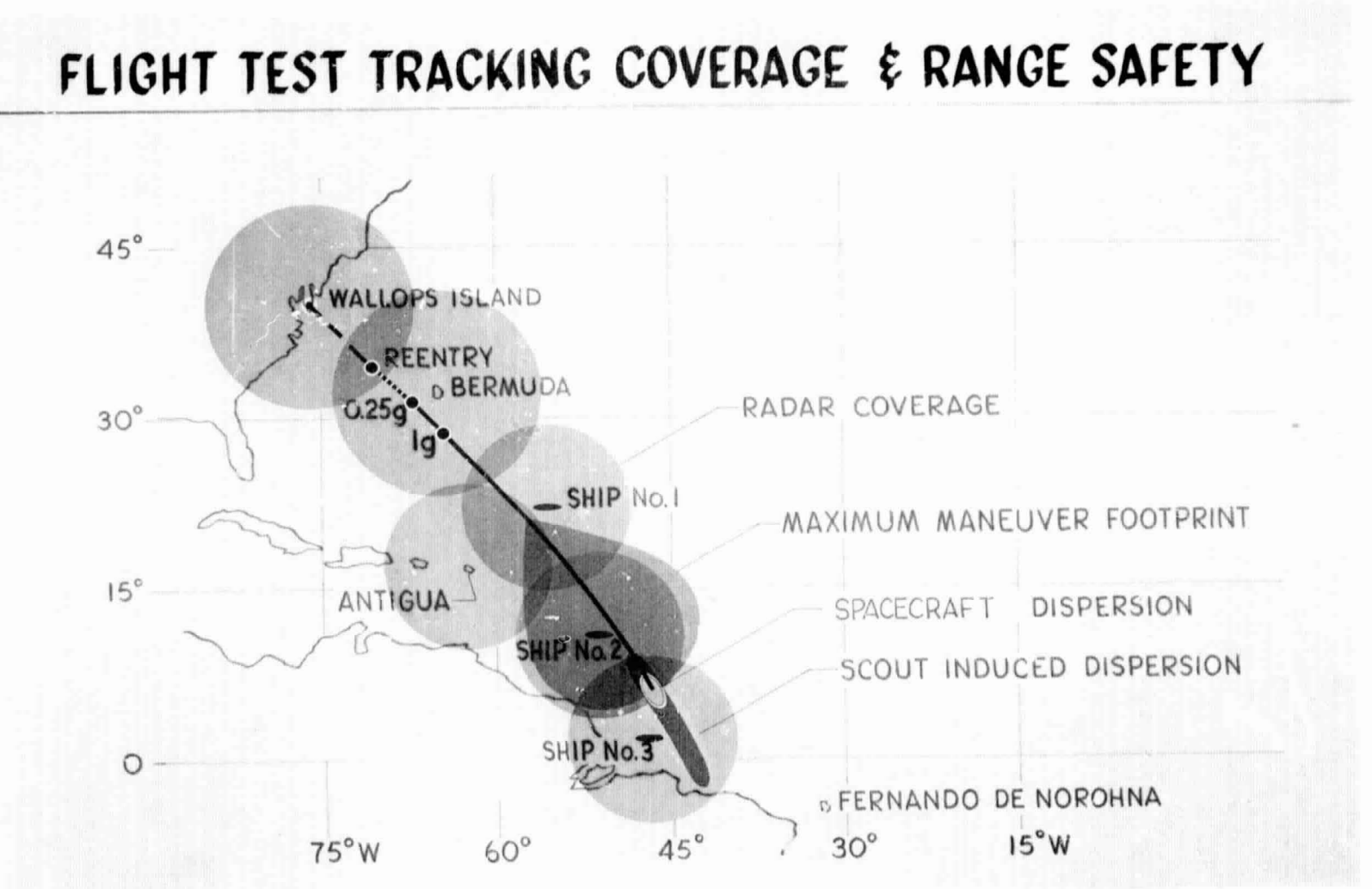

Fig.6.4

	High	Low
Downrange	+556	-222
Crossrange	+ 18	- 18

The dispersion sources for the spacecraft discussed in Section 4 yield a reasonable impact zone for recovery operations. The resultant RSS magnitudes are then:

Downrange	± 20 n.m.
Crossrange	± 15 n.m.

The dispersion represents the estimated accuracy with which the revised impact point could be controlled with updated Scout performance information from Bermuda.

The shallow profile and long flight time for the lifting trajectory should considerably enhance the tracking acquisition and continued coverage as compared to previous ballistic tests especially from ships. The trajectory control demonstrated for the concept will further improve the tracking capability by reducing the altitude deviations from injection dispersion. Comparison of data of Ref. 6 indicates that blackout may be encountered for C band radar tracking at about 240,000 feet altitude during the pullout maneuver and persist to about 22,000 fps velocity at 185,000 feet altitude. During this period primary tracking coverage is from Bermuda. The 400 second capacity of the tape recorder was selected to account for the expected data transmission with S band.

7. TEST ENVIRONMENT COMPARISON

7.1 Test Simulation Division

As mentioned in Section 1, a contract objective is to demonstrate the test capability to simulate the heating environment for major portions of manned entry spacecraft returning from orbital missions. A typical moderate L/D manned spacecraft design (HL-10) and its environment are to be considered representative for the comparison. For ablating bodies, the local shear, pressure, and enthaply influence the material response and require duplication in addition to the cold wall heat input. Manned lifting entry trajectories from orbit fly at low Reynolds numbers without transition to turbulent flow as reported in Ref. 8 , thus only laminar boundary layer flow will be considered.

The problem of simulating a heat pulse history can be clarified by dividiing it into two distinct parts. The first relates to the time history of the heat pulse (trajectory simulation) and the second to the level of the heating rate (the aerodynamics and flow field related simulation). The resulting separation of trajectory and configuration related parameters is shown in Fig. 7-1. The derivation of these relationships is given in Appendix J. The reference heating, shear, and pressure are those quantities evaluated at orbital speed for a 1-g deceleration. For reasonable descent profiles, the reference quantities are nearly constant with the changing density and velocity. (A similar assumption is that the local to stagnation heating rate-ratio does not vary.) For a change of angle-of-attack, the reference quantities require reevaluation. Since the heating, shear, and pressure are interrelated, duplication of the heating rate will insure that the other quantities are of the correct order of magnitude.

The trajectory effects are handled by $a_D/g - V/V_{orbit}$ relationship which accounts for the change in heating rate with velocity and the time since time history is unique for a given $a_D/g - V/V_{orb}$ history. (For a specified landing point, the $a_D/g - V/V_{orbit}$ history is set since this relationship

HEATING ENVIRONMENT SIMULATION DIVISION

$$\text{HEATING RATE} \cong \times \left(\frac{a_D}{g}\right)^{1/2} \left(\frac{V}{V_{ORBIT}}\right)^{2.15}$$

$$\text{SHEAR STRESS} \cong \times \left(\frac{a_D}{g}\right)^{1/2} \left(\frac{V}{V_{ORBIT}}\right)^{1.15}$$

$$\text{PRESSURE} \cong \times \left(\frac{a_D}{g}\right)$$

TRAJECTORY DEPENDENT

Fig. 7.1

also governs the atmospheric flight range.)

From this point the discussion is divided into two parts, first, the simultion of the trajectory (a_D/g - V/V_{orbit}) and secondly, the capability of the test configuration to provide an adequate match of $\dot{q}_{ref}$ with the HL-10.

7.2 Trajectory Simulation

7.2.1 HL-10 Trajectory Boundaries

To show the test spacecraft capability to duplicate HL-10 heating environment over the HL-10 reentry flight corridor, a new HL-10 corridor description is provided which presents corridor boundaries in terms of the matching relationships, a_D/g and V/V_{orbit} (using the vehicle aero characteristics), rather than the more conventional altitude-velocity contours. The derived corridor consistent with data of Ref. 8 is presented in Fig. 7-2 for the $(L/D)_{max}$. flight condition. The equilibrium glide boundary represents the only aerodynamic limit in the diagram. An arbitrary 40 BTU/ft^{2}sec. limit line was chosen to indicate that a heat rate limit line may exist, especially where the spacecraft has some metallic heat shielding. For the limit line chosen based on Eqs. (7) and (16) of Reference 3 and data from Ref. 8 , the HL-10 lifting capability will permit equilibrium flight along this constraint boundary to the drag deceleration corresponding to the limit flight load factor (assumed to be that corresponding to vertical descent). An example of the modification to the diagram by a limit transition Reynolds number is also shown.

The defined drag deceleration-velocity diagram provides the map of entry trajectories and environments that an HL-10 reentry flight research spacecraft would explore. A single drag deceleration-velocity trace defines a unique reentry trajectory. For example, a constant Reynolds number descent appears as a straight line through zero. Maximum time to ground occurs along the equilibrium glide boundary while minimum descent time follows the lower contours. The nominal equilibrium glide, the undershoot, and the maximum

HL-10 DRAG DECELERATION BOUNDARIES

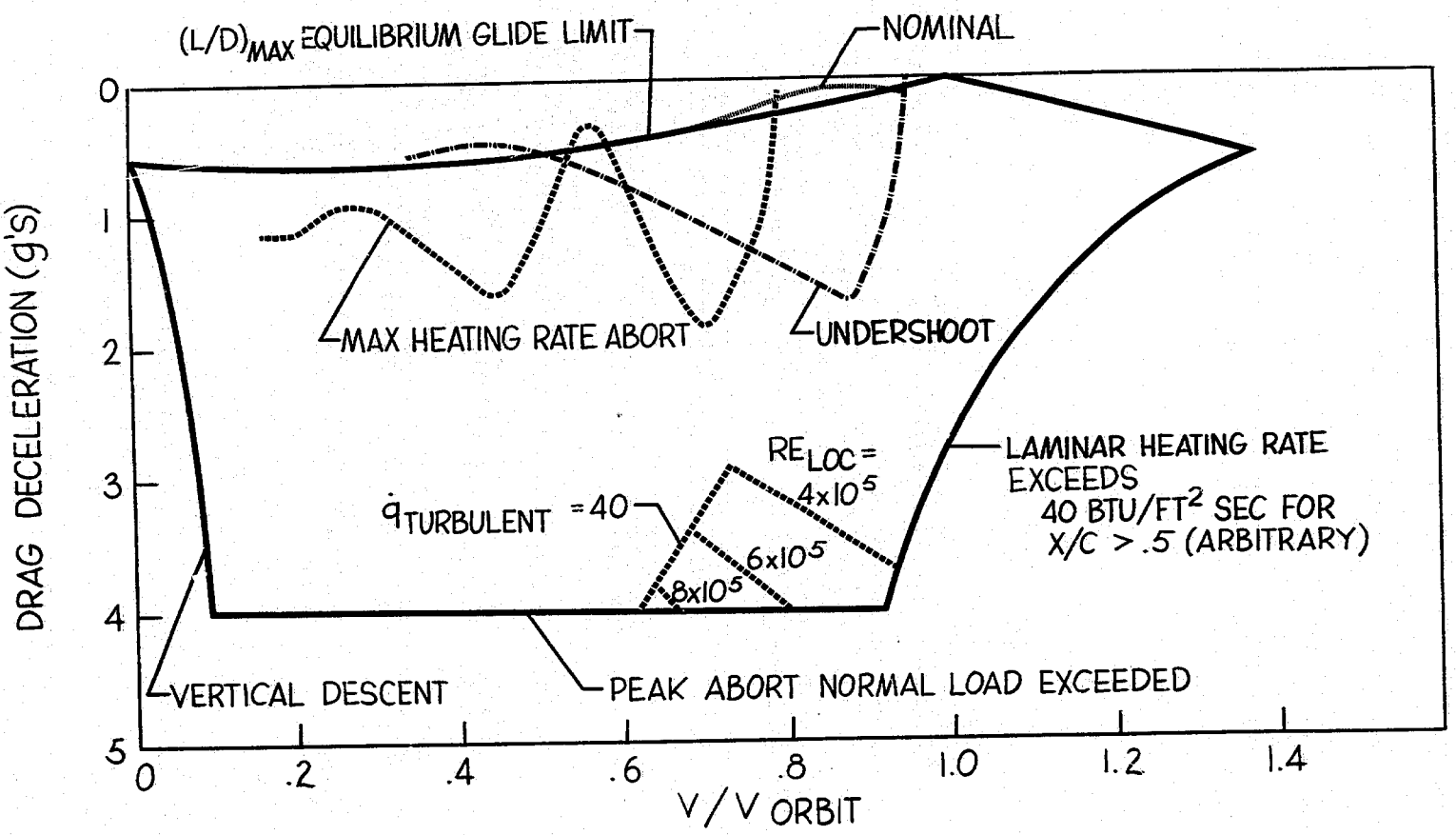

Fig. 7.2

heating rate abort trajectories from Ref. 8 are transformed into their drag deceleration-velocity curves in the diagrams.

For the reentry test model to conduct research applicable to HL-10 development, it should have the capability for flight over as much of the HL-10 drag-deceleration-velocity map as possible and also be capable of accurately duplicating HL-10 trajectories (expressed as $a_D/g - V/V_{orbit}$ curves).

Before presenting the corresponding map for the test spacecraft, it is instructive to examine some of the more interesting trajectory examples not covered by Ref. 8. These example descents are shown in Fig. 7-3. Resultant load factors of 1.0, 1.4, and 1.7 were computed from the a_D/g values for trajectories flow at $(L/D)_{max}$. The lateral range available at $(L/D)_{max}$ for these constant deceleration descents is also shown. Note that maximum lateral range occurs for a resultant load factor greater than 1. Since (L/D)'s greater than 1 are necessary primarily to provide lateral range (and secondarily to fly above heat rate boundaries for reusable systems), the flight trajectories of greatest interest lie between the equilibrium glide and the 1 g deceleration descent trajectory. These fortunately are mild environments from the passenger standpoint. Cold wall stagnation heating data are given in Figs. 7-4 and 7-5. Since the approach trajectories are the same for all three cases, the heating rate histories vary little to 400 seconds. The integrated heating curves emphasize the small differences. The net effect of the heating differences after 400 seconds is probably a prelanding substructure temperature increase for the longer flight times, since reradiation from the char surface will account for a major portion of the heat rate difference. Since time to impact is then the important variable, simulation of the 1-g drag deceleration (1.4 g resultant load factor) descent should then prove sufficient since parachute descent times are added to the model flight times.

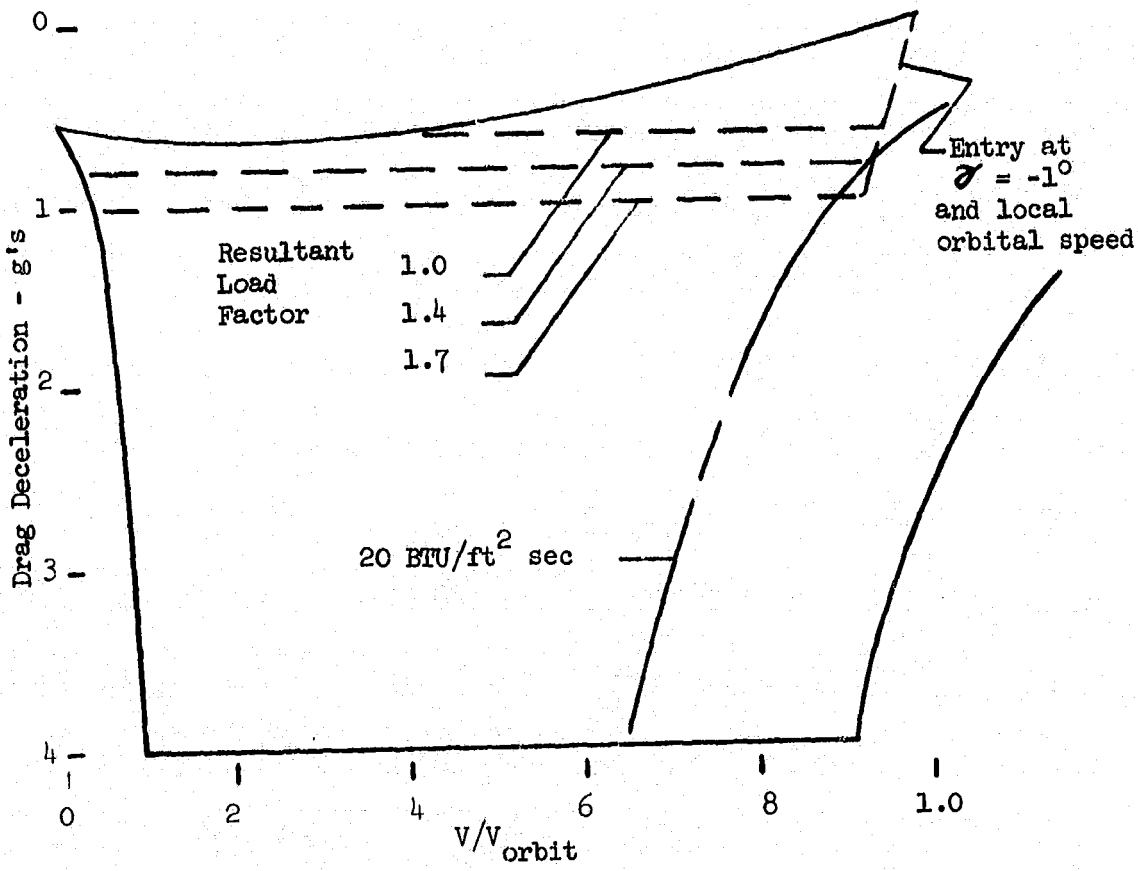

(a) Deceleration - Velocity Map

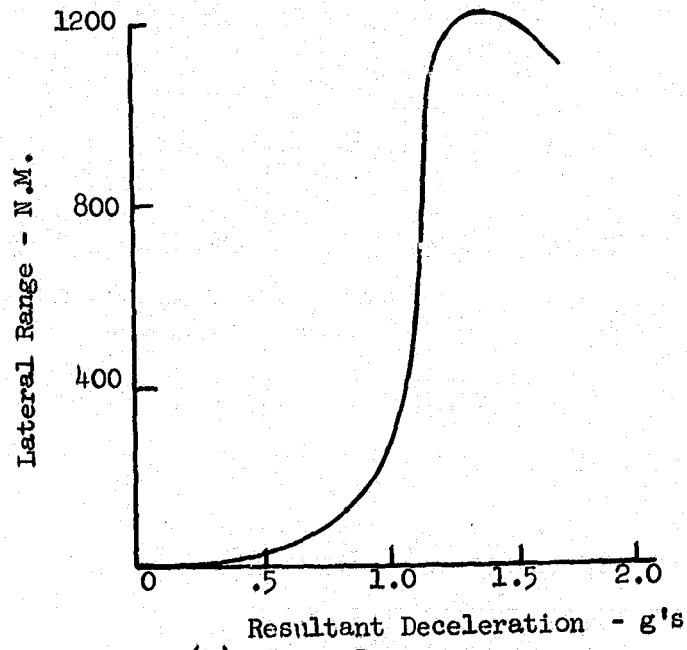

(b) Cross Range

Fig. 7.3 EXAMPLES OF HL-10 CONSTANT DECELERATION DESCENTS

HL-10 CONSTANT DECELERATION DESCENTS - HEAT RATE HISTORY

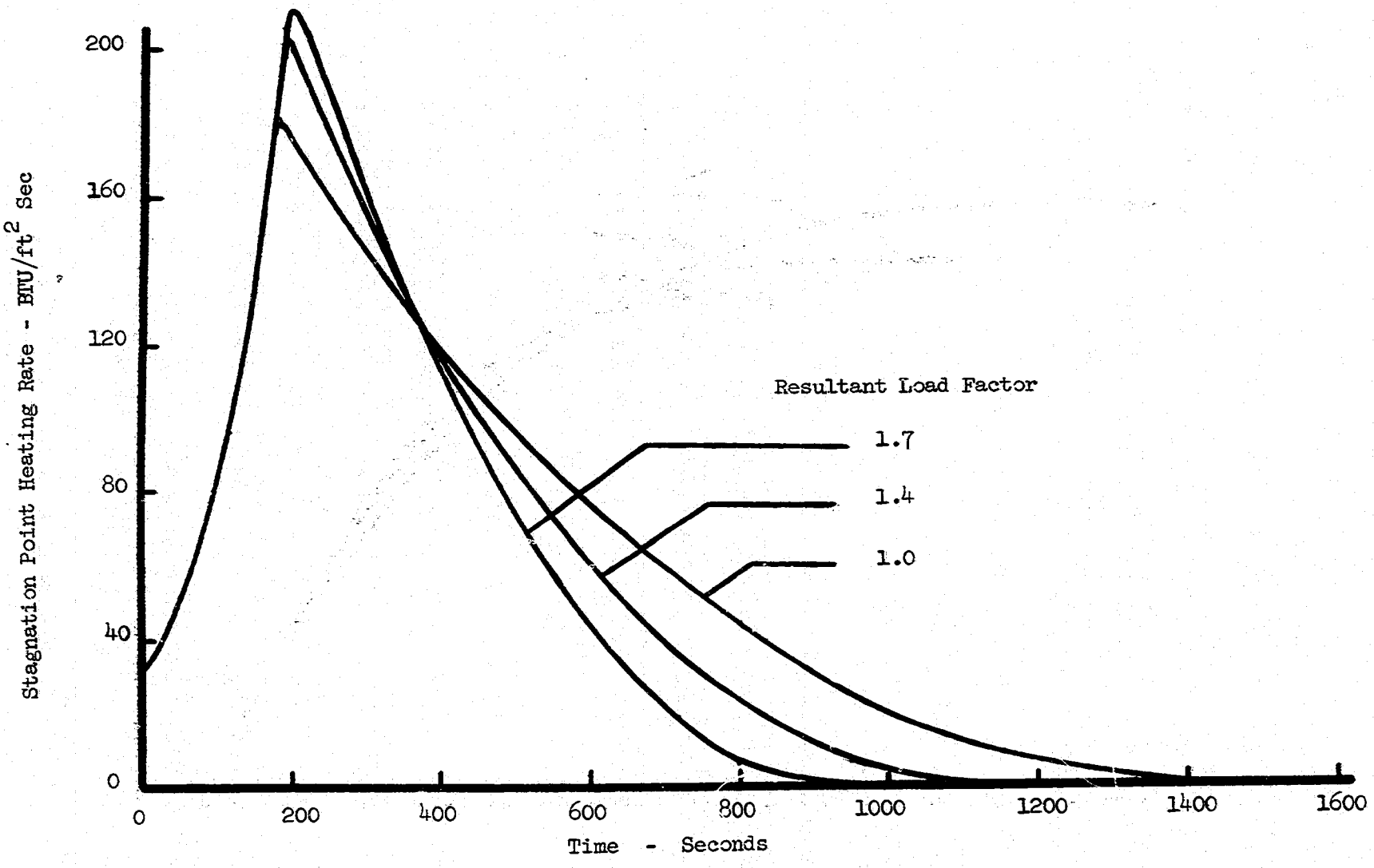

Fig. 7.4 HL-10 CONSTANT DECELERATION DESCENTS - HEAT RATE HISTORY

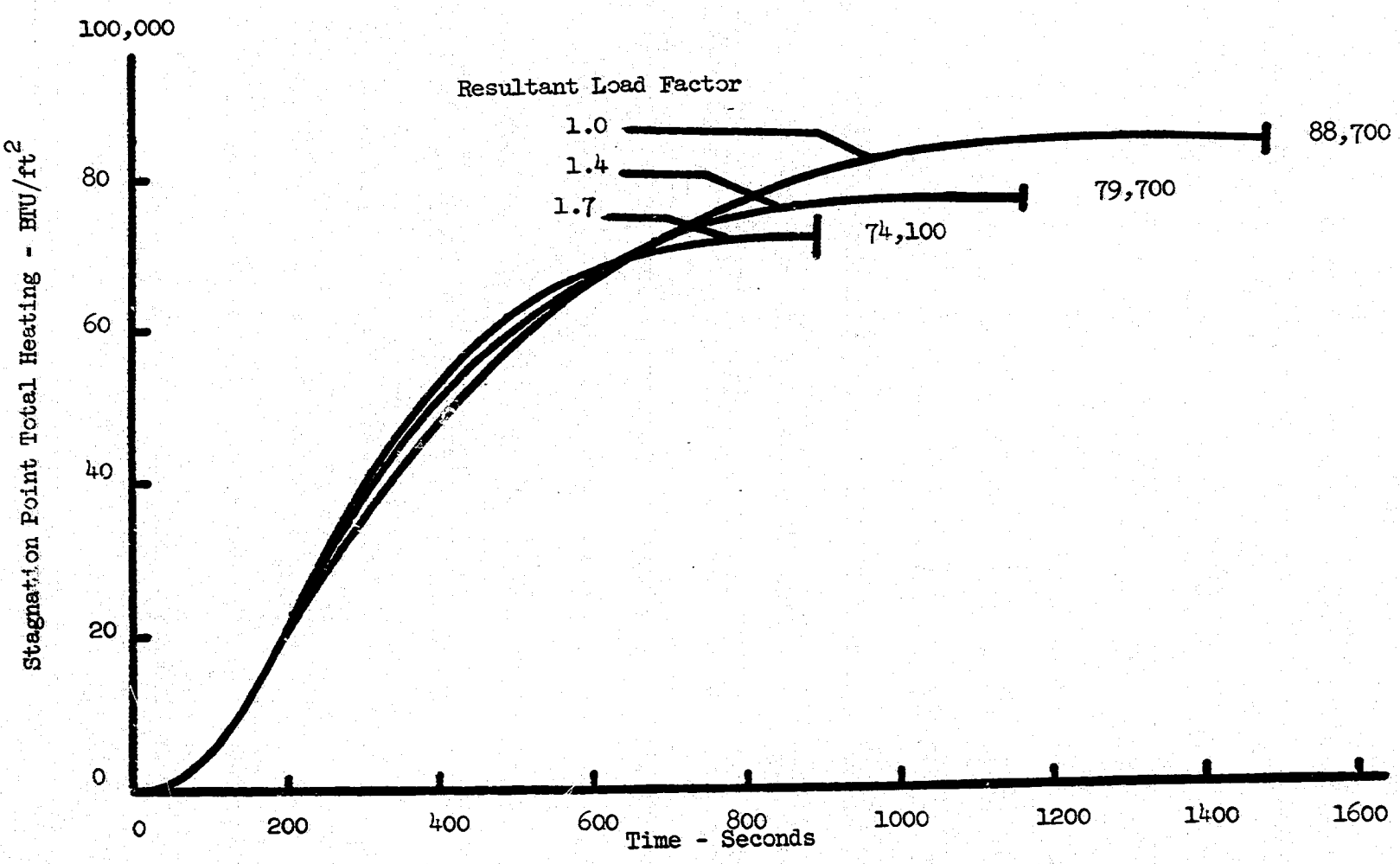

Fig. 7.5 HL-10 CONSTANT DECELERATION DESCENTS - TOTAL HEATING

7.2.2 Test Spacecraft Deceleration Boundaries and Trajectory Simulation Capability

The basic test spacecraft guidance approach is to capture and follow with reasonable accuracy a programmed deceleration-velocity history through the primary heating period. Later in the trajectory the deceleration level is adjusted to correct errors that have built up the entry point so as to minimize impact point dispersions. This late correction of preguidance errors is tailored to error magnitudes representative of Scout. For precise injection systems (inertially guided boosters), the small errors in altitude and flight path angle can be corrected during capture without significantly influencing the environment.

The requirement for a programmed deceleration-velocity history in the test model is not restrictive since an HL-10 entry from orbit to a fixed landing site implies a preset nominal deceleration-velocity history. This contract has placed primary emphasis on constant deceleration descents, thus eliminating a requirement for on-board programming of the deceleration with changes in velocity. The basic concept is not so restrictive since the aerodynamic, trajectory, and roll control capability will not be impared by a varying deceleration history if the boundaries to be presented are not exceeded.

Figure 7-6 presents the boundaries for the proposed test spacecraft based on the aerodynamics of Section 2 and the guided flight simulations of Section 4. The $(L/D)_{max}$ equilibrium glide boundary does not represent a practical deceleration limit since errors in actual L/D from the predicted value will lead to range errors. A realistic trajectory control limit has been set, based on Appendix B. The boundary represents a fixed ability to adjust altitude (or correct deceleration level) for a given roll angle increment from that required for the specified deceleration. The vertical acceleration value chosen is double the value for which deceleration control (at 1 g) has been demonstrated. Note the small increment in deceleration required for control at twice orbital speed, indicating that good control capability can be obtained for more advanced flight tests. (Flight speed influences the

SPACECRAFT DECELERATION BOUNDARIES

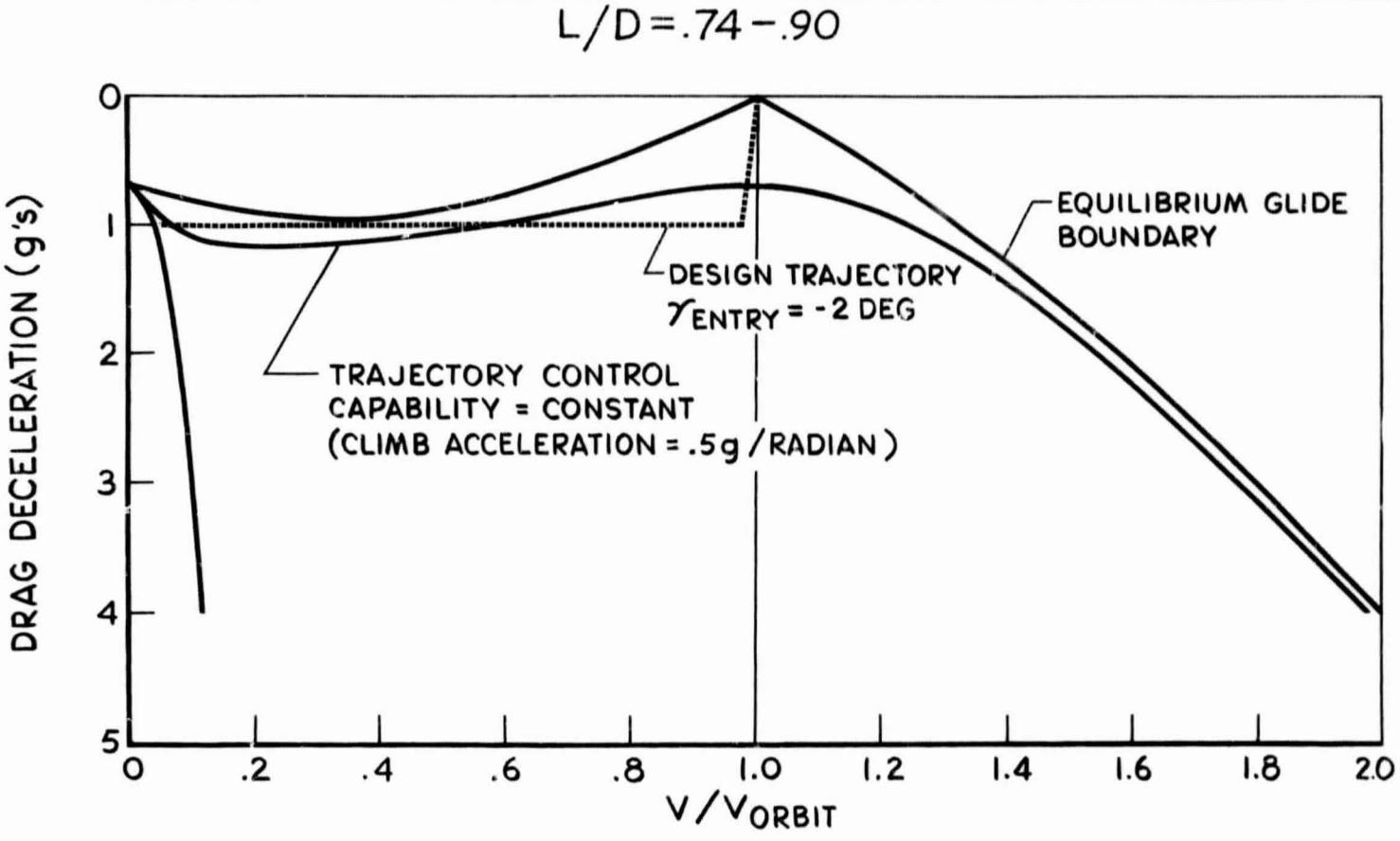

Fig. 7.6

trajectory control equation only in the vicinity of the equilibrium glide boundary.) For the design trajectory shown operating between the control and equilibrium glide boundaries at less than half orbital speed will not produce excessive errors with less than 500 N.M. to go.

An upper limit to the test model drag deceleration level has not yet been identified. It will probably be set by mechanical limitations of the moving mass roll control system.

An overlay of the test spacecraft deceleration boundaries on the HL-10 diagram in Fig. 7-7 shows the trajectory coverage possible. The design trajectory is also presented for reference and indicates the heating of the type shown in Figs. 7-4 and 7-5 is readily obtained.

7.3 Heating Level Simulation

From the previous section an important range of HL-10 reentry trajectories can be duplicated by the test spacecraft, thus providing the correct time variation of the heating related quantities. If the reference heating rate values are duplicated, then an adequate simulation is accomplished since enthalpy, shear, and pressure are of the proper level. (These must be near the required values with the flight velocity simulated since their reference values are interrelated.)

A comparison with HL-10 heating predictions is shown in Fig. 7-8. The heating distributions for the test model top, sides, and lower centerline are corrected to reference values from those given in Section 3. The comparison indicates that the test model will adequately simulate a major portion of the HL-10 environment. The HL-10 windward ray heating is adequately bracketed over the length of the spacecraft. Model windward ray heating is more representative at forward body stations while the side heating appears to provide an extremely good simulation for aft stations.

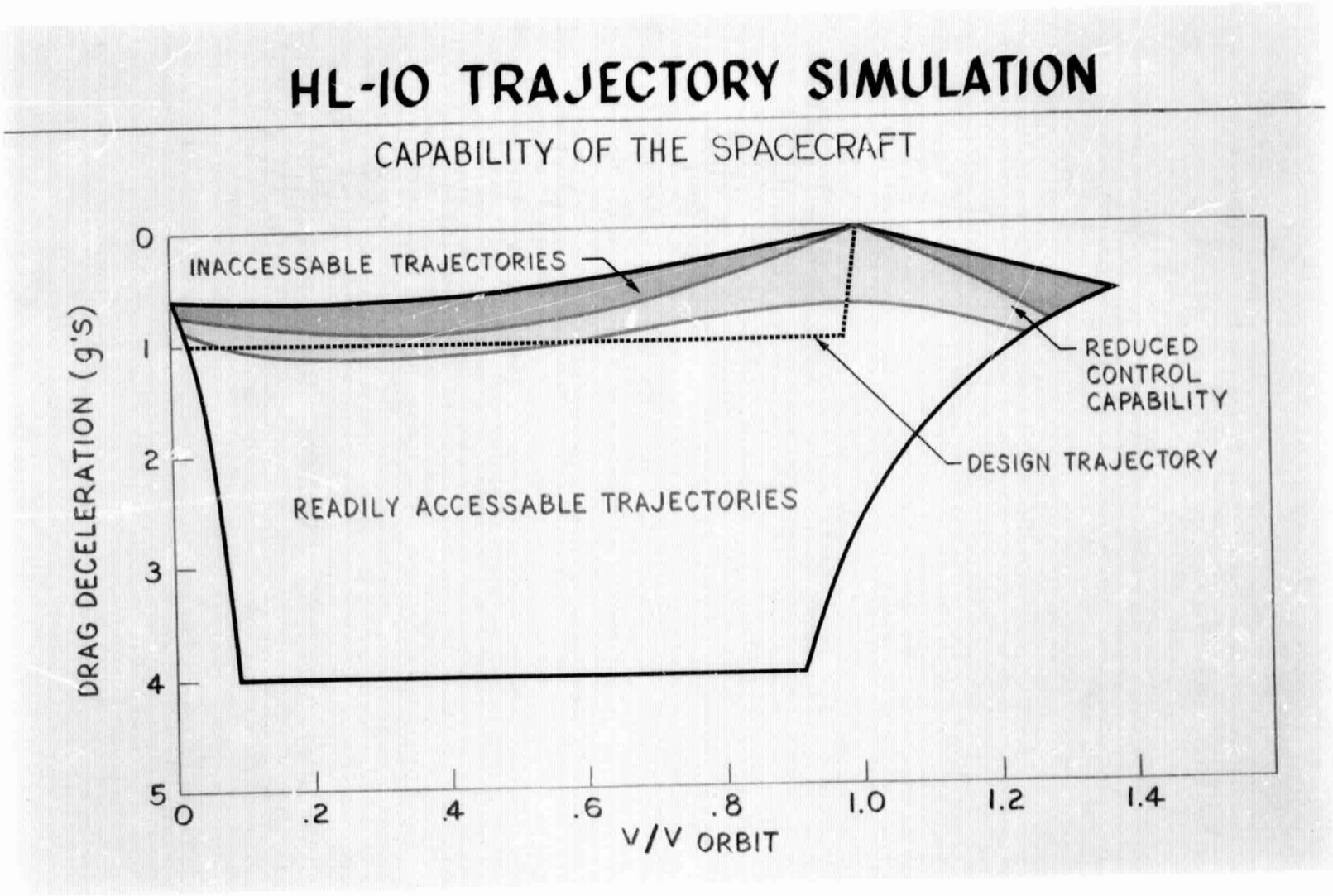
HL-10 TRAJECTORY SIMULATION
CAPABILITY OF THE SPACECRAFT
INACCESSABLE TRAJECTORIES
REDUCED CONTROL CAPABILITY
DESIGN TRAJECTORY
READILY ACCESSABLE TRAJECTORIES
DRAG DECELERATION (g'S)
0
1
2
3
4
5
0
.2
.4
.6
.8
1.0
1.2
1.4
V/V ORBIT

Fig.7.7

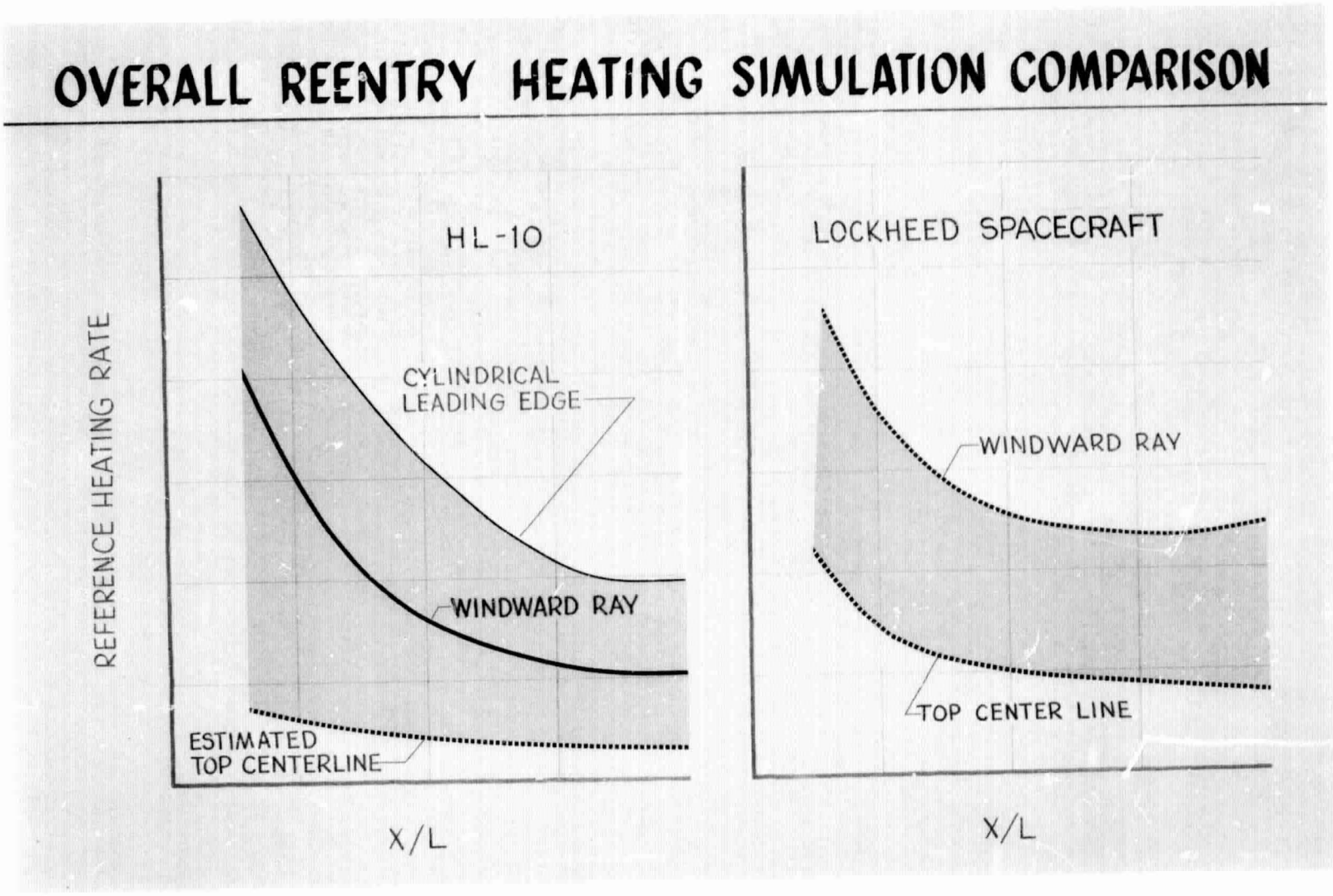
OVERALL REENTRY HEATING SIMULATION COMPARISON
REFERENCE HEATING RATE
HL-10
CYLINDRICAL LEADING EDGE
WINDWARD RAY
ESTIMATED TOP CENTERLINE
X/L
LOCKHEED SPACECRAFT
WINDWARD RAY
TOP CENTER LINE
X/L

Fig. 7.8

A comparison of the windward ray heating distribution between the test model and other possible test configurations is shown in Fig. 7-9. HL-10 and SV-5 heating and environment data are taken from Ref. 8. As a consequence of the constant flow inclination angle of 15° and the pressure overexpansion on the lower centerline of the Lockheed test model and the fact that the SV-5 re-enters at a high angle-of-attack (α = 30°), the heating rate gradient along the windward ray is much less than that along the SV-5 vehicle and a scaled HL-10. (For both of these vehicles the corresponding flow inclination varies from 30° to negative values.) Hence, if ablation material tests are desired in a more uniform heating environment, the Lockheed approach would provide a more adequate test bed. Note that neither a scaled HL-10 or SV-5 could provide proper heat rate simulation on the HL-10 forebody and could not provide the heating level spread of Fig. 7-8 except possibly in the separated flow region on the top where the flow uncertainties complicate the simulation.

Figure 7-10 summarizes the results of Sections 7.2 and 7.3 by combining the trajectory and configuration effects and demonstrates that duplication of manned entry from orbit heating is achieved by the test model.

COMPARISON

HEATING SIMULATION CAPABILITY vs OTHER SPACECRAFT
WINDWARD RAY

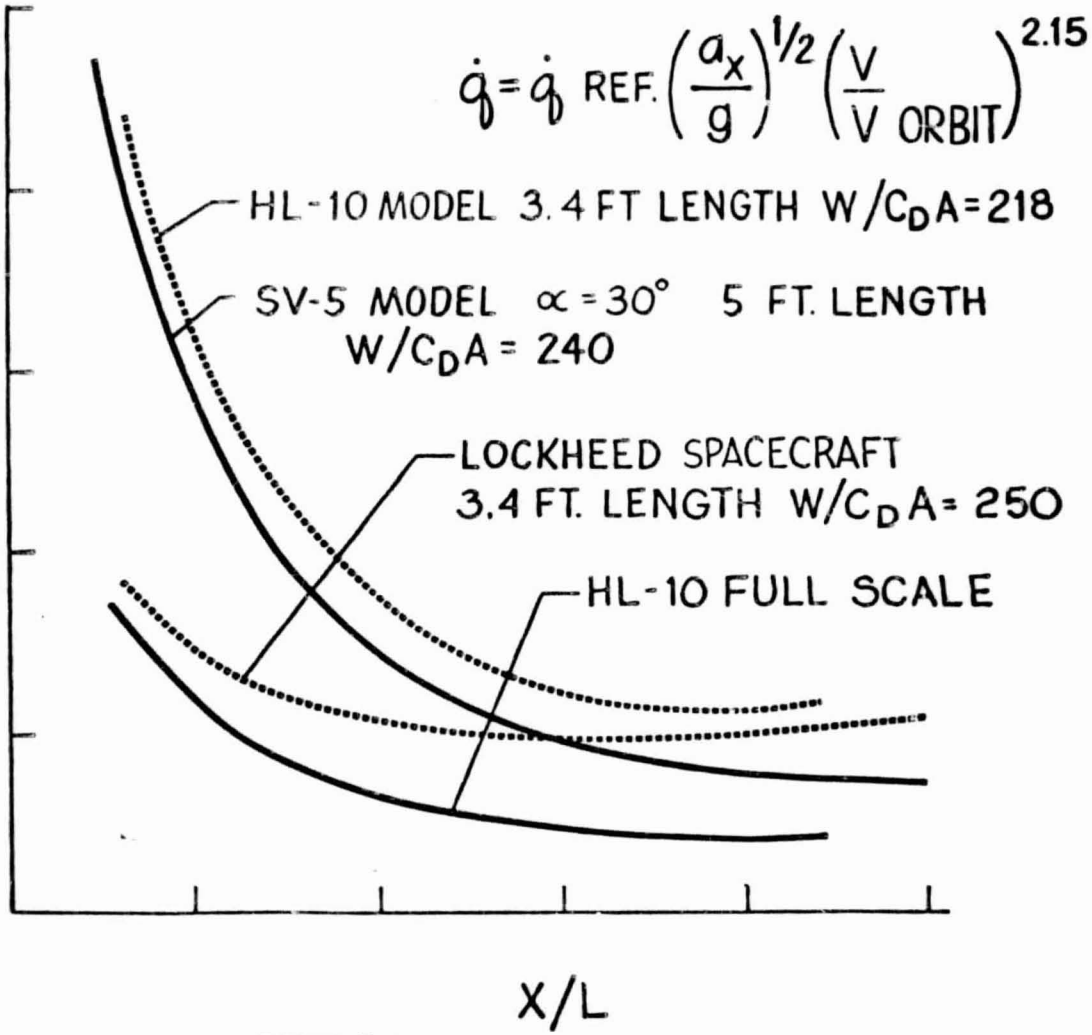

FIGURE 7.9

HEATING ENVIRONMENT SIMULATION

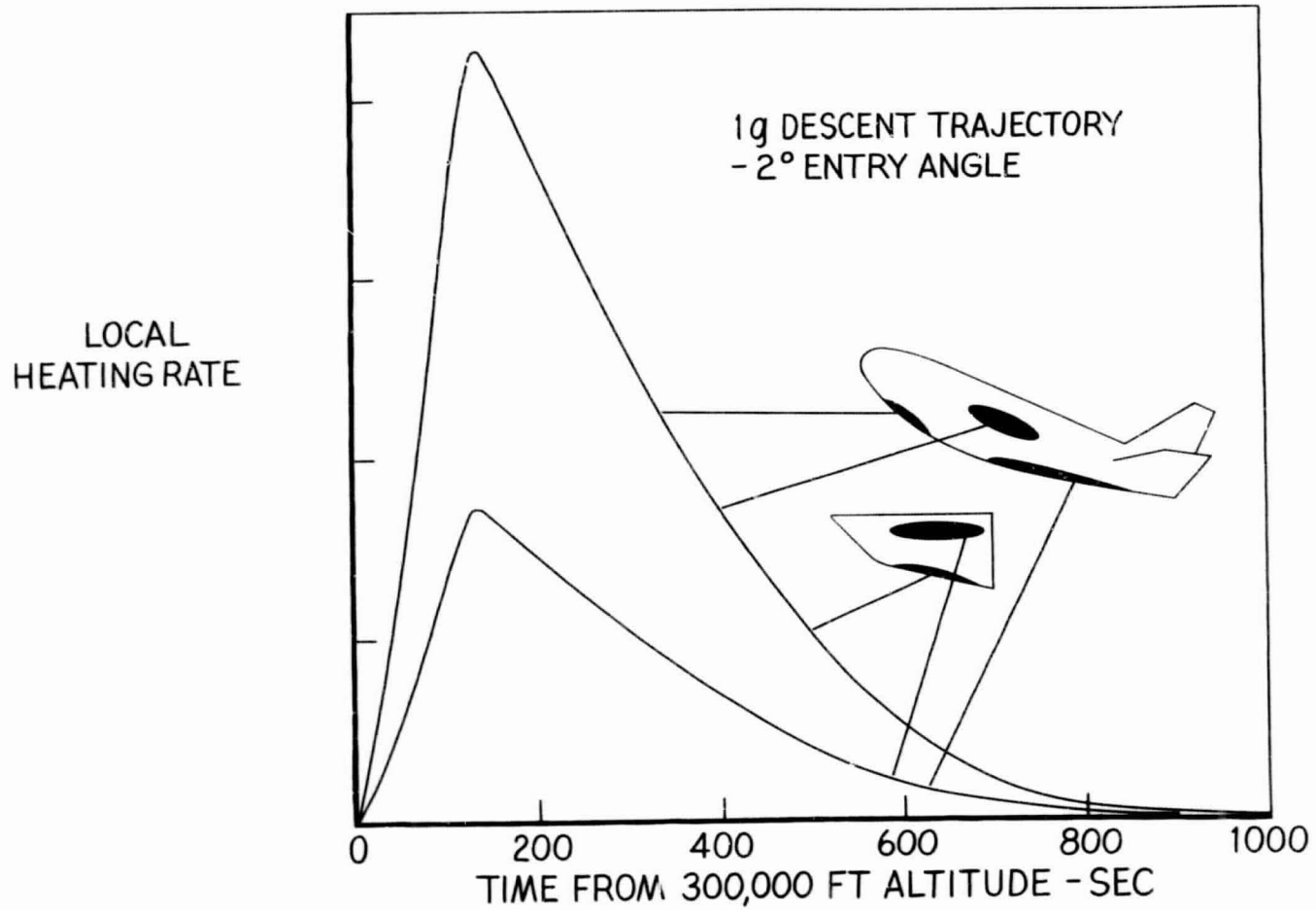

Fig. 7.10

8. CONCLUSIONS

From the results of the investigation, the following conclusions can be drawn:

1) Precisely controlled Scout lifting entry testing becomes practical through the concept.
2) Manned lifting entry spacecraft heating is duplicated by the test model.
3) Optimum Scout performance is obtained for the required flight profile.
4) Maximum speed capability is 29,000 ft/sec for the design.
5) The test model concept is not restricted by Scout dimensional constraints.

These results point out the importance of total concept research and integration. For the concept to work, current approaches to the configuration, the trajectory and the guidance and control required re-examination and modification.

9. REFERENCES

1. Price, D.A., and Nelson, E.O., Final Report for the Aerobee 150A Roll Lock-In Study, Contract No. NAS 5-9061, LMSC, Palo Alto, California, March 1965

2. McNeal, D.R., Description and Users Manual for Roll-Pitch Motion Digital Computer Program, LMSC Report No. M-60-64-2, LMSC, Palo Alto, California, March 1956.

3. Nelson, R.L., A New Solution for Guided Entry Trajectory Relationships, LMSC Report No. LMSC-677801, 16 December 1966

4. Mirels, H., and Thornton, P.R., Effect of Body Perturbations on Hypersonic Flow Over Slender Power Bodies, NASA TR R-45 (1959).

5. Wagner, R.D., Jr. and Watson, R., Induced Pressures and Shock Shapes on Blunt Cones in Hypersonic Flow, NASA TN D-2182 (1964).

6. Edquist, L.T., and Strapp, M.G., A Sphere Cone Heating Analysis Program - ENVY LMSC TIAD 837, 13 October 1966.

7. Nelson, R.L., A Method for Correcting Conical Body Aerodynamic Properties for Nose Tip Bluntness Effects, LMSC Report No. LMSC-677800, 16 December 1966

8. Wing, L.D. and Eilertson, W.H., Research Studies and Analysis to Define Manned Lifting Entry Flight Environment, Confidential Report, NASA CR-639 (U).

References (Cont.)

9. Study of Heat Shielding Requirements for Manned Mars Landing & Return Missions, LMSC 4-74-64-1, December 1964, Hearne, L.F. et al.

10. Vaglio, R. - Laurin, Laminar Heat Transfer on Three-Dimensional Blunt-nosed Bodies in Hypersonic Flow, ARS Journal, Feb. 1959 pp. 123-129.

11. Fay, J.A., and Riddell, F.R., Theory of Stagnation Point Heat Transfer in Dissociated Air, JAS, Vol. 25, No. 2, P. 73, Feb. 1958.

12. Lees, Lester, Laminar Heat Transfer Over Blunt-Nosed Bodies at Hypersonic Flight Speeds, Jet Propulsion, p. 259, April 1956.

13. Eckert, E.R.G., Survey of Boundary Layer Heat Transfer at High Velocities & High Temperatures, WADC TR 59-624, April 1960.

14. Meyer. M.G., Charring in Re-Enforced Plastics (CHIRP) an IBM 7090 Digital Computer Program.

15. Goldstein, H.E., Kinetics of Nylon and Phenolic Pyrolysis, LMSC-667876, October 1965.

16. Cleary, J.W. and Axelson, J.A., Theoretical Aerodynamic Characteristics of Sharp and Circularly Blunt-Wedge Air Foils, NASA TR R-202, July 1964.

17. Willwerth, R.E., and Rosenbaum, R.C., Wong, G., Program for Rapid Earth-to-Space Trajectory Optimization (PRESTO), LMSC-4-36-61-1, 18 May 1964.

References (Concl.)

18. LTV-3-30000/6R-9, Flight Test Plan SLV-1A Vehicle S-147C, Astronautics Division, LTV Aerospace Corporation, Dallas, Texas, 3 May 1966.

19. Private Communication between J. W. Burns, LMSC and Dr. Max Petersen, Consultant to the Instrumentation Laboratory, M.I.T.

20. LMSC Final Report, Scout Operational Performance and Dispersion Computer Program, LMSC, Sunnyvale, California, Sept. 1966.

21. Whittney, C. K., Owens, T. F., Paskind, J. and Rubin, M. B., Scout Motor Performance Analysis and Prediction Study (PAPS), NASA CR-336, Dec. 1965.

22. Kanno, J. S., Spin Induced Forced Resonant Behavior of a Ballistic Body Re-entering the Atmosphere, General Research in Flight Sciences Jan. 1959-Jan. 1960, Vol. III, LMSC-288139, Sunnyvale, California, Jan. 1960.

APPENDIX A

Programmed Deceleration Descent Properties

Basic Considerations

The descent equations relating entry altitude and velocity for a spherical non-rotating central body are:

$$\frac{1}{g}\frac{dV}{dt} = -\frac{a_D}{g} - \sin\gamma \qquad \text{(A-1)}$$

$$\frac{dh}{dt} = V \sin\gamma \qquad \text{(A-2)}$$

For a programmed drag deceleration, equation(A-2)is restricted. The rate of change of altitude has with it a corresponding change in atmospheric density which is coupled to the programmed deceleration. The restriction is made clearer if equation (A-2) is recast in terms of the atmosphere density using the relationship:

$$\rho = \rho_o \, e^{-\beta h}$$

The resulting equation developed without any simplifying assumptions is:

$$\left[1 - \frac{2}{\beta r}\left(\frac{V_{orb}}{V}\right)^2\right] \sin\gamma = \frac{2\,g(a_D/g)}{\beta V^2}\left[1 + \frac{V}{2g}\frac{d}{dt}\frac{1}{a_D/g}\right] + \frac{2\,g}{\beta V^2}\frac{d}{dt}\log\frac{W}{C_D A} \qquad \text{(A-3)}$$

For a slowly varying W/C_DA, as is the case when the angle-of-attack is <u>not</u> changed for trajectory control, the flight angle is shown to be uniquely determined by the drag deceleration time history.

As a result range control is achieved by controlling to a prescribed drag deceleration history. In addition, the trajectory adjusts for aerodynamic and density uncertainties.

An interesting series of programmed deceleration descents results if the following approximations and substitutions are made in the flight path angle equation:

$$\frac{2}{\beta r}\left(\frac{V_{orb}}{V}\right)^2 << 1$$

$$W/C_D A = \text{Constant}$$

$$\left[1 + \frac{V}{2g}\ \frac{d}{dt}\ \frac{1}{a_D/g}\right] = \text{Constant} = K$$

Then:

$$\sin \gamma = \frac{-2Kg}{\beta}\left(\frac{a_D}{V^2}\right) \qquad \text{(A-4)}$$

Reference 3 makes use of this flight path angle assumption in deriving a wide range of programmed deceleration descents and corresponding flight environmental data. Table A-I indicates the drag deceleration-velocity relationships of special interest.

Table A-I

SOME PROGRAMMED DECELERATION DESCENT OPTIONS

———	$a_D/g = (a_D/g)_{orb} (V_{orb}/V)^{2(K-1)}$	General Form
K = 0	$a_D/g = (a_D/g)_{orb} (V_{orb}/V)^{-2}$	Constant density altitude
K = $\frac{1}{2}$	$a_D/g = (a_D/g)_{orb} (V_{orb}/V)^{-1}$	Constant free stream Reynolds number
K = 1	$a_D/g = (a_D/g)_{orb}$	Constant deceleration
K = 2	$a_D/g = (a_D/g)_{orb} (V_{orb}/V)^{2}$	Constant turbulent heating rate
K = 3.15	$a_D/g = (a_D/g)_{orb} (V_{orb}/V)^{4.3}$	Constant laminar heating rate

APPENDIX B

Perturbation Equations for Trajectory Control

Some insight into the ease or difficulty with which trajectory control can be attained for varying flight conditions can be obtained by examining the perturbation equation of motion about the nominal vertical plane trajectory. This appendix develops the perturbation equation for roll only control system in terms of the nominal trajectory conditions.

For the small flight angles typical of lifting entry the vertical trajectory equation over a spherical non-rotating central body is:

$$\frac{V\dot{\gamma}}{g} = \frac{C_L}{C_D} a_D/g - \left[1 - \left(\frac{V}{V_{orb}} \right)^2 \right]$$

Redefining variables in terms of trajectory (t) and perturbation (Δ) parts:

$$\gamma = \gamma_t + \Delta\gamma$$

$$C_L = C_{L_t} + \Delta C_L$$

and assuming that control is sufficiently good that,

$$V = V_t$$

$$a_D/g = (a_D/g)_t$$

The trajectory equation becomes,

$$\frac{V_t}{g}\left(\dot{\gamma}_t + \Delta\dot{\gamma}\right) = \frac{C_{L_t} + \Delta C_L}{C_D}\left(\frac{a_D}{g}\right) - \left[1 - \left(\frac{V}{V_{orb}}\right)^2\right]$$

$$\frac{V_t}{g}\Delta\dot{\gamma} + \boxed{\frac{V_t}{g}\dot{\gamma}_t = \frac{C_{L_t}}{C_D}\left(\frac{a_D}{g}\right) - \left[1 - \left(\frac{V}{V_{orb}}\right)^2\right]} + \frac{\Delta C_L}{C_D}\frac{a_D}{g}$$

Defined Equal

$$\frac{V_t}{g}\Delta\dot{\gamma} = \frac{\Delta C_L}{C_D}\frac{a_D}{g}$$

From the relationship,

$$\frac{dh}{dt} = V\sin\gamma = V\gamma$$

$$V\dot{\gamma} = \frac{d^2h}{dt^2} - \gamma\dot{V}$$

The second term in the above equation can be ignored in view of the small flight path angle

$$V\dot{\gamma} = \frac{d^2h}{dt^2}$$

In terms of trajectory and perturbation parts,

$$V_t\left[\Delta\dot{\gamma} + \dot{\gamma}_t\right] = \frac{d^2h_t}{dt^2} + \frac{d^2\Delta h}{dt^2}$$

$$V_t\,\Delta\dot{\gamma} + \boxed{V_t\,\dot{\gamma}_t = \frac{d^2h_t}{dt^2}} + \frac{d^2\Delta h}{dt^2}$$

Defined Equal

Then:

$$V_t\,\Delta\dot{\gamma} = \frac{d^2\Delta h}{dt^2} = g\frac{\Delta C_L}{C_D}\left(\frac{a_D}{g}\right)_t$$

This equation shows that the ability to adjust the g-level by changing altitude can be affected by velocity only through its effect on ΔC_L,

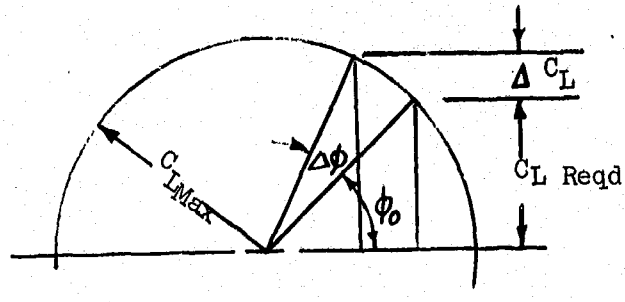

Referring to the accompanying sketch and with the roll control angle $\Delta\phi$ assumed small,

$$\Delta C_L = C_{L\ max} \sin (\phi_o + \Delta\phi) - C_{L\ Reqd}$$

$$\Delta C_L = C_{L\ max} \left[\sin \phi_o + \Delta\phi \cos \phi_o \right] - C_{L\ max} \sin \phi_o$$

$$\Delta C_L = \Delta\phi \; C_{L\ max} \cos \phi_o$$

$$\frac{\Delta C_L}{\Delta\phi} = \sqrt{C_{L\ max}^2 - C_{L\ Reqd}^2}$$

In approximate form $C_{L\ Reqd}$ is given by

$$C_{L\ Reqd} = C_D \left[\frac{1 - (V/V_{orb})^2}{a_D/g} \right]$$

Then,

$$\frac{\Delta C_L}{\Delta\phi} = \frac{C_D}{a_D/g} \sqrt{\left(\frac{L}{D}\right)_{max}^2 \left(\frac{a_D}{g}\right)_t^2 - \left[1 - \left(\frac{V}{V_{orb}}\right)^2\right]^2}$$

Combining this equation with the trajectory equation provides the desired result.

$$\frac{d^2 \Delta h}{dt^2} = g \Delta\phi \sqrt{\left(\frac{L}{D}\right)_{max}^2 \left(\frac{a_D}{g}\right)_t^2 - \left[1 - \left(\frac{V}{V_{orb}}\right)^2\right]^2}$$

The equation can be rearranged to provide $a_D/g - V/V_{orb}$ contours for a fixed trajectory controlability. In this form,

$$(a_D/g)_t = \frac{1}{L/D}\sqrt{\left(\frac{1}{g\,\Delta\phi}\frac{d^2\Delta h}{dt^2}\right)^2 + \left[1 - \left(\frac{V}{V_{orb}}\right)^2\right]^2}$$

This equation is the basis of the controllability contours of Sections 1 and 7.

APPENDIX C

ALTERNATE CONFIGURATION STUDIES

This Appendix covers a number of the aerodynamics studies performed in arriving at the final test spacecraft configuration. In performing these aerodynamic studies, a Newtonian aerodynamics computer program (FORMAC) was employed. This computer program, which can be used on the IBM 7094, the RR 1108, and the CDC 3200 computers, was developed especially for configurations of the type under study. The configuration can be made up of as many as 9 subsurfaces composed of flat plates, cones, cylinders, and elipsoids. As many as 54 geometric and aerodynamic quantity can be computed for the individual components or all of them in combination. A full range of angles-of-attack and sideslip is permitted. The program has also been adapted to Computer Graphics operation with the CDC display console and the CDC 3200 computer. This mode of operation was extremely valuable in the selection of the final test model configuration.

Figure C-1 summarizes the non-Newtonian aerodynamic contributors responsible for the L/D degradation for the basic configuration. Since the aerodynamic trim is an important consideration in the configuration development, consideration of the effects of these non-Newtonian contributors on the center of gravity for trim is necessary. Figure C-2 presents a graphical assessment of these effects on trim CG for the basic

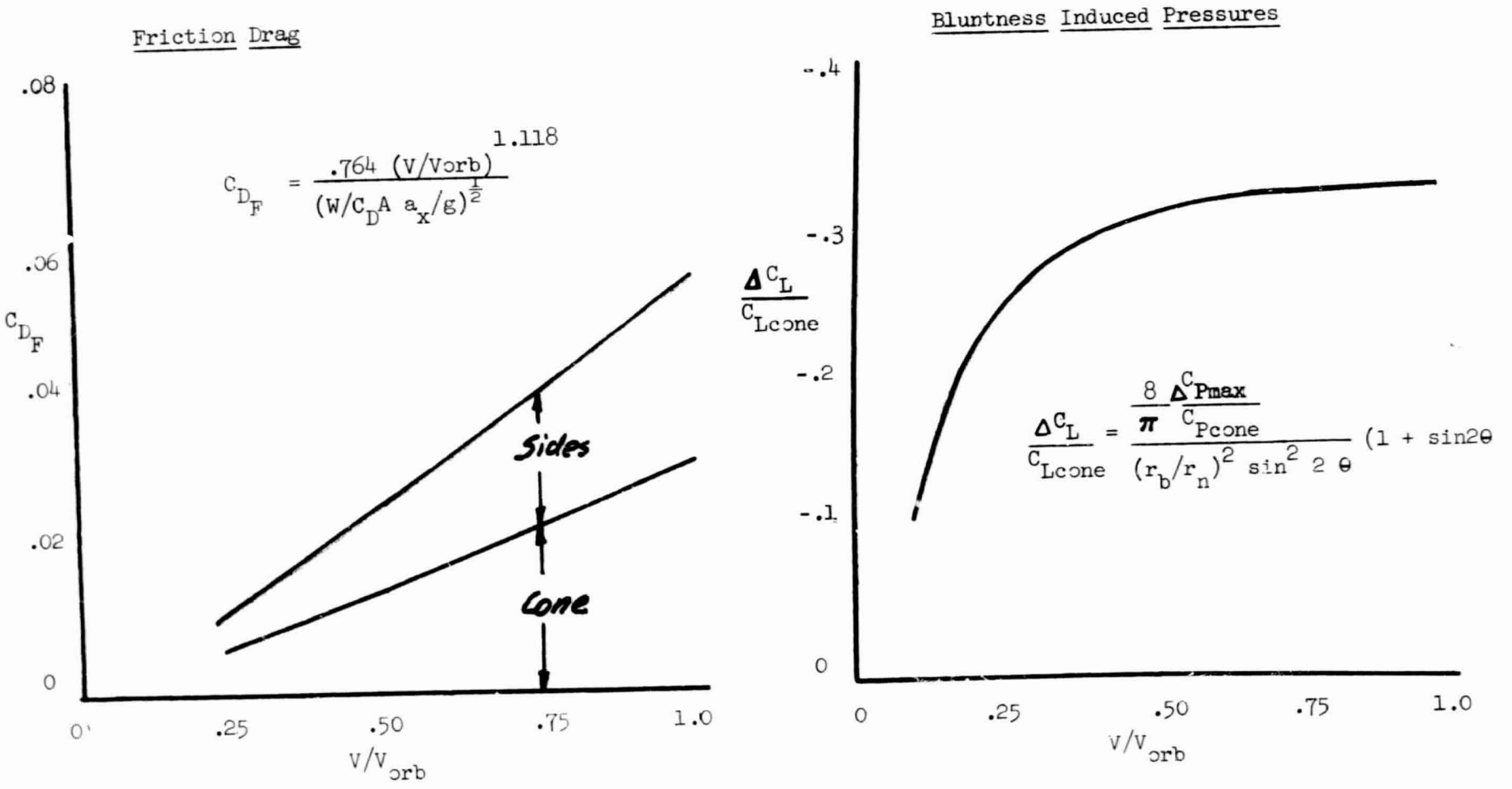

Fig. C.1 NON-NEWTONIAN AERODYNAMIC CONTRIBUTORS (Basic Configuration)

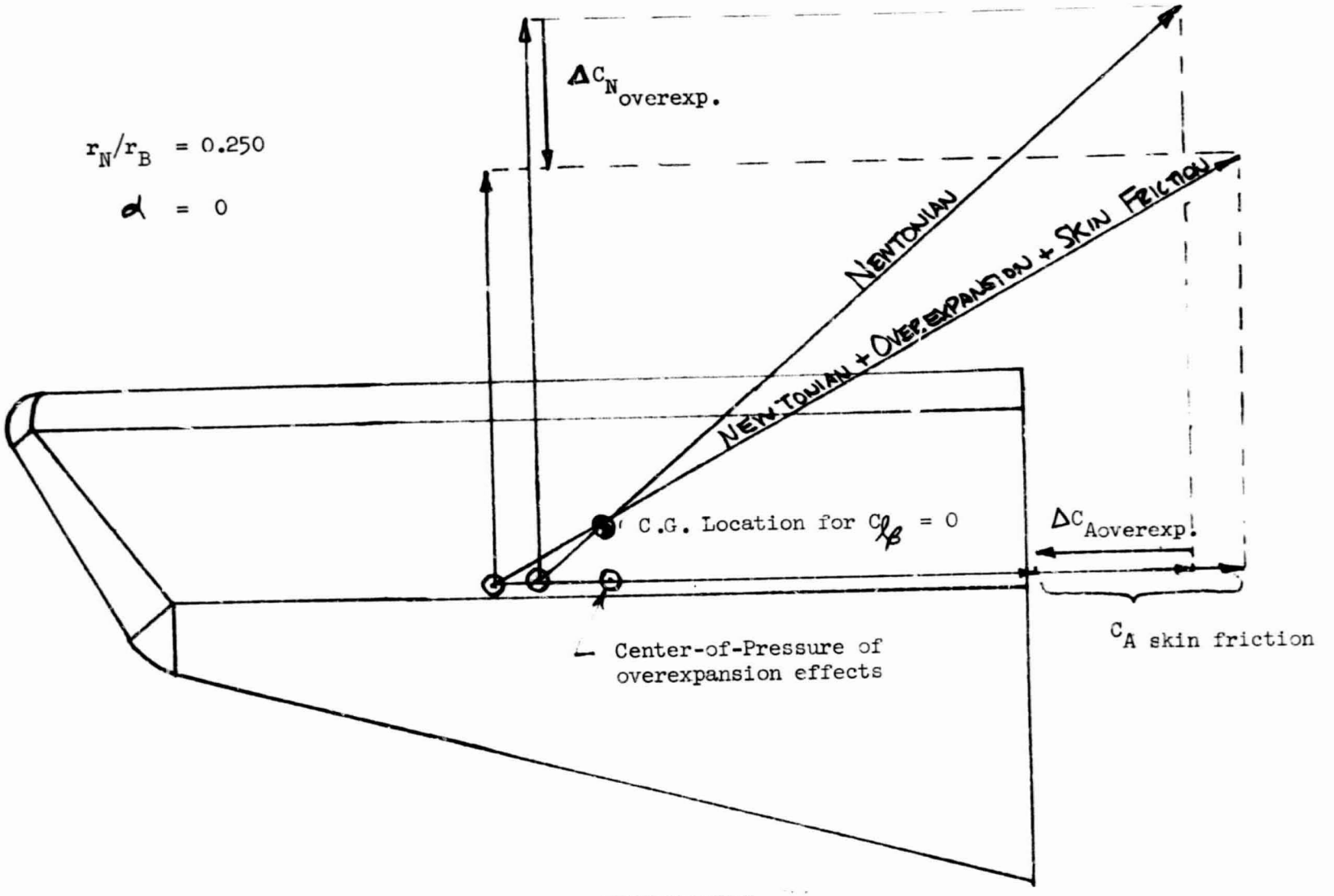

Fig. C.2 EFFECTS OF OVEREXPANSION AND FRICTION DRAG UNCERTAINTIES ON TRIM ANGLE-OF-ATTACK

configuration and shows that for the bluntness considered the Newtonian center of gravity is nearly correct. Thus, in the alternate shape studies effects of non-Newtonian contributors on trim was not a factor in the evaluation (so long as the effective bluntness is similar to that for the basic configuration). Assessment of the effects of bluntness induced pressures on the CG for trim will require detailed wind tunnel testing to clarify the phenomena.

The most obvious approach for reducing the over-expansion effect would be to reduce the effective bluntness since as shown by the equation in Fig. C-1 the lift reduction is proportional to the square of the bluntness ratio. Figure C-3 shows the effect on L/D by extending the configuration keeping the nose geometry the same as for the basic configuration. The L/D is plotted versus the lower body bluntness ratio which is proportional to the length extension. By operating at 5^{o} angle-of-attack, a significant improvement in L/D takes place. However, from Section 3 the predicted cross-flow effects on aerodynamic heating were considerable, even at 5^{o} angle-of-attack. Since low heating levels are desirable, the remaining configurations studied were of the non-cross-flow type (except at the nose tip). For the extended configuration family at zero angle-of-attack, small bluntnesses are required to bring the L/D to values approaching the basic configuration Newtonian value. Figure C-4 shows that extending the body in this manner is not permissible. To keep some lateral stability the requirement for zero C_{l_β} must be relaxed. A bluntness ratio of .15 will produce a $C_{l_\beta}/C_{n_\beta} > 1$, and will negate the direct rolling moment due to control mass displacement.

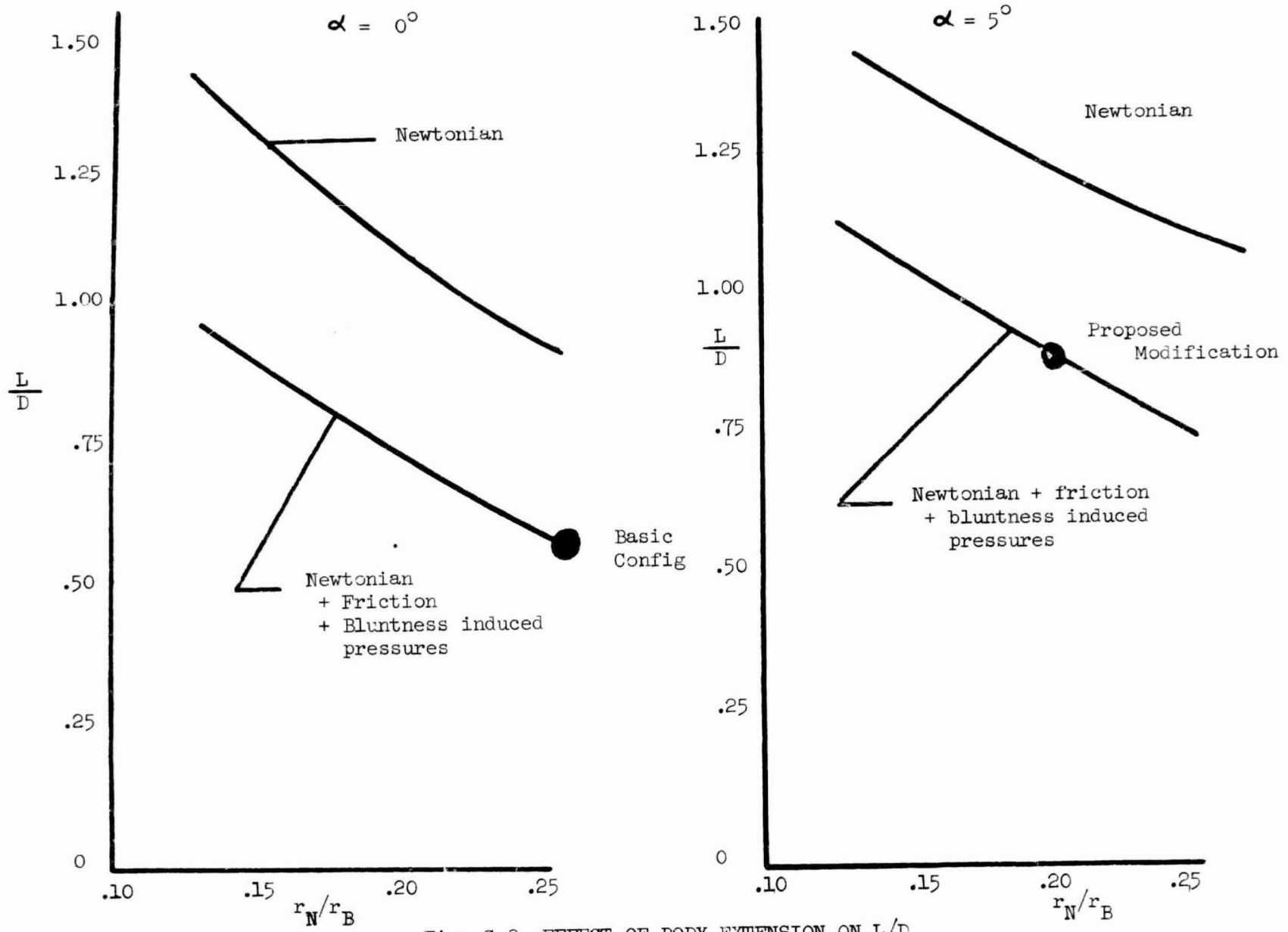

Fig. C.3 EFFECT OF BODY EXTENSION ON L/D

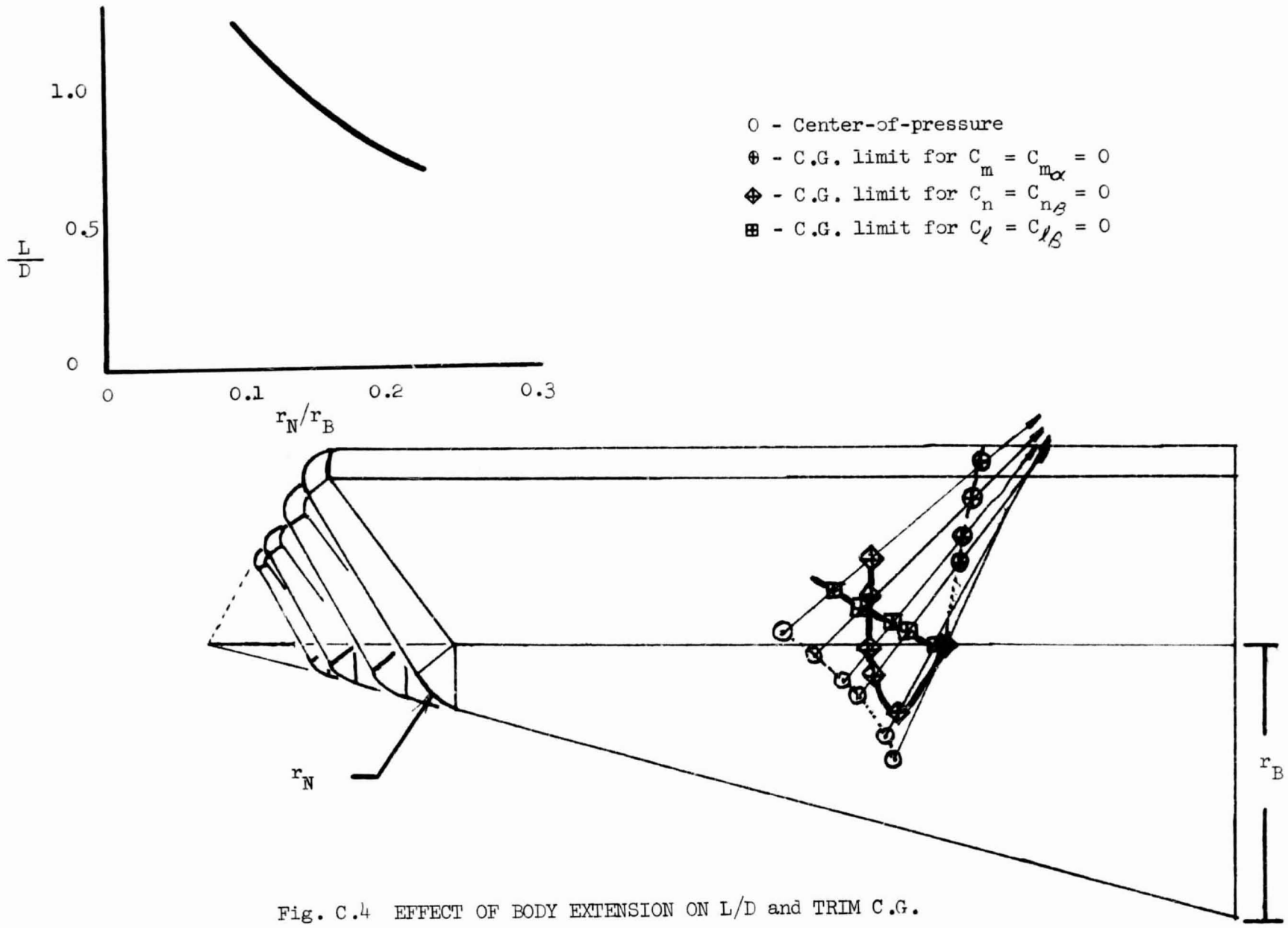

Fig. C.4 EFFECT OF BODY EXTENSION ON L/D and TRIM C.G.

An alternate configuration having raked-in sides was thought to improve the roll stability - yaw stability picture by lowering the side force center of pressure. The effect of this modification is shown in Fig. C-5. This approach reduced the Newtonian lift-drag ratio and degraded the yaw stability at the roll stability limit. Indeed, raking out the sides would produce a more desirable configuration. The result is attributed to the changed nose tip geometry that comes about with raking the sides and hints at the strong trimming effect of the nose tip. The effect of nose tip geometry changes on the zero angle-of-attack aerodynamics is shown in Fig. C-6 and shows that small displacements of the resultant force vector and the roll stability limit take place for quite large changes in nose tip geometry. The L/D is also shown to be more affected than for the other modifications. From Fig. C-6 and more detailed nose tip investigations, a final nose tip geometry was selected for the test model.

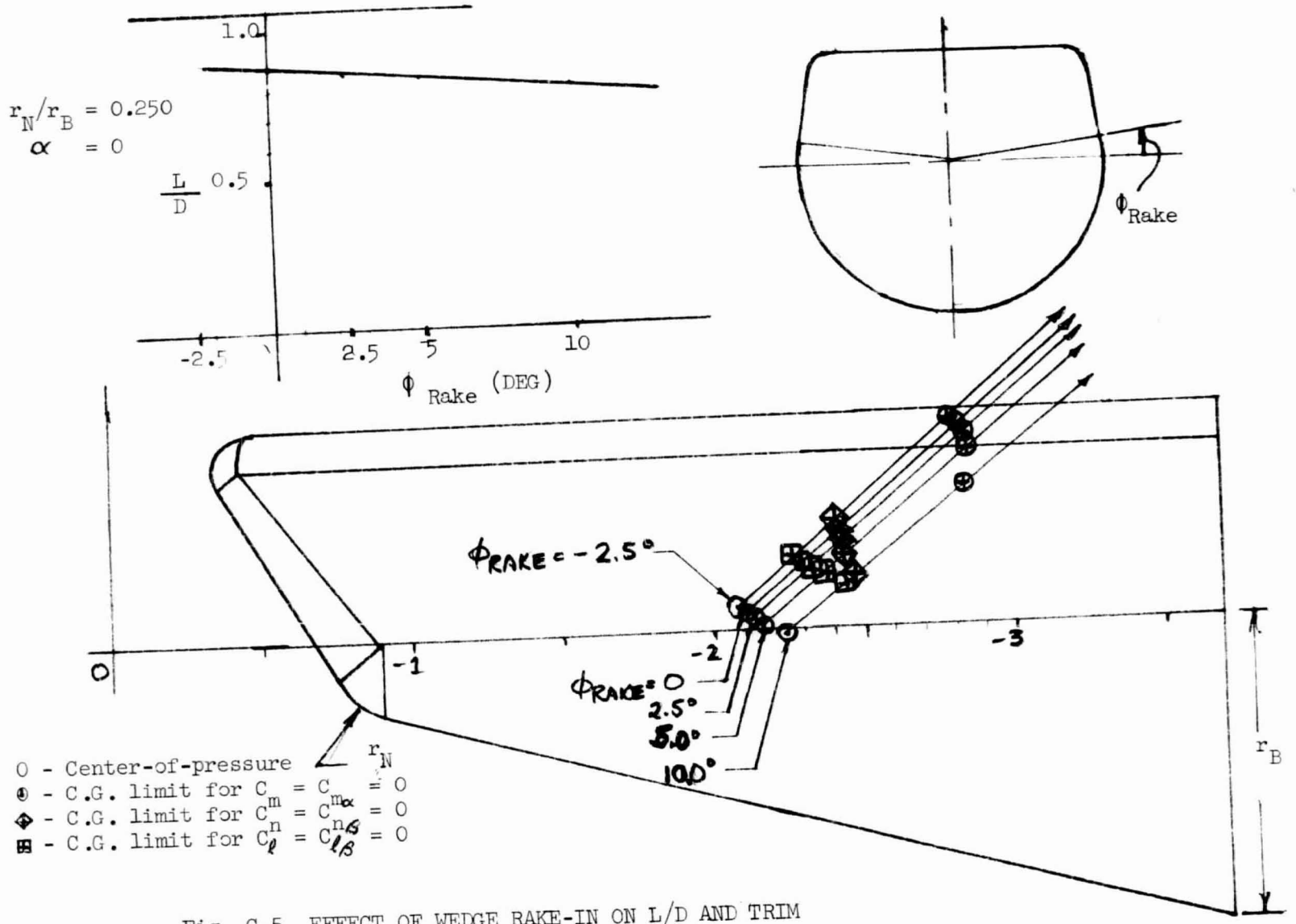

Fig. C.5 EFFECT OF WEDGE RAKE-IN ON L/D AND TRIM

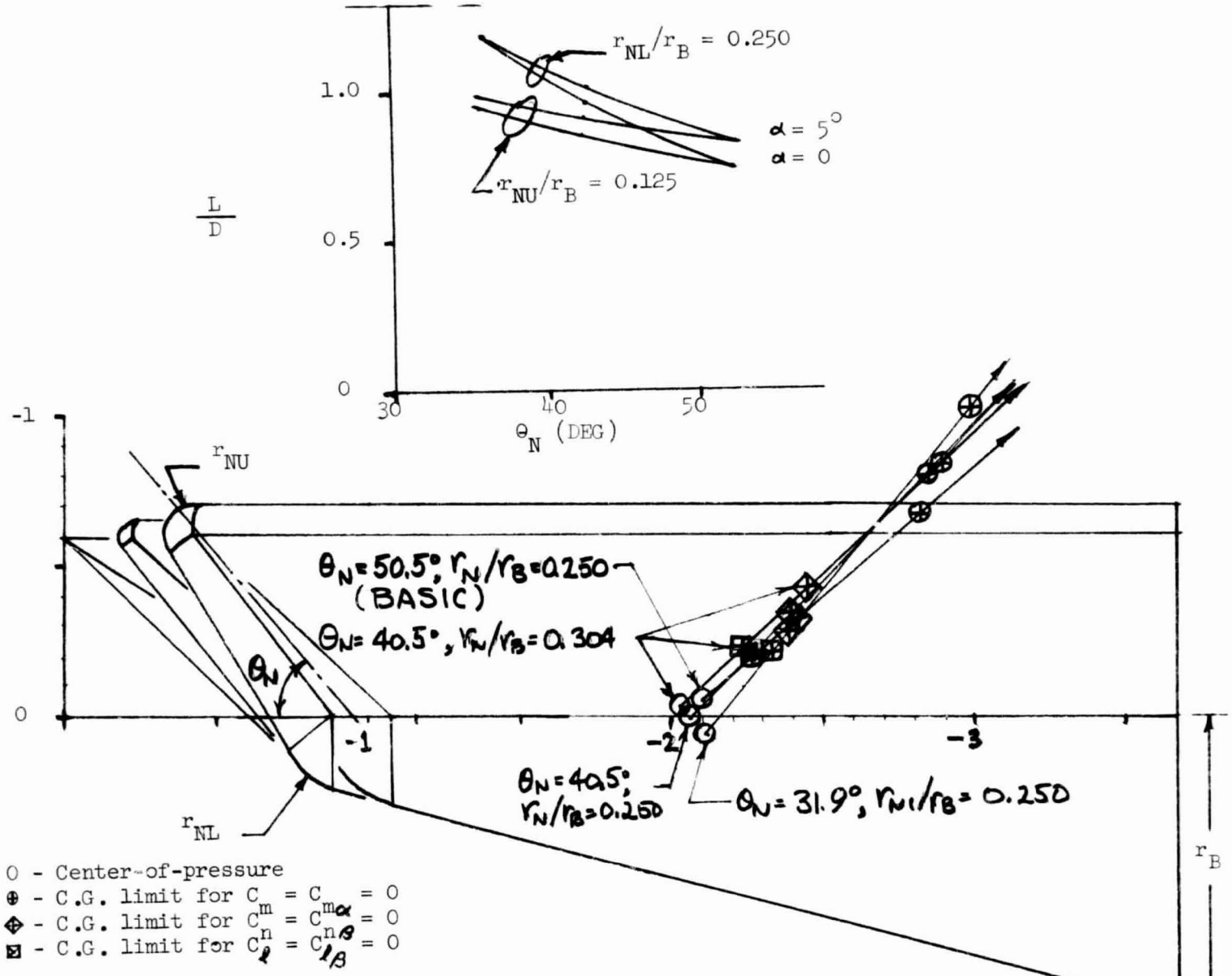

Fig. C.6 EFFECT OF NOSE-TIP GEOMETRY ON L/D & TRIM

APPENDIX D

IMPACT RANGE PREDICTION WITH BODY MOUNTED ACCELEROMETER MEASUREMENTS

The range control capability of the guidance system of Section 4 is based on the assumption of:

1) No downrange wind effect
2) Predictable crossrange wind effect
3) Precise measurement of drag deceleration

The effect of these assumptions upon range control accuracy is described in this Appendix.

Downrange Wind

The downrange component of wind will not be effective in altering the total range to any appreciable extent. The mechanism through which the downrange component operates will be the increase (or decrease) of the aerodynamic velocity at any given instant along the flight path. Since the accelerometer and control system are maintaining a preset inertial deceleration, the aerodynamic velocity has no direct effect. An indirect effect is the slight alteration in the flight path angle time history, which, in the rigorous sense, does effect net range. The practical effect, though, is measured in feet rather than miles because a 200 ft/sec

wind will only change the flight path angle a few thousandths or a degree, even after 700 seconds.

Crossrange Wind

The effect of crosswind on downrange distance brings out some interesting characteristics. It will take the entire flight time for the vehicle to assume the crossrange wind velocity. Also, the heading remains constant after the spacecraft has weathercocked into the relative wind. Figure D-1 shows the vector relationship that exists when the spacecraft first reenters The spacecraft weathercocks to an angle whose tangent is the ratio of crosswind velocity to vehicle velocity. Then the crossrange accelerating force is the drag deceleration multiplied by the sin of the heading angle ($a_D \sin \beta$). Since the downrange decelerating force is $a_D \cos \beta$, the ratio of the two accelerations is $\tan \beta$. The two velocities then are changing at a rate whose ratio equals the ratio of their magnitudes, and the process therefore continues throughout the flight. The average crossrange velocity is $\frac{1}{2}$ the crosswind velocity and a small downrange error accumulates as a result of the downrange deceleration being less than the desired level by $\cos \beta$. The wind angle, β, is on the order of a few tenths of a degree so the error involved is minute. For a prediction error in crosswind of 100 fps, the crossrange error is 6.5 n.m.

The foregoing analysis of error sources inherent in the basic concept shows that if a circular error probability in the order of 20 miles is acceptable for impact dispersion, then even the simplest means of

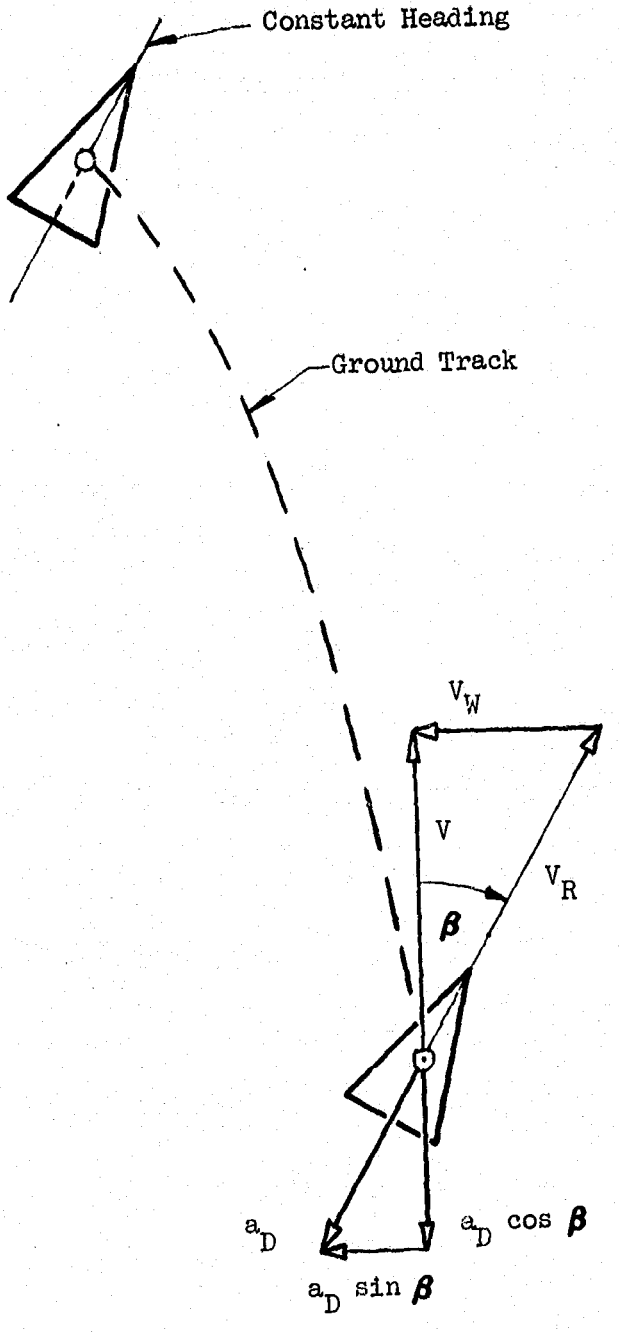

Fig. D-1 EFFECT OF CROSSWIND ON DOWNRANGE DISTANCE

compensating for these error will easily result in an order of magnitude safety factor, insofar as downrange is concerned.

Accelerometer Orientation

For precise control of the impact point, the deceleration along the flight path must be accurately measured. An angular orientation of the accelerometer from the flight path can result from misalignment of the instrument with the vehicle geometric axis and from a trim angle-of-attack other than zero. In Fig. D-2, α represents the sum of the misalignment and trim. The error rate in the drag deceleration is 1.75% per degree of misalignment (L/D =1). Since the deceleration propagates directly to range, the range error rate is 30 n.m. per degree. For the trim uncertainty of 0.25 deg and a misalignment of 0.1 deg, the resulting range error is 10 n.m.

A second error which is closely associated with the error caused by pitch trim accelerometer misalignment, is the error caused by pitch oscillations about the trim position. If such oscillations are held to magnitudes of less than $\pm$ 5 degrees then the contribution due to the cosine of the pitch angle is less than .2%, corresponding to about 3 miles. The sin term of Equation D-2 can be considered to vary plus and minus in equal amplitudes for all practical purposes so that the net effect is zero.

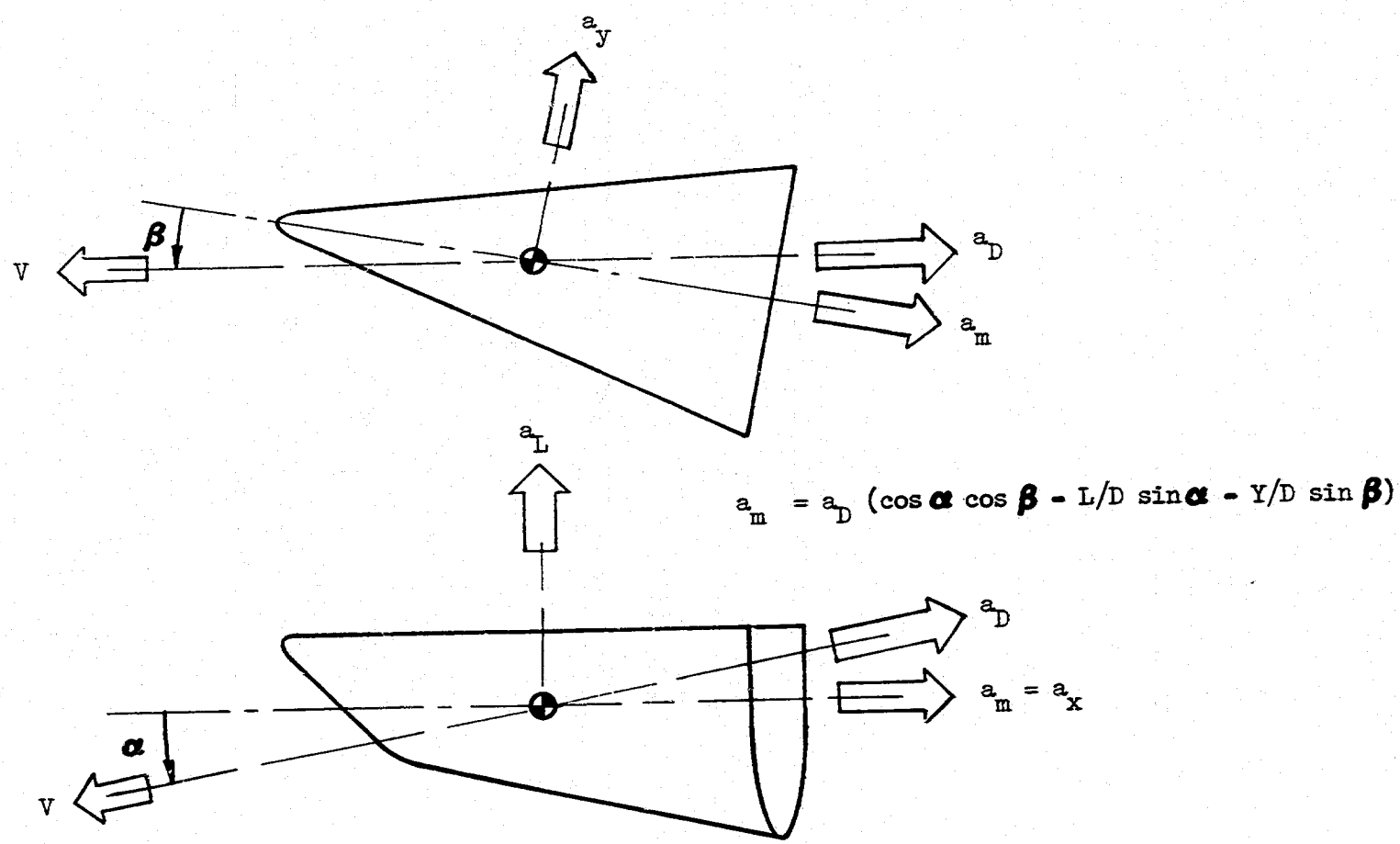

Fig. D-2 TRIM & ACCELEROMETER ORIENTATION EFFECTS

The angle of sideslip, beta, introduces a component of the side force coefficient, C_Y, into the measured acceleration. The error in a_D is about .3% per degree of β. The corresponding downrange error is then 4.5 miles. This indicates that the vehicle should be prevented from oscillating in yaw with amplitudes greater than about $2\frac{1}{2}$ degrees.

APPENDIX E

Guidance System Performance and Stability Analysis

The basic guidance loop is outlined in Fig. E-1 and shows the important transfer functions which determine the characteristics of the guidance system. The LaPlace transform notation is used where $1/s$ is an integration and $1/(s+\alpha)$ is a simple exponential time lag. "G" is used for "gain" where the designer has a choice and K where the coefficient is physical.

Starting at the left, the guidance electronics compares the measured longitudinal deceleration with the commanded level to generate an error signal. The transfer function, "G_1/s", is an integrator which computes the time integral of the deceleration error or the velocity error. This is a standard "type 1" servo technique which will reduce the static error of a_x to zero. The gain term, G_1, is very low because the integral error loop is destabilizing in its effect on the system. The value used is .005 g/ft/sec. "G_2" transforms the error signal to a commanded roll angle at a gain of 1,800 degrees per g. In the practical mechanization of the loop, a limiter prevents command of more than 180 degrees, which is upside down. The lag term, $1/(s+\alpha)$, represents the time required for the roll control system to physically deliver the commanded roll angle. The "K_1" block converts roll angle to vertical acceleration, h double dot. Two integrations of vertical acceleration, (s^2), will give the change in vertical position, or altitude, which determines the change in deceleration.

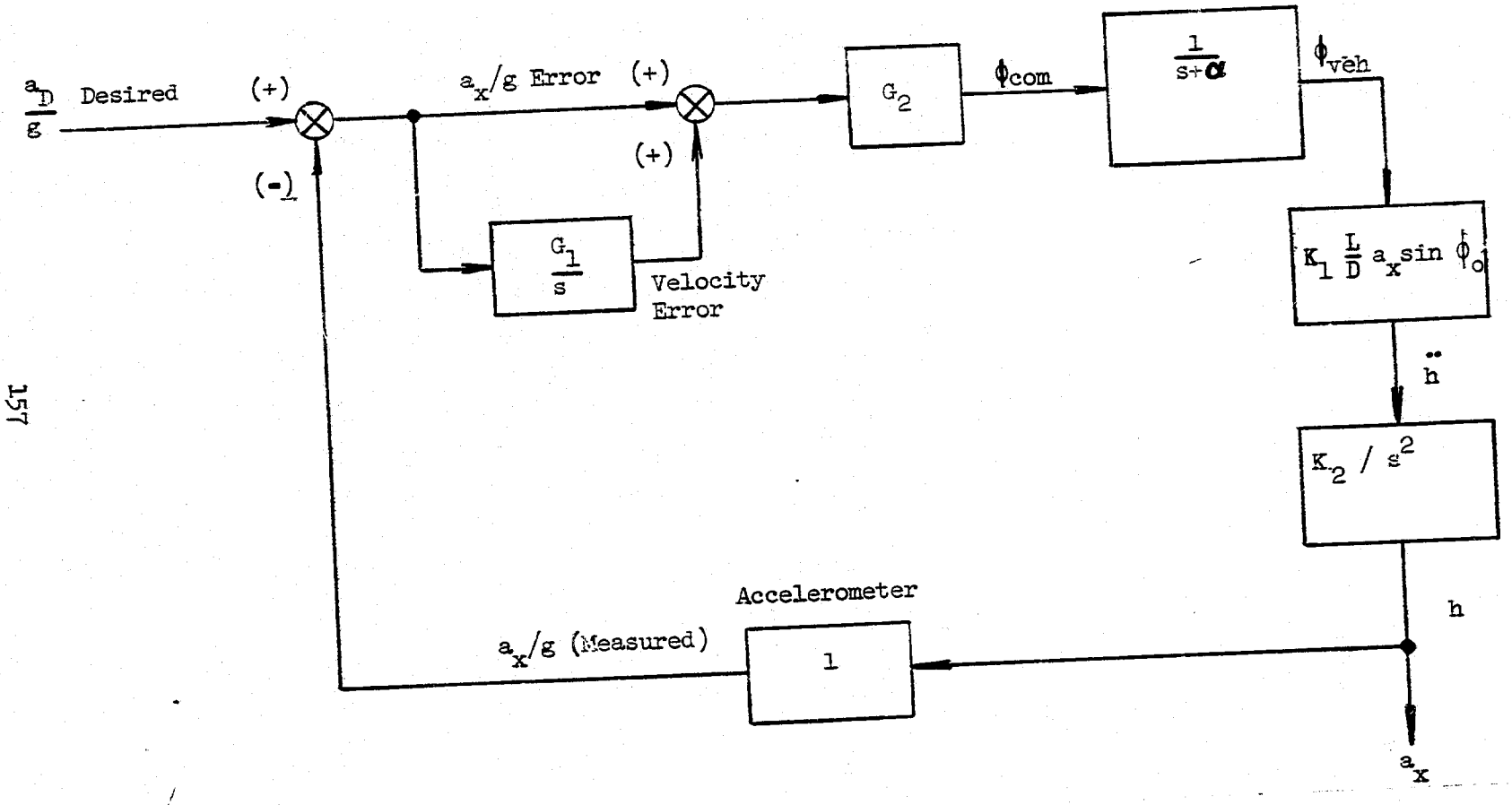

Fig. E-1 BASIC GUIDANCE LOOP

The velocity error loop is included in order to control guided flight range precisely. Its function is to provide the nominal roll angle history which varies from 90 degrees at orbital velocity to zero near the end of the flight. The roll angle varies linearly with velocity, as shown in Fig. E-2. The primary loop then commands roll angle deviations from this nominal history to control acceleration errors to zero. With the spacecraft performing small oscillations about the nominal roll angle history, the range will be controlled quite precisely to the programmed range with a small bias. Only a small initial velocity error is needed to produce satisfactory operation and adequate range control. From computer studies an initial velocity error of 100 ft/sec. with a gain of 0.9 degrees per ft/sec. was selected as depicted in Fig. E-2. The range bias accruing from the linear "controlling" velocity error is 40,000 feet for the 1 g descent profile. This bias is predictable and is included in the range calculation.

For purposes of stability analysis, when considered over small ranges, all coefficients are considered to be constant. G_1 and G_2 are fixed by the design of the electronics. K_1 contains a_x/g and so depends on the instantaneous value of a_x. Perturbations about the nominal value of a_x will generally be less than five percent, which is negligible in its effect on overall stability. However, the last part in the K_1 coefficient, sin phi_o, varies from one at the orbital speed to zero at the end of the flight so that the net coefficient will experience a considerable change over the flight time. Note that the phi_o is the roll angle for zero excess lift at the instantaneous value of altitude and velocity. K_2 relates change in altitude to change in deceleration. For an exponential atmosphere, which is sufficient for stability

Fig. E-2 NOMINAL ROLL ANGLE PROGRAM

purposes, K_2 relates change in altitude to change in deceleration. For an exponential atmosphere, which is sufficient for stability purposes, K_2 will be constant because a given "h double dot" will produce the same rate of change in longitudinal deceleration when considered in the region very close to the nominal value of a_x.

The root locus of Fig. E-3 shows the instability expected from such a control loop but that the operating point is very close to the origin for the gain coefficients discussed. The addition of a practical passive lead network provides complete stability as indicated in Fig. E-3. The method of design used for Fig. E-3 was to construct the locus for 270 degrees of phase shift without the lead network, then to add in a 90-degree semicircle tangent to the 270-degree locus. The lead network is assumed to be practical if the ratio of zero to pole is less than 0.1 so the radius of the semicircle was adjusted until this criterion was met, always maintaining tangency.

At the point of tangency the net phase shift will be 270-90, or 180 degrees. The gains over which the designer has control must be adjusted to give a total loop gain such that the operating point will be close to the point of tangency. The meaning of such a coincidence is that the loop will have its best possible damping. For a_x/g and L/D values of 1, an almost optimum total gain of 0.476 is obtained for a roll gain (G2) of 1,800 degrees/g.

Effect of L/D and Acceleration Level

Two characteristics of the loop gain should be mentioned here.

1) Gain is proportional to a_x/g squared.

2) Gain is proportional to L/D.

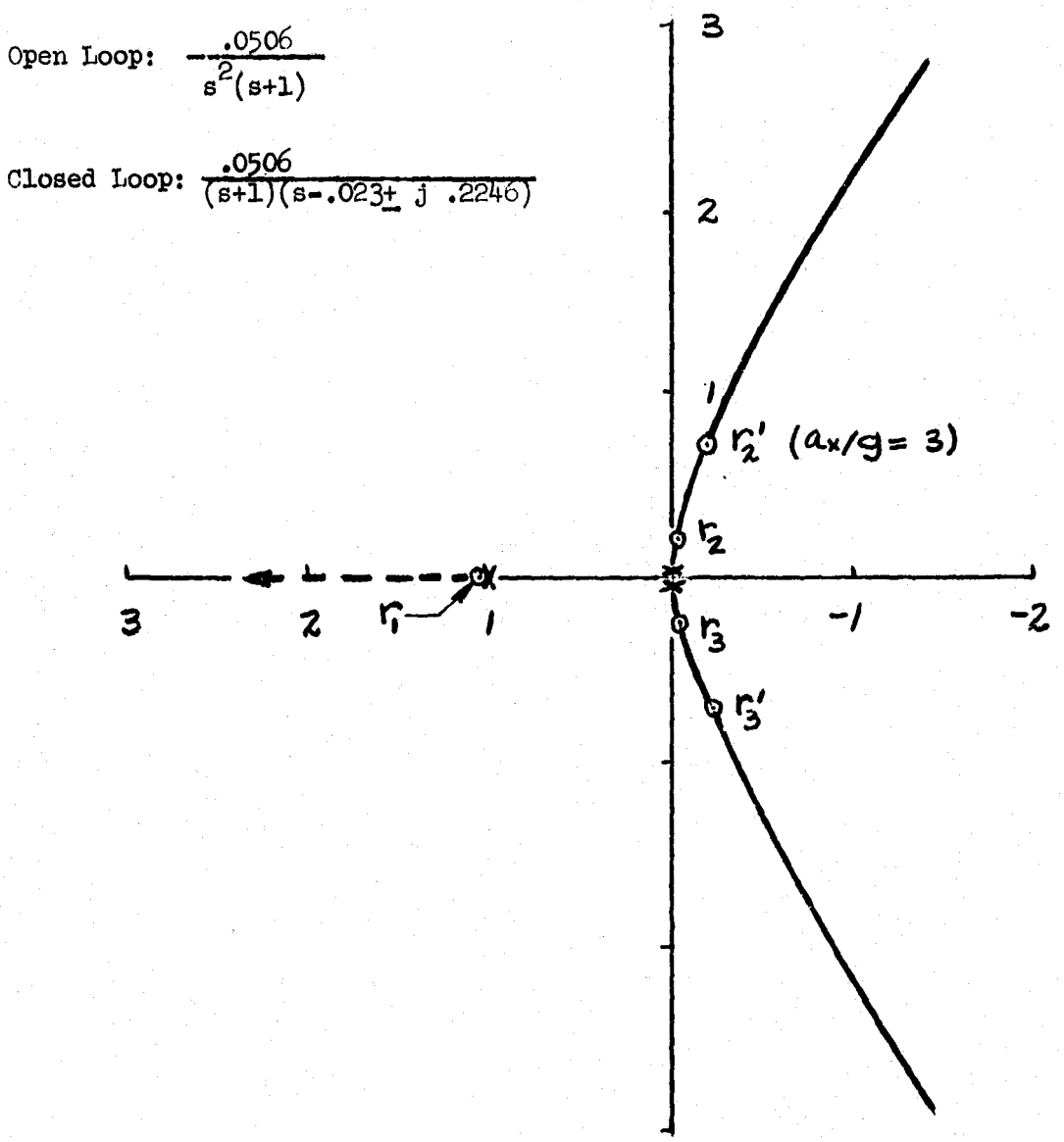

Fig. E-3 ROOT LOCUS FOR GUIDANCE LOOP

In terms of a practical mission profile, the first of these characteristics means that if a nominal 1 g flight is required to fly at 2 g or higher in order to correct for range dispersion, the gain will go beyond the 1.6 limit permissable for positive stability unless the roll gain is reduced to keep the product less than 1.6. On Fig. E-4 1.6 gain is the operating point where the locus crosses the $j\omega$ axis. Roll gain may be reduced somewhat but at the expense of range accuracy since the velocity "controlling" error will be increased.

The consequences of exceeding the positive stability gain limit are not catastrophic because of the pseudo stability inserted by the non-linear circuits of the guidance electronics, which limit the amplitude of any oscillatory tendencies.

The maximum value of a_x/g or L/D which may be feasible is a function of what performance would be considered acceptable. In terms of maintaining a desired g level for some period of time with peak excursions in the order of 10 percent, levels of 5 g will be controllable providing the L/D ratio is reduced by a factor of g/a_x. However, the range correction capability is decreased to a point which makes impact prediction questionable as shown in Fig. E-5. If the L/D ratio is maintained near 1, then controllability is deteriorating rapidly at g levels of 3 even with partial compensation through reduction of roll gain.

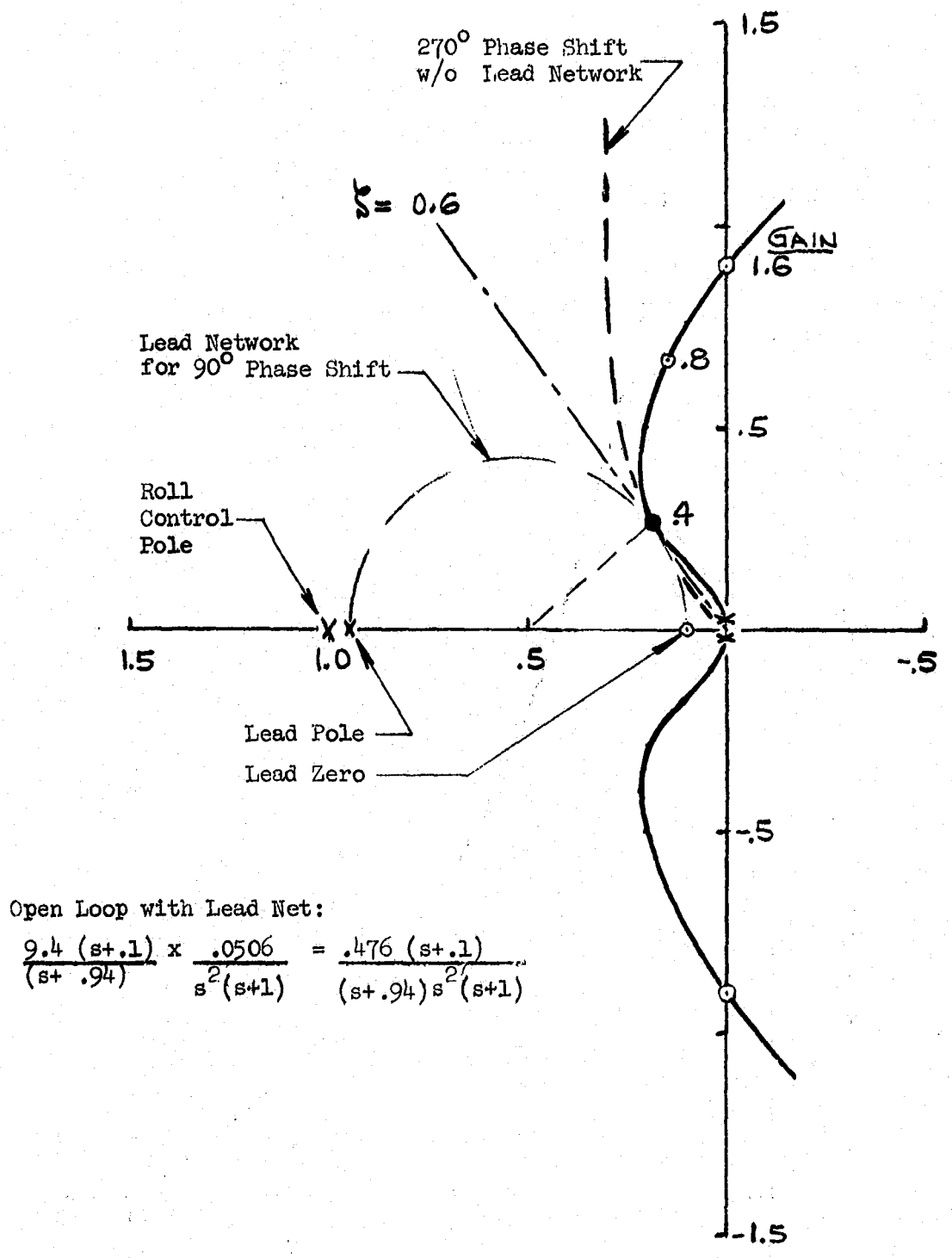

Open Loop with Lead Net:

$$\frac{9.4\ (s+.1)}{(s+\ .94)} \times \frac{.0506}{s^2(s+1)} = \frac{.476\ (s+.1)}{(s+.94)s^2(s+1)}$$

Fig. E-4 ROOT LOCUS FOR GUIDANCE LOOP WITH LEAD NETWORK

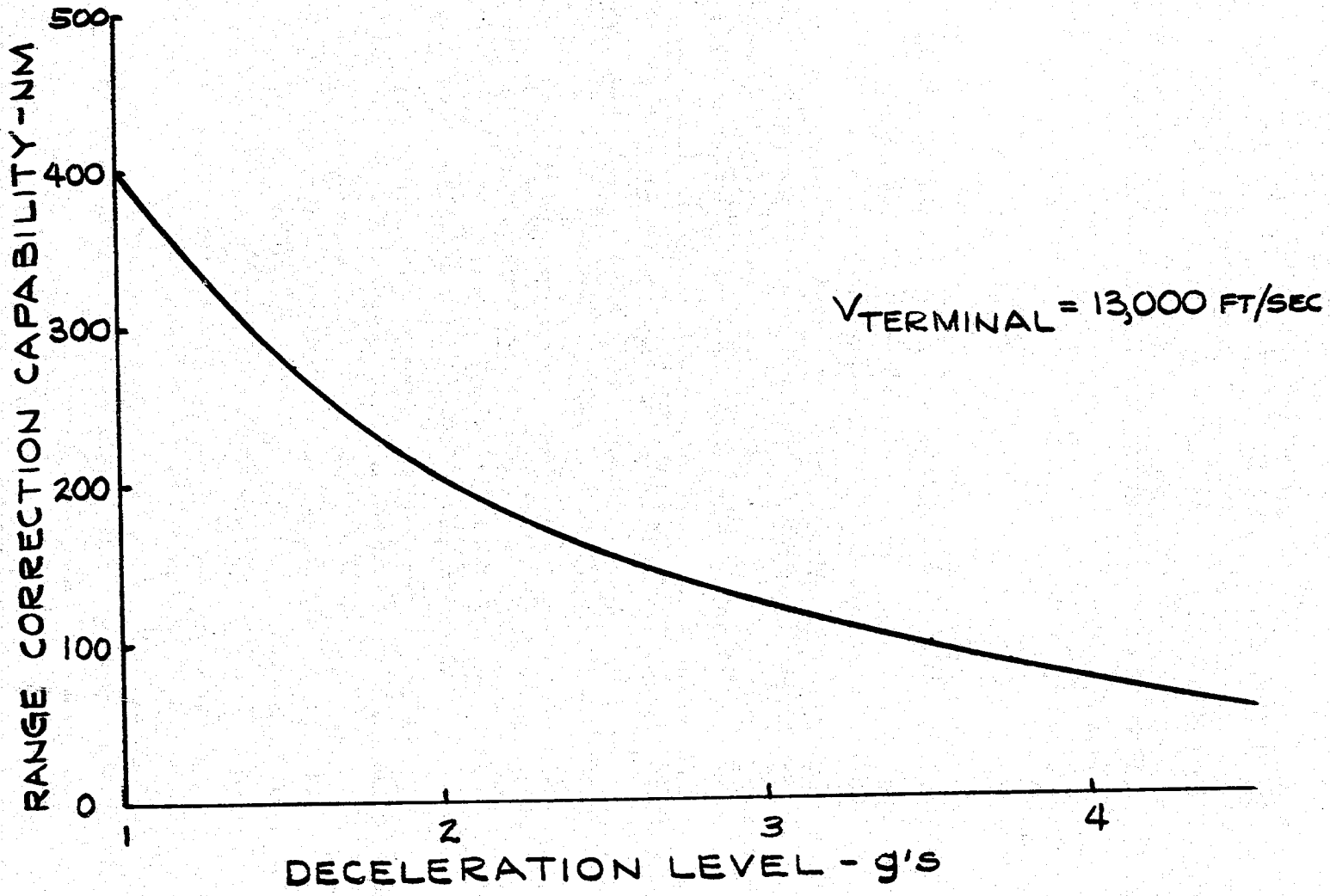

Fig. E-5 RANGE CORRECTION CAPABILITY FOR PULLDOWN TO TERMINAL VELOCITY

APPENDIX F

RANGE CORRECTION TECHNIQUE

Two techniques for correcting down range errors resulting from launch vehicle injection errors (a) g-level change and (b) flight termination are described. Cross range control is also described.

Assessment of Injection Errors

The basic guidance task is to control the deceleration level in a pre-determined way between two points. The first point is designated T_s and is in reality a time rather than a point, and the second is T_{st}, a stop or "dump" time.

The start of guided flight is arbitrarily chosen to be the time of arrival at 0.25 g deceleration, a choice which permits the control system to make a smooth pullout into the desired deceleration level with minimum perturbations from initial condition errors. This time has been designated "T_o" and signals the start of the internal "velocity error" integrator.

The time interval between T_s and T_o is used to determine what action is necessary to guide to the desired impact point. A variation in T_o, the reentry time, is sensed and handled by the guidance system, but only as a function of the time elapsed since T_s. If the vehicle is not at its proper pre-calculated geographical position at T_s, no correction can be made for the position error, and the impact point will be off by the same amount, nominally.

In the event that it is feasible to transmit real time ground commands to the spacecraft from a tracking ship or station, the T_S would be accurately determined and errors in impact point from this source eliminated.

One of the contributors to an error in geographical position at time T_S is an error in velocity prior to T_S. The pre-calculated geographical position at time T_S will be off if the spacecraft has been travelling at the wrong speed. For this reason, it is desirable to choose a trajectory such that T_S may be set to occur as soon after separation from the boost stage as possible. Errors in velocity continue to propagate distance errors after the start of guided flight because the spacecraft has no way of measuring velocity directly and compensating. The "velocity error" integrator can only compute the accumulated velocity error resulting from errors in deceleration which is directly measured, but has no information on the initial velocity. In the case where ground commands are available, velocity information might possibly be sent directly or a close enough estimate of velocity error might be inferred from a radioed position as compared to the on-board programmed T_S. These alternatives were not considered to be a part of the guidance study but are mentioned to aid in developing a useful perspective on possible overall systems.

The deceleration program proposed to correct for errors in geographical position at the time of reentry is shown in Fig. F-1. Reentry is effected in a standard way with 1/2 the maximum range flown at the desired deceleration level. In the case of a 1 g trajectory, this would amount to 240 seconds. The balance of the flight would then be at some higher level as required to

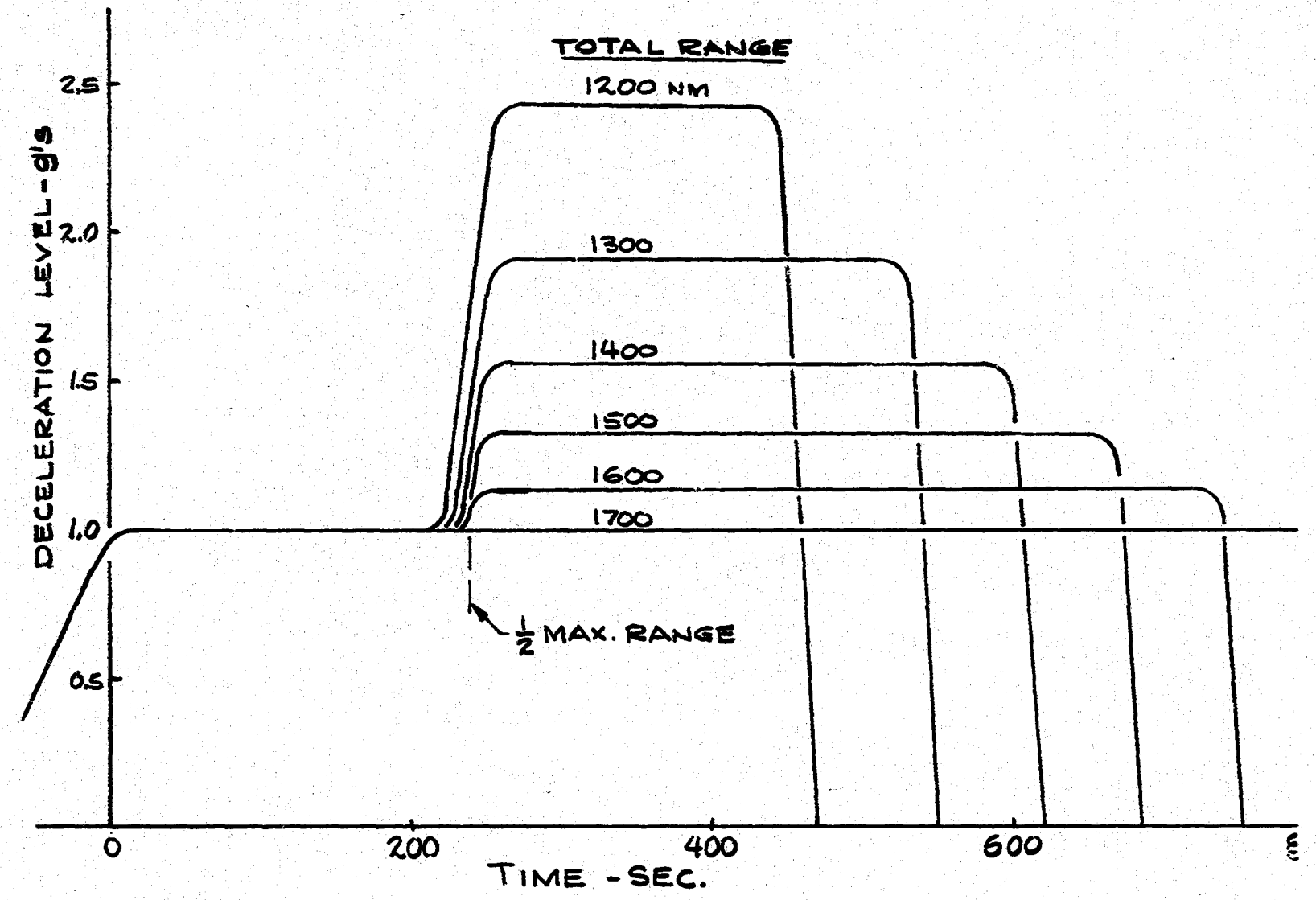

Fig. F-1 DECELERATION PROGRAM FOR RANGE ERROR CORRECTION

correct for the initial range error. For example, a range error of 555 N.M. would require an increase in g level to about 2.6 g. The "step" method is preferable to a straight "dump" at the end of the flight because there is sufficient time at the new deceleration level to stabilize and sense errors associated with the transient situation. There is a degree of uncertainty in the "dump" method if termination is required at high velocity because the spacecraft is in an uncontrolled pulldown maneuver which may take 90 miles or more to complete. In cases where the velocity is not so great, a flight termination technique would be satisfactory. The cross-over point is probably in the range of velocities below about 9,000 ft/second.

Range Correction Mechanization

Two mechanization schemes for range correction are illustrated in Fig. F-2 and F-3. The on-board timer, possibly updated by radio command, sends a "time-zero" discrete to an interval timer. "Time-zero" represents the time at which the vehicle is supposed to be a particular position on the earth. A second discrete is sent from the accelerometer signalling arrival at 0.25 g of longitudinal deceleration. Nominally, the spacecraft will pullout and fly a fixed distance from the 0.25 g point and therefore the impact point will be predictable if 0.25 g occurs at the precomputed point and time. If 0.25 g occurs at some other time, the net range will be in error by an amount determined by the velocity and the error in the time interval between time-zero and time-0.25. The "g-level compute" block translates this time interval into a new g level which will be commanded at time-240, which is the half-range time, as covered in Fig. F-1. The on-board timer enables the new g-level to be

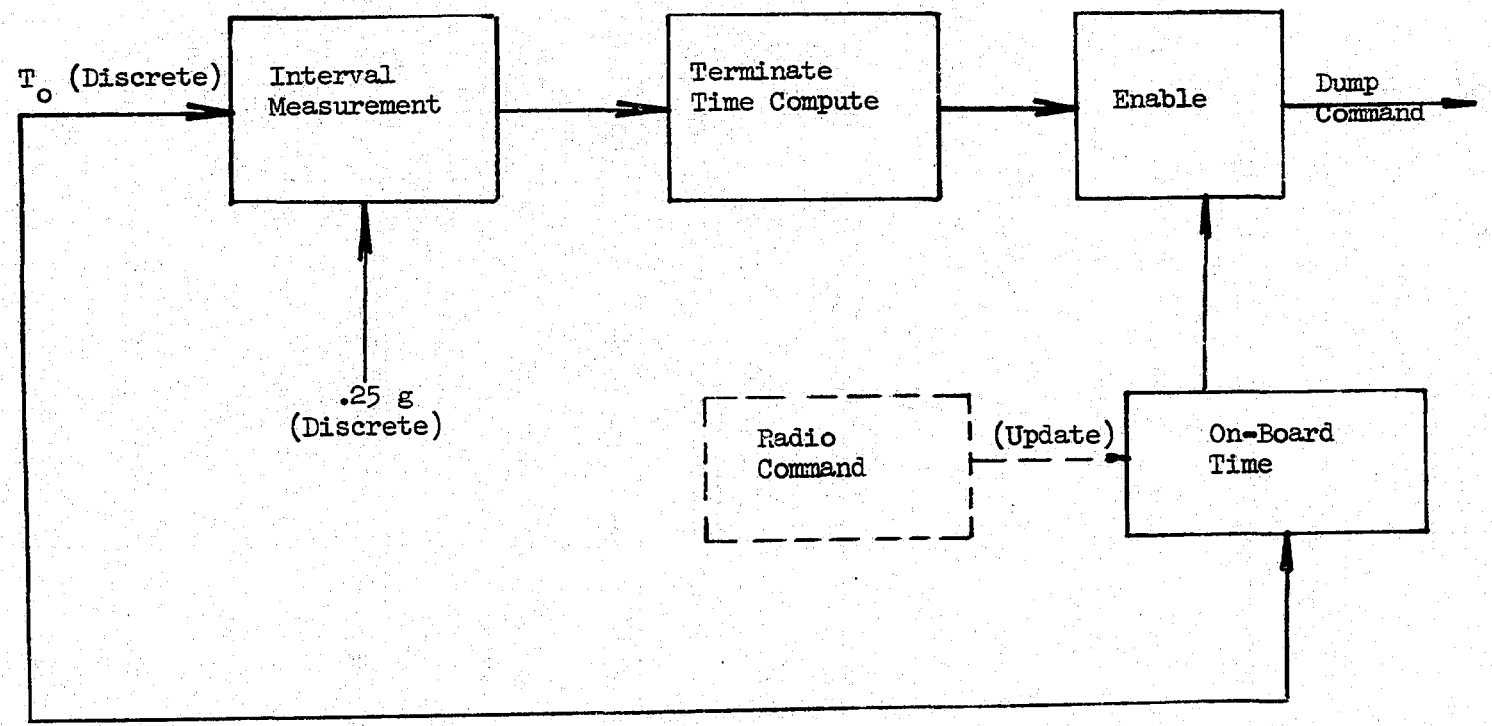

Fig. F-2 RANGE CORRECTION BY FLIGHT TERMINATION

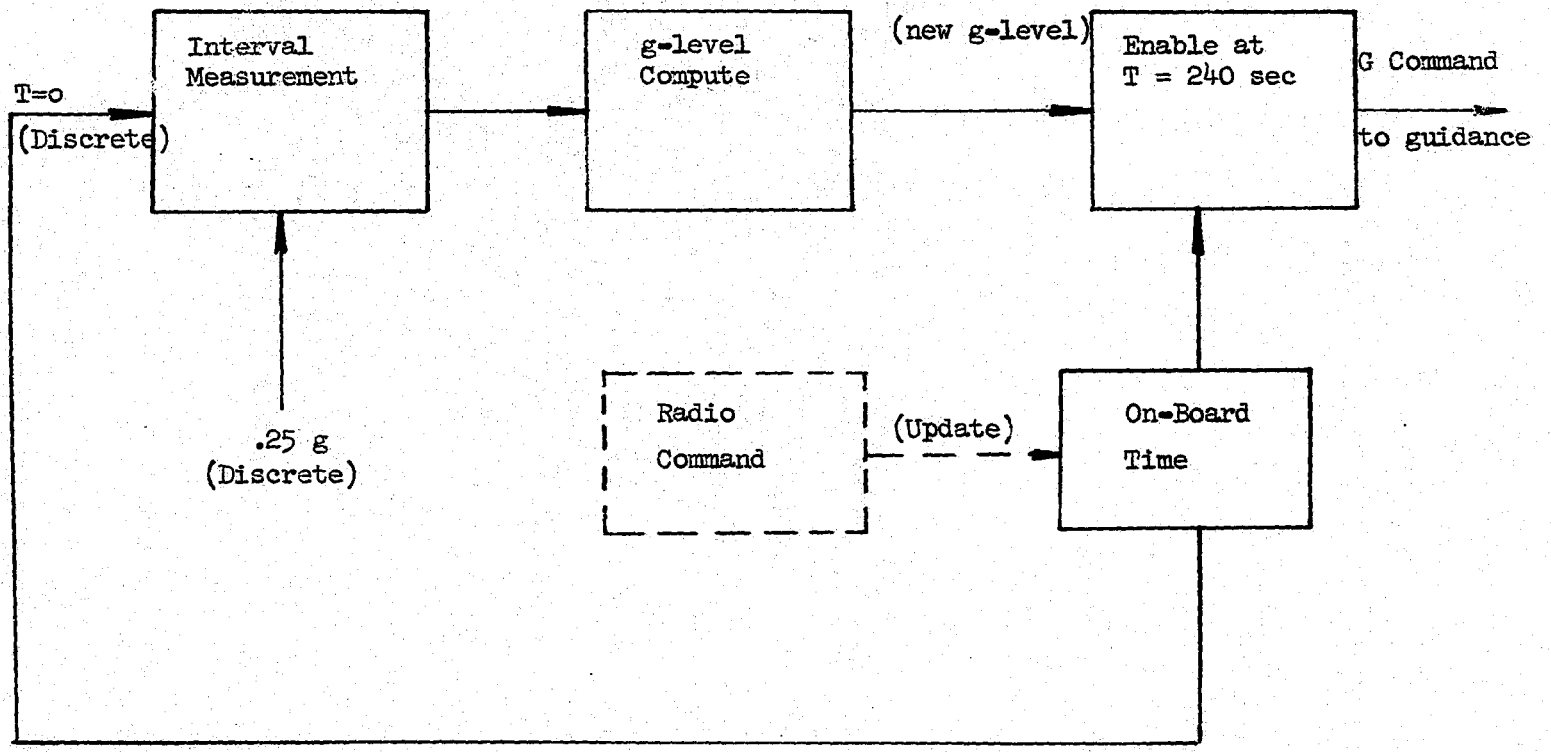

Fig. F-3 GUIDANCE SYSTEM FOR G-LEVEL RANGE CORRECTION

commanded when the 240-second time arrives, and the spacecraft completes the flight at this new g-level, arriving at the predicted impact point with zero velocity.

The alternate method, Fig. F-3, computes a flight termination time instead of a new g-level, and when the termination time arrives, the spacecraft pulls down by flying inverted.

Cross Range Considerations

For initial missions cross range control is concerned only with steering a straight course, or at most, correcting out the effect of a predicted cross-wind. If desired, the techniques used to steer a straight course may be used to command a definite cross range distance.

The most important characteristic of the cross range performance is the nearly constant rate of azimuth change available during the entire flight. This capability is shown in Fig. F-4 in terms of the azimuth rate coefficient based on a roll angle of 90 degrees and finishes the flight at a "wings level" attitude. The required roll angle is taken from Fig. F-2 to compute the coefficient "C" as a function of time.

The significance of a constant rate of change of azimuth is that the cross range distance contributed by the guidance may be predicted with sufficient accuracy by a simple timing procedure. The method recommended involves the integration of a constant times the sine of the roll angle. When the value of this integration reaches some convenient level, the direction of roll is reversed. By commanding some net value for this integral, a net cross range

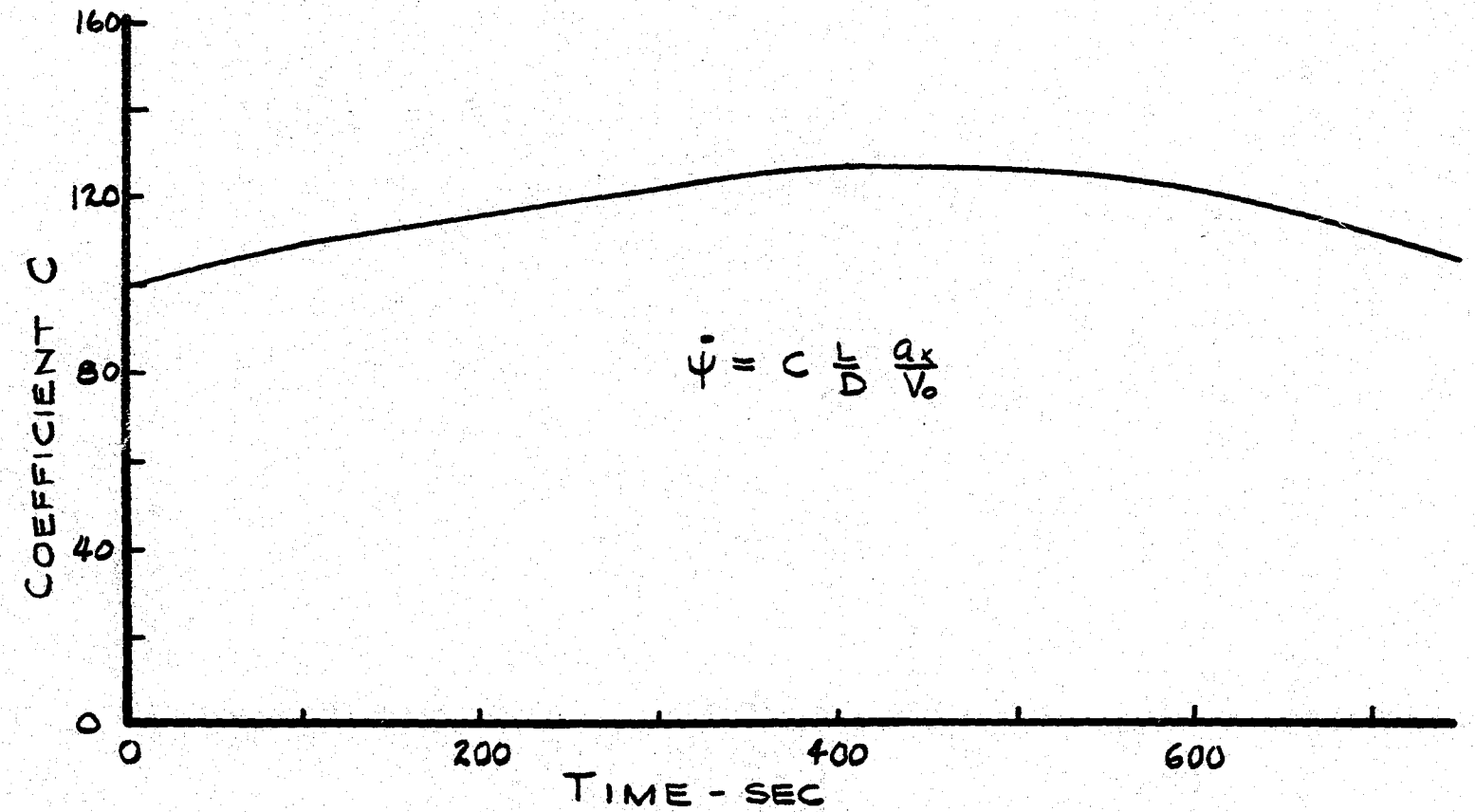

Fig. F-4 CROSSRANGE TURNING RATE CHARACTERISTICS

will be attained which can be easily calibrated. A slight refinement is available if the value of the constant is vaired linearly with time. This method will weight a given azimuth rate depending on the spacecraft's position downrange so that a given angle attained early in the flight contributes more than the same angle attained later in the flight when there is less range to go. Figure F-5 gives an indication of how the crossrange changes with flight time spent rolled in one direction.

Errors associated with the guidance concept and the physical construction of the spacecraft are very slight if the requirement is for a straight flight. The reversal of roll direction at frequent intervals cancels out the effects of the L/D tolerance, yaw oscillation, and pitch trim discrepancies. Even the effect of mislocating the local vertical does not become noticeable until the nominal roll angle reaches some 45 degrees which is 75 percent of the total range. For example, if the computed roll angle were off by 5 degrees, the rate of turn in one direction would be computed at 6 percent greater than actual, and the other direction 6 percent less than actual. The net effect would be slight even if the maximum crossrange were being commanded. In general, it would be expected that a maximum of 300 seconds would be required to pick up the desired azimuth angle and the rest of the flight would be a straight track over the ground. The nominal roll angles used during the early part of the flight are greater than 50 degrees where an error of five degrees will effect the net azimuth angle less than 1 degree at 300 seconds, or about 10 miles. The estimated tolerance in roll angle is $\pm$ 1.5 degrees.

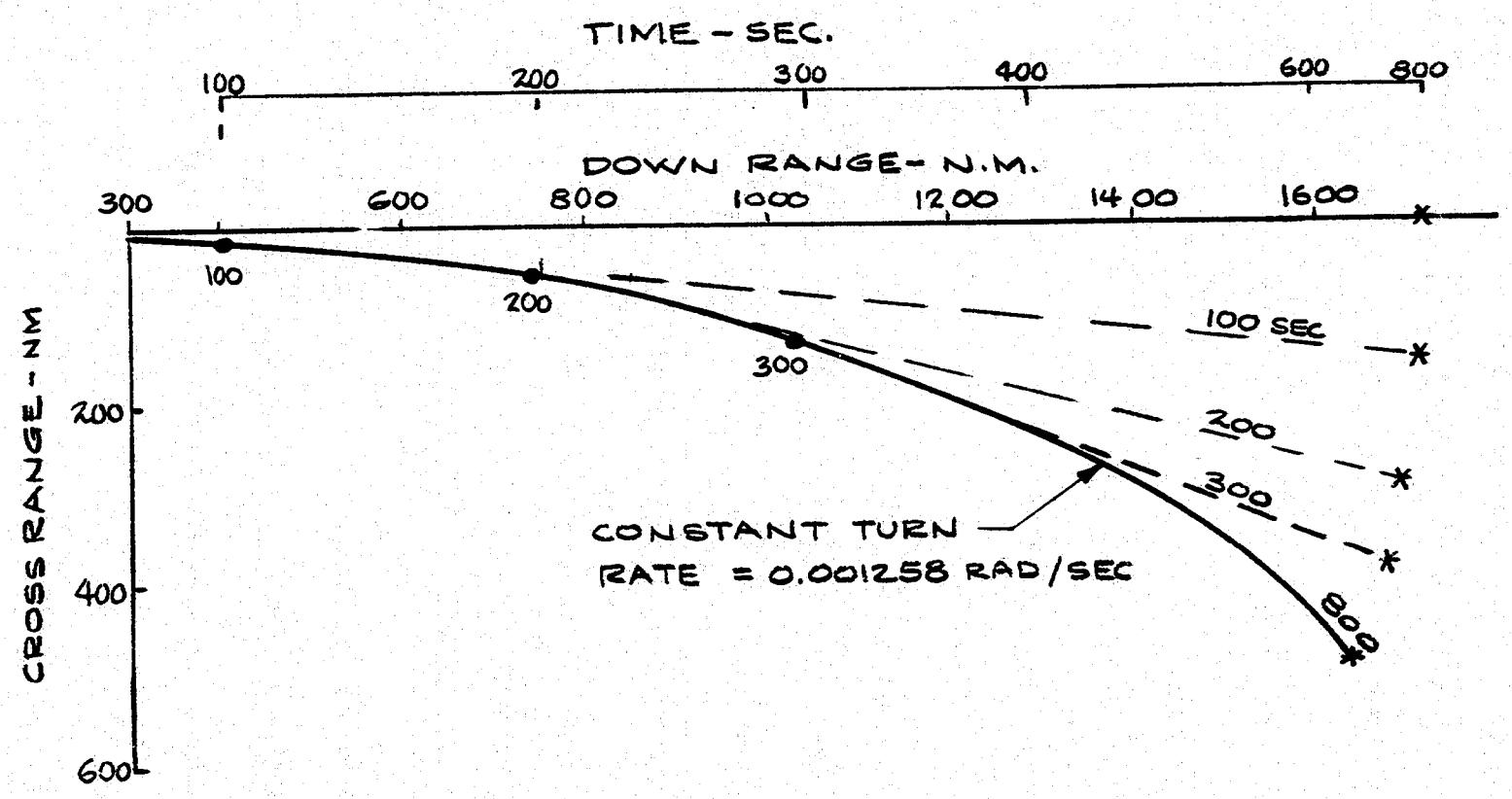

Fig. F-5 CROSS-RANGE vs TURNING TIME

The effect of a mislocated vertical reference is more noticeable during the pull-up maneuver where the wings are level. Any error during this period will generate an azimuth rate which can be an important contributor to the total cross range error.

The pull-up maneuver for an entry angle of 2 degrees will require some 20 g-seconds of lift. If the vertical reference is off 5 degrees, 2.6 g-seconds will be directed cross range. The net azimuth change for a spacecraft going at orbital speed will be 0.2 degrees corresponding to a cross range error of about 7 miles. Again, it is emphasized that 5 degrees is more than twice the error in roll to be expected.

APPENDIX G

ROLL CONTROL SYSTEM PERFORMANCE AND STABILITY ANALYSIS

The basic roll control loop for the control mass only is outlined in Fig. G-1 and depicts the applicable transfer functions which determine the characteristics of the control system. The corresponding root locus of Fig. G-2 shows stable operations for the representative spacecraft, control mass and drive motor.

Figure G-3 illustrates the effect of varying gains k_1 and k_3. k_1 is able to raise the resonant frequency and improve the overall response somewhat, but the damping remains low as would be expected from the root locus of Fig. G-2. Reduction of the rate gyro feedback, k_3, also improves the speed of response slightly. Regardless of the combination of gains chosen, the oscillatory nature of the system will remain. Also, it should be kept in mind that the responses shown are for linear systems and so are only valid for ranges of operation demanding less than the limiting values of motor torque and velocity. The effect of reaching a limit in torque or velocity is to increase the overall time to reach the commanded output without effecting the damping noticeably.

From the operational standpoint, the low damping is disadvantageous because of the reduced margin of stability against degraded performance from any unforeseen source. Some additional power is required to continually move the slug.

Early in the study it was thought that faster reaction than provided by the slug alone might be needed. Hence, a mechanism to rotate the control mass for

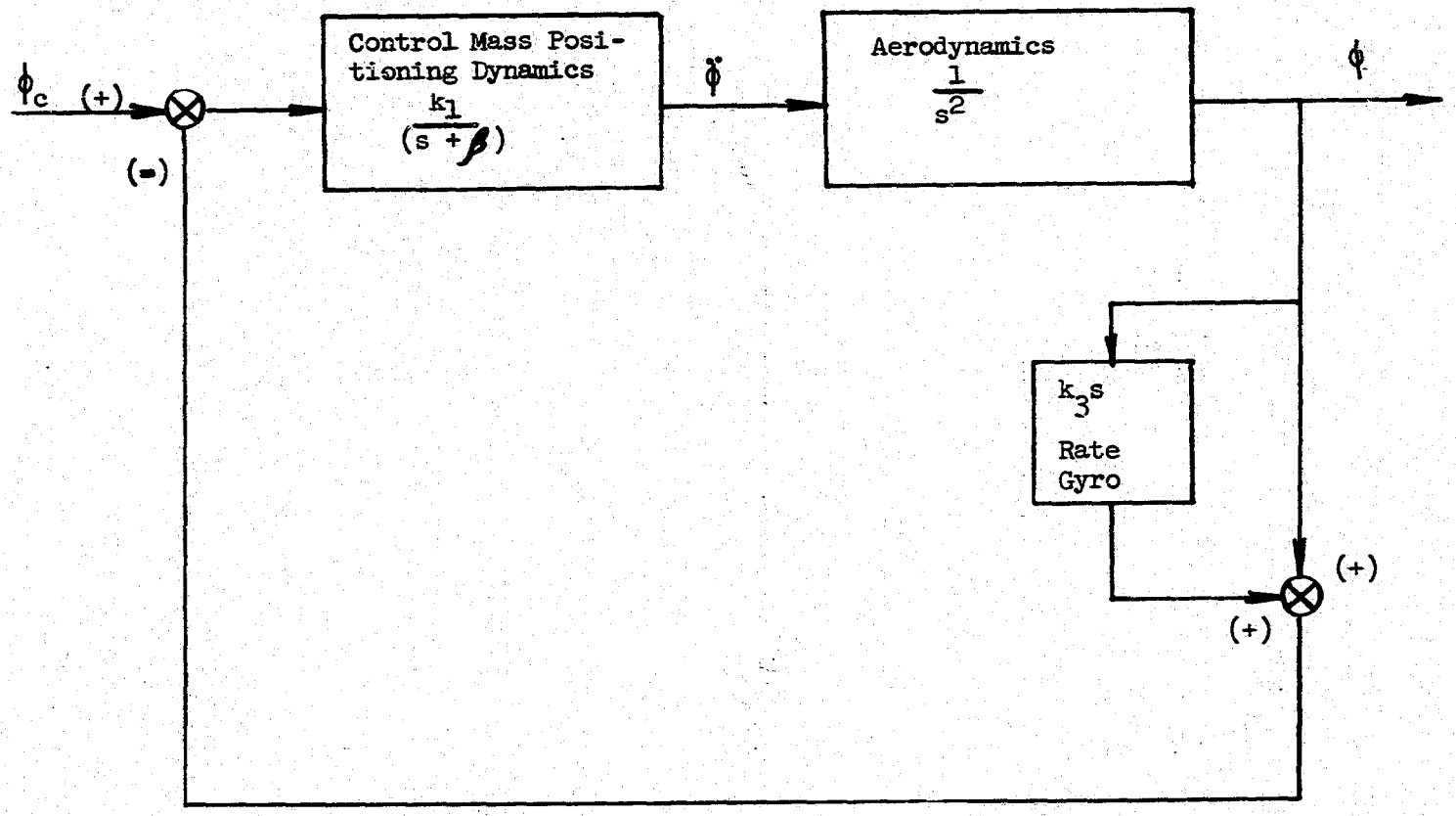

Fig. G-1 ROLL CONTROL TRANSFER FUNCTIONS

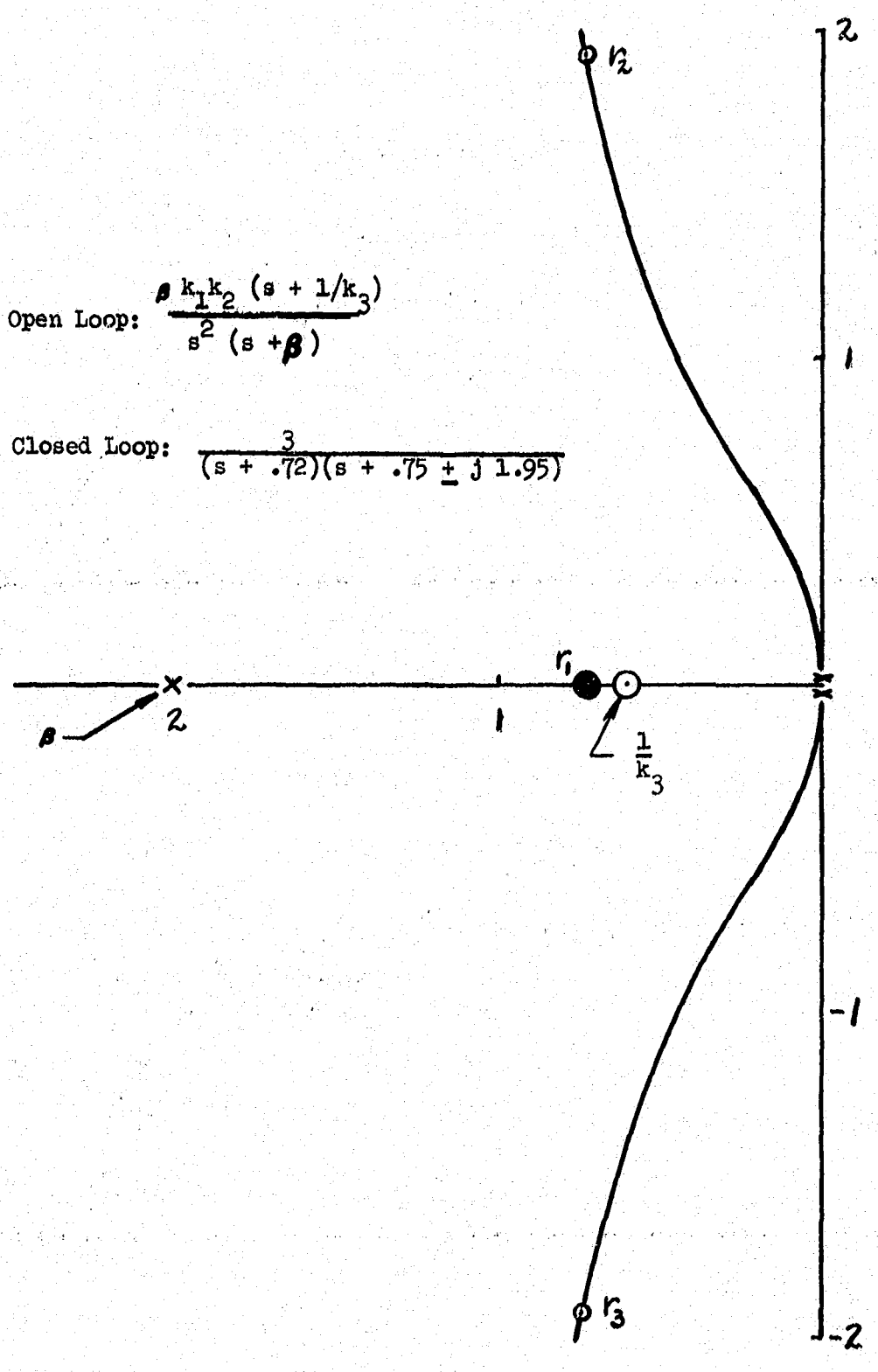

Fig. G-2 ROOT LOCUS FOR MASS ROLL CONTROL

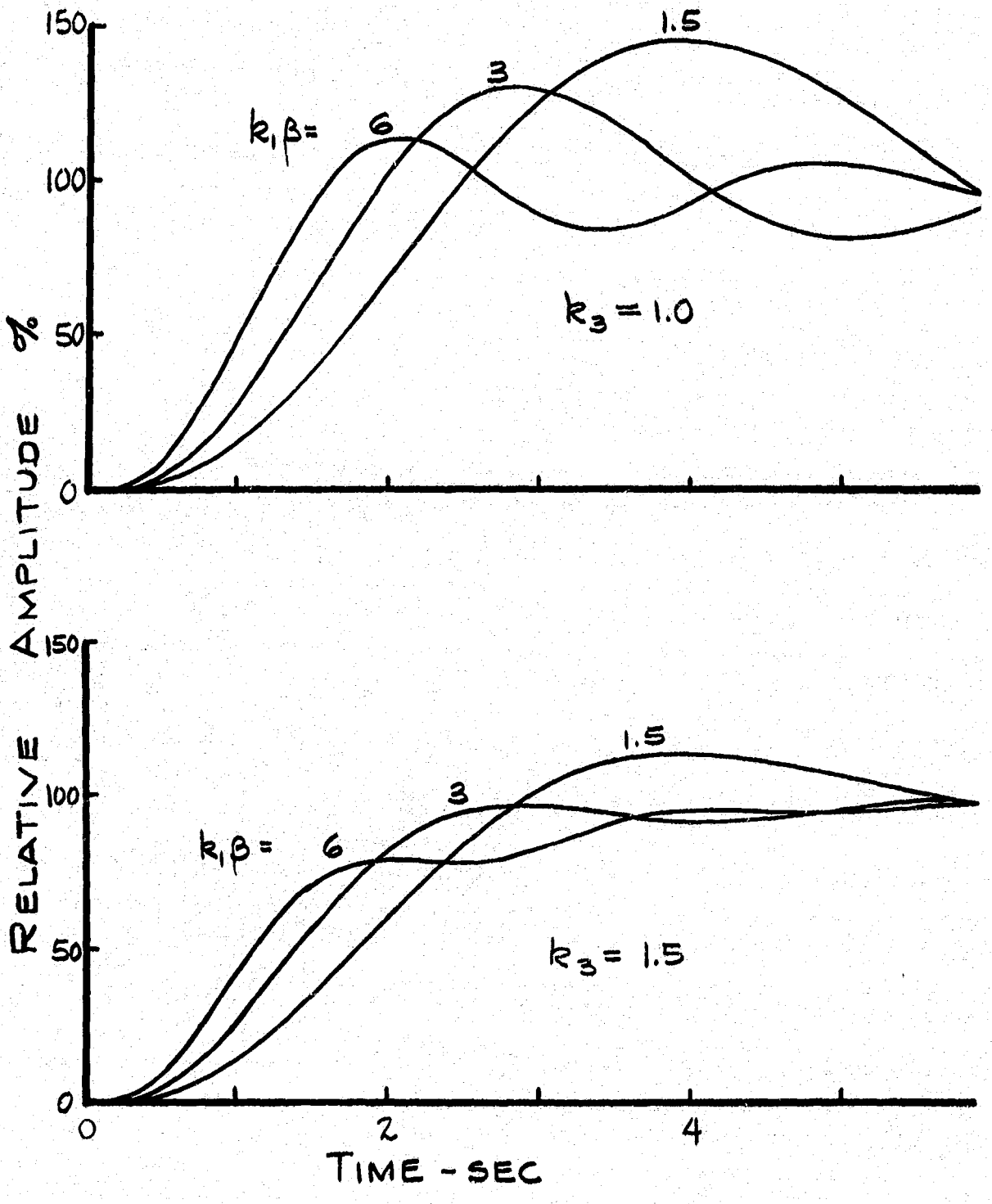

Fig. G-3 TRANSIENT RESPONSE FOR MASS SYSTEM

a torque reaction in addition to translation was devised. Some additional complexity was introduced by the clutching requirement to limit wheel speed.

The control loop for the mass plus wheel is shown in Fig. G-4. The corresponding root locus of Fig. G-5 demonstrates somewhat greater stability and damping than obtained with the translating mass only. The transient roll response with the wheel is shown in Fig. G-6 and illustrates the control available over the damping characteristic. By changing the rate gyro feedback, the system may be overdamped, as shown for $k_3 = 1$, or slightly underdamped, as shown for $k_3 = 0.5$. Note also that the response is twice as fast as before.

Figure G-6 was generated with a system using only 1/3 of the mass translational velocity and distance of Fig. G-3. The advantages obtained are (1) twice the available torque for the same translational mass; (2) reduced mass velocity generating less yaw perturbation; (3) complete control of damping for optimum stability margin; and (4) best response time by a factor of 2.

Guidance Errors Associated with Roll Angle Control

The control of roll angle is "inside the loop", and, therefore, the accuracy of the control system is not particularly critical. For example, if the control system gave an angle of 100 degrees when only 90 degrees were asked for, we would experience a 10 ft/sec. velocity discrepancy at the beginning of the flight. If the source of the error were such that it decreased linearly to zero when zero roll is called for (the most likely type of error), then the flight would be flown with an average velocity error of 5 ft/sec., and

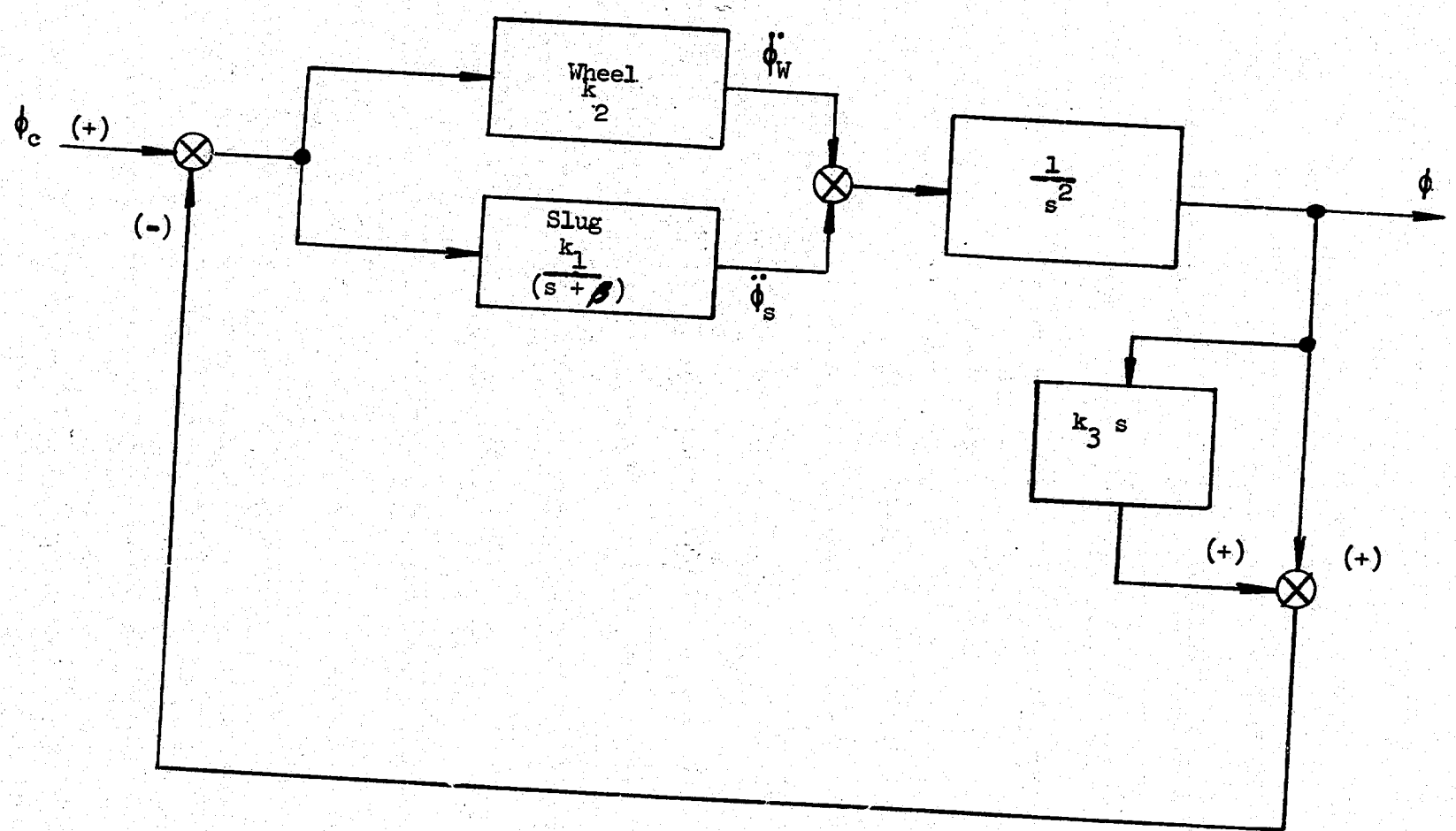

Fig. G-4 ROLL CONTROL TRANSFER FUNCTION

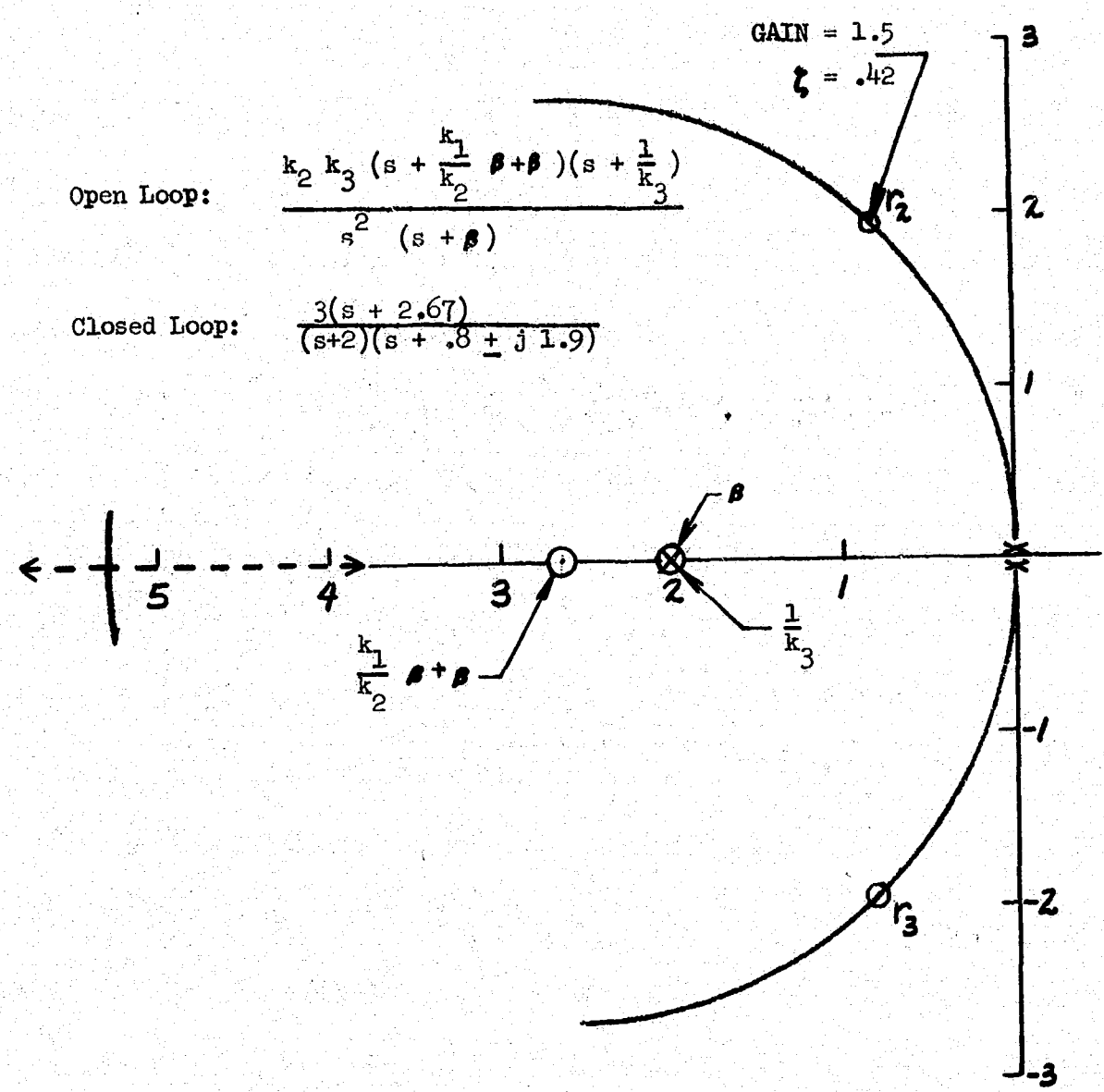

Fig. G-5 ROOT LOCUS FOR MASS AND WHEEL ROLL CONTROL

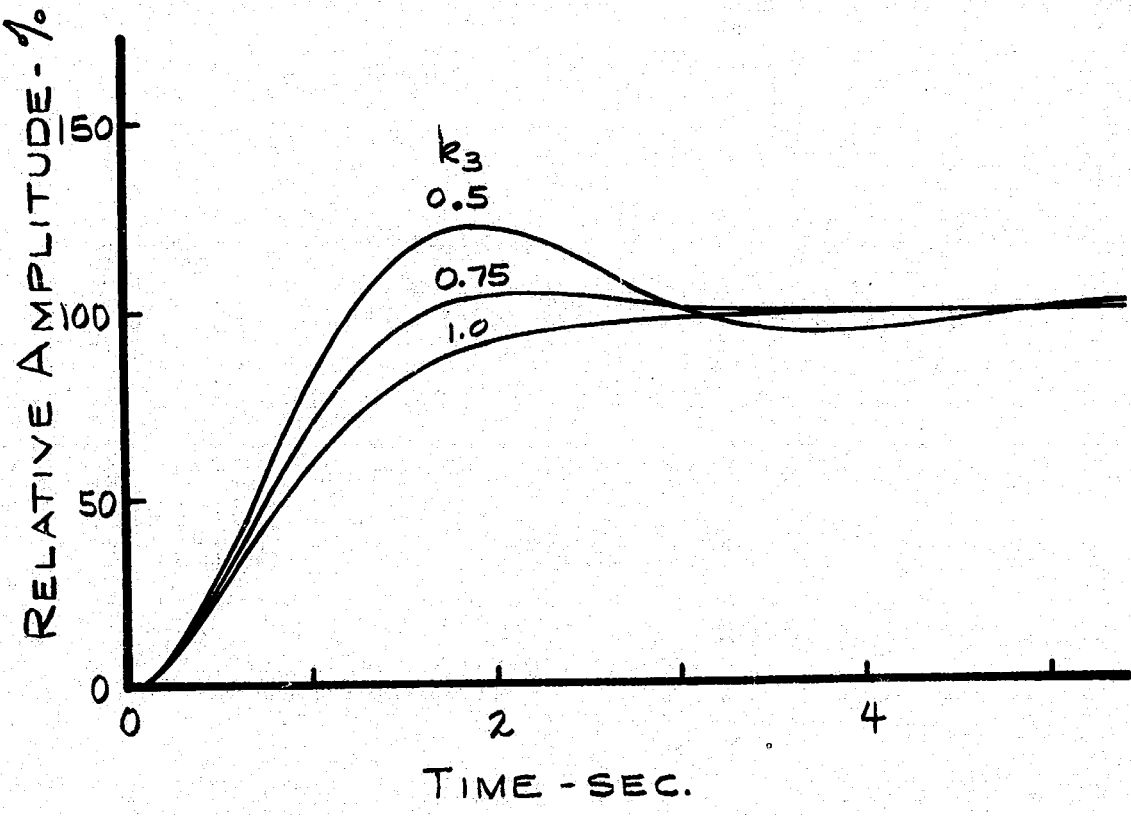

Fig. G-6 TRANSIENT REPONSE FOR MASS & WHEEL

the accumulated range error would be roughly 4,000 feet. The insensitivity of the distance flown to errors in roll angle is evident; 0.004 percent range error per percent of roll error.

APPENDIX H

DESPIN MOTION CHARACTERISTICS FOR ASYMMETRIC LIFTING VEHICLES

One feature of the concept which simplifies the design considerably is the aerodynamic despin with the offset control slug. A reaction despin system is eliminated saving weight and complexity. Furthermore, despin is constrained until entry into the sensible atmosphere, and hence, dynamic pressure is available to aerodynamically stabilize the spacecraft.

To insure that satisfactory prediction and control of despin behavior and spacecraft oscillations could be achieved, a critical examination of the motion characteristics for lifting spacecraft with unsymmetrical aerodynamics and inertial properties was undertaken. The results are described briefly in this Appendix.

Existing motion theory for spinning symmetrical spacecraft with small asymmetrics was found to provide conservative prediction for angle-of-attack convergence and despin. A technique for eliminating the build-up of trim caused by control mass displacement during passage through roll resonance was developed.

Despin

The despin deceleration with the slug displaced is given by,

$$\frac{dp}{dt} = - \frac{y_G C_N A \bar{q}}{I_x}$$

where C_N includes trim and angle-of-attack effects. For an exponential atmosphere and with

$$\frac{dh}{dt} = V \sin \gamma$$

$$dp = \frac{y_G C_N V^2 A \rho_o e^{-\beta h} dh}{2 I_x V \sin \gamma}$$

During entry with zero angle-of-attack, constant velocity and constant flight path angle,

$$\Delta p = - \frac{y_G C_L V^2 A}{2 I_x \beta V \sin \gamma} (\rho - \rho_e)$$

$$= \frac{y_G C_L \bar{q} A}{I_x \beta V \sin \gamma}$$

or

$$\Delta p = - \frac{y_G}{K_x^2} \frac{C_L}{C_D} \frac{g(a_D/g)}{\beta V \sin \gamma}$$

This relation specifies the control mass required to despin a given spacecraft prior to a desired g-level. (See Fig. 2-1). For a given control mass, the despin performance of the spacecraft can be assessed easily for the range of injection conditions obtained with the launch vehicle as shown in Fig. H-1. Good agreement with the numerical integration (RPM) is

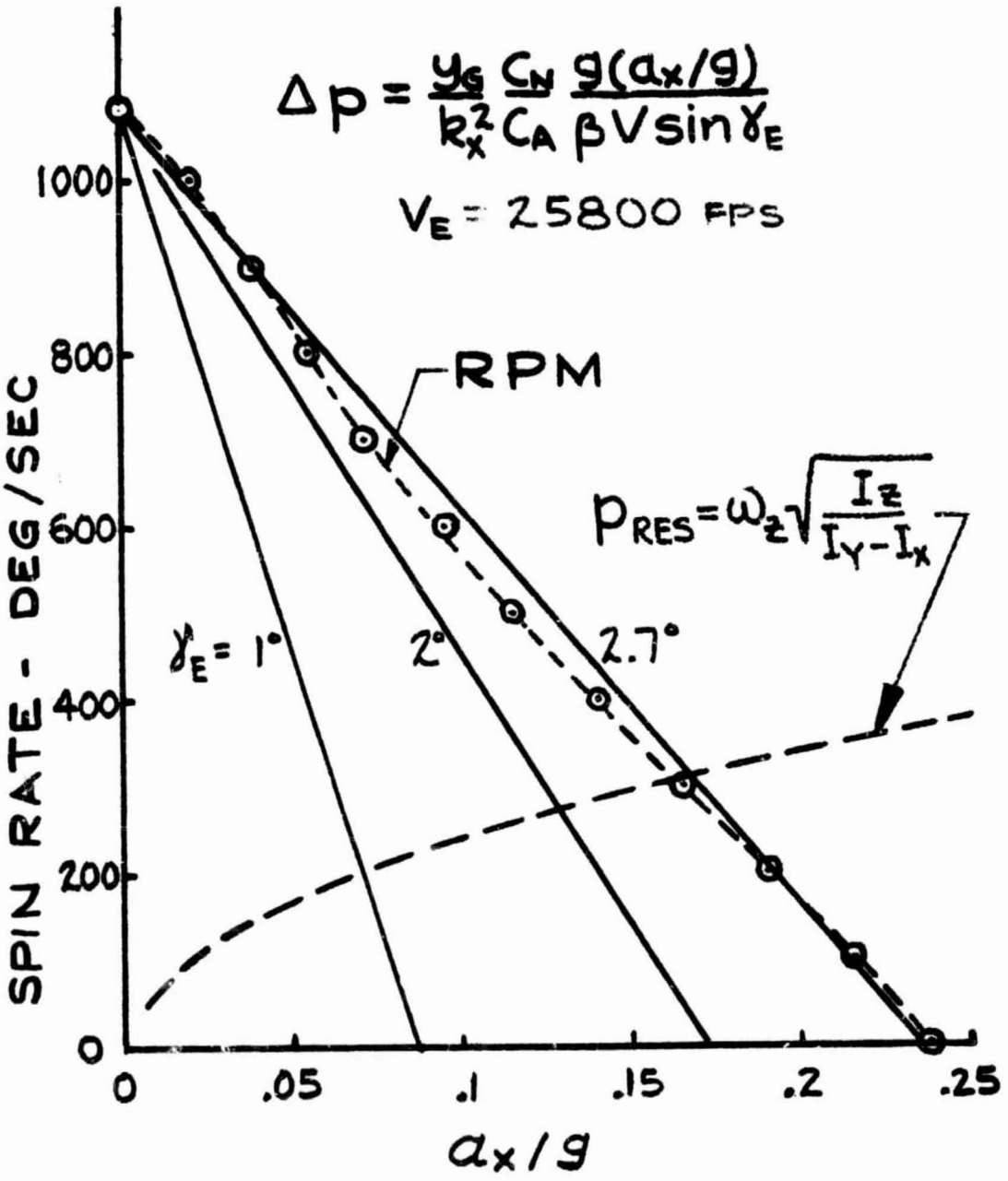

(a) Despin - a_x/g Relationship

Fig. H.1 PREDICTION OF DESPIN PERFORMANCE AND ANGLE-OF-ATTACK CONVERGENCE

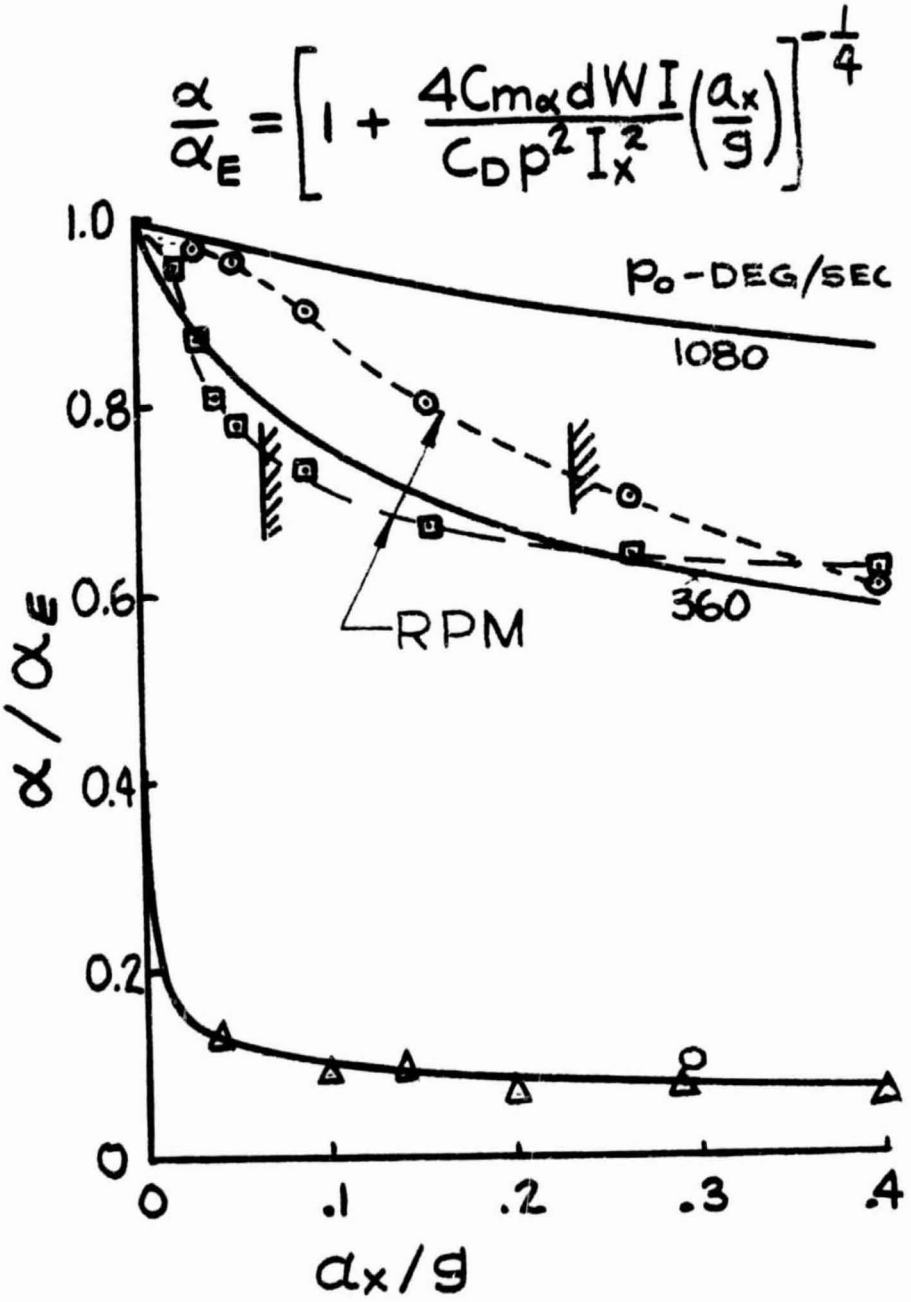

(b) Angle-Of-Attack - a_x/g Relationship

Fig. H.1 - (Concluded)

illustrated for the $\gamma_E = 2.7$ deg case. The minor differences accrue from the variable scale height β^{-1} of the 1962 U.S. standard atmosphere used in the RPM computation. Note that the spin rate for roll resonance is proportional to the square root of a_x/g. Prediction of angle-of-attack convergence with current theory for symmetrical reentry spacecraft at constant spin rate is conservative as shown in Fig. H-1.

The despin and angle-of-attack behavior with roll control is illustrated in Fig. H-2 for various initial spin rates. Because of the large built-in normal force asymmetry, the angle-of-attack oscillations from the initial 10 degrees cause only a small ripple in the roll rate histories. Excellent convergence of the reentry angle-of-attack is depicted on the right with a 22% reduction in amplitude at despin in each case. Subsequent pitch and yaw oscillations are well damped with increasing dynamic pressure. From despin at 0.25 g to pullout at 1.0 g, the pitch and yaw amplitudes are reduced by factor of 2 yielding an overall convergence of 2.5 results from reentry. Even with large reentry angles-of-attack such as shown here, satisfactory attitude control is maintained.

Roll Resonance Control

The moveable control mass must be located in the proper longitudinal position to achieve the angle-of-attack convergence of Figure H-1 and H-2. The lateral movement of the center of gravity induces a yaw trim from the resulting drag moment. When passing through resonance at high altitude, an amplification of this trim occurs as illustrated in Figure H-3. The peak

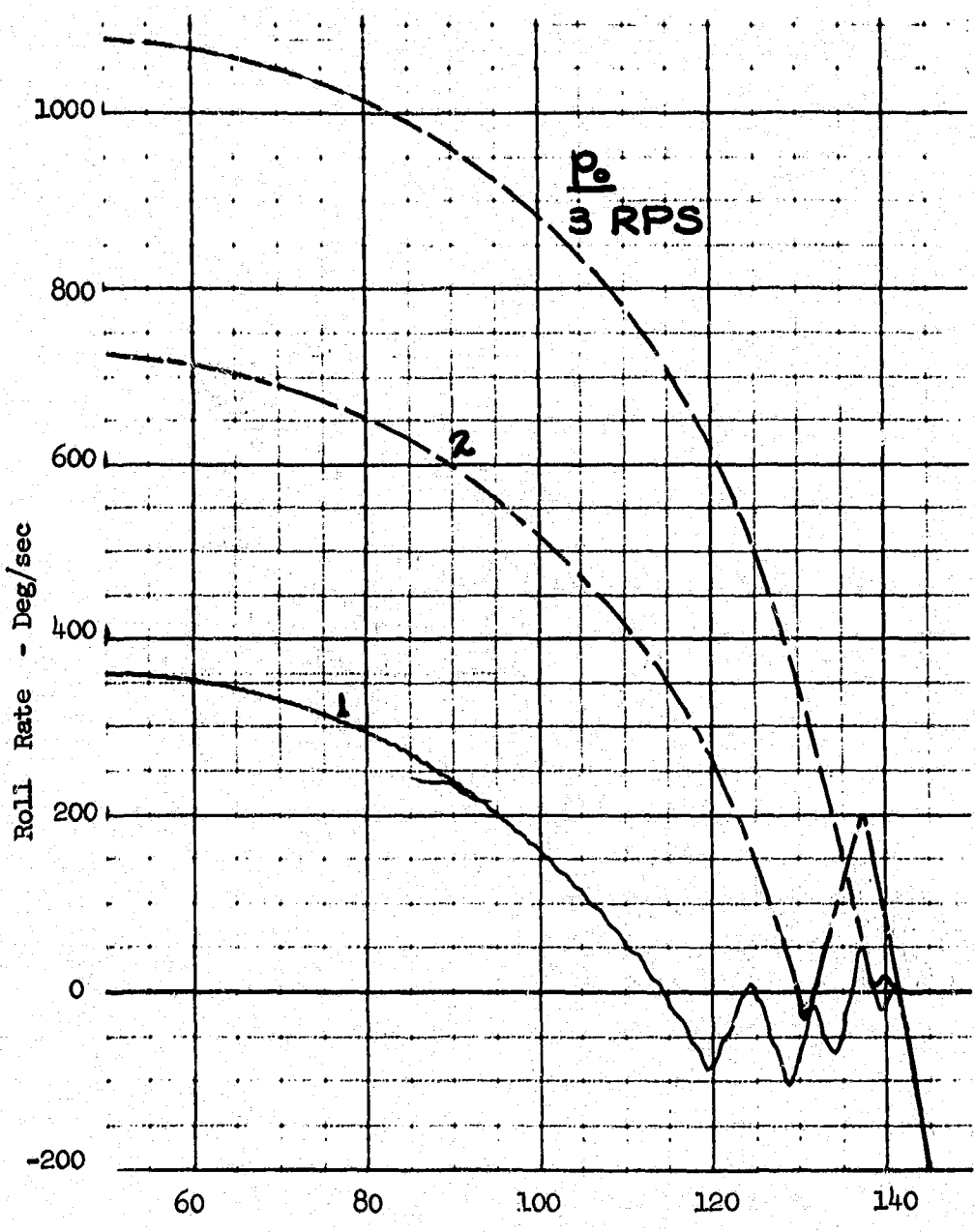

a) Despin Performance

Fig. H.2 DESPIN DYNAMICS WITH ROLL CONTROL

γ_E = 2.7 deg

V_E = 25,800 fps

$\dot{y}$ = $k_1 (\phi_c - \phi) + k_2 \dot{\phi} + k_3 y$

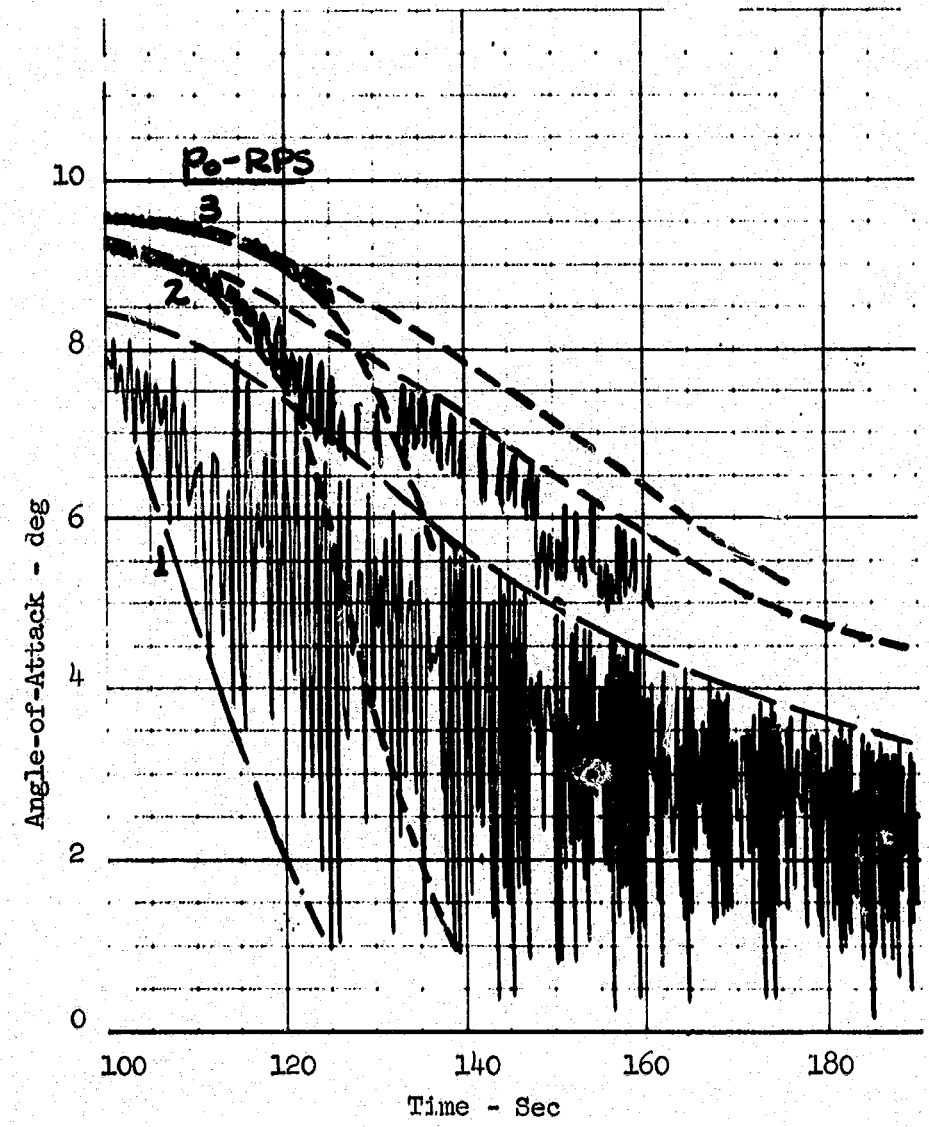

b) Angle of Attack Convergence

Fig. H.2 - (Concluded)

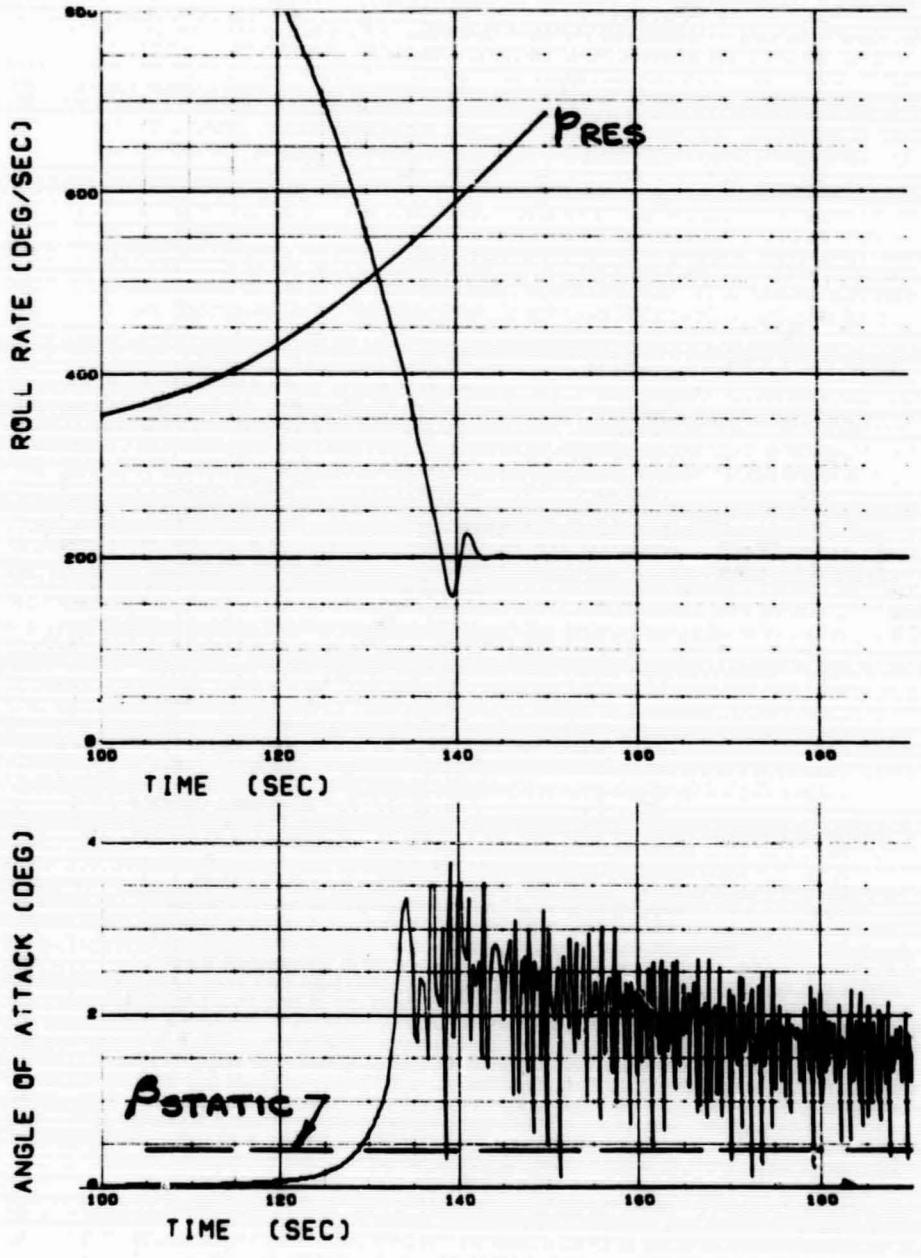

(a) Typical Time History

Fig. H.3 TRIM RESONANT BEHAVIOR

V_E = 25,800 fps

γ_E = 2.7 deg

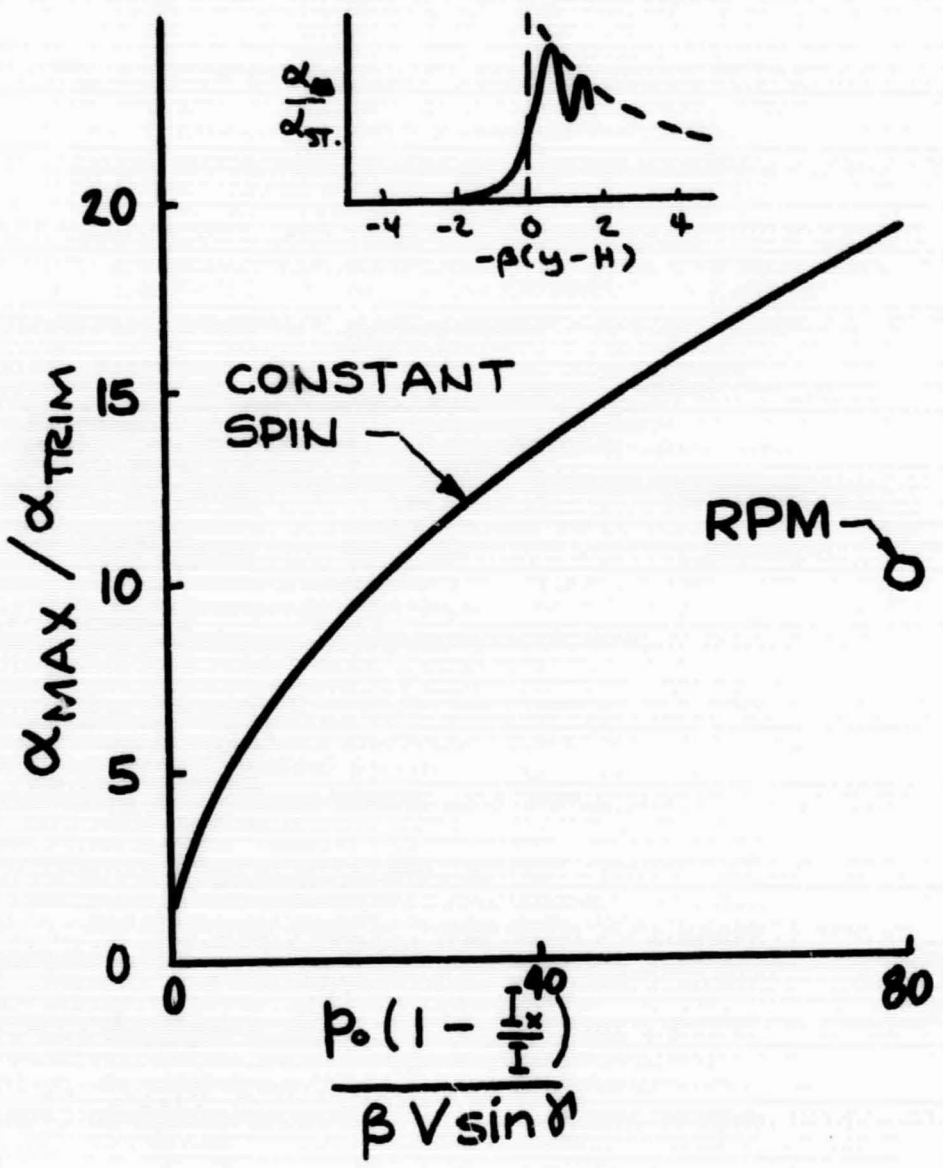

(b) Peak Response Characteristics

Fig. H.3 - (Concluded)

oscillation amplitude reaches 3.8 degrees, an amplification of 10, after despin. The peak amplitude after passage through resonance correlates with the rate of passage through resonance as shown in the right hand side of Fig.H-3. The prediction for constant spin (Ref. 22) is seen to be conservative.

The trim angle β_{trim} can be cancelled by locating the control mass ahead of the vehicle c.g. as shown in Fig.H-4. With the control mass at the longitudinal c.g., the principal axis translateswith the c.g. causing the resultant β_{trim} from the drag moment. With the control mass forward, the principal axis rotates when the slug is shifted laterally. By selecting x_m appropriately, the principal axis rotation can be made equal to the static trim angle. Hence,

$$x_m = \frac{C_D}{C_L \beta^d} \frac{y_G}{m y_m} \frac{I_z - I_x}{} = \frac{C_D}{C_L \beta^d} (K_z^2 - K_x^2)$$

An uncertainty in the c.g. longitudinal position or aerodynamic characteristics then causes a discrepency between the principal axis of rotation and the trim angle. Although the trim discrepancy is amplified by 10, the effects on the despin and angle-of-attack convergence is small as shown in Fig.H-5.

After despin and capture to 1 g, the attitude oscillations are reduced further by aerodynamic damping as shown in Fig. H-6. The expression for convergence was developed in Ref. 3. Note that after 300 seconds of guided flight, the residual oscillations from entry would be reduced by a factor of 10.

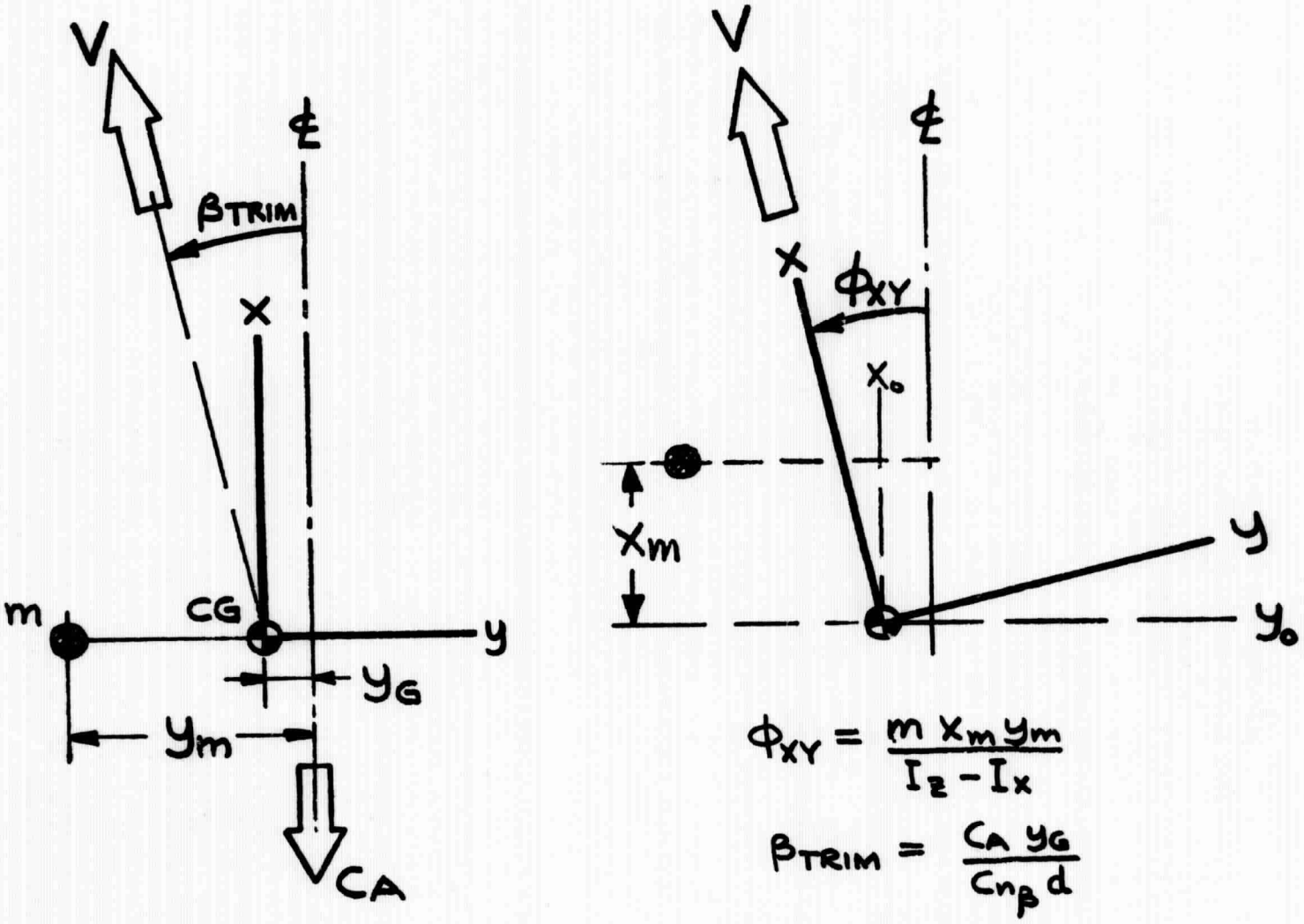

$$\phi_{XY} = \frac{m\, x_m\, y_m}{I_z - I_x}$$

$$\beta_{TRIM} = \frac{C_A\, y_G}{C_{n_\beta}\, d}$$

Fig. H.4 Control Mass Location Requirements

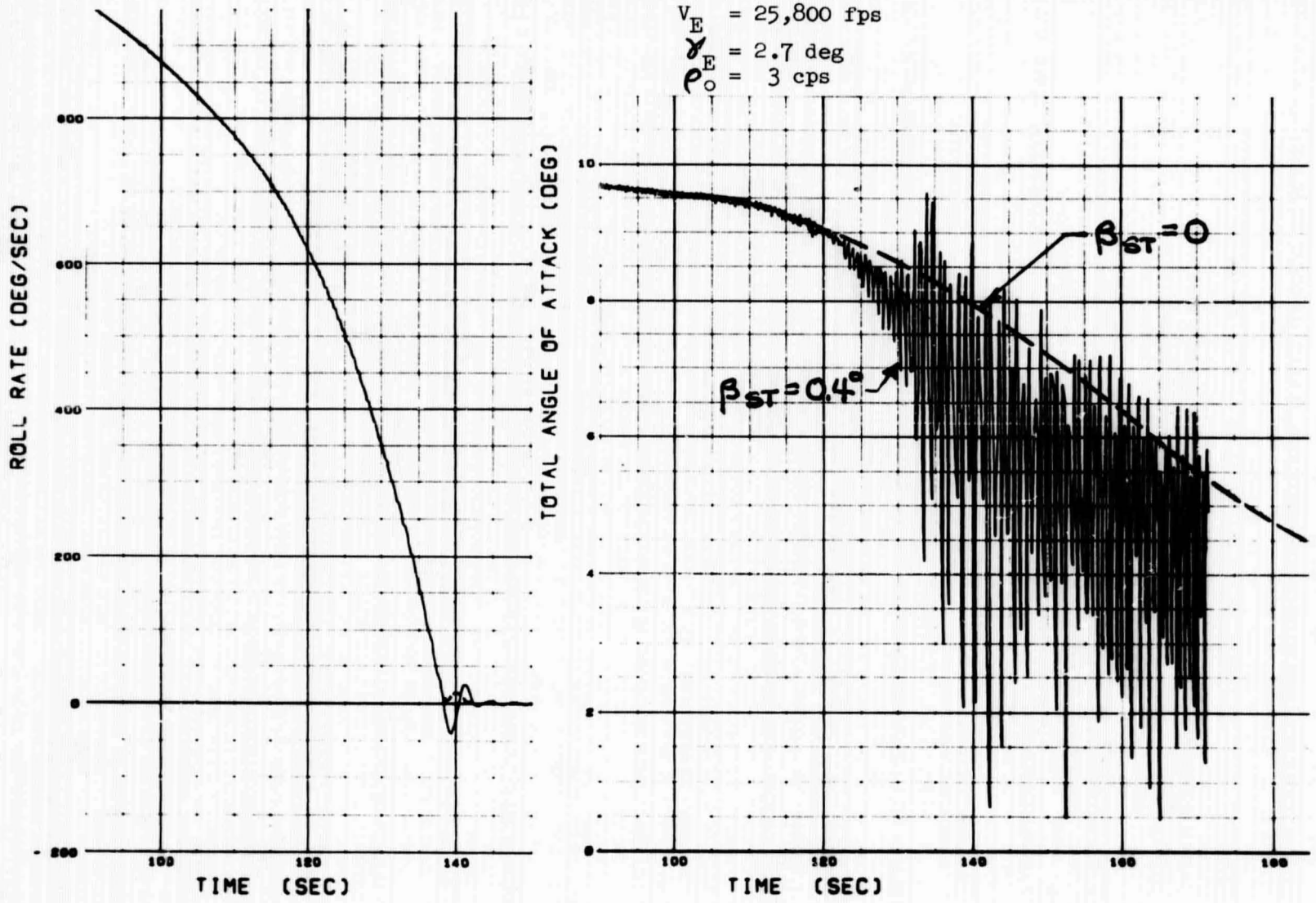

Fig. H.5 Effect of Trim Asymmetry on Despin Dynamics

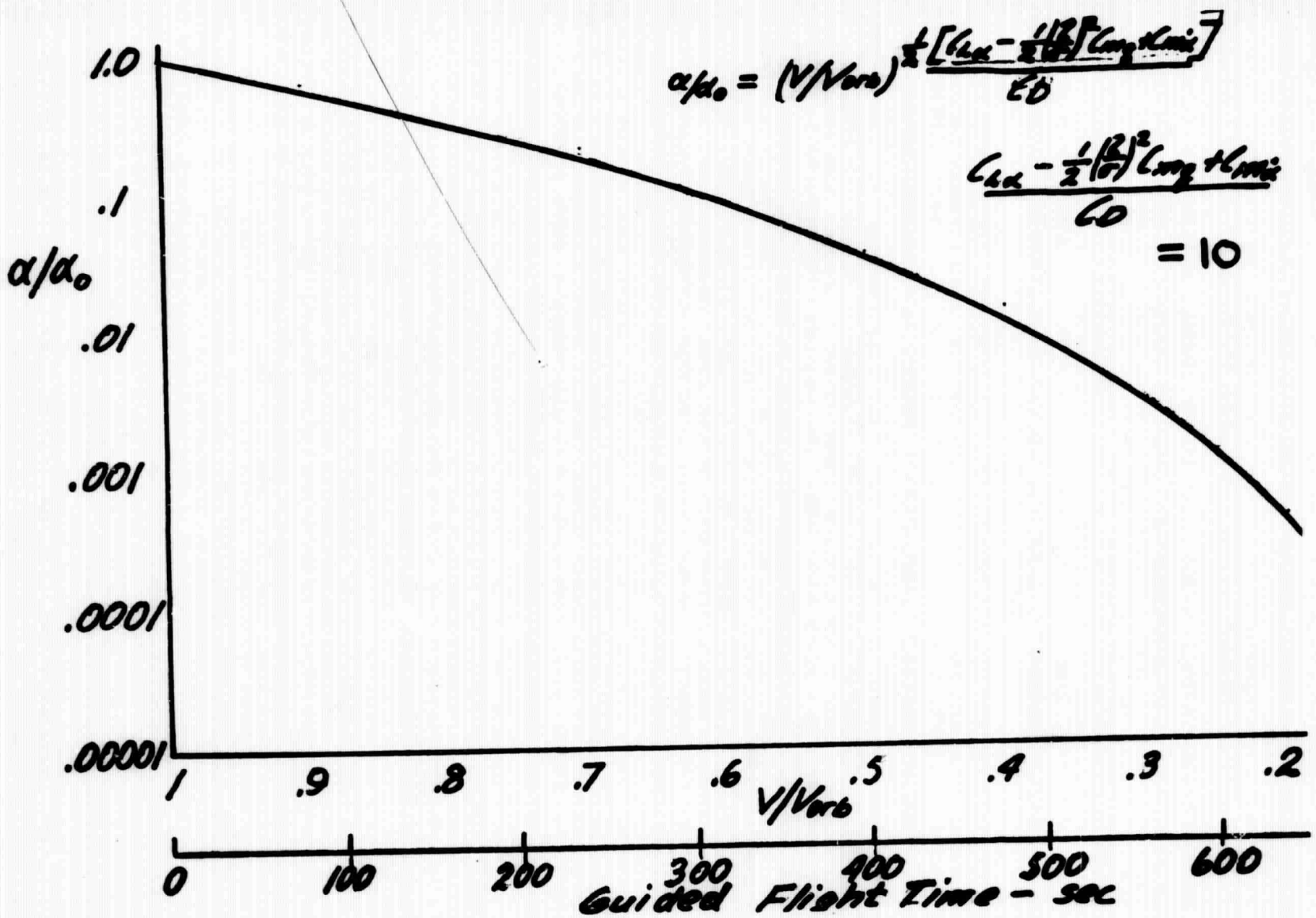

Fig. H-6 ANGLE-OF-ATTACK CONVERGENCE DURING GUIDED FLIGHT

APPENDIX I

SIX-DEGREE OF FREEDOM ENTRY GUIDANCE AND CONTROL SIMULATION (EGADS) PROGRAM

The Roll Pitch Motion (RPM) program (Ref. 2) used for the despin and dynamic motion analyses of Section 4 and Appendix H was modified to incorporate the translational degrees of freedom and the guidance mechanization in addition to the control system and asymmetric spacecraft aerodynamic and inertia properties.

The equations of motion used are:

$$\ddot{\beta} - A_{11}\dot{\beta} - A_{21}\dot{\alpha} - B_{11}\beta + B_{21}\alpha = C_1$$

$$\ddot{\alpha} + A_{12}\dot{\alpha} + A_{22}\dot{\beta} - B_{12}\alpha - B_{22}\beta = C_2$$

$$\dot{p} = \frac{\bar{q}\,Ad}{I_x}\left[C_{l_\beta}\beta - (C_{N_\alpha}\alpha + C_{N_o} - \phi_{xy}C_A)\frac{\Delta CG}{d}\sin\Gamma - (C_{Y_\beta}\beta + C_{Y_o})\frac{\Delta CG}{d}\cos\Gamma\right]$$

$$\dot{V} = -\frac{C_D\,\bar{q}\,A}{m} - g\sin\gamma$$

$$\dot{\gamma} = \frac{C_L\cos\phi\,\bar{q}\,A}{m\,V} - \frac{g}{V}\left[1 - \frac{V^2}{gr}\right]\cos\gamma$$

$$\dot{\psi} = \frac{C_L\sin\phi\,\bar{q}\,A}{m\,V}$$

$$\dot{h} = V\sin\gamma$$

$$\dot{R} = V \cos\gamma \cos\psi$$

$$\dot{XR} = V \cos\gamma \sin\psi$$

The guidance equations are

$$\phi_{com} = G_3 \left[g_{set} - a_x/g - REFER \right]$$

where $$REFER = REFER_{\cdot} + \int_{t-dt}^{t} G2 \left[g_{set} - a_x/g - G_1 V_e \right] dt$$

$$V_e = V_{offset} + \int_{o}^{t} a_x/g \, dt - \int_{\tau}^{t} g_{set} \, dt$$

and $$g_{set} - a_x/g - 0.05 \leq REFER_{\cdot} \leq g_{set} - a_x/g$$

The Control Equations are

$$\ddot{y}_m = K_1 \left[\phi_{CL} - \phi - K_2 \dot{\phi} - K_3 y_m - K_4 \dot{y}_m \right]$$

$$\dot{p}_{wheel} = \frac{K_5}{I_x} \left[\phi_{CL} - \phi - K_2 \dot{\phi} \right]$$

The coefficients of the α-β equations are:

$$A_{11} = \frac{\bar{q} A}{mV} \left(C_{y_\beta} - C_A - \frac{md^2}{Ig} C_{n_r} \right)$$

$$A_{12} = \frac{\bar{q} A}{mV} \left(C_{L_\alpha} - \frac{md^2}{Iy} C_{m_q} \right)$$

$$A_{21} = p \left(1 + \frac{I_y - I_x}{I_g} \right)$$

$$A_{22} = p \left(1 + \frac{I_g - I_x}{I_y} \right)$$

$$B_{11} = -C_{n_\beta} \bar{q} \, Ad/I_g + p^2 (I_y - I_x)/ I_g$$

$$B_{12} = C_{m_\alpha} \bar{q} \, Ad/I_y + p^2 (I_g - I_x)/I_y$$

$$B_{21} = -p \frac{\bar{q}A}{mV} \left[C_{L_\alpha} \frac{I_y - I_x}{I_z} - \frac{md^2}{I_z} C_{n_r} \right] - \dot{p}$$

$$B_{22} = -p \frac{\bar{q}A}{mV} \left[(C_{y_\beta} - C_A) \frac{I_z - I_x}{I_y} - \frac{md^2}{I_y} C_{m_q} \right] - \dot{p}$$

$$C_1 = (C_{m_o} \cos \lambda - C_A \frac{\Delta Cg}{d} \cos \Gamma + \phi_{xy} C_{n_\beta}) \bar{q} Ad/I_z$$

$$C_2 = (C_{m_o} \sin \lambda - C_A \frac{\Delta Cg}{d} \sin \Gamma) \bar{q} Ad/I_y$$

The primary feature of the program is that it calculates the angular motion of the principal axis about the trajector/ where the trajectory interaction is included in the coefficients. The spacecraft aerodynamics are described in the geometric axis and transformed to the rotated principal axis when the control mass is displaced.

Variable spacecraft mass properties (m, Ix, Iy, I_z vs. time) and linear aerodynamic characteristics (C_{m_α}, C_{m_q}, $C_{n_{p\alpha}}$, C_A, C_{L_α}, C_{y_β}, C_{n_β}, C_{l_β} versus Mach no.) are handled by table look-up. C_{l_β} is also a function of angle-of-attack. The atmosphere is described by a piece-wise exponential fit. The Adams-Moulton routine adjusts the time interval to maintain accuracy. Graphical output for the Stromberg-Carlson 4020 plotter is included.

The resultant program is economical to operate as indicated on the next page for the available programs options:

Option	Flight Time/Computer Time Sec/Sec
Guidance	22
Guidance & Control	8
Guidance & Control & Dynamics	4

APPENDIX J

DERIVATION OF ENVIRONMENTS SIMULATION EQUATIONS

This Appendix derives the relationships which permit separation of the reentry flight environment into trajectory and configuration related parts and forms the analytical basis for the comparisons of Section 7.

Convective Heating Rate

The local heating rate can be expressed as:

$$\dot{q} = \dot{q}_{stag} \; \dot{q}/\dot{q}_{stag}$$

Substituting the usual expression for stagnation heating:

$$\dot{q} = \frac{17,600}{\sqrt{R_n}} \left(\frac{\rho}{\rho_{sea\ level}}\right)^{\frac{1}{2}} \left(\frac{V}{26,000}\right)^{3.15} \dot{q}/\dot{q}_{stag}$$

In terms of drag deceleration,

$$\dot{q} = \frac{18.6}{\sqrt{R_n}} \left[\frac{W}{C_D A}\right]^{\frac{1}{2}} \dot{q}/\dot{q}_{stag} \left(\frac{a_D}{g}\right)^{\frac{1}{2}} \left(\frac{V}{V_{orb}}\right)^{2.15}$$

The reference heat rate is defined as,

$$\dot{q}_{ref} = \frac{18.6}{\sqrt{R_n}} \left[\frac{W}{C_D A}\right]^{\frac{1}{2}} \dot{q}/\dot{q}_{stag}$$

$$\dot{q} = \dot{q}_{ref} \left(\frac{a_D}{g}\right)^{\frac{1}{2}} \left(\frac{V}{V_{orb}}\right)^{2.15}$$

For flight at constant angle-of-attack for lifting entry trajectories of interest, the reference heat rate can be considered a constant.

Shear Stress

From Reynolds analogy, assuming a cold wall and a Prandl number of unity, the local skin friction coefficient based on stream conditions is related to the heating rate through the equation,

$$C_f = 3430\left(\frac{V_{edge}}{V}\right) \frac{\dot{q}}{\rho V^3}$$

The local shear stress is then,

$$\tau = 1715 \left(\frac{V_{edge}}{V}\right) \frac{\dot{q}}{V}$$

and from the equation for heating rate

$$\tau = 1715\left(\frac{V_{edge}}{V}\right) \frac{\dot{q}_{ref}}{V}\left(\frac{a_D}{g}\right)^{\frac{1}{2}}\left(\frac{V}{V_{orb}}\right)^{2.15}$$

$$\tau = \frac{1715}{25,600}\left(\frac{V_{edge}}{V}\right) \dot{q}_{ref}\left(\frac{a_D}{g}\right)^{\frac{1}{2}}\left(\frac{V}{V_{orb}}\right)^{1.15}$$

or

$$\tau = \tau_{ref} \left(\frac{a_D}{g}\right)^{\frac{1}{2}}\left(\frac{V}{V_{orb}}\right)^{1.15}$$

with

$$\tau_{ref} = .067\, \dot{q}_{ref} \frac{V_{edge}}{V}$$

Pressure

The local pressure is available directly from the pressure coefficient,

$$P = C_p q + P_o$$

$$P = q\left[C_p + \frac{1}{.7M^2}\right]$$

At the high Mach numbers of interest, the second term in the brackets may be ignored, then

$$P = C_p q$$

$$P = C_p \frac{W}{C_D A}\left(\frac{a_D}{g}\right)$$

Thus:

$$P_{ref} = C_p \frac{W}{C_D A}$$

$$P = P_{ref}\left(\frac{a_D}{g}\right)$$